

**UNSTEADY AERODYNAMICS OF FLAPPING WINGS**

**ZHANG LIUHANG**

*(B. Eng. (Hons.), NUS)*

**A THESIS SUBMITTED FOR THE DEGREE OF  
DOCTOR OF PHILOSOPHY**

**DEPARTMENT OF MECHANICAL ENGINEERING**

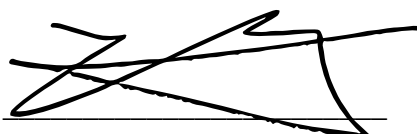
**NATIONAL UNIVERSITY OF SINGAPORE**

**2013**

## Declaration

I hereby declare that this thesis is my original work and it has been written by me in its entirety. I have duly acknowledged all the sources of information which have been used in this thesis.

This thesis has also not been submitted for any degree in any university previously.

A handwritten signature in black ink, consisting of several overlapping, fluid strokes that form a stylized representation of the name 'Zhang Liuhang'.

Zhang Liuhang

30 August 2013

## Acknowledgements

First and foremost, I would like to express my sincerest appreciations to my supervisor, A/Prof Yeo Khoon Seng for his academic guidance and invaluable support throughout my candidature. I have benefitted extensively from his remarkable patience, persisting enthusiasm, creative insights and immense knowledge in my research work and thesis writing. I would like to especially thank him for giving me the opportunity to pursue a PhD degree and work with many great and wonderful individuals within his research group.

I also wish to thank all the members of A/Prof Yeo Khoon Seng's unsteady aerodynamics research group. In particular, I would like to thank Dr Shyam Sundar for constantly inspiring and enlightening me in both research and life. I would like to thank Dr Wu Di for all the fruitful research discussions we had in the years past and for spending his own leisure time to proofread my thesis. I appreciate all the help and support I have received from Dr Yu Peng, Mr Nguyen Tan Trong and Dr Wang Xiaoyong. I would also like to thank Prof Lim Tee Tai and Dr Lua Kim Boon for their valuable comments and suggestions during research meetings.

I am grateful for all the support and encouragement I have received from my colleagues in the Department of Material Science and Engineering, NUS during my thesis writing while working as a full-time teaching assistant at the same time. Special thanks should be given to Asst/Prof Chiu Cheng-Hsin, Dr Kong Hui Zi and Dr Liyanage Chamila for their understanding and help.

I would also like to acknowledge the financial support from National University of Singapore and the research facilities provided by the Fluid Mechanics Laboratories and the Computer Centre of NUS for my PhD study.

I would also like to thank my most important friends: Cai Yexin, Cao Yanyan, Chen Xiaodong, Hong Jiang, Huang Xiaonan, Jiang Xiaofeng, Jing Peng, Li Xin, Liu Lu, Lu Ziyu, Luan Xiaolei, Luo Qian, Shou Chong, Su Dan, Wang Biaodong, Wang Yadong, Wu Shenghua, Xu Xiao, Xu Yi, Yang Kai, Zhao Yanyan, Zhuang Zhong. It is wonderful to have you guys in my life.

I am deeply indebted to my father Zhang Jianmin and my mother Liu Xuequn for

their great love and unconditional support. Last but not least, my deepest gratitude goes to my beloved wife, Tang Qing. Without her, I would not have had the faith to make it this far.



# Table of Content

<b>Declaration</b>	<b>i</b>
<b>Acknowledgements</b>	<b>ii</b>
<b>Table of Content</b>	<b>iv</b>
<b>Summary</b>	<b>x</b>
<b>List of Tables</b>	<b>xii</b>
<b>List of Figures</b>	<b>xiii</b>
<b>List of Symbols</b>	<b>xxii</b>
<b>CHAPTER 1: Introduction</b>	<b>1</b>
<b>1.1 Background</b>	<b>1</b>
<b>1.2 Insect Flight Studies Overview</b>	<b>2</b>
<b>1.3 Numerical Studies in Insect Flight</b>	<b>6</b>
<b>1.4 Motivation and Outline</b>	<b>8</b>
<b>CHAPTER 2: Numerical Scheme</b>	<b>10</b>
<b>2.1 Introduction</b>	<b>10</b>
<b>2.2 Governing Equation</b>	<b>10</b>
<b>2.3 A Hybrid Meshfree Method</b>	<b>11</b>
<b>2.4 SVD-GFD Scheme</b>	<b>12</b>
<b>2.5 Projection Method</b>	<b>14</b>
<b>2.6 Iterative Solver for Pressure Poisson Equation</b>	<b>16</b>

<b>2.7</b>	<b>Other Numerical Implementations</b>	<b>18</b>
2.7.1	Artificial Dissipation	19
2.7.2	Upwind Scheme	19
2.7.3	Adaptive Time Stepping	20
2.7.4	Parallelization	21
<b>2.8</b>	<b>Fluid-Structure Interaction</b>	<b>22</b>
<b>2.9</b>	<b>Handling of Hybrid Grid</b>	<b>23</b>
2.9.1	Nodal Classification	24
2.9.2	Nodal Class Transition	25
2.9.3	Nodal Selection	26
<b>2.10</b>	<b>Special Numerical Treatment for Handling of Body Collisions</b>	<b>29</b>
<b>2.11</b>	<b>Validation Cases</b>	<b>31</b>
2.11.1	3D Flow Past Sphere	31
2.11.2	Validation of Artificial Dissipation Model	34
2.11.3	3D Falling Sphere FSI	35
<b>2.12</b>	<b>Summary</b>	<b>36</b>
<b>CHAPTER 3:</b>	<b>Geometric and Kinematic Modelling of Flapping Wings</b>	<b>38</b>
<b>3.1</b>	<b>Introduction</b>	<b>38</b>
<b>3.2</b>	<b>Geometric Modelling</b>	<b>38</b>
3.2.1	3D CAD Modelling	39
3.2.2	Rigid Body Assumption	42
3.2.3	Mesh Generation	42

<b>3.3</b>	<b>Kinematics of Flapping Motion</b>	<b>47</b>
3.3.1	Coordinate System Definition	47
3.3.2	Flapping Motion Definitions	50
3.3.3	Prescribed Flapping Kinematic Models	54
3.3.4	Simple Harmonic Flapping Kinematics	55
3.3.5	Trapezoidal Function Kinematic Model	57
3.3.6	Natural Cubic Spline Fit Function Kinematic Model	62
3.3.7	Other Implementations for Resolving Insect Flapping Kinematics	64
<b>3.4</b>	<b>Non-dimensionalisation</b>	<b>65</b>
<b>3.5</b>	<b>Definition of Reynolds Number, Lift Coefficient and Drag Coefficient</b>	<b>65</b>
<b>3.6</b>	<b>Summary</b>	<b>66</b>
 <b>CHAPTER 4: Analysis of Kinematic Effects on Unsteady Aerodynamics of Prescribed Flapping Flight</b>		 <b>68</b>
<b>4.1</b>	<b>Introduction</b>	<b>68</b>
<b>4.2</b>	<b>Verification of a Flapping Wing Pair Simulation</b>	<b>68</b>
4.2.1	Mechanical Setup	69
4.2.2	Numerical Setup	71
4.2.3	Validation with Experimental Data	72
4.2.4	Flow Structure Analysis	73
<b>4.3</b>	<b>Kinematic Models of Insect Flapping Wings</b>	<b>76</b>
4.3.1	Numerical Simulation Setup	77
4.3.2	Comparison of Aerodynamic Lift Between SHM and TF Kinematic Models	79

4.3.3	Augmentation of Lift by Wing Twist Phase Leading in SHM Kinematic Model	84
4.3.4	Augmentation of Lift by Wing Twist Phase Leading in TF Kinematic model	89
4.3.5	A Proposed Trapezoidal Function Kinematic model	92
4.3.6	Power Calculations of Flapping Flight Using Prescribed Kinematic models	95
<b>4.4</b>	<b>Summary</b>	<b>96</b>
<b>CHAPTER 5: Numerical Study of 3D Clap-and-Fling of Flapping Wings</b>		<b>97</b>
<b>5.1</b>	<b>Introduction</b>	<b>97</b>
<b>5.2</b>	<b>The Kinematics of Clap-and-Fling</b>	<b>99</b>
<b>5.3</b>	<b>Analysis of Flow in 3D Clap-and-Fling</b>	<b>104</b>
5.3.1	Augmentation of Overall Lift and Drag due to Clap-and-Fling	104
5.3.2	3D Aerodynamic Aspects of Clap	107
5.3.3	3D Aerodynamic Aspects of Fling	117
<b>5.4</b>	<b>The Effect of Reynolds Number on Lift Enhancement by Clap-and-Fling</b>	<b>126</b>
<b>5.5</b>	<b>The Effect of Clap on Fling</b>	<b>129</b>
<b>5.6</b>	<b>The Effect of Wing Tips Separation Distance on Lift Enhancement</b>	<b>131</b>
<b>5.7</b>	<b>Further Analysis of Wing Proximity Effect on Clap-and-Fling Lift Enhancement</b>	<b>133</b>
<b>5.8</b>	<b>The Effect of Wing Roots Separation Distance on Lift Enhancement</b>	<b>137</b>
<b>5.9</b>	<b>An Investigation of Lift Augmentation to Increased Power Requirement Relationship</b>	<b>139</b>
<b>5.10</b>	<b>Summary</b>	<b>140</b>
<b>CHAPTER 6: Parameterisation of Flapping Kinematics for Control</b>		<b>143</b>

<b>6.1</b>	<b>Introduction</b>	<b>143</b>
<b>6.2</b>	<b>Parameterisation of Flapping Kinematics</b>	<b>145</b>
6.2.1	Definition of Kinematic Parameters	145
6.2.2	The Reference Kinematics	149
6.2.3	Force and Moment Evaluations	150
<b>6.3</b>	<b>Effects of Kinematic Parameters on Aerodynamic Force and Moment Productions</b>	<b>151</b>
6.3.1	Effect of Variations in Mean Positional Angle of Mid-Sweep Plane on Mean Aerodynamic Force and Moment Productions	152
6.3.2	Effect of Changes in Sweep Amplitude on Mean Aerodynamic Force and Moment Productions	153
6.3.3	Effect of Variations in Mean Positional Angle of Mid-Twist Plane on Mean Aerodynamic Force and Moments Productions	155
6.3.4	Effect of Changes in Twist Amplitude on Mean Aerodynamic Force and Moment Productions	156
6.3.5	Effect of Variations in Twist Phase Difference on Mean Aerodynamic Force and Moment Productions	157
6.3.6	Effect of Variations in Mean Positional Angle of Mid-Elevation Plane on Mean Aerodynamic Force and Moment Productions	159
6.3.7	Effect of Changes in Elevation Amplitude on Mean Aerodynamic Force and Moment Productions	161
6.3.8	Effect of Changes in Elevation Phase Difference on Mean Aerodynamic Force and Moment Productions	162
<b>6.4</b>	<b>The Proposed Model for Preliminary Control of Flapping Flight</b>	<b>164</b>

6.4.1	The Approach for Derivation of a Simplified Model	165
6.4.2	Determination of the Coefficient Matrix	166
6.4.3	Verification of the Model	167
6.4.4	The Dynamic Response to Parameter Adjustments Based on the Preliminary Model for Targeted Mean Non-Dimensional Lift Force Increase of 0.5	167
6.4.5	The Dynamic Response to Parameter Adjustments Based on the Preliminary Model for Targeted Mean non-dimensional Drag (Thrust) Force Increase of 0.5	168
6.4.6	The Dynamic Response to Parameter Adjustments Based on the Preliminary Model for Targeted Mean Non-Dimensional Lateral Force Increase of 0.02	170
6.4.7	The Dynamic Response to Parameter Adjustments Based on the Preliminary Model for Targeted Mean Non-Dimensional Pitch Moment Increase of 0.2	171
6.4.8	The Dynamic Response to Parameter Adjustments Based on the Preliminary Model for Targeted Mean Non-Dimensional Roll Moment Increase of 0.05	172
6.4.9	The Dynamic Response to Parameter Adjustments Based on the Preliminary Model for Targeted Mean Non-Dimensional Yaw Moment Increase of 0.2	173
6.4.10	FSI Testing of the Preliminary Model	174
<b>6.5</b>	<b>Summary</b>	<b>176</b>
<b>CHAPTER 7:</b>	<b>Conclusions and Recommendations</b>	<b>178</b>
<b>7.1</b>	<b>Conclusions</b>	<b>178</b>
<b>7.2</b>	<b>Recommended Future Works</b>	<b>180</b>
<b>Reference</b>		<b>181</b>

## Summary

The Singular Value Decomposition General Finite Difference based computational fluid dynamic solver for three dimensional incompressible, viscous fluid flow at low Reynolds number with immersed moving boundaries is further developed and adapted to study the unsteady aerodynamics of flapping wings. The present study establishes a systematic geometric modelling method for construction of morphologically accurate and rigid insect wing models. A natural spline interpolation based flapping kinematics definition framework is outlined. It has shown to be robust and effective at mathematically describe any natural or simplified flapping kinematic models for numerical simulations.

The investigation of unsteady aerodynamics associated with different flapping kinematics reveals that SHM flapping kinematics of geometrically accurate insect wing is capable of generating more lift force than TF based flapping kinematics at the same Reynolds number. An optimised TF based flapping kinematic model which is capable of producing equivalent mean aerodynamic lift as the corresponding SHM flapping kinematic model is proposed. The aerodynamic power analysis shows that the proposed kinematics model is more efficient than SHM kinematics and hence a possibly better design for future flapping wing based MAVs.

A systematic three dimensional numerical study of clap-and-fling mechanism for a pair of rigid fruit fly wings at Reynolds number of 150 was conducted. The flapping kinematics was redesigned and justified to prevent interpenetration of wing models due to constraints of 3D simulations. Data analysis of the result have revealed interesting three dimensional unsteady aerodynamic effects that has been substantiated with flow field observations which demonstrates clearly the lift augmentation effects of “clap” and “fling” mechanisms separately. The strong vortex link formation in the opening gap between the wings during the fling phase was first observed in three dimensional flow visualisations. Effect of radial force enhancement due to clap-and-fling mechanism was also revealed which further demonstrates the significant difference of current 3D flow evolution results compared to 2D analysis.

Although lift enhancement ratio increases with decreasing Reynolds number of the

identical clap-and-fling mechanism, the result suggests that the drag is significantly increased at lower Reynolds number which leads to substantially reduced efficiency of the clap-and-fling motion. Present study also shows that lift augmentation ratio decreases with increasing wing root separation which suggests that the absence of clap-and-fling flapping motion in many insects is due to the anatomical separation of their wing roots. Further analysis suggests that clap-and-fling mechanism is favourable for insects to exploit due to linear lift to aerodynamic power ratio in reducing wing proximity.

A systematic approach to describing flapping flight kinematics using a set of 8 parameters external to the mathematical descriptions of kinematic functions are proposed for flapping flight control. A linear correlation of the mean aerodynamic forces and moments produced by the flapping wing with respect to each individual kinematic parameter is established within small limit of perturbation from the reference state. A preliminary control model is derived and the dynamic response is tested to demonstrate the effectiveness of the present approach.



## List of Tables

<i>Table 3-1 Important morphological parameters of fruit fly (Shyy et al., 2010)</i>	39
<i>Table 3-2 Summary of mesh generation on rigid bodies</i>	46
<i>Table 3-3 Piecewise continuous polynomial function describing translational motion of flapping wing</i>	59
<i>Table 3-4 Piecewise continuous sinusoidal polynomial function describing the rotational motion of the flapping wing</i>	60
<i>Table 4-1 Comparison of experimental wing morphology and actual wing morphology used in the following numerical studies</i>	71
<i>Table 4-2 Non-dimensionalised parameters of experimental setup for numerical simulation</i>	71
<i>Table 4-3 Mean lift coefficient and mean drag coefficient of a SHM and a TF kinematic model prescribed flapping flight</i>	80
<i>Table 4-4 Table of mean lift coefficient <math>C_l</math> comparison for variations of SHM kinematic model</i>	86
<i>Table 4-5 Decreasing Lift to Drag ratio and Lift to Power ratio as leading phase angle increases</i>	88
<i>Table 4-6 Calculated mean lift coefficient and lift to drag ratio and lift to power ratio of TF kinematic model prescribed flapping motions with different phase leading of twist over sweep</i>	92
<i>Table 4-7 The characteristic kinematic parameters describing the proposed kinematic model</i>	93
<i>Table 4-8 Specific aerodynamic power computed on the insect wings based on CFD solutions of different kinematic model prescribed flapping motions</i>	95
<i>Table 5-1 Parameters of wing roots separations and the corresponding dorsal bias of the mean positional angle of mid-sweep plane to achieve physical clap (* default wing roots separation in current studies)</i>	138
<i>Table 6-1 Parameterisation of kinematic functions</i>	145

## List of Figures

<i>Figure 2.1 Order of convergence within 6 iterations of different iterative methods</i>	17
<i>Figure 2.2 Relative computational cost for 4 cycles of flapping wing simulation, SOR's computational cost is taken as 1</i>	17
<i>Figure 2.3 Aerodynamic lift coefficient computed on the flapping wing as a result of different iterative methods used for solving pressure Poisson equation</i>	18
<i>Figure 2.4. Nodal distribution surrounding an insect wing where circular nodes represent Cartesian background nodes and square nodes represent meshfree nodes.</i>	25
<i>Figure 2.5 Cone based nodal selection</i>	28
<i>Figure 2.6 Sphere based nodal selection</i>	28
<i>Figure 2.7 3D nodal selection results from actual simulation: (a) nodal selection of Category 3 node near to a flat solid boundary; (b) nodal selection of Category 3 Cartesian background node.</i>	29
<i>Figure 2.8 Streamline plot of flow past sphere at different Reynolds number (A) <math>Re=50</math>, (B) <math>Re=100</math>, (C) <math>Re=150</math>, (D) <math>Re=200</math>, (E) <math>Re=250</math>, (F) <math>Re=300</math>, (G) <math>Re=350</math></i>	33
<i>Figure 2.9 Mean drag coefficient measured on sphere varied with respect to Reynolds number, this trend agrees well with the published experimental results of Roos and Willmarth (Roos &amp; Willmarth, 1971)</i>	33
<i>Figure 2.10 Vorticity iso-surface plot showing the periodic shedding of the wake vortices in a 3D flow past sphere problem at <math>Re=300</math></i>	34
<i>Figure 2.11 Computed drag coefficient of flow past sphere at <math>Re=150</math> shows minor deviation of aerodynamic effect due to the introduction of artificial dissipation</i>	35
<i>Figure 2.12 Velocity of the falling sphere with FSI computations showing the terminal velocity of <math>Re=50</math> to be approximately 1.62</i>	36
<i>Figure 3.1 Fruit fly with extended wing from top view, with courtesy of Phillip N. Appiah "<a href="http://www.discoverlife.org">http://www.discoverlife.org</a>"</i>	39
<i>Figure 3.2 Contour plot in accordance to actual fruit fly body geometry from top view, with courtesy of "<a href="http://flybase.org">http://flybase.org</a>"</i>	40

<i>Figure 3.3 Contour plot of actual fruit fly body geometry from side view, with courtesy of “<a href="http://www.uamont.edu/">http://www.uamont.edu/</a>”</i>	40
<i>Figure 3.4 Fruit fly wing contour mapping for 3D model construction, the wing root section to the left is omitted, with courtesy of “<a href="http://www.mheresearchfoundation.org/">http://www.mheresearchfoundation.org/</a>”</i>	41
<i>Figure 3.5 Flat and smooth thin fruit fly wing with thickness of 2% wing length (or 5% mean chord) and sharp edges</i>	42
<i>Figure 3.6 Denser surface node distribution along the wing edges and coarser surface node distribution in the remaining area of the wing are observed in this fruit fly wing model. Triangles are used for plotting and area computation purposes and are not used in the meshless based numerical method</i>	44
<i>Figure 3.7 Four view schematic showing half exposed view of the meshless cloud volume surrounding the fruit fly wing, partial surface boundary of the meshless cloud volume is shown in grey in contrast to the wing volume in yellow (in the middle surrounded by the meshless cloud volume)</i>	45
<i>Figure 3.8 Exposed view of tetragonal finite volume elements within the meshless cloud volume surrounding fruit fly wing, the tetragonal elements are randomly distributed and size parameters are specified according to the desired mesh density</i>	45
<i>Figure 3.9 The full computational model of fruit fly in its computational domain demonstrating the surface mesh free nodes (purple colour rigid body surface) and the meshless nodal cloud surrounding the rigid bodies</i>	46
<i>Figure 3.10 The wing definition frame, showing a pseudo wing geometry defined. It can be seen that the wing boundary does not touch the origin as the wing root section is neglected in the geometric model for the simulation</i>	48
<i>Figure 3.11 The insect wing in the wing motion frame where the wing can be made to rotate about the wing root</i>	49
<i>Figure 3.12 Orientation of rotation axes of insect wing in the wing motion frame</i>	50
<i>Figure 3.13 Illustration of "figure of eight" and “oval” shape wing motion trajectory by (Sane &amp; Dickinson, 2002)</i>	56
<i>Figure 3.14 A typical SHM flapping kinematic model. In this case, there is no time delay to the flapping motion in any of the rotations and results in a synchronous flapping motion</i>	57

<i>Figure 3.15 A typical trapezoidal function kinematic model, there is no time delay to the flapping motion in any of the rotations, the elevation rotation is put to 0 throughout the wing beat cycle</i>	58
<i>Figure 3.16 Trapezoidal function kinematics of wing stroke during which acceleration and deceleration of the wing translational motion takes place within the segments marked by the dashed lines</i>	59
<i>Figure 3.17 Kinematic model of the wing twisting showing rapid rotation of wing during stroke reversals and constant angle of attack during majority of wing translation</i>	60
<i>Figure 3.18 The transient lift coefficient within a wing beat cycle showing the aerodynamic force peaks produced due to discontinuity in the derived polynomial equation based trapezoidal function kinematic model</i>	61
<i>Figure 3.19 An example of natural fruit fly flapping kinematic model (Left) mapped through point segmentation and fitted by natural cubic spline for simulations (Right), courtesy Aono and Liu (Aono &amp; Liu, 2012)</i>	63
<i>Figure 4.1 3D CAD drawing of physical experiment setup, courtesy of Lua (Lua et al., 2010)</i>	69
<i>Figure 4.2 Fruit fly wing model used in the experimental investigation (A), and data points obtained from line tracing and smoothing for spline fit reconstruction of the wing morphology for numerical simulation (B)</i>	70
<i>Figure 4.3 Dickinson fruit fly wing morphology (red) vs. actual drosophila melanogaster wing morphology (blue)</i>	70
<i>Figure 4.4 SHM kinematics used in the validation process</i>	71
<i>Figure 4.5 Mean lift coefficient computed per wing beat cycle showing that the effect of slow start diminishes after about 5 cycles</i>	72
<i>Figure 4.6 Computational Cd Cl compared with the experimental result</i>	73
<i>Figure 4.7 Pressure contour and velocity vector plot in the plane along the wing orientation during flapping motion at a time the wings reaches maximum translation velocity</i>	74
<i>Figure 4.8 Velocity magnitude contour and vorticity contour lines showing the vortex pair structure driving the downwash before dissipation</i>	75

<i>Figure 4.9 Vorticity iso-surface plots showing the vortex structure evolution during a wing flapping motion, the LEV, TEV and WTV during the beginning of wing down stroke are clearly seen from this plot</i>	75
<i>Figure 4.10 The full fruit fly model consisting of 2 wings and a body flapping in an horizontal plane simulating a hovering flight. This is the configuration used in current kinematic studies</i>	78
<i>Figure 4.11 Comparison of SHM and TF kinematic models, (A) sweep angle and (B) twist angle</i>	79
<i>Figure 4.12 Non-dimensional lift production by a SHM and a TF kinematic model prescribed flapping flight as given in Figure 4.11</i>	79
<i>Figure 4.13 Comparison of non-dimensional lift generated by SHM kinematic model flapping flight vs. modification of the same SHM to TF in sweep only</i>	81
<i>Figure 4.14 Angular time plot showing the difference of sweep motion when SHM kinematic function is changed to TF kinematic function</i>	81
<i>Figure 4.15 Mean lift coefficient per wing beat cycle showing a decreasing trend as phase duration of sweep acceleration and deceleration <math>\Delta\tau</math> is shorten as the SHM kinematic model is partially changed to TF</i>	81
<i>Figure 4.16 Comparison of non-dimensional lift generated by SHM kinematic model flapping flight vs. modification of the same SHM to TF in twist only</i>	82
<i>Figure 4.17 Angular time plot showing the difference of twist motion when SHM kinematic function is changed to TF kinematic function</i>	82
<i>Figure 4.18 Mean lift coefficient per wing beat cycle shows that the lift force generated does not change due to the reduced rotation period <math>\Delta\tau_r</math> of the wing at ends of strokes</i>	82
<i>Figure 4.19 Comparison of non-dimensional lift generated by SHM kinematic model flapping flight vs. modification of the same SHM to TF in both sweep and twist, the phase durations of acceleration in sweep and rotation in twist are made the same</i>	83
<i>Figure 4.20 Mean lift coefficient per wing beat cycle shows that the lift force generated decreases as expected when the SHM kinematic model is changed to TF kinematic model at the same Reynolds number</i>	83
<i>Figure 4.21 Typical SHM kinematic model prescribed flapping motion with no phase difference between twisting and sweeping angle</i>	85

<i>Figure 4.22 SHM kinematic model prescribed flapping motion with twisting angle leading sweeping angle by phase difference <math>\tau = -0.1T</math>, the wing twisting takes place before the wing reaches end of the stroke and the wing twists to minimum attack angle before reaching maximum translation velocity at mid-sweep point of the following stroke</i>	85
<i>Figure 4.23 SHM kinematic model prescribed flapping motion with twisting angle lagging sweep angle by phase difference <math>\tau = 0.1T</math>, the wing twisting takes place after the wing reaches the end of the stroke and into the beginning of the next stroke, this delay causes the wing minimum angle of attack to be reached after the mid-stroke point of the following stroke</i>	86
<i>Figure 4.24 Non-dimensional combined lift produced by the fruit fly wing pair</i>	86
<i>Figure 4.25 (A) The vorticity line plot and pressure field around the wing at slightly after mid-stroke position in a SHM kinematic model flapping flight, (B) the vorticity line plot and pressure field around the wing at the same time step in a SHM kinematic model with leading twist phase angle showing a stronger attached LEV and larger pressure field difference above and below the wing</i>	88
<i>Figure 4.26 Non-dimensional combined drag force acting on the fruit fly wing pair, drag force changes direction from up stroke to down stroke, the plotted drag force is the magnitude force along the insect heading direction</i>	88
<i>Figure 4.27 TF kinematics mode prescribed flapping kinematic model with no phase difference between twisting and sweeping angle</i>	90
<i>Figure 4.28 TF kinematic model prescribed flapping motion with twisting angle leading sweeping angle by phase difference <math>\tau = -0.05T</math>, the wing twisting starts before the wing sweep starts to decelerate near the end of the stroke</i>	91
<i>Figure 4.29 TF kinematic model prescribed flapping motion with twisting angle leading sweeping angle by phase difference <math>\tau = -0.1T</math>, the wing twisting starts before the wing sweep decelerates and completes before the wing reaches the end of the stroke.</i>	91
<i>Figure 4.30 The combined aerodynamic lift produced by the wing pair in TF kinematic model prescribed flapping motion with slightly different phase leading of twist over sweep</i>	92
<i>Figure 4.31 The drag force acting on the wing pairs in TF kinematic model prescribed flapping motion with slightly different phase leading of twist over sweep</i>	92
<i>Figure 4.32 Angular time plot of the proposed TF based kinematic model</i>	93
<i>Figure 4.33 Comparing lift coefficient over a wing beat cycle between the proposed kinematic model and SHM kinematic model prescribed flapping motion</i>	94

<i>Figure 4.34 Pitch moment over a wing beat cycle showing the proposed kinematic model producing higher torque peaks at ends of strokes</i>	94
<i>Figure 5.1 Illustration of the rotation of mean mid-sweep plane of the flapping wings in order to create the clap-and-fling flapping motion</i>	101
<i>Figure 5.2 Illustration of wing planform and axis of wing sweep and axis of wing twist, the marked out point is the wing root</i>	102
<i>Figure 5.3 Angular time plot of kinematic model used for current clap-and-fling study where clap occurs at <math>t = 0</math></i>	103
<i>Figure 5.4 The top-down view on the stroke plane showing the onset of physical clap at <math>t=0</math>, where <math>\Delta\phi = -22^\circ</math> and the gradual separation of the wing trailing edges from wing tip to wing root section after <math>t=0.06</math> into the fling phase. The wing roots has a separation distance of <math>0.1R</math></i>	104
<i>Figure 5.5 The top down view showing the minimum wing tips separation distance of the symmetric sweep reference kinematics of flapping wings</i>	105
<i>Figure 5.6 Comparison of lift coefficient throughout one wing beat cycle between the symmetrical sweep reference case and the clap-and-fling case</i>	105
<i>Figure 5.7 Comparison of drag coefficient throughout one wing beat cycle between the symmetrical sweep reference and the clap-and-fling case</i>	106
<i>Figure 5.8 X-Z plane view (normal to y-axis) at about the <math>3/4</math> span of the fruit fly wing from wing roots showing the LEV and TEV and the downward velocity of fluid around the wing (A) and the pressure contour, the velocity vector (B) induced during clap-and-fling flapping motion</i>	115
<i>Figure 5.9 Vorticity magnitude iso-surface in the flow field close to the wing edge showing a generally higher vortex strength wing tip vortex (WTV) and relatively weaker leading edge vortex (LEV) and trailing edge vortex (TEV)</i>	118
<i>Figure 5.10 Y-Z plane view of pressure contour and velocity vector in between the wing pair during clap-and-fling motion</i>	123
<i>Figure 5.11 Y-Z plane view of pressure contour and velocity vector of the symmetric reference case showing the absence of the wake vortex connection between the two wings as observed in the clap-and-fling case</i>	124
<i>Figure 5.12 Three dimensional iso-vorticity surface plot showing the vortex link between the wings formed during fling phase persists further into downstroke</i>	125

<i>Figure 5.13 The radial force component computed on a single wing executing the reference symmetric flapping kinematics, the near clap-and-fling kinematics and the physical clap-and-fling kinematics</i>	126
<i>Figure 5.14 The Reynolds number effect on lift enhancement of clap-and-fling mechanism, lift coefficient (A) and drag coefficient (B) are computed based on the left wing</i>	127
<i>Figure 5.15 Lift augmentation ratio (mean lift force in clap-and-fling)/(mean lift in reference kinematics at same Reynolds number) and drag augmentation ratio (mean lift force in clap-and-fling)/(mean lift in reference kinematics at same Reynolds number) plotted against Reynolds number</i>	128
<i>Figure 5.16 Lift to drag ratio of clap-and-fling mechanism at different Reynolds number (A), lift enhancement per additional aerodynamic power expenditure (B)</i>	129
<i>Figure 5.17 Sweep angle of the wing in a flapping cycle showing the different cases of relative clap to fling</i>	130
<i>Figure 5.18 Comparison of aerodynamic lift produced in one flapping cycle in the case of varied clap speed with ensuing fling duration maintained constant</i>	130
<i>Figure 5.19 Comparison of aerodynamic drag produced in one flapping cycle in the case of varied clap speed with ensuing fling duration maintained constant</i>	130
<i>Figure 5.20 Effect of varying speed of clap on lift peak generation at the onset of fling motion of wings</i>	131
<i>Figure 5.21 Comparison of lift coefficient over one wing beat cycle of cases from clap-and-fling to wing tip separation of larger than <math>2c</math></i>	132
<i>Figure 5.22 Lift augmentation ratio to wing tip separation and bias in mean positional angle of mid-sweep plane</i>	133
<i>Figure 5.23 The pressure contour and velocity vector of physical clap-and-fling case (LEFT) compared to near clap-and-fling case (Right) at the same fraction time of a wing beat cycle</i>	135
<i>Figure 5.24 The comparison of vortex strength of the vortex link between the wings in physical clap-and-fling case (LEFT) and near clap-and-fling case (RIGHT)</i>	135
<i>Figure 5.25 Comparison of vertically downward fluid momentum between the physical clap-and-fling case (Left) and the near clap-and-fling case (Right) at <math>t = 0.04</math></i>	135



<i>Figure 5.26 The lift coefficient comparison between the physical clap-and-fling case and the near clap-and-fling case with the measured peak values identified</i>	137
<i>Figure 5.27 Lift augmentation ratio to wing roots separation distance plot</i>	138
<i>Figure 5.28 Lift to power ratio as relative to the different wing-wing kinematics configurations explored in the study of clap-and-fling</i>	140
<i>Figure 6.1 Visualisation of effect of changing flapping kinematic parameters, where dotted lines represent wing in reference symmetric flapping motion, dark lines represent wing in flapping motion kinematics with individually adjusted parameters and blue arrow represent the reference stroke plane. (A) <math>\Delta\phi</math>, variation of mean positional angle of the mid-sweep plane, (B) <math>\Delta\phi_0</math>, the change in sweep amplitude, (C) <math>\Delta\psi</math> variation of mean positional angle of the mid-twist plane, (D) <math>\Delta\psi_0</math> the change in twist amplitude, (E) <math>\tau\psi</math> the phase change of twist kinematic function relative to sweep kinematic function, (F) <math>\Delta\theta</math>, variation of the mean positional angle of the mid-elevation plane, (G) <math>\Delta\theta_0</math> the change in elevation amplitude, (H) <math>\tau\theta</math>, the phase change of elevation kinematic function relative to sweep kinematic function, results in change of wing tip path of a cycle, ie. "figure of 8".</i>	147
<i>Figure 6.2 Illustration of the force and moment definition produced by the left wing in the body frame, the cube represents the body coordinate centre, which is the mid-point of the line joining the two wing roots, and indicates the coordinate axes respectively. The symbol <math>\bullet</math> represents the centre of mass of the insect which usually lies in the abdomen.</i>	151
<i>Figure 6.3 The effect of variations in mean positional angle of mid-sweep plane on aerodynamic force and moment productions of flapping wings</i>	153
<i>Figure 6.4 The effect of changes in sweep amplitude on aerodynamic force and moment productions of flapping wings</i>	154
<i>Figure 6.5 The effect of variations in mean positional angle of mid-twist plane on mean aerodynamic force and moment productions of flapping wings</i>	155
<i>Figure 6.6 The effect of changes in twist amplitude on mean aerodynamic force and moment productions of flapping wings</i>	157
<i>Figure 6.7 The effect of variations in twist phase angle difference on mean aerodynamic force and moment productions of flapping wings</i>	158
<i>Figure 6.8 The effect of variations in mean positional angle of mid-elevation plane on mean aerodynamic force and moment productions of flapping wings</i>	160
<i>Figure 6.9 The effect of changes in elevation amplitude on mean aerodynamic force and moment productions of flapping wings</i>	162

<i>Figure 6.10 The effect of variations in elevation phase difference on mean aerodynamic force and moment productions of flapping wings</i>	163
<i>Figure 6.11 The observed difference of drag force in upstroke compared to downstroke due to wing wake interaction in an "oval" shaped wing flapping kinematics</i>	164
<i>Figure 6.12 The dynamic response of parameter adjustments based on the preliminary model for targeted mean non-dimensional lift force increase of 0.5 while maintaining the other forces and moments constant</i>	168
<i>Figure 6.13 The dynamic response of parameter adjustments based on the preliminary model for targeted mean non-dimensional drag (thrust) force increase of 0.5 while maintaining the other forces and moments constant</i>	169
<i>Figure 6.14 The dynamic response of parameter adjustments based on the preliminary model for targeted mean non-dimensional lateral force increase of 0.02 while maintaining the other forces and moments constant</i>	170
<i>Figure 6.15 The dynamic response of parameter adjustments based on the preliminary model for targeted mean non-dimensional pitch moment increase of 0.2 while maintaining the other forces and moments constant</i>	171
<i>Figure 6.16 The dynamic response of parameter adjustments based on the preliminary model for targeted mean non-dimensional roll moment increase of 0.05 while maintaining the other forces and moments constant</i>	173
<i>Figure 6.17 The dynamic response of parameter adjustments based on the preliminary model for targeted mean non-dimensional yaw moment increase of 0.2 while maintaining the other forces and moments constant</i>	174
<i>Figure 6.18 The effect of parameter variation to cause non-dimensional lift force increase of 0.1 in accordance to the preliminary model on Z-Axis (vertical) positional change and Y-Axis (forward) position change of the centre of mass over the wing beat cycles in a simulation with FSI computations</i>	176
<i>Figure 6.19 The effect of parameter variation to cause non-dimensional drag force increase of 0.2 in accordance to the preliminary model on Z-Axis (vertical) positional change and Y-Axis (forward) position change of the centre of mass over the wing beat cycles in a simulation with FSI computations</i>	176

## List of Symbols

$\bar{c}$	Mean chord
$C_L$	Lift coefficient
$\overline{C_L}$	Mean lift coefficient
$C_d$	Drag coefficient
$C_T$	Curvature of angular time plot at $t_0$
$D$	Aerodynamic drag
$\bar{D}$	Mean aerodynamic drag
$f$	Flapping frequency
$f_\phi(t)$	Kinematic function of wing sweep
$f_\psi(t)$	Kinematic function of wing twist
$f_\theta(t)$	Kinematic function of wing elevation
$F_x$	Aerodynamic force
$g$	Gravitational acceleration
$g^n$	Non-dimensional gravitational acceleration
$i_j$	Basis vector in wing motion frame
$i_j^{wd}$	Basis vector in wing definition frame
$I$	Moment of inertia
$l_{ij}$	Transformation vector
$L$	Aerodynamic lift
$\bar{L}$	Mean aerodynamic lift
$L(t)$	Angular Momentum
$\mathbf{L}(t)$	Transformation matrix
$m$	Mass

$m^n$	Non-dimensional mass
$M$	Coefficient matrix of preliminary control model
$M_x, M_y, M_z$	Moment acting on insect body
$O^W$	Origin of wing motion frame
$O^{wd}$	Origin of wing definition frame
$p$	Pressure
$P$	Aerodynamic power
$\bar{P}$	Mean aerodynamic power
$P(t)$	Linear Momentum
$\hat{r}_2$	Second moment arm of inertia
$r^W$	Positional vector of wing nodes
$R$	Wing length
$R^n$	Non-dimensional wing length
$R_c$	Rotational transformation matrix
$Re$	Reynolds number
$s_i(x)$	Piecewise spline function
$S$	Wing planform area
$[S]_{n \times m}$	Derivative matrix
$t$	Time
$t^n$	Non-dimensional time
$t_0$	Fractional time of end of wing translational acceleration
$t^*$	Time limit of “slow start”
$T$	Non-dimensional unit time of 1 wing beat cycle
$u, v, w$	Velocity vector in Cartesian coordinates
$u_c$	Convection velocity vector
$u^*$	Intermediate projection velocity

$U_{ref}$	Reference velocity
$U_{ref}^n$	Non-dimensional reference velocity
$U_{tip}$	Wing tip velocity
$v(t)$	Linear velocity
$W$	Weighting function
$X, Y, Z$	Cartesian axes of computational domain
$X^W, Y^W, Z^W$	Cartesian axes of wing motion frame
$X^{wd}, Y^{wd}, Z^{wd}$	Cartesian axes of wing definition frame
$X_c$	Translation transformation matrix
$\alpha$	Angle of attack
$\alpha_{min}$	Minimum angle of attack
$\alpha$	Artificial dissipation coefficient
$\beta$	Artificial dissipation limit
$\nu$	Kinematic viscosity
$\rho_{air}$	Air density
$\rho_f$	Fluid density
$\rho_s$	Solid density
$\omega(t)$	Angular velocity
$\bar{\omega}$	Mean angular velocity
$\omega_\phi$	Angular velocity in azimuthal axis
$\omega_\psi$	Angular velocity in twisting axis
$\omega_\theta$	Angular velocity in elevation axis
$\tau$	Phase difference in fractional time of a wing beat cycle
$\tau_\phi$	Phase difference of sweep relative to reference flapping phase
$\tau_\psi$	Phase difference of twist relative to reference flapping phase

$\tau_\theta$	Phase difference of elevation relative to reference flapping phase
$\Delta t$	Time step
$\Delta\tau_t$	Fractional time duration of translation acceleration of wing
$\Delta\tau_r$	Fractional time duration of wing rotation
$\Delta\phi$	Mean positional angle of mid-sweep plane
$\Delta\psi$	Mean positional angle of mid-twist plane
$\Delta\theta$	Mean positional angle of mid-elevation plane
$\partial\Omega$	Solid boundary
$\phi(t)$	Periodic function of wing sweep angle
$\phi_0$	Sweep amplitude
$\psi(t)$	Periodic function of wing twist angle
$\psi_0$	Twist amplitude
$\theta(t)$	Periodic function of wing elevation angle
$\theta_0$	Elevation amplitude

# **CHAPTER 1: Introduction**

## **1.1 Background**

Insects are the first animals on earth to evolve active flight and remain unsurpassed in many aspects of the aerodynamic performance and manoeuvrability. The feats of taking off backwards, transiting from hovering flight to motion flight back and forth freely, turning at virtually zero radius and landing upside down onto plant surfaces have demonstrated the superiority of insect flight dynamics. It is of great interest to scientists, engineers, biologists and entomologists to study and understand the physical phenomenon of insect flights. It is believed that by understanding the aerodynamics associated with insect flight, a completely new theory of lift generation dynamic system can be formulated which would be a complete break away from the conventional aerodynamics that has seen its development with the invention of aircrafts. This unsteady aerodynamics, especially in the micro scale of the size of typical insects (from 5mm to 5cm), could spur advanced development in science and technology in the area of Micro Air Vehicle (MAV), and as such has tremendous potential in both military and civil applications.

As computer technology developed rapidly in the last several decades, more powerful super computers and ever increasing storage capacities that were made available have pushed the study of fluid mechanics into the new frontier of using Computational Fluid Dynamics (CFD). The development of CFD has advanced at a phenomenal speed in the past decade while a diverse variety of numerical schemes have been developed to assist in the study of aerodynamics in aviation, automobile, electronics, biomedical, environmental and many other industries. However, experimental fluid dynamics still remains a fundamental tool in understanding the physics and evaluating mathematical predictions. It is obvious to point out that CFD offers far more convenience and affordability as compared to traditional experimental fluid dynamics studies in many scientific and engineering applications. Study of insect flight represents such a case in which experimentation has been proven to be extremely difficult due to the small physical scales, complexity of the unsteady aerodynamics flow and controlling of test parameters involving live insects that have a mind of their own.

Computational Fluid Dynamics tools are widely available in the industry and institutions in standard software packages such as Fluent<sup>®</sup>, Flow3D<sup>®</sup> and etc. These standard software packages offer the most convenience in carrying out quick numerical simulations of fluid flow for various problems. However, these readily available software packages have inherent drawbacks, such as inflexible choice of numerical solvers, poor numerical accuracy (for complex unsteady problems) and in many cases, have restricted features and capabilities in dealing with new and unconventional problems, and thus impose limitations in actual applications in the field of engineering research.

Singular Value Decomposition based Generalised Finite Difference (SVD-GFD) is a novel numerical scheme that was continually developed in the Department of Mechanical Engineering, National University of Singapore. This numerical scheme is capable of achieving high numerical accuracy in solving for complex immersed boundary (IB) problems with improved computational efficiency as compared to the generally adopted Finite Element and Finite Volume methods in solving such problems. The author adapted the 3D version of SVD-GFD method to solve immersed and moving boundary flow problems particularly associated with insect flapping flight studies.

The purpose of the current research work is to use the aforementioned CFD scheme to simulate and study insect flapping flight problems and attempt to gain understanding of the unsteady aerodynamic force generations involved in insect hovering flights and manoeuvring.

## **1.2 Insect Flight Studies Overview**

The earliest study of insect flight could be traced to the beginning of last century, when entomologists and biologists studies insect anatomy and diversities (Dudley, 2002). However, the systematic study of insect flight did not begin until more advanced scientific equipment were made available that permitted practical observations and experimentations on real insects in flight.

Early theoretical studies attempted to estimate aerodynamic lift force generations in insect flight using quasi-steady assumptions based on observed insect flapping wing kinematics(Weis-Fogh, 1973). For a variety of insects, calculation of quasi-steady lift



coefficients were exceedingly large, mostly more than 1.0 (Osborne, 1951). However, as more systematic experimental studies were carried out later, the quasi-steady assumption based on conventional aerodynamic theory is proven to be inadequate. Wind tunnel testing results showed that the lift coefficient is about 0.23-0.60 for fruitfly wing at varying attack angles, and if it were used to calculate the lift generated based on quasi-steady model it is substantially smaller than those required to support the weight of the insect (Ellington, 1984). This was also the case for many other insects. In a study of hawkmoth flight, it was even determined that the actual lift performance of the wing exceeds maximum quasi-steady value during hovering flight (Willmott, Ellington, & Thomas, 1997). Hence, the significant transient force peak effects not included in quasi-steady models cannot be neglected.

The failure of quasi-steady aerodynamic model suggested that unsteady aerodynamic mechanisms must be the main reason insects are able to maintain active flight motion. Various unsteady aerodynamic mechanisms, such as Wagner Effect, Virtual Mass Forces, Clap and Fling and Delayed Stall have been proposed and suggested based on theoretical analysis and observations (Ellington, 1984).

Wagner effect is the transient effect describing the temporal evolution of circulation and lift on a time-dependent motion of the wings (Wagner, 1925). When an inclined wing suddenly sets into a translational motion, the circulation around it does not immediately attain its steady state value, instead, the circulation rises slowly. This could substantially affect the overall lift build-up of insect flight as translation of the wings hardly reach steady-state before they decelerate and accelerate in the reverse direction. However, the transient aerodynamic characteristics of linearly translating insect wing models evaluated experimentally showed that the delay in lift build-up is less pronounced at lower Reynolds number range particularly relevant to flight of small-to-medium-sized insects (Dickinson & Gotz, 1993). Wagner effect relates directly to the growth of vorticity at the onset of motion, both its measurement and theoretical treatment are complicated due to complex flow field interactions and thus have been neglected in most theoretical models of flapping insect wings.

When a wing immersed in air is forced to move, it must set the surrounding air in motion. This inertia of the wing is increased by the mass of the air that is accelerated, and so there is an apparent increase in the wing mass called the virtual (or added) mass

(Ellington, 1984). The virtual mass of flapping wings can be empirically related to the wing geometry and with wing orientation relative to the axis of flapping. Since the wing translational acceleration usually reaches maximum towards the end of wing strokes, when the wing surfaces are approximately perpendicular to the translation direction, the virtual mass of a thin wing can be estimated to be equal to the mass of air in an imaginary circular cylinder around the wing with the chord as its diameter. It was suggested that the virtual mass forces would not significantly alter the mean lift of the wing, but has substantial effect on the instantaneous force generations at ends of the stroke (Ellington, 1984), which could contribute to the asymmetry of the force generated from up and down strokes.

Clap and Fling was the first significant unsteady aerodynamic effect discovered, which is associated with many small insects (Weis-Fogh, 1973). Clap-and-fling mechanism describes the close apposition of the two wings at the end of an upstroke phase preceding the next downstroke phase combined with the rotational motion of the wings, which results in a rapid development of circulation during the downstroke. This mechanism could substantially increase the lift generation above the steady-state values, and is most commonly adopted by small insects and insects with particular shape of wings to maximise the effect (Wakeling & Ellington, 1997). Clap-and-fling augments lift by enhancing circulation around each of the wing during the end of upstroke and the beginning of downstroke, this phenomenon can also be achieved in a completely inviscid fluid (Lighthill, 1973). However, in spite of potential advantages, many insects never perform the clap in their flight (Marden, 1987), instead, near or partial clap and fling mechanism was actually more common in nature due to the anatomical limitations that prevent many insects from performing flapping sweep amplitude angle of beyond 180° (Ellington 1984d). In a study on the viscous effect of this mechanism, it is found using a three-dimensional model that the wings do not have to touch each other to benefit from the enhanced circulation achieved from this mechanism (Maxworthy, 1979).

During translational motion of wing in stroke, the incidence angle of the wing leading edge usually reaches values of 35° to 45°, way above the threshold for wing stall in steady motion. It was discovered that wing can travel at several chord lengths at large incidences before separation associated with stall begins, and the large transient circulations can be developed during that period and the circulation measured could be

40-55% higher when final stall begins. Rotation towards the end of each stroke provides a second method of delaying stall for translating wings and providing enhanced maximum lift coefficient (Ellington, 1984). Recent studies have also pointed out that the vortex generated at the leading edge of the insect wings (LEV) during high angle of attack in translational motion of wing appears to be stabilised by the presence of spanwise flow (Berg & Ellington, 1997; Birch & Dickinson, 2001).

Other unsteady aerodynamic effects have also been proposed by some researchers in explanation of the augmented lift achieved by insect flapping flights. The rotation of wing at ends of upstroke and downstroke could cause rotational force to be generated that could add to or subtract from the net force generated during translation, and this “Kramer Effect” has been quantified using rotational coefficients and included in the translational coefficients in the quasi-steady models (Sane & Dickinson, 2002). Wake capturing mechanism can be frequently observed during wing-wake interaction of insect hovering flight and has been suggested to result in significant force generations from two-dimensional studies of an inclined plate in wake interactions (Dickinson, 1994). Further studies using robotic fruitfly like wings at Reynolds number of 100 to 200 have also shown an unsteady increased force generation due to wing-wake interaction (Birch & Dickinson, 2003; Lehmann, Sane, & Dickinson, 2005).

Experimental studies of insect flapping flight were becoming common closer to the end of last century. Advanced high speed cameras, Digital Particle Image Velocimetry (DPIV) technique, precise actuator and controller technologies allowed researchers to approach the modelling of insect flapping flight using morphologically accurate and dynamically scaled robotic wings. The robotic wings are immersed in tank of mineral oil and driven by computer controlled actuators, capable of generating rotational motions in all three axes (Dickinson, Lehmann, & Sane, 1999). In the study of larger insect flight,  $Re > 1000$ , tank of water is used instead of mineral oil. Larger plan area of robotic wings also allowed control of wing flexibility to study the effect of deformable wing on aerodynamic force generations (Lua, Lai, Lim, & Yeo, 2010). Force measurements are usually taken from sensors attached to the base of robotic wings and flow structures captured by DPIV.

### 1.3 Numerical Studies in Insect Flight

A more recent approach to the study of unsteady aerodynamics of insect flight is through numerical simulation. The advantages of numerical simulation as compared to the experimental methods are obvious, among which are the relatively easier measurement of forces everywhere along the wing span and the much easier visualization of the flow field at different time steps that are crucial to the understanding of the unsteady aerodynamics associated with the actual insect flight. However, numerical simulation of unsteady aerodynamics is still a relatively new field and faces several obstacles. The complexity of simulating the flapping wing motion still poses challenge to the computational researchers. There is still no single best and most efficient numerical scheme that has been identified to be suitable to simulate the flow field and study the physics of flapping wing motions. Many researchers around the world have approached the problem using different numerical methods. For example, a numerical simulation by Sun and Tang (Sun & Tang, 2002b) of fruit fly wings uses a coordinate transformed and overlying grid method, in which the Navier-Stokes equations were solved using the method of artificial compressibility developed by Rogers and Kwak (Rogers, Kwak, & Kiris, 1991; Rogers & Kwak, 1990). The grid topology used was an O-H grid generated by using Poisson solver based on the work of Hilgenstock (Hilgenstock, 1988). Sun and Tang's work provided useful vorticity plots at different time steps that demonstrated the "delayed stall" phenomenon and wake formation. Gilmanov and Sotiropoulos (Gilmanov & Sotiropoulos, 2005) developed a hybrid Cartesian/immersed boundary method to simulate 3D flow with geometric complex and moving bodies, in which the governing equations are discretised on a hybrid staggered/non-staggered grid layout using second-order accurate finite difference formulas. Gilmanov tested this numerical method on a single insect flapping wing problem that is similar to Dickinson's experimental method and the results are comparable. Ramamurti and Sandberg (Ramamurti & Sandberg, 2006) made use of incompressible Navier-Stokes equation in Arbitrary Lagrangian-Eulerian (ALE) formulation discretised in space using Galerkin procedure with linear tetrahedral finite elements. They computed the unsteady forces and moments on a modelled fruit fly *Drosophila* and the compared their results with experiments. The obtained result show good agreement for the entire hover and saccade maneuver, consisting of over 20 wing beat cycles. Miller and Peskin (L. A. Miller & Peskin, 2005) applied immersed

boundary method to solve the two-dimensional Navier-Stokes equations for two immersed wings of very small insects performing an idealised “clap and fling” stroke. The investigated Reynolds number are between 5 and 125, and the numerical findings show that the “clap and fling” technique first discovered by Weis-Fogh (Weis-Fogh, 1973) indeed helps to enhance lift generation for insects by up to 30% averaged across the entire translational flapping motion, and it demonstrated that “clap and fling” is more effective at lower Reynolds number than higher Reynolds number values tested.

A more recent systematic numerical study of single wing pair insect flapping flight is carried out by H. Liu, who have published several papers detailing his numerical investigations on hovering insect flight problems. He has also extended his findings in the aerodynamics of insect free flight into design and experimentation of MAV using flapping wings. He makes use of a fortified FVM-based Navier-Stokes solver for dynamically moving multi-blocked overset-grid system to numerically simulate insect flapping flight (Aono, Liang, & Liu, 2008; Liu, 2009). The governing equations are the 3D incompressible unsteady Navier-Stokes equations written in strong conservative form for momentum and mass (Liu & Kawachi, 1998). Three structured grid systems are generated to fit each of the body and the two wings, moving with the object and trilinear interpolation is employed to communicate velocities and pressure among overlapping grids (Aono et al., 2008). This method has shown its versatility by generating results in three different types of insects, hawkmoth, honeybee and fruitfly, in hovering flight over a range of Reynolds number from 120 to 140. His results was also able to demonstrate the accuracy of modeling and quantitative evaluation of the unsteady aerodynamics associated with insect flapping flight.

The Three-Dimensional (3-D) Singular Value Decomposition based General Finite Difference (SVD-GFD) method used in this study is based on the previous work carried out in the Mechanical Engineering Department of National University of Singapore (Chew, Yeo, & Shu, 2006; X. Y. Wang, Yeo, Chew, & Khoo, 2008; Yu, Yeo, Sundar, & Ang, 2011). The numerical code employs hybrid Cartesian cum mesh free grid and has been evaluated and proven capable of performing flow simulations to solve both steady and unsteady immersed boundary problems, such as the complex insect flapping flight and fish swimming problems. The computational efficiency and accuracy has been demonstrated to be much better than traditional CFD techniques. Further adaptation and improvement have been carried out by the author in the context

of current research work. In particular, a more advanced nodal selection scheme, artificial dissipation model, fluid-solid interaction (FSI) model, numerical model for accurate parametric description of flapping kinematics and basic flight control model based on flapping kinematic parameters have been introduced to achieve the most comprehensive simulation of insect flight.

## **1.4 Motivation and Outline**

In the present set of studies, with the advantage of three dimensional numerical solutions, numerous insect flapping flight simulations are carried out to systematically investigate the unsteady aerodynamic behaviours associated with insect flapping flight. It is therefore, the objective of current research to perform systematic simulations of various flapping flight mechanisms governed by specific kinematic models to explore the critical effects of unsteady aerodynamics that the insects have mastered and allow it to hover, free flight and manoeuvre. Many of the flow field information extracted in association with specific kinematic behaviours of the flapping flight are new, and reveal interesting three dimensional flow evolutions that are then further analysed to offer qualitative explanations.

This thesis is divided into 7 Chapters with each chapter's brief summary given below.

Chapter 1 provides the overview of the recent progress of insect flapping flight research both from historical, experimental and numerical perspectives. It serves as the introduction to the current research topic and provides the outline for the rest chapters of the thesis.

Chapter 2 explains the basic features of the current numerical scheme, and the numerical adaptations implemented to allow for the simulation of insect flapping flight.

Chapter 3 explains the implementation methodology for studying insect flapping flight problems in the current research. This includes geometric and kinematic modelling as well as the simulation set up and the meshless nodal generation process.

Chapter 4 consists of two parts. The first part, the numerical studies is compared to an equivalent experimental study of rigid insect wing flapping in sinusoidal function

kinematic mode. The results are compared to establish validity of the model. The second part, a systematic approach to investigate the effect of kinematic model on aerodynamic force productions is explored and a proposed kinematic model with good flapping efficiency is explored.

Chapter 5 presents a systematic three dimensional clap-and-fling study which explores the unsteady aerodynamic effects associated with this special kinematic model that can be observed on some insect's flapping flight patterns. The main difference of the 3D results from the 2D estimations are explored and interesting flow field observations are presented.

Chapter 6 explores a systematically proposed kinematic parameterisation methodology that attempts to establish a kinematics to aerodynamic forces and moments generated by the flapping wings relationship matrix that will then enable a derivation of preliminary control model for flapping flights.

Chapter 7 summarises the whole thesis with conclusion and suggested future research directions.

# CHAPTER 2: Numerical Scheme

## 2.1 Introduction

In this chapter, the details of the Singular Value Decomposition based General Finite Difference numerical method is explained and the adaptation work carried out to tune the numerical method into solving insect flapping flight problems are elaborated. The basic idea of the numerical work was previously developed within the research group and can be found in literature (X. Y. Wang et al., 2008; Yeo, Ang, & Shu, 2010).

## 2.2 Governing Equation

The dynamics of the three-dimensional incompressible flow in insect flapping flight problems is governed by the three-dimensional incompressible Navier-Stokes equations in the non-dimensional Arbitrary Lagrangian-Eulerian (ALE) form.

$$\begin{aligned}\partial_t \mathbf{u} &= -(\mathbf{u} - \mathbf{u}_c) \cdot \nabla \mathbf{u} + \frac{1}{\text{Re}} \Delta \mathbf{u} - \nabla p \\ \nabla \cdot \mathbf{u} &= 0\end{aligned}\tag{2.1}$$

Where  $\mathbf{u}$  and  $p$  represent the velocity vectors and pressure fields of the fluid domain respectively, and  $\mathbf{u}_c$  denotes the convection velocity of the computational nodes. It is usually equal to zero ( $\mathbf{u}_c = 0$ ) for the background Cartesian nodes that are usually stationary, except in the case when background Cartesian nodes are made to convect with respect to the computational domain in an effort to follow the insect movement during forward flight, whereas  $\mathbf{u}_c$  for meshless nodes follow the movement of the body or boundary. The Reynolds number is defined as  $\text{Re} = UL/v$ , where  $U$ ,  $L$  denotes the respective characteristic velocity and length scale,  $v$  represents the fluid kinematic viscosity. Detailed definition of Reynolds number in insect flight problem will be explained in later chapter.



## 2.3 A Hybrid Meshfree Method

As have explained in Chapter 1, in the past decades, computer technology improvements and wider use of CFD techniques in applications have resulted in much expanded capabilities of traditional Finite Difference (FDM), Finite Element (FEM) and Finite Volume (FVM) methods. However, many have also realised limitations of such standard methods in studying of more complicated fluid flow with complex boundary shape problems. In solving moving and complex boundary problem, the standard mesh based methods usually requires constant regeneration of grid points to accommodate the changing solution domain as well as to maintain good mesh qualities. This inevitably resulted in increased costs in mesh administration and interpolation of data that could easily lead to increase in numerical errors.

The rapid development of meshless or meshfree methods ensured in recent history, and provided many distinctive advantages in solving complex moving boundary flow problems. The underlying concept of meshless methods is that the solution domain is represented by a set of nodal points without any prescribed relationship and connectivity. The discretization of the governing equations of flow does not depend on the availability of a mesh and therefore making the method extremely flexible as compared to standard mesh based methods.

Many such meshless methods have been proposed, and among those, the smoothed particle hydrodynamics method (Morris, Fox, & Zhu, 1997) and the meshfree Galerkin method (Duan & Tan, 2005) are the most popular. Other methods such as the Immersed Boundary Method (Kim & Choi, 2006; Palma, Tullio, Pascazio, & Napolitano, 2006) and the level set methods (Li & Lai, 2001; Xu, Li, Lowengrub, & Zhao, 2006) have also received much attention and been used to treat problems with complex boundaries. These methods all attempt to solve the flow field using various numerical approaches while no mesh information is directly needed.

The meshless method offers an easy way of generating computational nodes around complex and unusual geometries and requires no remeshing due to movement of boundaries and change of computation domain shapes. However, it is worth noting that most meshless methods incur additional computational costs and face more challenges in dealing with complicated numerical stability issues. For three-dimensional external flow problems, the computational domain is usually large, and it

is too tedious to carry out meshless computation throughout the entire domain. Therefore, it is a natural idea to use a hybrid grid system that combines a meshless grid surrounding the complex geometry with a simple Cartesian background mesh covering the rest of the computational domain. Since the meshless grid points required to discretise the complex geometry and its adjacent regions may constitute only a small fraction of the total grid points involved in computation, despite the fact that computer time required in solving such meshless nodes is disproportionately larger than solving the background Cartesian nodes, the total computational cost is substantially reduced.

The basic three-dimensional meshless scheme used in the research work is based on the aforementioned hybrid-grid system that uses a meshless body attached grid set over a Cartesian background grid domain. This method is originally developed by Chew et al. (Chew et al., 2006), Wang et al. (X. Y. Wang et al., 2008) and Yu et al. (Yu et al., 2011). ALE form of the governing equations are used to solve flow at the convecting meshfree nodes. This hybrid grid combines great geometry flexibility and accuracy of boundary definition with the computational efficiency of Cartesian background grid solving the bulk of the flow domain.

## **2.4 SVD-GFD Scheme**

In order to discretise the aforementioned hybrid-grid system, the Singular Value Decomposition-Generalised Finite Difference scheme is applied. The method of using finite difference scheme to arbitrary irregular nodal points is originally proposed by Liszka and Orkisz (Liszka & Orkisz, 1980) and used in applied mechanics. This method originally came from finite element method and in theory can be used on any scattered nodes. Duarte (Duarte, Liszka, & Tworzydło, 1996) proposed the so-called Hp-clouds methods in moving least square form to treat arbitrary boundary problems. This least-square based finite difference scheme was later refined by Ding (Ding, Yeo, & Xu, 2004) to solve two-dimensional natural convection in a cavity flow problems. Chew (Chew et al., 2006) further developed this method to generalised finite difference scheme to simulate two-dimensional moving boundary problems. Wang (X. Y. Wang et al., 2008) and Yu (Yu et al., 2011) further developed and demonstrated the capability of the scheme in solving three-dimensional moving boundary flow problems.

The GFD is based on the Taylor series expansion. For a node within the three-dimensional domain  $(x_0, y_0, z_0)$ , one can select a local support volume with a specified radius. The functional value  $f(x_0)$  of this central node can be expressed in terms of the functional values of the neighbouring supporting nodes within the local support volume. The 3D Taylor series expansion of the functional values of the  $n$  supporting nodes in terms of the computations at the central node is given by

$$\begin{aligned}
f_i(i = 1 \dots n) = & f_0 + \Delta x_i \frac{\partial f_0}{\partial x} + \Delta y_i \frac{\partial f_0}{\partial y} + \Delta z_i \frac{\partial f_0}{\partial z} + \frac{1}{2} \Delta x_i^2 \frac{\partial^2 f_0}{\partial x^2} + \frac{1}{2} \Delta y_i^2 \frac{\partial^2 f_0}{\partial y^2} \\
& + \frac{1}{2} \Delta z_i^2 \frac{\partial^2 f_0}{\partial z^2} + \Delta x_i \Delta y_i \frac{\partial^2 f_0}{\partial x \partial y} + \Delta x_i \Delta z_i \frac{\partial^2 f_0}{\partial x \partial z} + \Delta y_i \Delta z_i \frac{\partial^2 f_0}{\partial y \partial z} \\
& + \frac{1}{6} \Delta x_i^3 \frac{\partial^3 f_0}{\partial x^3} + \frac{1}{6} \Delta y_i^3 \frac{\partial^3 f_0}{\partial y^3} + \frac{1}{6} \Delta z_i^3 \frac{\partial^3 f_0}{\partial z^3} + \frac{1}{2} \Delta x_i \Delta y_i^2 \frac{\partial^3 f_0}{\partial x \partial y^2} \\
& + \frac{1}{2} \Delta x_i \Delta z_i^2 \frac{\partial^3 f_0}{\partial x \partial z^2} + \frac{1}{2} \Delta y_i \Delta z_i^2 \frac{\partial^3 f_0}{\partial y \partial z^2} + \frac{1}{2} \Delta x_i^2 \Delta y_i \frac{\partial^3 f_0}{\partial x^2 \partial y} \\
& + \frac{1}{2} \Delta x_i^2 \Delta z_i \frac{\partial^3 f_0}{\partial x^2 \partial z} + \frac{1}{2} \Delta y_i^2 \Delta z_i \frac{\partial^3 f_0}{\partial y^2 \partial z} + \Delta x_i \Delta y_i \Delta z_i \frac{\partial^3 f_0}{\partial x \partial y \partial z} \\
& + O(\Delta^3)
\end{aligned} \tag{2.2}$$

One may truncate the Taylor series equation appropriately and approximate the derivatives of the function at the reference node by solving a system of linear equations. For such approximations, it is usually a common practice to choose supporting nodes in the immediate or near neighbourhood of  $(x_0, y_0, z_0)$ . In order to maintain second-order spatial accuracy, the leading 19 derivative terms are retained while the remaining terms are truncated as error. Thus, one can form matrix equation:

$$\Delta f_{n \times 1} = [S]_{n \times 19} \partial f_{19 \times 1} \tag{2.3}$$

Where:

$$\begin{aligned}
\Delta f_{n \times 1} = & (f_1 - f_0, f_2 - f_0, f_3 - f_0, \dots, f_n - f_0)^T \\
[S]_{n \times 19} = & \begin{bmatrix} \Delta x_1 & \Delta y_1 & \Delta z_1 & \frac{1}{2} \Delta x_1^2 & \frac{1}{2} \Delta y_1^2 & \frac{1}{2} \Delta z_1^2 & \dots \\ \Delta x_2 & \Delta y_2 & \Delta z_2 & \frac{1}{2} \Delta x_2^2 & \frac{1}{2} \Delta y_2^2 & \frac{1}{2} \Delta z_2^2 & \dots \\ \Delta x_3 & \Delta y_3 & \Delta z_3 & \frac{1}{2} \Delta x_3^2 & \frac{1}{2} \Delta y_3^2 & \frac{1}{2} \Delta z_3^2 & \dots \\ \vdots & & & \vdots & & & \\ \Delta x_n & \Delta y_n & \Delta z_n & \frac{1}{2} \Delta x_n^2 & \frac{1}{2} \Delta y_n^2 & \frac{1}{2} \Delta z_n^2 & \dots \end{bmatrix} \\
\partial f_{19 \times 1} = & \left( \frac{\partial f_0}{\partial x}, \frac{\partial f_0}{\partial y}, \frac{\partial f_0}{\partial z}, \frac{\partial^2 f_0}{\partial x^2}, \frac{\partial^2 f_0}{\partial y^2}, \frac{\partial^2 f_0}{\partial z^2}, \dots, \Delta x_1 \Delta y_1 \Delta z_1 \frac{\partial^3 f_0}{\partial x \partial y \partial z} \right)^T
\end{aligned}$$

The matrix  $[S]_{n \times 19}$  contains only information about the position of the  $n$  supporting points relative to the reference or central node  $(x_0, y_0, z_0)$ . For second-order accuracy of the second-order spatial derivatives, 19 supporting nodes ( $n = 19$ ) are needed to exactly close the linear system. If the matrix is non-singular, one may in principle solve the linear equation system to obtain the derivative vector  $\partial f_{19 \times 1}$ . However,  $[S]_{19 \times 19}$  tends to be ill-conditioned.

The ill-conditioning of matrix  $[S]_{19 \times 19}$  tends to arise from the generally poor spatial arrangement of supporting nodes that are either having extreme close separation or irregular distribution around the central node. To overcome this difficulty, an over-determined algebraic system is used by including more supporting points than needed ( $n > 19$ ). Since standard least square optimization cannot be performed on the non-square matrix obtained in this case, SVD approach is used. SVD is more robust and will yield a solution (one with minimum  $L_2$  norm) even when the system is under-determined ( $n < 19$ ), such is the case when very small eigenvalues in matrix  $[S]_{n \times 19}$  are omitted to avoid ill-conditioning.

In addition, a distance based weighting function  $W$  is also introduced to further enhance the accuracy of derivative approximation.

$$\partial f_{19 \times 1} = [WS]^+[W]\Delta f_{n \times 1} \quad [2.4]$$

The weighting function is applied before the calculation of the pseudoinverse, and then  $[WS]^+$  is solved using SVD. The weighting function are designed to give greater weight to errors at nearer nodes. Some of the applicable weighting functions are discussed in Wang et al. (X. Y. Wang et al., 2008).

## 2.5 Projection Method

A so called continuous projection method based on semi-implicit second order Crank-Nicolson method fractional step method is used in solving the temporal part of the governing equation. The momentum equation discretised by the second-order Crank-Nicolson method can be written as:

$$\begin{aligned} \frac{u^{n+1} - u^n}{\Delta t} = \frac{1}{2} \left\{ \left[ -\nabla p - (u - u_c) \cdot \nabla u + \frac{1}{Re} \nabla^2 u \right]^n \right. \\ \left. + \left[ -\nabla p - (u - u_c) \cdot \nabla u + \frac{1}{Re} \nabla^2 u \right]^{n+1} \right\} \end{aligned} \quad [2.5]$$

In the projection method, the momentum equation is first advanced in time to provide an approximation of  $u^*$  for the velocity field of  $u^{n+1}$  at the next time level. The approximated intermediate velocity field  $u^*$  usually will not satisfy the divergence-free condition for incompressible flow. Then a correction step is performed by solving the Poisson equation for pressure while enforcing the continuity equation, which is used to project  $u^*$  onto  $u^{n+1}$  in the subspace of divergence-free solution. The intermediate velocity field  $u^*$  is thus obtained in accordance to the momentum equation:

$$\begin{aligned} \frac{u^* - u^n}{\Delta t} = \frac{1}{2} \left\{ \left[ -\nabla p - (u - u_c) \cdot \nabla u + \frac{1}{Re} \nabla^2 u \right]^n \right. \\ \left. + \left[ -(u - u_c) \cdot \nabla u + \frac{1}{Re} \nabla^2 u \right]^{n+1} \right\} \end{aligned} \quad [2.6]$$

And the velocity correction step follows:

$$\frac{u^{n+1} - u^*}{\Delta t} = \frac{1}{2} \nabla p^{n+1} \quad [2.7]$$

Applying the divergence-free condition in velocity field at  $n + 1$  time step gives the pressure Poisson equation:

$$\nabla^2 p^{n+1} = \frac{2}{\Delta t} \nabla \cdot u^* \quad [2.8]$$

At the solid boundary, the no-slip boundary dictates that

$$u^*|_{\partial\Omega} = u_c^{n+1}|_{\partial\Omega} \quad [2.9]$$

And the computational domain boundary is specified as non-reflecting far field boundary. The boundary condition for the pressure Poisson Equation is:

$$n \cdot \nabla p_{\partial\Omega}^{n+1} = \frac{\partial p^{n+1}}{\partial n} \Big|_{\partial\Omega} = \frac{2}{\Delta t} (u^*|_{\partial\Omega} - u_c^{n+1}|_{\partial\Omega}) \cdot n \quad [2.10]$$

The computational algorithm involves stepping forward in time to give the intermediate velocity field  $u^*$  subject to the aforementioned boundary condition. The

pressure Poisson equation is then solved in an iterative manner using SOR or GMRES methods which yields the pressure field  $p^{n+1}$ , which is then substituted back into the velocity correction equation to give the velocity field at the new time step  $u^{n+1}$ . This implicit coupling ensured good overall numerical stability and accuracy under condition of continuous moving boundary, which has been proven to be fully second-order (Chew et al., 2006).

## 2.6 Iterative Solver for Pressure Poisson Equation

There are many iterative methods available for solving the pressure Poisson equation in the projection method. However, the convergence of the Poisson equation is essential for the convergence of the overall numerical solution. It was discovered that the stability of the numerical method can be improved by using more robust and rigorous iterative methods, however, such iterative methods also lead to higher computational costs which is not quite desirable. Thus, the fine balance of solution convergence and computational cost need to be achieved for optimal simulations.

A few of the iterative methods are explored and compared in the study. Successive over-relaxation (SOR) method is one of the first iterative method used in the numerical scheme. SOR is originally proposed by Young (Young, 1950), and is a fast convergence scheme based on Gauss-Seidel iterative method used to solve large linear system of equations. It is a local error minimization scheme that helps to achieve convergence quickly but not necessarily guaranteed convergence of the solution. In order to improve convergence of Poisson equation, a global residual minimization method was implemented. The Generalised Minimal Residual Method was originally developed by Saad and Schultz (Saad & Schultz, 1986) to solve non-symmetric system of linear equations. It has since been developed as one of the most robust and rigorous convergence iterative method. This method uses Arnoldi iteration to approximate the solution by finding minimal residual in the Krylov subspace. In addition, another iterative method suggested by Wu is used for comparison. The biconjugate gradient stabilised method (BICGStab) developed by (Vorst, 1992) is based on biconjugate gradient method (BICG) originally proposed by Fletcher (Fletcher, 1976) to overcome limitations of BICG method in convergence behaviour. BICGStab has a limited advantage over GMRES method due to its ease of parallelization and hence reduced

overall computational time required.

For the current study of unsteady nature of simulations, numerical solutions are not allowed for indefinite convergence during each time step. Instead, only limited number of iterations are performed at each time step when solve the pressure Poisson equation before moving onto the next time step. Therefore, it is generally desirable to use a fast convergence method. However, from the results shown, one can see that due to the highly unsteady nature of the flow structures evolving in the near field of the moving insect wings, the solution convergence is very poor for localised error minimization methods like SOR and Jacobi. The L2 norm minimization of GMRES and BICGStab methods are much better in comparison, however the computational costs are approximately 4 to 6 times that of SOR method.

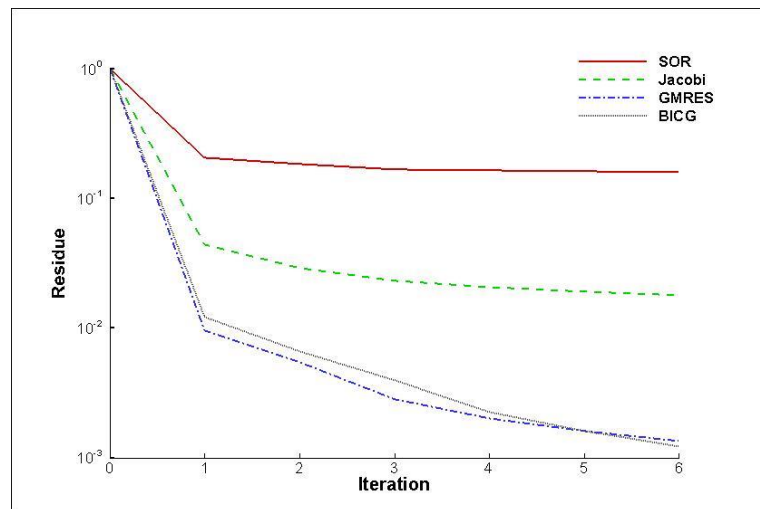


Figure 2.1 Order of convergence within 6 iterations of different iterative methods

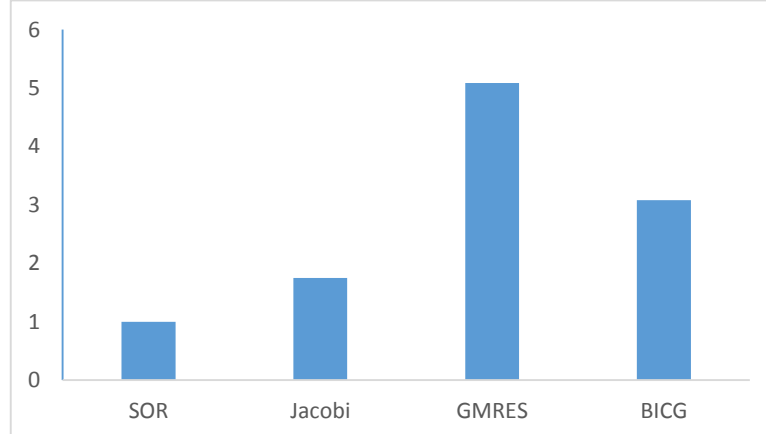


Figure 2.2 Relative computational cost for 4 cycles of flapping wing simulation, SOR's computational cost is taken as 1

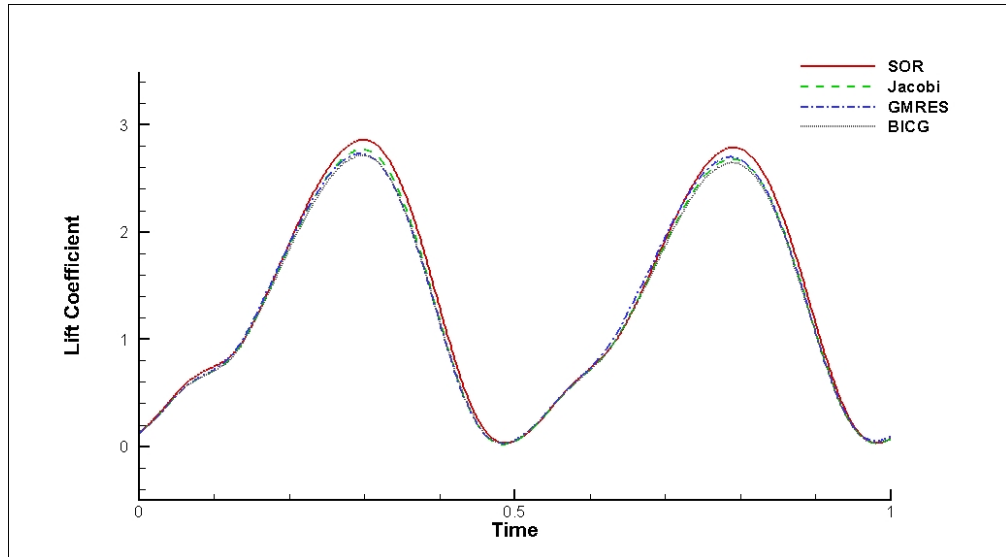


Figure 2.3 Aerodynamic lift coefficient computed on the flapping wing as a result of different iterative methods used for solving pressure Poisson equation

It can be seen from Figure 2.3 that the lift force computed using SOR and Jacobi methods tend to have higher peaks than GMRES and BICGStab methods. This is due to the poorer convergence of the pressure Poisson equation at these high velocity phases of the flapping motion which resulted in larger extreme pressure values obtained at the wing surface. Otherwise, the results are very comparable considering the small difference at peak only contribute to about 1% of the average force difference. In consideration of the computational costs involved in GMRES and BICGStab methods despite its higher convergence results, a minor change to numerical solution strategy is implemented such that the projection method iterations are executed with an alternating Poisson solver based on GMRES iterative method and SOR iterative method to take advantage of both good convergence and fast solutions.

## 2.7 Other Numerical Implementations

Insect flights could range from very low Reynolds number ( $Re < 100$ ) such as fruit fly and hoverflies to relatively large Reynolds number range ( $Re > 2000$ ) such as dragonflies (Wakeling & Ellington, 1997). The aforementioned incompressible viscous computational scheme tends to become unstable at larger Reynolds numbers. A few additional implementations are added into the numerical scheme to improve the stability of method.

On the other hand, an external flow problem usually involves a very large



computational domain and it is also necessary to have high spatial resolution within the computational domain to capture all the flow structures evolved during an unsteady motion of the body. The increase of computational costs associated with such large domain and high resolution could make even the high performance computers used for scientific research sweat to cope. Therefore, to improve the efficiency of computations, parallelization is performed to the majority of the code to take advantage of the multi-core multi-thread structures of today's computers.

### 2.7.1 Artificial Dissipation

The following isotropic artificial dissipation model is implemented only in the background Cartesian nodes as the implementation requires good distribution and redistribution, and the meshless nodes' Lagrangian nature makes this difficult in flows with extensive boundary motions.

$$C_x = C_y = \max\{\alpha |\nabla p|, \beta\} \quad [2.11]$$

$$\text{Where } |\nabla p| = +\sqrt{\left(\frac{\partial p}{\partial x}\right)^2 + \left(\frac{\partial p}{\partial y}\right)^2}$$

### 2.7.2 Upwind Scheme

Upwind scheme is originally developed by Chorin (Chorin, 1969) in conjunction with the pseudo-compressibility method. However, in the current implementation, the upwind scheme is simply a flow biased backward differencing scheme in which the differencing direction follows the physics of the flow, so the approximation is obtained with physical importance rather than mere mathematical expression.

The upwind scheme implemented in the numerical scheme here is second-order accurate and has two different treatments for the uniform and nonuniform (expanding) background Cartesian grid nodes.

$$\Delta x_{i+1} = x_{i+1} - x_i \quad [2.12]$$

For nonuniform grid:

When  $U_i < 0$

$$\left. \frac{\partial \phi}{\partial x} \right|_i = - \frac{\Delta x_{i+1}}{(\Delta x_{i+1} + \Delta x_{i+2})\Delta x_{i+2}} \phi_{i+2} + \frac{\Delta x_{i+1} + \Delta x_{i+2}}{\Delta x_{i+1}\Delta x_{i+2}} \phi_{i+1} - \left( \frac{1}{\Delta x_{i+1}} + \frac{1}{\Delta x_{i+1} + \Delta x_{i+2}} \right) \phi_i \quad [2.13]$$

When  $U_i > 0$

$$\left. \frac{\partial \phi}{\partial x} \right|_i = \frac{\Delta x_i}{(\Delta x_{i-1} + \Delta x_i)\Delta x_{i-1}} \phi_{i-2} - \frac{\Delta x_{i-1} + \Delta x_i}{\Delta x_{i-1}\Delta x_i} \phi_{i-1} + \left( \frac{1}{\Delta x_i} + \frac{1}{\Delta x_{i-1} + \Delta x_i} \right) \phi_i \quad [2.14]$$

For uniform grid

When  $U_i < 0$

$$\left. \frac{\partial \phi}{\partial x} \right|_i = \frac{1}{2\Delta x} (-\phi_{i+2} + 4\phi_{i+1} - 3\phi_i) \quad [2.15]$$

When  $U_i > 0$

$$\left. \frac{\partial \phi}{\partial x} \right|_i = \frac{1}{2\Delta x} (\phi_{i-2} - 4\phi_{i-1} + 3\phi_i) \quad [2.16]$$

The upwind scheme simulates physical direction of propagation of information in flow field and improves numerical stability in a highly unsteady flow field. It is only applied in the background Cartesian grid, similar to artificial dissipation described in the earlier section. Upwind scheme is usually not implemented together with artificial dissipation.

### 2.7.3 Adaptive Time Stepping

Adaptive time stepping is a technique to dynamically scale the temporal component for the numerical solution according to the flow condition given by the Courant-Friedrich-Lery (CFL) criterion. This helps to accelerate the computation at times when the flow field evolves slowly due to small movement of the solid body and reduces time step advancement at times when the motion of the solid body induces high flow velocity in the flow field.

The adaptive time step is thus determined based on the following relation:

$$\Delta t = C_{max} \min \left\{ \frac{\Delta x}{u}, \frac{\Delta y}{v}, \frac{\Delta z}{w} \right\} \quad [2.17]$$

Where  $C_{max}$  is the maximum CFL condition allowed in the discretization and usually smaller than 1.0. The adaptive time stepping is applied over the entire computational domain including the meshless nodes ( $\Delta x, \Delta y, \Delta z$  of meshless nodes are determined based on the average distance of the node with 3 of its closest neighbours). This further improves stability in the semi-implicit numerical scheme.

#### 2.7.4 Parallelization

The numerical scheme for the current study is implemented using C++ programming code, which offers great flexibility in implementing parallelism in computation by utilizing the increasing number of processing cores made available in modern supercomputers. OpenMP is chosen as a simple and flexible way of parallelizing the existing code with minimal changes of coding structure required.

OpenMP offers many advantages in parallel programming than other existing parallel programming techniques such as MPI. OpenMP is more portable and generic across different processing platforms, such that the same numerical code can be easily executed on supercomputers or even personal computers with much modifications. There is no memory management and information passing processes required, memory is shared among all the multi-thread processing in OpenMP (Amritkar, Tafti, Liu, Kufirin, & Chapman, 2012), and the implementation is incremental that makes debugging more much convenient. When data placement is carefully planned, the computational efficiency of OpenMP at up to 256 cores are comparable to that of MPI while at the same time maintain a clear benefit of flexibility of the later (Sato, 2002).

In the present study, the implementation of OpenMP on 16 threads has shown to effectively reduce computational time required for simulating flapping wing motions by 4 times, while the coding length is only increased by 10%. This is a significant improvement and allowed the computation of 20 wing beat cycles of flapping wings using GMRES and SOR iterative methods to be completed in 4 days.

## 2.8 Fluid-Structure Interaction

Fluid-structure interaction (FSI) is an important additional implementation in the numerical scheme in the current research that offers the capability of simulating actual insect flight problems within a single iterative process.

The dynamics of the solid body can be divided into two components, in which one is due to the prescribed motion of the body itself, and the other is due to the fluid-structure interaction induced by the flow field. The rotation and translation of the solid body about its own centre of mass can be calculated using a simple equation of transformation based on translation coordinates  $X_c$  and rotational matrix  $R_c$ , details will be explained in the next chapter. The motion of the body due to the fluid force obeys Newtown's Laws:

$$P(t) = m \cdot v(t) \quad [2.18]$$

$$L(t) = I \cdot \omega(t) \quad [2.19]$$

Where  $P(t)$  and  $L(t)$  are the total linear and angular momentums of the rigid body.  $v(t)$  and  $\omega(t)$  are the linear and angular velocities of the body with respect to its centre of mass.  $M$  is the mass and  $I$  is the moment of inertia of the body. Then the rate of change of the linear momentum  $\dot{P}(t)$  and angular momentum  $\dot{L}(t)$  are related to the fluid induced total force  $F(t)$  and torque  $\tau(t)$  are given:

$$\dot{P}(t) = F(t) + G \quad [2.20]$$

$$\dot{L}(t) = \tau(t) \quad [2.21]$$

Where  $G$  is an external force such as gravitational force.  $F(t)$  and  $\tau(t)$  can be determined at every new time step  $(n + 1)$  after solving the flow field using the aforementioned iterative method.

Thus, we can now use a time-implicit iterative procedure to determine the dynamically coupled solution of the flow field  $(\partial\Omega, \mathbf{u}, p)^n$  and the body  $S^n \equiv (X_c, R_c, P, L)^n$  at the time step  $(n + 1)$  as follows:

1. Progress time to time step  $(n + 1)$  and obtain the solid body/boundary configuration of  $\partial\Omega^{n+1}$  based on a prescribed motion.
2. Evaluate the  $i$ th approximate of  $v^{n+1,i}$  and  $\omega^{n+1,i}$  based on the intermediate

solution of the body  $S^{n+1,i}$ ,  $i = 0$  refers to the initial solution of the body due to the prescribed motion without FSI effect.

3. Solve the flow field equations using projection method to obtain  $(\partial\Omega, \mathbf{u}, p)^{n+1,i}$
4. Update the total force  $F^{n+1,i}$  and torque  $\tau^{n+1,i}$  due to the flow field acting on the solid body.
5. Evaluate  $(i + 1)$ th approximate of the solid solution  $S^{n+1,i+1}$  due to the force and torque.
6. Check for convergence of the body solution  $\|S^{n+1,i+1} - S^{n+1,i}\| < TOL$
7. If convergence criterion is satisfied, then the required flow and body solution due to prescribed motion and FSI effects have obtained. If convergence criterion is not satisfied, repeat step 2-7 until criterion satisfied or iteration limit is reached.

## 2.9 Handling of Hybrid Grid

As previously explained, SVD-GFD scheme employs a hybrid grid structure that takes advantage of both the numerical accuracy of mesh free body fitting grid and efficiency of simple fixed background grids for solving a complex geometry moving boundary problem. In the specific case of insect flight problem, the meshless nodal points are only generated around and surrounding the boundary of the wing structure, leaving the total number of meshless nodal points a small fraction of all the nodal points involved in the computation. There are many ways of generating the meshless nodes around the complex geometry of the solid body in the flow domain, and more details of the meshless node generation technique used will be explained in the later chapters. The zone of meshless cloud is then superposed onto a coarser Cartesian background grid in the computational domain. A uniform background Cartesian grid is used in the vicinity of the moving body while an expanding grid structure is used in the far field to reduce the computational resources required of dealing with a relatively large computational domain and the demanding details of flow structure close to the moving body.

### 2.9.1 Nodal Classification

The implementation of a nodal classification system is critical to the numerical implementation of the case in study. The nodes used in computation can be broadly classified in three main categories.

Category 1 nodes. These are background Cartesian nodes that are not involved in computation when they are covered by the solid body or the surrounding meshfree nodal cloud. These set of overlapped nodes changes with time because of motion of the body or boundary. The determination of these nodes relies on taking dot product of the vector  $r_{BP}$  of Cartesian nodes B (technique for special cases involving non-C/artesian grids will be discussed later) from surface point P with the normal vector of surface  $n_p$  at point P according to equation [2.22].

$$r_{BP} \cdot n_p > 0 \quad [2.22]$$

The approximate surface vector at point P (P is a meshless nodal point on the physical boundary of the body or the invisible boundary of the meshless cloud) can be determined based on the mean weighted equally algorithm of Thürmer (Thürmer & Wüthrich, 1997), which computes the surface normal at a boundary node as the simple average of the unit normal at the triangular faces formed by the node with a selected set of its neighbouring boundary nodes. This triangular face information can be generated using any finite element nodal generator that may not be the same as the nodal points involved in fluid computations. Further optimization of the normal by taking distance weighted global averaging of the normal vectors can be applied for smoother normal distributions on a complex geometry surface. This approach represents the general principle of classifying overlapped nodes, however, more detailed processing are implemented in actual case simulations with careful considerations and will be explained later.

Category 2 nodes. These are Cartesian background nodes that make up the bulk of the external flow domain and are relatively far from the solid body/boundary. These nodes have only other Cartesian background nodes in the immediate neighbourhood (6 nodes in three dimensional central difference scheme) in a structured grid formation and only require simple and accurate finite difference approximations to solve.

Category 3 nodes. These nodes include both the mesh free nodes describing the

surface of the solid bodies and the meshless cloud nodes surrounding the bodies as well as the Cartesian background nodes which their immediate neighbourhood are partially filled by meshless nodes in which case the standard finite difference method for structured grid cannot be applied. The Cartesian nodes included in this category usually represents the “interface” between the meshless cloud and the uniform background nodes. General finite difference method are then applied to this category of nodes to solve the flow field in the vicinity of the moving body/boundary at second-order accuracy. In a general insect flight simulations, number of nodes in Category 3 and Category 2 has a ratio of approximately 1 to 200 and therefore, reduces the amount of costly GFD calculations to a very minimal while maintaining the flexibility and accuracy of the numerical method.

A figure illustrating the distribution of each category of nodes in a two-dimensional view of the chord section of the insect wing together with the near field flow domain is shown in Figure 2.4.

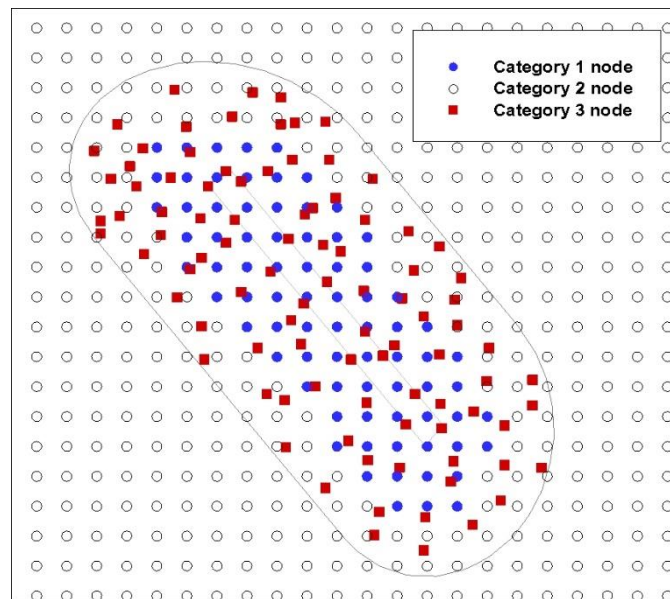


Figure 2.4. Nodal distribution surrounding an insect wing where circular nodes represent Cartesian background nodes and square nodes represent meshfree nodes.

## 2.9.2 Nodal Class Transition

The nodal categories changes with the motion of the solid body, and careful consideration are taken to take care of the transition of such nodal categories to ensure accuracy and stability of the computation.

When the solid body moves into a set of existing Category 2 nodes (Cartesian

background nodes), these nodes are immediately removed from participations of computations and their classifications are changed to Category 1 in the new time step. Their flow field velocity and pressure information are lost until they immerge from being overlapped by the solid body or the meshless cloud and become a non-Category 1 nodes again.

When the solid body moves away, a set of existing Category 1 nodes would immerge from the rear of the solid body, a special treatment is required to include these nodes in the ensuing computations. These nodes would be temporarily designated as “fresh” nodes. Since these nodes contain no information of the flow field in the previous time step, an interpolation to second-order accuracy based on Taylor series expansions of the GFM approximations of available solutions at the neighbouring nodes is carried out. Caution has to be exercised as the number of “fresh” nodes should not be too substantial in the limited vicinity of the flow field, as it would affect the convergence of the solution due to the error involved in the linear approximation process. As soon as the velocity and pressure information are obtained for these “fresh” nodes, they then participate in the GFD computations like all the other Category 3 nodes.

The meshless Category 3 nodes surrounding the solid body usually remains as Category 3 nodes with convection velocity specified by the motion of the body. These nodes do not require transition as they are usually always available for computations with previous time step solutions. Except in very specific scenarios, such Category 3 nodes can also be transitioned to Category 1 nodes and taken out of the computation process similar to the background Cartesian nodes as in the aforementioned case. However, it is noted that the transition of these Category 3 nodes to Category 1 and back could lead to solution divergence if not handled carefully. More details of such case handling will be discussed in later chapters.

### **2.9.3 Nodal Selection**

Another critical aspect of hybrid grid handling in the numerical method is the nodal selection. It has been shown that the condition of the matrix  $[S]_{n \times 19}$  depends largely on the relative spatial distribution of the supporting nodes (Yu et al., 2011). In the description of the numerical scheme, we have shown that by taking information of more supporting nodes ( $n > 19$ ) than the minimum required for second-order accuracy of



the scheme, and solve the over determined matrix using SVD method could in general overcome the singularity conditions in the matrix. Therefore, usually a minimum of 40 to 80 supporting nodes are selected during the numerical computations.

In the previous works, distance based nodal selection schemes are used (X. Y. Wang et al., 2008), in which preference are given to nodes that are closer to the centre node. Simple filtering technique was implemented to prevent very close proximity or overlapping of convecting meshless nodes with the background Cartesian nodes (Yu et al., 2011). If such case are discovered, the background Cartesian nodes will be classified to become Category 1 nodes and removed from the computation. However, due to the limitation of the proximity detection routine used, this technique does not help to enforce better spatial distribution of the remaining nodes in the vicinity. An observation is made that a good nodal selection of the supporting nodes is particularly important around sharp edged solid boundaries for the numerical solution to converge.

A cone based nodal selection scheme is developed together with colleague at National University of Singapore and applied to improve the nodal selection technique in insect flight simulations. The idea is that by assuming the centre node as a point source and its surrounding nodes as spheres with finite radius, then one can find a projection cone in the radial direction from the centre node to the supporting node. The angle of the projection cone is specified as a constant and the path of the projection indicates an exclusive zone for the supporting node in questions. Therefore, in order to prevent biased nodal selection, the subsequent supporting nodes are selected by giving priority to closer supporting nodes that have no overlapping of their projection cones with that of the previously selected supporting nodes. In the event that not enough supporting nodes are selected by the cone based nodal selection technique, the solver will fall back to the distance based nodal selection for the remaining supporting nodes required to complete the matrix. Figure 2.5 shows the selection priority in this scheme in a two-dimensional case, where node 2 is selected in the nodal selection scheme despite that it is further away from the centre node than node 3, as node 3 has overlapping projection cone with node 1 which has been selected in the previous process. Circle represents the sphere of neighbourhood where supporting nodes are selected from.

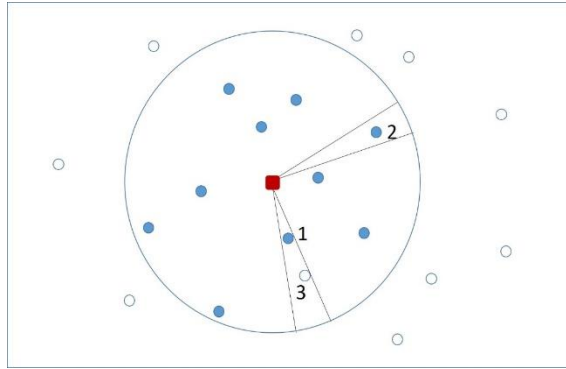


Figure 2.5 Cone based nodal selection

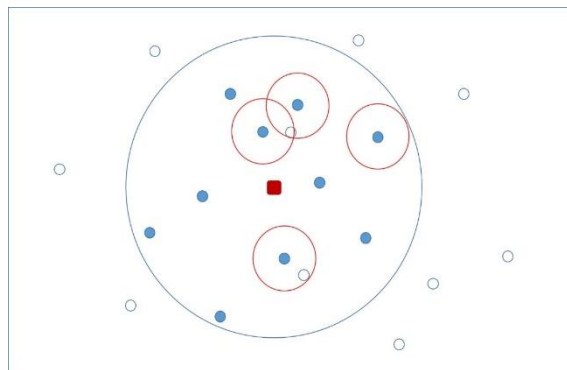


Figure 2.6 Sphere based nodal selection

Another technique is also proven to be quite effective, in which a sphere based nodal selection is applied. In this nodal selection scheme, each supporting node is given a sphere of “influence” based on a predetermined radius. When node selection routine is executed, each supporting node is used to check if there is already a selected supporting node in its sphere of “influence”. This ensures evenly distributed supporting nodes surrounding the centre node in the case even when supporting nodes are clustered together on one side and sparsely distributed on the other side (usually happens close to the sharp edge of the boundary). There are two approaches to specify the radius of “influence”: one is to set the radius to a constant value for all supporting nodes and the other is to determine the radius based on the supporting node’s proximity to the centre node. The second approach is usually more favourable due to the distance based weighting function that favours contribution of nearby supporting nodes. The detailed implementation is modified case by case during simulations based on observation of the solution convergence and experimentation. Figure 2.6 shows the sphere based nodal selection technique, where square nodes represent the central node for solution computation, solid circle nodes represent the selected supporting nodes and hollow circles are nodes that are not selected. Red circles represent the exaggerated spheres of “influence” for supporting nodes and subsequent nodes that fall within the sphere of

influence of previously selected supporting nodes are discarded from the computation. Blue circle represents the sphere of neighbourhood space where supporting nodes are selected from.

However, it is worthwhile pointing out that the above mentioned nodal selection scheme inevitably increased computational cost of the numerical scheme. For a number of 20,000 and more Category 3 nodes involved in the process, it is important to consider the cost and benefit of implementing such nodal selection schemes. In the present study a combination of distance based and cone or sphere based nodal selection is used at different stages of the computation.

A typical nodal selection outcome from actual three-dimensional simulations of insect flight are shown in Figure 2.7. A total of 60 supporting nodes are selected for each case where the red node is the centre node and blue nodes are the supporting nodes.

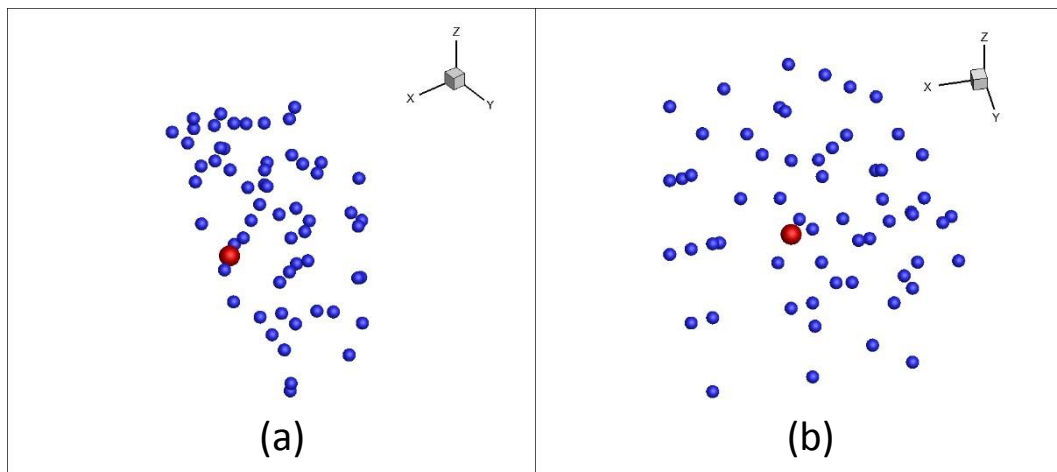


Figure 2.7 3D nodal selection results from actual simulation: (a) nodal selection of Category 3 node near to a flat solid boundary; (b) nodal selection of Category 3 Cartesian background node.

## 2.10 Special Numerical Treatment for Handling of Body Collisions

In the above mentioned numerical scheme, the hybrid meshless method has difficulty in handling multiple bodies with close proximities. However, this issue is overcome by an innovative numerical treatment in meshless nodal handling which can be summarised in two steps, the meshless nodal classification and the node selection treatment implemented. This treatment allowed the following study in insect clap-and-fling flapping (presented in Chapter 5) mechanism possible, in which physical contact or very close proximity of the insect wings are required.

In a normal single body or multiple bodies with large enough body clearance case simulations, the meshless points in the meshless nodal cloud surrounding the rigid bodies are all classified as Category 3 nodes which are all solved simultaneously during the finite difference computations. The relative distance of these nodes with the neighbouring body surface nodes and meshless nodes are fixed throughout the computations and their position convect together with the rigid bodies given by the kinematic model descriptions. The flow field in close vicinity of the rigid bodies are solved using general finite difference method for the meshless nodes together with limited number of Cartesian nodes at the interface between meshless nodal cloud and Cartesian background nodes, the rest of the flow field is solved using normal finite difference method on a regular grid.

However, when close body proximity is required for special case studies such as clap-and-fling of flapping wings, it is inevitable for meshless nodal cloud to intrude into the opposite rigid bodies in which no physical flow can penetrate and the flow domain boundary conditions vary accordingly. In such cases, nodal classification of Category 4 (similar to Category 1 nodes in the Cartesian background nodes) is introduced into the meshless cloud that was previously not carried out, to remove these intruding nodes from the ensuing flow field computations. When the wings sweep and twist following clap, these meshless nodes will re-emerge from inside the rigid bodies to the flow field where flow resolution requires these nodes to be computed in the subsequent computations. Their classifications therefore must be changed back to Category 3 nodes with the values fitted by least square interpolation from the neighbouring flow field nodes. It is important to note that for such method to work without causing numerical instabilities, small time steps need to be used to prevent large area of fresh Category 3 meshless nodes disrupting the flow field continuum in the computational domain. To further enhancing numerical stability, nodal classification changes are also applied to background Cartesian nodes in which smaller number of Cartesian Category 1 nodes are defined, with larger number of Category 3 Cartesian nodes filling in the background of the meshless cloud to improve resolution and minimise disruptions in the flow continuum except at physical convergence of the rigid bodies in limited time duration during clap.

Hence, additional numerical treatments are required to implement nodal classification and nodal selections during every time step on all the meshless nodal

points used in the computations. Such nodal selections include body collision detection, extra neighbouring supporting node selection criteria implementation, and distance weighted supporting point contribution computations from all neighbouring meshless nodes and background Cartesian nodes. Due to the kinematics description differences of different wing bodies, the convective velocity of the meshless surrounding nodes differ and requires carefully processing in the following finite difference computations. In the interpolation of fresh Category 3 meshless nodes emerging from the inside of rigid bodies, a preferred source of interpolation solutions from nearby Category 3 background Cartesian nodes and the body fitting surface meshless nodes with known boundary conditions are applied.

The result is a reliable numerical setup that could simulate and study close wing-wing interaction in insect flapping flights such as the aerodynamic effect of clap-and-fling mechanisms. Comparative results with published results of experimental and numerical works, and further flow structure observations and discussion on aerodynamic effects of such mechanisms will be explained in Chapter 5.

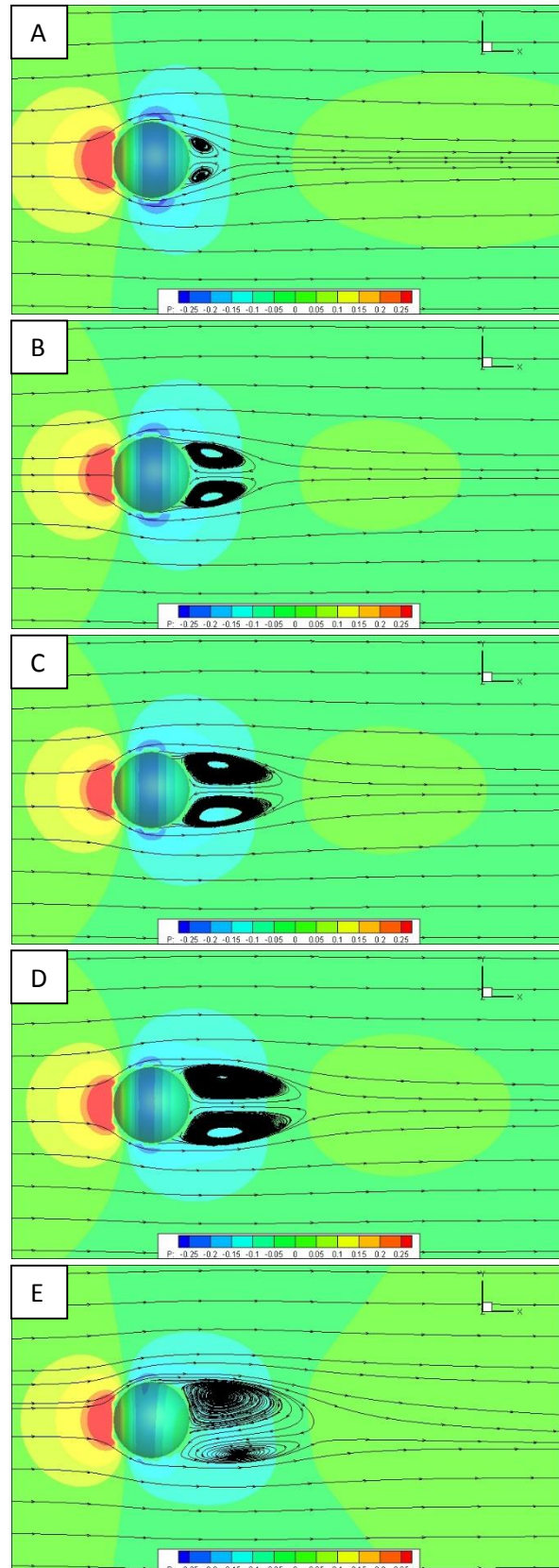
## **2.11 Validation Cases**

Simple validations were carried out and the results are shown and discussed in the following section in order to establish the accuracy of the current numerical method.

### **2.11.1 3D Flow Past Sphere**

Flow past sphere is simulated across a range of Reynolds numbers from axisymmetric steady flow to unsteady flow regime with vortex shedding. The streamline plot of the flow along the XY plane of the flow domain showing the vortex formation downstream of the sphere show good agreement with the reported results from Johnson et al. (Johnson & Patel, 1999). It can be seen that the flow is initially axisymmetric at  $Re=50$ , and the wake region grows as Reynolds number increases. When  $Re=250$ , the wake vortex starts to shed and an asymmetric wake region is observed. The drag coefficient plot also agrees well with the experimental results of Roos and Willmarth (Roos & Willmarth, 1971). The three dimensional iso-vorticity contour plot shown, further demonstrates the ability of the numerical scheme in

capturing the unsteady flow structures in 3D. The Strouhal number ( $St = fL/V$ ) of vortex shedding for case  $Re=300$  is evaluated to be 0.140, agrees with similar values of 0.137 by Johnson and 0.136 Tomboulides (Johnson & Patel, 1999).



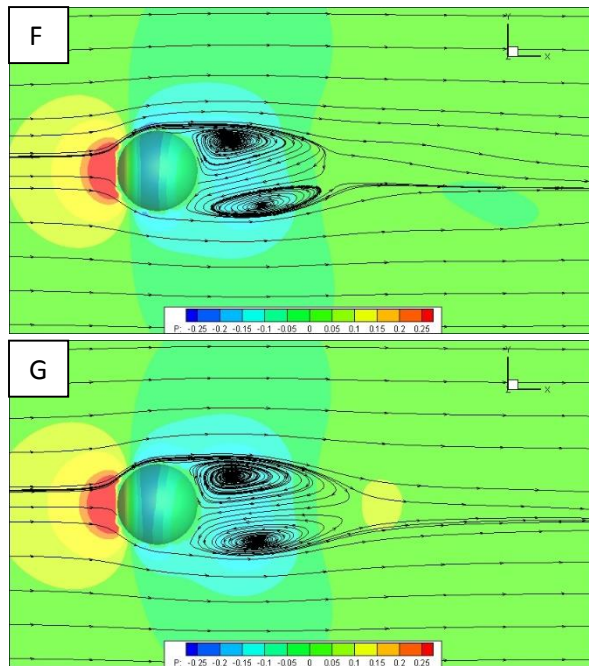


Figure 2.8 Streamline plot of flow past sphere at different Reynolds number (A)  $Re=50$ , (B)  $Re=100$ , (C)  $Re=150$ , (D)  $Re=200$ , (E)  $Re=250$ , (F)  $Re=300$ , (G)  $Re=350$

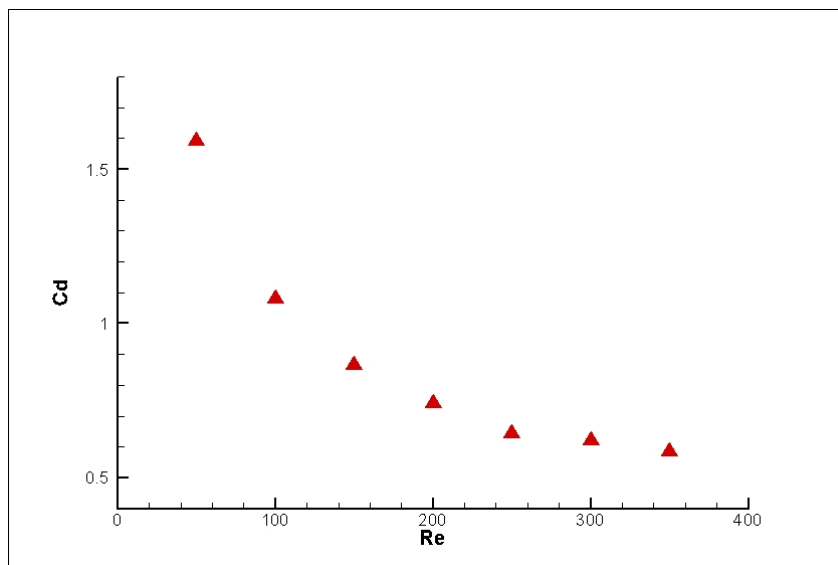


Figure 2.9 Mean drag coefficient measured on sphere varied with respect to Reynolds number, this trend agrees well with the published experimental results of Roos and Willmarth (Roos & Willmarth, 1971)

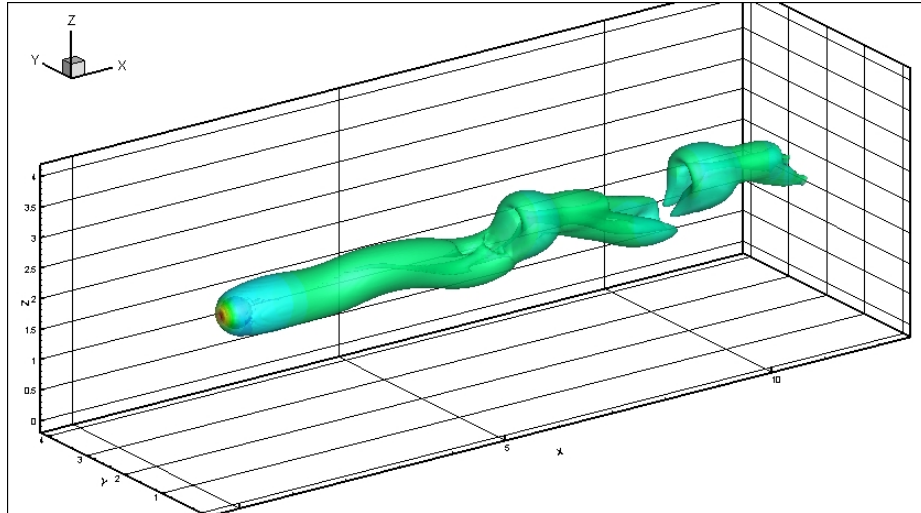


Figure 2.10 Vorticity iso-surface plot showing the periodic shedding of the wake vortices in a 3D flow past sphere problem at  $Re=300$

### 2.11.2 Validation of Artificial Dissipation Model

Further validation on the accuracy of artificial dissipation model is carried out on the same 3D flow past sphere case presented in section 2.11.1. The parameters of the artificial dissipation are specified as  $\alpha = 2.5$  and  $\beta = 25$  in the isotropic artificial dissipation model presented in section 2.7.1. The Reynolds number of the case verified is 150, which corresponds to the majority of flapping wing simulation cases shown in the present work.

At  $Re = 150$ , a generally symmetrical steady flow is observed as shown in Figure 2.10C. The computed drag coefficient acting on the sphere using present numerical scheme with and without artificial dissipation are shown in Figure 2.11. The two lines representing the computed aerodynamic drag acting on the sphere differ by approximately 5% at maximum, in which the estimated aerodynamic force production is lowered with the introduction of the artificial dissipation. Further analysis of the initial transient evolution of the flow captured by both simulations demonstrate the negligible difference in capturing of the physical phenomenon of unsteady flow structures most critical to the present studies.

Hence, it is sufficient to demonstrate the accuracy of the current implementation of artificial dissipation model and the use of which in the ensuing case studies are justified in order to overcome numerical stability issues involved in solving significantly unsteady flow transients associated with flapping wings.



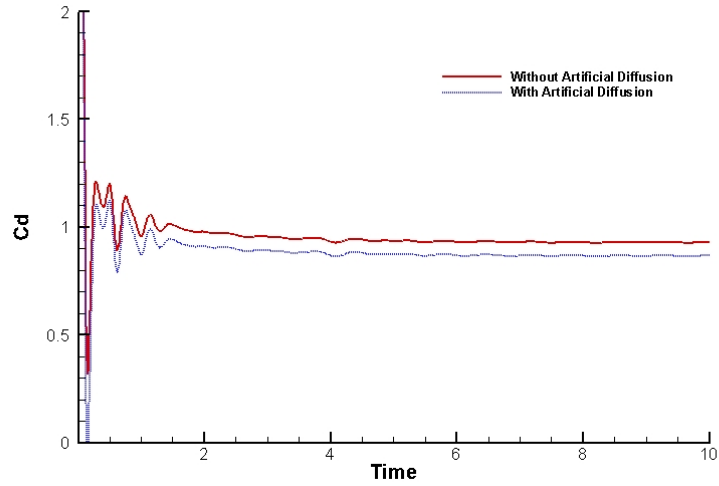


Figure 2.11 Computed drag coefficient of flow past sphere at  $Re=150$  shows minor deviation of aerodynamic effect due to the introduction of artificial dissipation

### 2.11.3 3D Falling Sphere FSI

The free falling sphere in a Newtonian fluid the effect of gravity is tested in the present numerical validation to verify the accuracy of fluid-structure interaction model implemented. The empirical relationship for the drag coefficient on Reynolds number for a sphere in motion is given by equation [2.23] (Abraham, 1970).

$$C_d = \frac{24}{9.06^2} \left( \frac{9.06}{\sqrt{Re}} + 1 \right)^2 \quad [2.23]$$

A sphere model is constructed with 3436 mesh free nodes on the surface and 6000 nodes in the meshless cloud surrounding the sphere. The flow domain is discretised by  $141 \times 141 \times 281$  background Cartesian nodes. The sphere has a non-dimensionalised diameter of 1 and density  $\rho_s = 1.05$ . The fluid density is specified as  $\rho_f = 1.0$ . The fluid dynamic viscosity  $\mu$  is computed to set the specified Reynolds number of  $Re = 100$  for the validation simulation.

Figure 2.12 shows the velocity results obtained. The terminal velocity  $U_t = 0.165$  is achieved at non-dimensional time of 9. The result shows good agreement with Abraham's empirical equation solutions of 1.52 at  $Re = 50$ . This demonstrates the accuracy of the present FSI implementation.

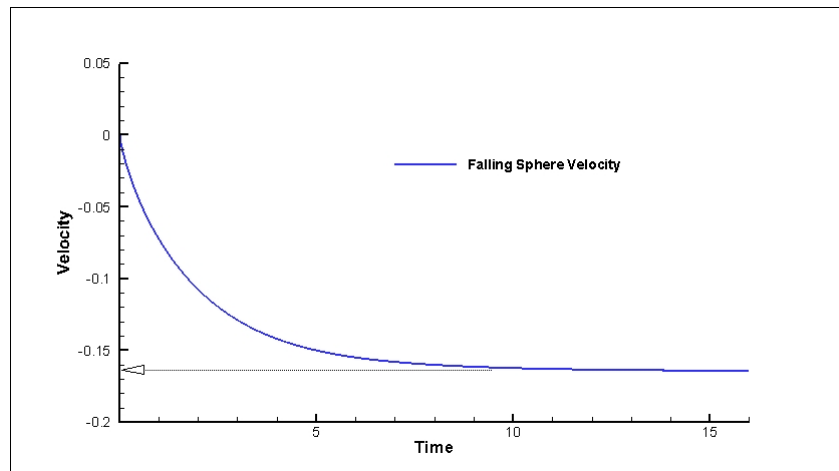


Figure 2.12 Velocity of the falling sphere with FSI computations showing the terminal velocity of  $Re=50$  to be approximately 1.62

## 2.12 Summary

The Singular Value Decomposition-General Finite Difference based computational fluid dynamics scheme for three dimensional incompressible, viscous fluid flow at low Reynolds number with immersed moving boundaries is outlined in this chapter. The method is further developed through numerical improvements by introducing artificial dissipation, upwind finite difference computation, adaptive time stepping, computational parallelization, fluid-structure interactions and innovative meshless nodal selection schemes such that it is fully capable of simulating insect flapping wing flights with great flexibility, good accuracy and high efficiency.

The numerical scheme's efficiency and convergence behaviour is examined using different iterative methods for solving the Poisson equation. The performance and accuracy characteristic is established and provides as a reference for future improvements of the numerical scheme.

Further numerical treatment is also explained in this chapter that are implemented for the study of clap-and-fling flapping wing motions. Clap-and-fling involves extensive wing-wing interactions within close proximities, which has been challenging for numerical simulations using other existing methods such as immersed boundary methods. The present numerical treatment together with SVG-GFD numerical scheme has shown to be capable and efficient in the study of clap-and-fling.

Validations using simple cased of flow past sphere and falling sphere due to

gravity at low Reynolds number have demonstrated the capability and accuracy of the present numerical scheme and provided confidence for the following studies of insect flapping wing flight problems.

# **CHAPTER 3: Geometric and Kinematic Modelling of Flapping Wings**

## **3.1 Introduction**

The main challenge with studying of insect flight lies in modelling the insect and mimicking the kinematics of its flapping wing, which are small in physical scales. Each wing (assumed rigid) has three degrees of rotational freedom that are actively driven to produce both lift and thrust required by the insect in flight. Unlike conventional flying vehicles where lift generation can be approximated by applying steady-state assumption, the evolutionary result of insect wing geometries and the respective flapping motion kinematics give each species its unique flying characteristics. In this study, a versatile and flexible geometric and kinematic modelling technique is presented and applied to demonstrate its feasibility in accurately simulating insect flight of varying Reynolds number and complexities. The technique is capable of mimicking realistic insect flapping motion kinematics and facilitate the ensuing numerical studies of the unsteady aerodynamics associated with flapping wings.

## **3.2 Geometric Modelling**

In this study, one particular insect, fruit fly (*Drosophila Melanogaster*), is chosen. The flapping wing motion of fruit fly has a frequency of approximately 200 (S. Fry, Sayaman, & Dickinson, 2005), and hence its Reynolds number usually falls in the range of 120 to 150, which is typical for most small size insects. The flapping flight of fruit fly has been well observed and extensive experimental measurements are available for referencing. Additionally, fruit fly is observed to have only 1 pair of flapping wings for generation of all aerodynamic forces, which simplifies the kinematic modelling process and allows more focus on the study of unsteady aerodynamic effects. The geometric modelling process involves the construction of 3D CAD models of fruit fly wing and body based on the morphologically accurate illustrations obtained from online sources, and followed by the grid generation of the solid 3D geometries required by the numerical scheme.

### 3.2.1 3D CAD Modelling

The 3D CAD modelling is carried out by carefully following the wing planform and the body profiles in accordance to accurate illustrations of the insect wing and body. The illustrations are obtained from reputable online databases. Minute details of body morphological structures and parts, such as the insect legs, are assumed to have little or no influence on the aerodynamic behaviour of its flapping flight motion, and hence ignored in the construction of models. However, the wing planform shape details are strictly followed (the venation structures are ignored), so that the numerical study would be able to accurately capture the unsteady aerodynamic effects due to the wing geometric shapes. The models are constructed using SolidWorks®.

The important geometric parameters of fruit fly are obtained from entomology database (“<http://flybase.org/>,” 2013) and cross referenced to experimental records from recent insect flapping flight studies (S. Fry et al., 2005; Shyy et al., 2010). The used values of the important morphological parameters are shown in Table 3-1.

*Table 3-1 Important morphological parameters of fruit fly (Shyy et al., 2010)*

<b>Parameter</b>	<b>Fruit fly</b>
<b>Mean Chord Length</b>	<i>0.78 mm</i>
<b>Body Length</b>	<i>2.54 mm</i>
<b>Wing Length (single wing)</b>	<i>2.39 mm</i>
<b>Total Mass</b>	<i>0.96 mg</i>



*Figure 3.1 Fruit fly with extended wing from top view, with courtesy of Phillip N. Appiah  
“<http://www.discoverlife.org>”*

The fruit fly geometric models are therefore obtained by plotting the surface contour of the insect's different perspective 2D view images, superimposed onto the 3D CAD drawing board. Then spline curves are used to join the 2D drawings to obtain the 3D geometric framework of fruit fly wing and body. Surface mapping and lofting techniques are then used to generate the full 3D solid models of the wing and body. Meanwhile, less important body features are omitted for simplicity of the model. The simplicity and accuracy of the 3D model is crucial as the quality of mesh generated on and around the complex surface geometry of the model would result in varying performance and efficiency of ensuing CFD simulations.

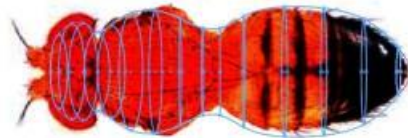


Figure 3.2 Contour plot in accordance to actual fruit fly body geometry from top view, with courtesy of "<http://flybase.org>"

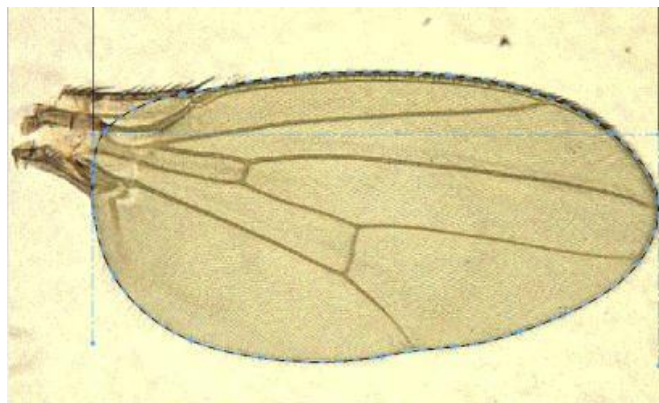


Figure 3.3 Contour plot of actual fruit fly body geometry from side view, with courtesy of "<http://www.uamont.edu/>"

From the viewpoint of modelling fidelity, the geometric details for the body are

less important than those of the wings, since the bulk of the aerodynamic forces are generated from interaction between the wings and the surrounding air. Nonetheless, the position of the centre of mass, which is largely governed by the disposition of the body that contains the majority of the insect's mass, needs to be ascertained with good accuracy. This is because the position of centre of mass will influence the dynamics of the insect in flight. We could determine mathematically the centre of mass of the insect from the accurately constructed geometric solid model of the fruit fly body by assuming relative constant density distribution within the model. The centre of mass parameter will be used in the simulation of insect flapping flight with FSI computations later on.

The insect wings are modelled in the similar way by plotting the contour of the wing planform based on photograph of actual fruit fly wing. The estimated wing span can be obtained by adding the wing length of the insect to the separation of the wing roots, where the centres of rotation of the respective left and right wing lie. The wing root section of the insect wings are ignored and removed from the 3D wing models for two main reasons. The insect wing root section only moves at very low speed as compared to the rest of the wing sections during flapping flight and the aerodynamic forces produced is very limited and can be safely ignored in computations. A minimum clearance of solid boundaries are required between the insect body and wing due to the need of the numerical method to generate meshless supporting nodes surrounding the solid boundary. And it is shown that as solid boundary interact or collide during the simulation, the numerical scheme tends to suffer from significant stability and efficiency issues.



*Figure 3.4 Fruit fly wing contour mapping for 3D model construction, the wing root section to the left is omitted, with courtesy of "<http://www.mheresearchfoundation.org/>"*

### 3.2.2 Rigid Body Assumption

Going through different evolutionary pathways, insects may have either one pair or two pairs of wings. Or in some insect species, the hind wing pair degenerates into halteres that flap rapidly to function as gyroscopes. The wings may have also developed into different planforms (shape and aspect ratio), venal structure and mechanical properties. All of these add to the modelling complexities. In particular, the information on the mechanical properties are not generally available and their determination requires considerable expertise. Thus, in the present study, we have assumed that the wings are effectively rigid and smooth on the surfaces, except along the wing edges, where it simply follows the geometric contour of the wing.

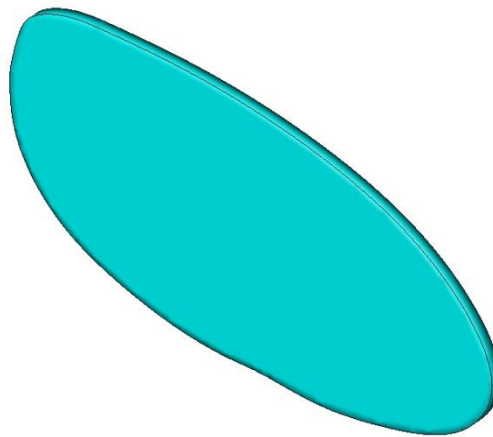


*Figure 3.5 Flat and smooth thin fruit fly wing with thickness of 2% wing length (or 5% mean chord) and sharp edges*

Insect wings are also thin, so that flow separates going around the edges which cause substantial transient aerodynamic effects that are critical for flapping wing flights. In particular, sharp leading edges are required for the formation of leading edge vortex, which is known to play a lead role in lift generated on insect wings. Thus, in this simulation, we have also designed the fruit fly wing to have a thickness of about 2% of wing length (or 5% of mean chord length). The 3D view of the fruit fly wing CAD model is shown in Figure 3.5.

### 3.2.3 Mesh Generation

As described in the previous chapter, the surface mesh generation and the meshless



nodal cloud generation are critical to the success of CFD simulations. The process of grid generation on the geometric models of insect body and wings can be divided into two steps, mesh node generation on the surface and creation of meshless nodal clouds in the nearby volume surrounding the rigid bodies.

Mesh node generation on the surface of insect wing model uses simple finite element discretization method where the nodal distribution is controlled by spatial parameters such that mesh is denser around and at the sharp edges of the wing. The nodes are more spread out at the centre of the smooth wing surface up to a predetermined limit so as to ensure sufficient number of surface boundary nodes for capturing of flow details. This method of nodal generation helps to improve computational stability and ability of the method to capture important aerodynamic information around the edges of the wing where flow structure tend to evolve more rapidly during the flapping motion. At the same time, the computational efficiency is also improved as the total number of surface nodes on each wing is limited to between 1000-3000 nodes.

Mesh node generation on the surface of the insect body uses the same finite element discretization with slightly coarser distribution. For most insects, the size of body is significantly larger than its wings, and require more nodes in support of computations. However, the amount of body movement of the insect during flapping flight is negligible compared to the flapping motion of the wings, leading to limited interaction with the flow and hence insignificant aerodynamic forces produced. Less number of nodes are thus required to computationally solve the flow around the body. It is however noted that, due to the more complex geometry of the insect body, which consists distinct sections of Head, Thorax and Abdomen, the meshing technique varies to cater for proper spatial distribution of the surface nodes in order to accurately describe the geometric shape of the insect body.

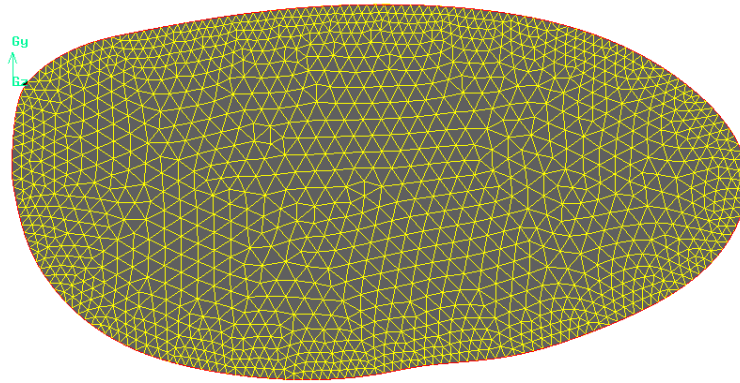


*Figure 3.6 Denser surface node distribution along the wing edges and coarser surface node distribution in the remaining area of the wing are observed in this fruit fly wing model. Triangles are used for plotting and area computation purposes and are not used in the meshless based numerical method*

Meshless supporting nodes in the surrounding volume of the rigid bodies are created first by expanding the volume of the original rigid body uniformly in the normal direction outwards to obtain a larger volume that contains the original rigid body. Then spatially discretization of the volume in-between, called the meshless cloud volume, is done using finite volume method. The volume expansion is carried out in the normal outbound direction to the extend of approximately four times the average surface nodal separation. This is to provide sufficient amount of supporting meshless nodes that are required for numerical computations. The boundary of the meshless cloud volume is then smoothed to eliminate any possible defects due to complex geometries on the original rigid bodies so as to facilitate an easier nodal selection process described in the Chapter 2. However, it is worth pointing out that the outer boundary of the meshless cloud volume is not necessarily required to be smooth, in which case the numerical method can still be used without issue.

The tetragonal relations of the generated meshless nodal points are only used for visualization of results and also plotting purposes. This information is not used in the actual numerical computations as the numerical methods employs a meshless approach in solving the flow field. However, the relative position of these meshless nodes within the meshless cloud volume remain constant throughout the flapping motion of the wing (the wing is assumed rigid as described in earlier section). This suggest that possible improvements on efficiency of the current numerical method can be implemented, but the detailed investigation is not the focus of current study and would require further studies to verify. These surface mesh free nodes and the meshless nodes within the

meshless cloud volume form the basis of Category 3 nodes, as described in Chapter 2, during computations.

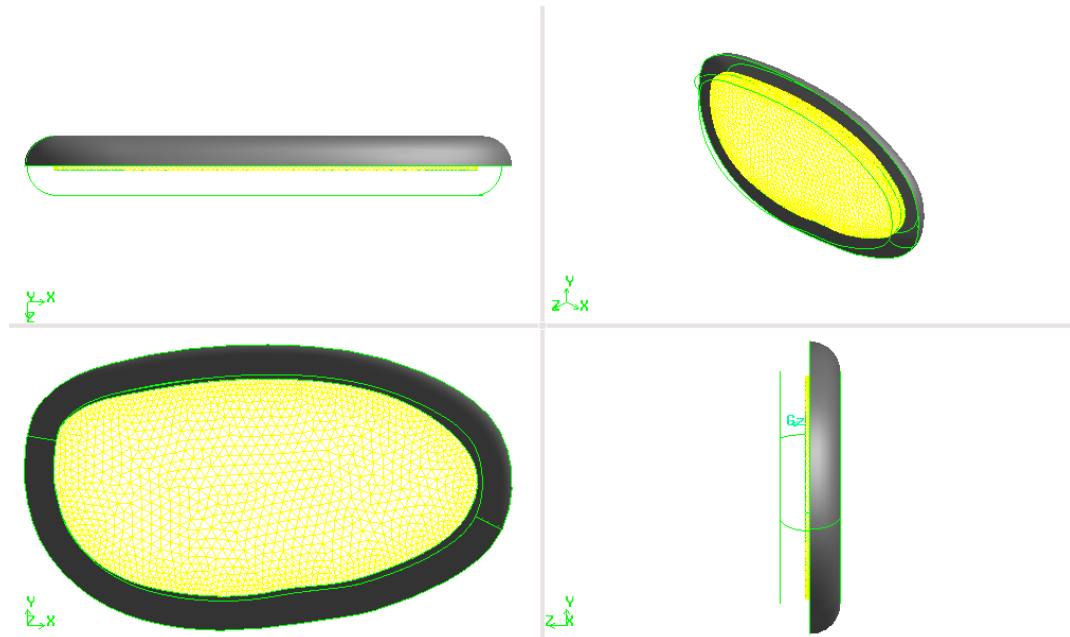


Figure 3.7 Four view schematic showing half exposed view of the meshless cloud volume surrounding the fruit fly wing, partial surface boundary of the meshless cloud volume is shown in grey in contrast to the wing volume in yellow (in the middle surrounded by the meshless cloud volume)

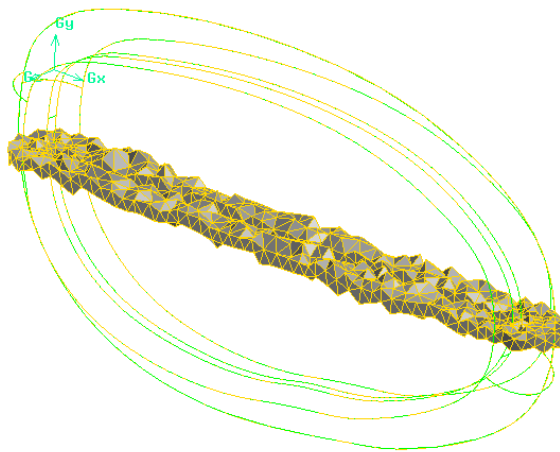


Figure 3.8 Exposed view of tetragonal finite volume elements within the meshless cloud volume surrounding fruit fly wing, the tetragonal elements are randomly distributed and size parameters are specified according to the desired mesh density

The success of the numerical method depends largely on the mesh quality of the surface nodal distribution on the rigid bodies and the surrounding meshless cloud. Many numerical treatment have been explored and implemented in dealing with this problem when a complex rigid body is introduced. The objective of much of the effort in numerical treatment is to allow more generalised and liberal ways for mesh generation

independent of the actual rigid body morphology and geometries. However, only limited success has been achieved in the study and the current state of simulation relies on a series of iterative mesh refinement process and corrective measures after each new rigid body geometries are introduced into the solver. Nonetheless, the described technique is applicable to all types of insect geometries and for flapping flight cases of various Reynolds numbers. This provides a common set of initial mesh setup for future studies of insect flapping flight problems and a stability analysis of the numerical method could also be further explored to improve efficiency of the current numerical scheme.

*Table 3-2 Summary of mesh generation on rigid bodies*

<b>WING LENGTH</b>	<i>1.0</i>
<b>MINIMUM SURFACE NODAL SEPARATION</b>	<i>0.01</i>
<b>SURFACE MESH GROWTH</b>	<i>1.2</i>
<b>MAXIMUM SURFACE NODAL SEPARATION</b>	<i>0.025</i>
<b>AVERAGE MESHLESS NODAL SEPARATION</b>	<i>0.02~0.03</i>
<b>MESHLESS CLOUD DEPTH</b>	<i>0.07~0.08</i>

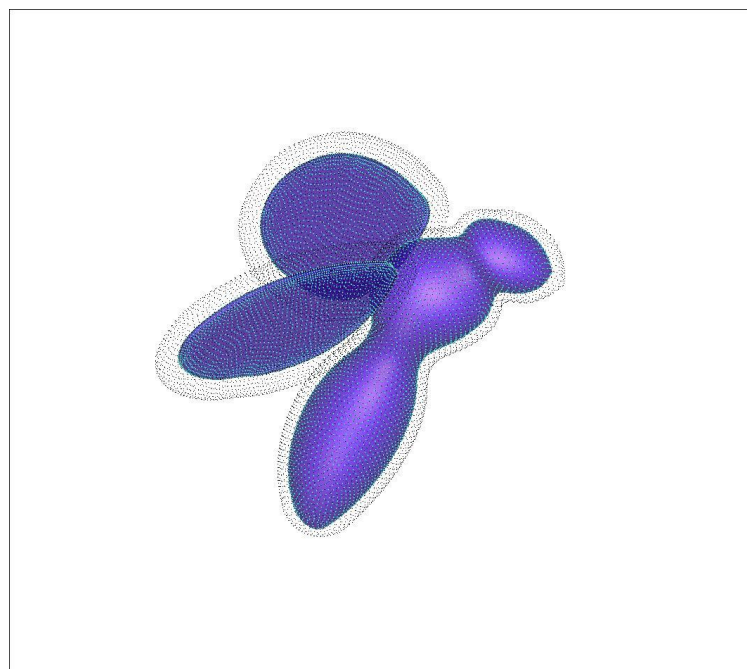


*Figure 3.9 The full computational model of fruit fly in its computational domain demonstrating the surface mesh free nodes (purple colour rigid body surface) and the meshless nodal cloud surrounding the rigid bodies*

### 3.3 Kinematics of Flapping Motion

Unlike conventional steady or quasi-steady state aerodynamic theories of flying for birds and airplane, it is observed that the aerodynamic flow in the vicinity of the insect body and wings never reach steady state during the insect's flapping flight (Ellington, 1984), be it hovering or manoeuvring. The flow structure is highly dependent on the transient behaviour of the insect's wing flapping kinematics. In order to study insect flight in a scientific and accurate manner, a flapping kinematic model needs to be established to numerically describe the motion of insect wings based on an appropriate set of parameters as well as empirically documented insect wing flapping wing patterns.

A systematic approach to fully describe insect flapping kinematics is presented in this study that would cover coordinate system definitions, flapping motion definitions, prescribed flapping kinematic models, and other implementations to resolving kinematic models.

#### 3.3.1 Coordinate System Definition

In the numerical study of insect flapping flight, a series of Euclidean spaces, each described by a three-dimensional coordinate system are defined. It was determined that four reference frame coordinate systems are required, namely, the basic insect wing definition frame, the wing motion frame, the insect body frame and the computational domain. Each are defined separately and are related through simple geometric transformations that can be determined based on the kinematic description of flapping motion and the coupled motion due to fluid solid interactions.

The most basic coordinate system defined in the numerical study is the insect wing definition ( $wd$ ) frame where the geometric models of the insect wings are individually defined in. The wing is constructed in this coordinate system following a standard procedures in which, the wing root is always defined at the origin of the coordinate system, and the  $X^{wd}$ ,  $Y^{wd}$  and  $Z^{wd}$  axes describes the half wing span, the chord and the thickness of the insect wing respectively. Since the wing is assumed as a rigid body, the positional vector of each individual mesh free nodes of the wing, including the surface nodes and the meshless cloud nodes, remain fixed in this coordinate system

throughout the computations. In addition, due to that the wing root section of the insect wing is neglected in the construction of the wing geometric model, the origin of the coordinate system  $O^{wd}$  appears to lie outside of the boundary of the wing as shown in.

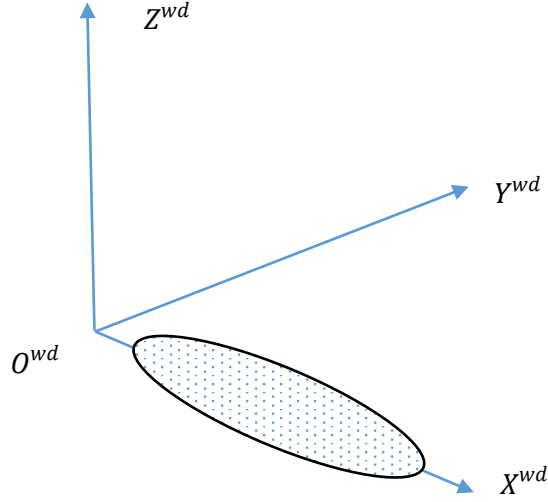


Figure 3.10 The wing definition frame, showing a pseudo wing geometry defined. It can be seen that the wing boundary does not touch the origin as the wing root section is neglected in the geometric model for the simulation

The wing defined the wing definition frame is made to flap in the wing motion frame (W) in accordance to the complex kinematic descriptions. This is done by firstly match the origin of the wing definition frame,  $O^{wd}$  with the origin of the wing motion frame,  $O^W$ , as the flapping motion of the wing is always assumed to be originating at the wing root. Then establish the initial position of the wing in the wing motion frame at  $t = 0$  through a transformation equation describing the orientation of the wing in the wing motion frame. The wing motion frame is defined separately for each individual wing of the insect, thus allowing the motion of the wings to be defined independently of each other and giving the scheme much flexibility in exploring different prescribed wing kinematics in insect flights. During the wing motion, the vector  $r^W$  of the wing nodes and the associated meshless cloud nodes can be described by equation [3.1].

$$\frac{dr^W}{dt} = \Omega(t) \wedge r^W \quad [3.1]$$

where  $\Omega(t)$  describes the detailed kinematics of the wing flapping motion at time  $t$  and can be determined in a simplified way using transformation matrix. The procedures of determining the transformation matrix is described in the next section.

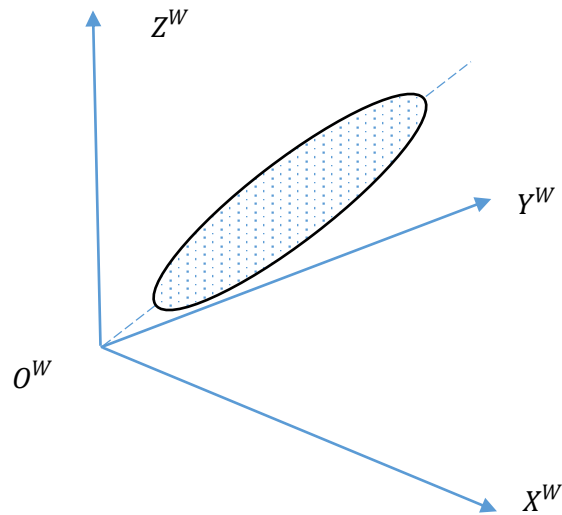


Figure 3.11 The insect wing in the wing motion frame where the wing can be made to rotate about the wing root

The insect body frame (B) is defined in which the coordinate system is fixed to the insect body as a whole and thus coupled with the changing orientation of the insect. The coordinate centre is always fixed at the centre of mass of the insect, which stays at a single coordinate point in the insect body throughout the motion, as the changing inertial effect due to the flapping wing motions is neglected in this study. The wing motion frame is defined in the insect body coordinate system such that the origin  $O^W$  of the wing motion frame is located at the physical position of the respective wing root on the insect thorax. The three orthogonal axes of the wing motion frame are initially defined to be parallel to the respective axis in the insect body coordinate system. However, it is noted that the wing motion frame can be allowed to rotate with respect to the insect body frame to simulate changing stroke planes by the insect for flight control purposes, similar to the rotor plane control system on helicopters. In simulation cases where FSI is evaluated, the insect body frame is also coupled with the FSI solver to solve for insect attitude changes in the physical domain during flapping flights due to fluid solid interactions.

The computational domain (G) describes the physical domain coordinate system in this numerical study. As described in the previous chapter, the computational domain is constructed by a standard Cartesian coordinate system and spatially discretised with a non-uniform Cartesian grid. The insect is only allowed to “fly” within the dense Cartesian grid region, usually the centre of the domain. The computational domain coordinate system is stationary throughout the computation.

### 3.3.2 Flapping Motion Definitions

The insect wing flapping motion is naturally controlled by a complex muscle structures in the thorax of the insect (Dickinson & Tu, 1997) in which both the power and control requirements of flapping flight can be achieved by the insect at any time during the flight. From a simplistic point of view, the insect wings attached to the insect body at the wing root have only three degrees of freedom in which, it can be described as limited rotation of the wings about three orthogonal axes—the azimuthal axis, the elevation axis and the rotational axis. Therefore, it is most intuitive to decouple the rotational angles about each of these axis used as the basic parameters defining the flapping kinematics of insect flight.

- 1) Stroke angle  $\phi$  about the azimuthal axis  $Z^W$  in the wing motion frame, parallel to  $Z^{wd}$  of the wing definition frame
- 2) Elevation angle  $\theta$  about the axis  $Y^{wd}$  of the wing definition frame
- 3) Twisting angle of wing  $\psi$  about axis  $X^{wd}$  of the wing definition frame

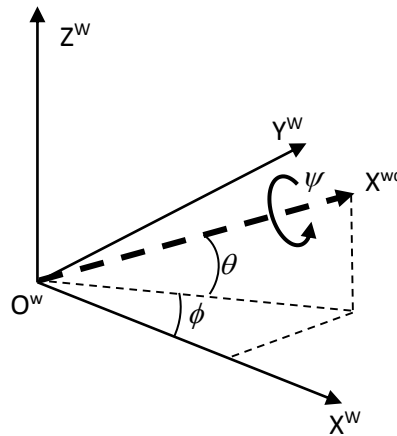


Figure 3.12 Orientation of rotation axes of insect wing in the wing motion frame

Where  $\phi(t)$ ,  $\theta(t)$ ,  $\psi(t)$  are functions of time defining the parameters of the wing orientation in the wing motion frame.

Due to the orthogonality constraint of the rotation axes, the angles of rotation are not truly decoupled and the computation of the rotation through transformation matrix do not commute. A specific sequence of computation of the rotational angles should be followed and presented in the right order as follows.



The unit basis vectors of the axes of rotation can thus be defined as:

- 1)  $\mathbf{i}_\phi = \mathbf{i}_z$
- 2)  $\mathbf{i}_\theta(t) = (-\sin\phi)\mathbf{i}_x + (\cos\phi)\mathbf{i}_y$
- 3)  $\mathbf{i}_\psi(t) = (\cos\phi\cos\theta)\mathbf{i}_x + (\sin\phi\cos\phi)\mathbf{i}_y + (\sin\theta)\mathbf{i}_z$  [3.2]

Where  $\mathbf{i}_x$ ,  $\mathbf{i}_y$ ,  $\mathbf{i}_z$  are unit vectors in the wing motion frame,  $\mathbf{i}_\theta(t)$  and  $\mathbf{i}_\psi(t)$  changes with time (superscript W denoting the wing motion frame is neglected here for simplicity).

The angular velocity vectors corresponding to each of the angles of rotation are:

- 1)  $\omega_\phi = \dot{\phi}(t)\mathbf{i}_\phi$
- 2)  $\omega_\theta = \dot{\theta}(t)\mathbf{i}_\theta$
- 3)  $\omega_\psi = \dot{\psi}(t)\mathbf{i}_\psi$  [3.3]

Then the total angular velocity vector about the wing's rotation within the wing motion frame can thus be described as:

$$\boldsymbol{\omega}(t) = \omega_\phi(t) + \omega_\theta(t) + \omega_\psi(t) \quad [3.4]$$

The rate of change of the angular velocity is given by:

$$\frac{d\mathbf{R}}{dt} = \boldsymbol{\omega} \wedge \mathbf{R} \quad [3.5]$$

We could then write the rate of change of angular velocity and angular velocity in the wing motion frame as:

$$\mathbf{r}(t) = r_1(t)\mathbf{i}_1 + r_2(t)\mathbf{i}_2 + r_3(t)\mathbf{i}_3 = r_j(t)\mathbf{i}_j \quad [3.6]$$

$$\boldsymbol{\omega}(t) = \omega_1(t)\mathbf{i}_1 + \omega_2(t)\mathbf{i}_2 + \omega_3(t)\mathbf{i}_3 = \omega_j(t)\mathbf{i}_j \quad [3.7]$$

Where  $\mathbf{i}_j(j = 1, 2, 3)$  are basis vectors in the wing motion frames.

Then we obtain that:

$$\begin{aligned}
1) \quad \omega_1(t) &= (\cos \phi \cos \theta)\dot{\psi} - (\sin \phi)\dot{\theta} \\
2) \quad \omega_2(t) &= (\sin \phi \cos \theta)\dot{\psi} + (\cos \phi)\dot{\theta} \\
3) \quad \omega_3(t) &= \dot{\phi} + (\sin \theta)\dot{\psi}
\end{aligned} \tag{3.8}$$

and

$$\frac{dr_i}{dt} = \omega_j r_k - \omega_k r_j \quad (i, j, k \text{ in cyclic order}) \tag{3.9}$$

The insect wing flapping motion can therefore be described as the rotation of the coordinate system of the wing definition frame inside the wing motion frame and the velocity vector of this rotation is simply given as:

$$\omega_\phi(t) + \omega_\theta(t) + \omega_\psi(t) = \omega_j(t)\mathbf{i}_j \tag{3.10}$$

So that the unit basis vector of the wing in wing motion frame can be obtained by transformation from the unit basis vector of the wing within the wing definition frame.

$$\mathbf{i}_i^{wd}(t) = l_{ij}(t)\mathbf{i}_j \tag{3.11}$$

The rotation of these unit basis vectors follows:

$$\frac{d}{dt}\mathbf{i}_i^{wd}(t) = \frac{dl_{ij}}{dt}\mathbf{i}_j = \boldsymbol{\omega}(t) \wedge (l_{ij}(t)\mathbf{i}_j) = (\omega_k(t)\mathbf{i}_k) \wedge (l_{ij}(t)\mathbf{i}_j) \tag{3.12}$$

So that for the basis vector:

$$\mathbf{i}_1^{wd}(t) = l_{1j}(t)\mathbf{i}_j \tag{3.13}$$

We have:

$$\frac{dl_{1j}}{dt}\mathbf{i}_j = (\omega_k(t)\mathbf{i}_k) \wedge (l_{1j}(t)\mathbf{i}_j) = (\omega_j l_{1k} - \omega_k l_{1j}) \tag{3.14}$$

Where  $i, j, k = 1, 2, 3$  and follows in cyclic order.

The full system can therefore be described generally:

$$\frac{d}{dt} \begin{pmatrix} l_{i1} \\ l_{i2} \\ l_{i3} \end{pmatrix} = \begin{pmatrix} \omega_2 l_{i3} - \omega_3 l_{i2} \\ \omega_3 l_{i1} - \omega_1 l_{i3} \\ \omega_1 l_{i2} - \omega_2 l_{i1} \end{pmatrix} \quad [3.15]$$

By integrating, we can obtain the  $l_{ij}(t)$  and from it we can determine changing unit basis vector  $\mathbf{i}_i^{wd}(t) = l_{ij}(t)\mathbf{i}_j$  in the wing motion frame. It is also worth pointing out that, only 2 out of 3 of the unit basis vectors are required for integration as the third can be found by  $\mathbf{i}_3^W(t) = \mathbf{i}_1^W(t) \wedge \mathbf{i}_2^W(t)$  at any time. Or alternatively, we can also write that:

$$l_{3i}(t) = l_{1j}(t)l_{2k}(t) - l_{1k}(t)l_{2j}(t) \quad [3.16]$$

Then the transformation matrix governing the rotation of insect wings are given by equation [3.17].

$$\mathbf{L}(t) = [l_{1j}(t)] \quad [3.17]$$

When the transformation matrix  $\mathbf{L}(t)$  is multiplied to the position vectors of all the nodal points on and around the wing of the insect in the wing definition frame, one can then obtain their corresponding vectors in the wing motion frame. The process can be described in the following equation:

$$\mathbf{r}(t) = (r_1, r_2, r_3)^T = \mathbf{L}(t)\mathbf{r}^{wd} = \mathbf{L}^T(t)(r_1^{wd}, r_2^{wd}, r_3^{wd}) \quad [3.18]$$

Note that the position vectors  $r_1^{wd}, r_2^{wd}, r_3^{wd}$  are fixed throughout the computation as described earlier, the nodal points and the surrounding meshless nodes of the wing are fixed inside the wing definition frame.

Computationally, elements  $l_{ij}$  of the transformation matrix  $\mathbf{L}^T(t)$  maybe obtained by fractional time integration according to equation [3.15].

In which the angular velocity terms  $\omega_j(t)$  ( $j = 1, 2, 3$ ) can be determined form the prescribed kinematic model of the flapping motion. More details of the prescribed kinematic model will be explained in the next section.

Similarly, the convection velocity vector of the nodal points and its surrounding meshless nodes of the wings can be determined according to equation:

$$\mathbf{v}(t) = v_j(t)\mathbf{i}_j = \frac{d}{dt} \mathbf{r}(t) = \frac{dr_j}{dt} \mathbf{i}_j = \frac{dl_{ij}}{dt} r_i^{wd} \mathbf{i}_j = (\omega_j l_{1k} - \omega_k l_{1j}) r_i^{wd} \mathbf{i}_j \quad [3.19]$$

Within the framework of the wing motion frame, by obtaining the transformation matrix, one can easily and reliably obtain the exact position of the wings and their respective velocities in the current coordinate system. This approach is further expanded sequentially to the next two higher levels of coordinate systems and the actual position and velocity of the insect wings can be obtained in the computational domain. The CFD solver then solves the flow field in the computational coordinate system and the dynamics response from FSI is then cascaded back down the hierarchy of the coordinate system to provide updated information of the transformation matrix corresponding to the orientation of the insect body and the attached wing motion frame. The new information will then be used to update position and velocity of wings and this iterative approach continues until a convergence criteria is met before moving onto the next time step.

This kinematic motion definition method allows flexibility in the description of various different flapping motions of vastly different species of different insects and for different intended motion types. It also provides the foundation for more complex insect kinematic models and FSI dynamic computations such as exploring insect flight control mechanism through wing stroke plane (the XY plane of the wing motion frame) rotations without altering the prescribed flapping kinematics within the wing motion frame, effect of insect body shape changes (change of centre of mass and relative position of wing root) observed on real insect during take-off and pendulum effect of insect body rotations on insect hovering characteristics and so on. These mentioned possible studies are beyond the scope of current thesis and are not presented.

### **3.3.3 Prescribed Flapping Kinematic Models**

The kinematic flapping model is a description of insect wing's translational and rotational motion with respect to time in a complete wing beat cycle (H. Wang, 2003), which repeats itself in the subsequent cycle. In a 3D rigid wing case, the kinematic model is simply the functions of stroke angle, elevation angle and rotation angle with respect to time  $\phi(t)$ ,  $\theta(t)$ ,  $\psi(t)$ . It provides the position and angular velocity of the insect wings at any instance of a wing beat cycle.

The kinematic model is critical in affecting the aerodynamic force production during insect flapping flights (Sane & Dickinson, 2001). An accurate kinematic model

is essential in the study of insect flapping flight and provides insight into the unsteady aerodynamic behaviour that is most interesting to understand. However, the attempt to define such kinematic model for flapping flight has proven to face several challenges. For the past many years, with the advent of technology, researchers have attempted to capture free-flight kinematics of real manoeuvring insect (Ennos, 1989). Such efforts reveals great details of natural insect flight kinematics and provides insight into what insects are capable of in steering during flight. However, such kinematic information tend to be generally transient and subtle, leading to errors in measurement and lacked repeatability (S. N. Fry, Sayaman, & Dickinson, 2003). Furthermore, free-flight insect kinematics is often associated with instantaneous aerodynamic force generations that are not yet fully understood and the relationships are unknown. Alternatively, tethered experiments (Dickinson et al., 1999) and numerical studies have focused on variations of simple kinematic models which do not necessarily describe actual insect flapping kinematics during hovering or free-flight. Furthermore, inconsistency in kinematic model specifications could lead to difficulty in aerodynamic data interpretation and comparisons.

In this study, several kinematic models are proposed, including a traditional simple harmonic motion model, a trapezoidal kinematic model and a natural cubic spline fit model, which offer good accuracy, flexibility and repeatability of insect wing flapping motion for studies.

### **3.3.4 Simple Harmonic Flapping Kinematics**

Simple harmonic flapping kinematic model is one of the simplest kinematic models applied in insect flight studies by many researchers (Ellington, 1999). It describes the rotational angles of the insect wings following a simple sinusoidal wave like time dependent function within a single wing beat cycle. The relative phase difference in each rotational angles are assumed to be zero. So mathematically, it can be described as:

$$1) \phi(t) = \phi_0 \cos(2\pi t)$$

$$2) \theta(t) = \theta_0 \cos(2n\pi t)$$

$$3) \psi(t) = \psi_0 \sin(2\pi t) \quad [3.20]$$

Where  $0 < t < 1$  is the time fraction of a wing beat cycle,  $\phi_0, \theta_0, \psi_0$  are the maximum amplitude of the flapping motion of the wing in the respective axis of rotations.  $n$  is an integer parameter describing the number of sine cycles the elevation angle rotation within a wing beat cycle. This value changes depending on insect species and is considered as 1 or 0 in a SHM flapping kinematic model where elevation angle deviations are simplified or neglected. It is also possible for  $n$  to have value of more than 1, such as typical “figure of eight” and “oval” shape wing motion trajectory observed in experiments.

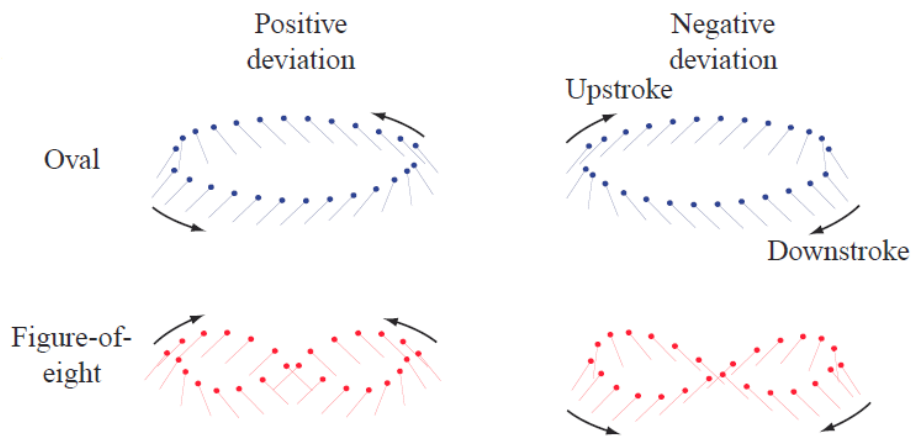


Figure 3.13 Illustration of “figure of eight” and “oval” shape wing motion trajectory by (Sane & Dickinson, 2002)

A wing beat cycle is defined from the start of downstroke ( $t = 0$ ) to the end of upstroke ( $t = 1$ ). The elevation angle  $\theta$  magnitude reaches maximum at the beginning of downstroke and upstroke, and the twisting angle  $\psi$  magnitude reaches 0 at that same time and reaches maximum in the middle of downstroke and upstroke when the stroke velocity is the highest. The twisting angle  $\psi$  is related to the more commonly used idea of insect wing’s angle of attack  $\alpha$  in the form  $\alpha = 90 - |\psi|$ . Therefore, in a SHM kinematic model, the wing reaches maximum angle of attack at  $90^\circ$  (vertical) when the wing is at the end of downstroke and upstroke. A typical SHM based flapping kinematics is shown in Figure 3.14.

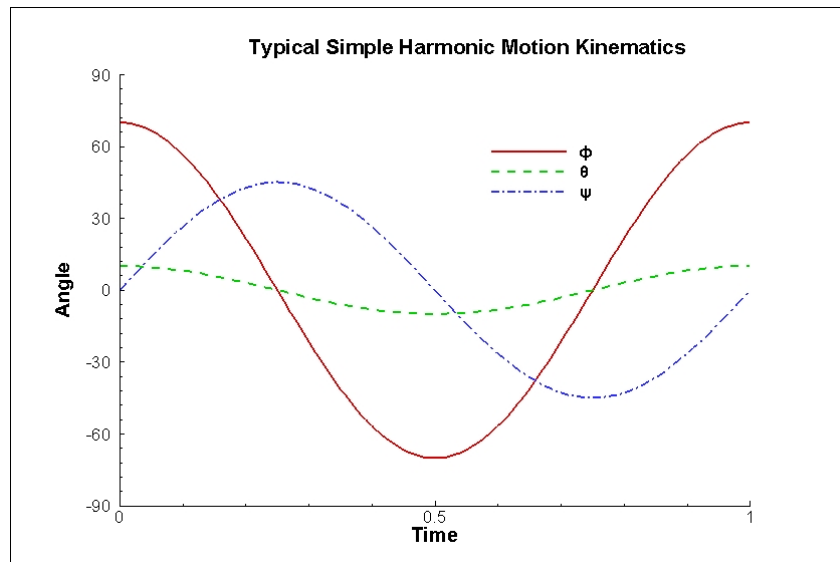


Figure 3.14 A typical SHM flapping kinematic model. In this case, there is no time delay to the flapping motion in any of the rotations and results in a synchronous flapping motion

SHM flapping kinematics is a simple kinematic model and desirable for simple derivation of aerodynamic force generation in association to flapping kinematics (Weis-Fogh, 1973). SHM also prevents unnatural flapping behaviours of insects with smooth gradient throughout the flapping cycle which induces no sudden impulses in flapping force. It also shows that SHM flapping kinematic model provides among the best average lift coefficients within multiple kinematic models tested in the study. More details of the study will be elaborated in the Chapter 4.

SHM kinematic model is most suitable for quasi-steady study of insect flapping flight. It has been applied for numerical studies investigating both aerodynamic effects of flapping flight and the coupled fluid solid interactions with the insect. Results have shown that through simple control model implementation, an insect flapping in SHM kinematic model could achieve hovering (Wu, Yeo, Lim, & Zhang, 2013).

### 3.3.5 Trapezoidal Function Kinematic Model

For some insects such as fruit fly, it was observed that during hovering, the translational velocity of the insect wings resemble a trapezoidal function (Zanker & Gotz, 1990). The translational velocity is constant throughout majority of a half-stroke, such as the angular time plot in Figure 3.15, followed by rapid acceleration at stroke reversal. This type of kinematic model results in exaggerated acceleration at the beginning of the stroke and deceleration at the end of the stroke, expanding the maximum translation velocity of the wing sweep to maximise lift generation through

majority of the flapping cycle. Combined with a similarly described wing rotation (twisting) kinematic function, the flapping motion generates desirable unsteady aerodynamic forces on the wing and have inspired much interest among researchers to study such aerodynamic behaviours (Birch & Dickinson, 2003).

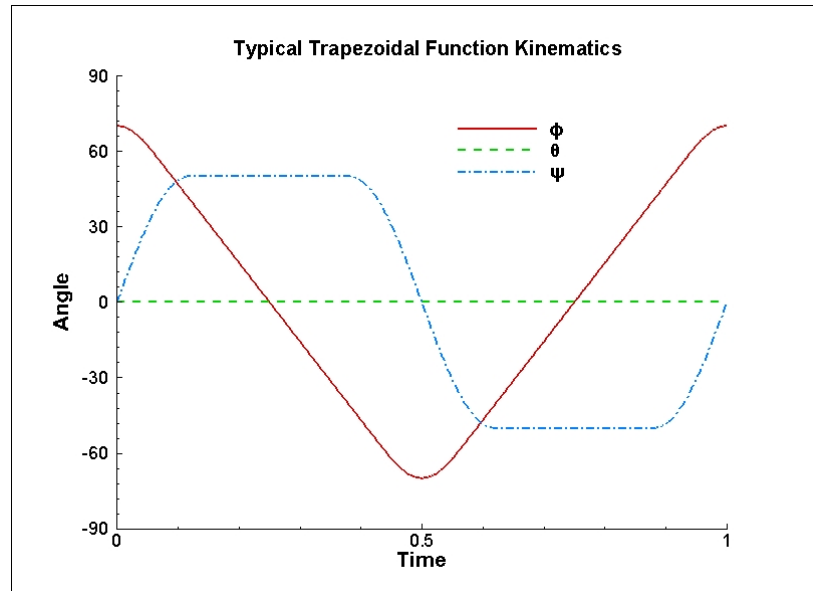


Figure 3.15 A typical trapezoidal function kinematic model, there is no time delay to the flapping motion in any of the rotations, the elevation rotation is put to 0 throughout the wing beat cycle

A similar trapezoidal function kinematic model is developed independently in this study with introduction of additional specific control parameters using a piecewise continuous polynomial function.

If one consider the amplitude of stroke angle, elevation angle and rotation angle in each wing beat cycle as a constant, then the time dependent function  $\phi(t), \theta(t), \psi(t)$  can be written as  $\phi_0 f_\phi(t), \theta_0 f_\theta(t), \psi_0 f_\psi(t)$  where functions  $f_\phi(t), f_\theta(t), f_\psi(t)$  describe the kinematic model in a given range. In a typical trapezoidal function kinematic model, the elevation angle variation is usually considered negligible or taken as a simple sinusoidal function, so  $f_\theta(t)=0$  or  $f_\theta(t) = \cos(n2\pi t)$  as in the SHM case.

Rapid acceleration and deceleration of insect wing at beginning and end of each stroke followed by constant wing stroke angular velocity characterise a typical trapezoidal function kinematic model. Parameter  $t_0$  is defined as the time fraction at which the wing sweep stops acceleration and transits to constant angular velocity. Figure 3.16 shows the value of  $t_0$  and  $\Delta\tau_t$  in the plot.



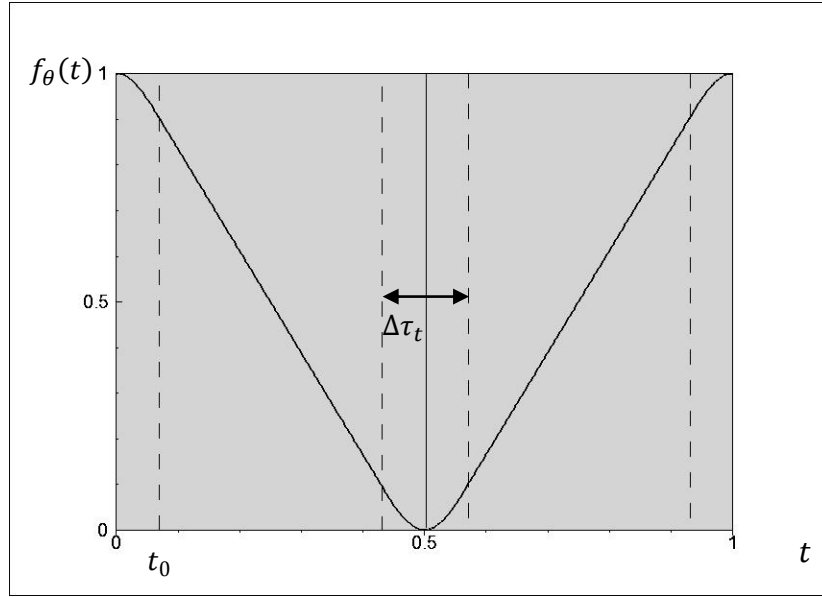


Figure 3.16 Trapezoidal function kinematics of wing stroke during which acceleration and deceleration of the wing translational motion takes place within the segments marked by the dashed lines

Since the transition from acceleration to constant velocity must be smooth, the first derivative of the angular time plot at  $t_0$  must equal to the gradient of straight line section at  $t_0$  as well. Therefore, we obtain the following relationship:

$$t_0 = \frac{1}{4} \left( 1 - \sqrt{1 - 8C_T^{-1}} \right) \quad (C_T \geq 8) \quad [3.21]$$

$$\text{or } C_T = \frac{8}{1 - (1 - 4t_0)^2} \text{ and } t_0 = \frac{1}{2} \Delta\tau_t$$

Where  $C_T$  is 1<sup>st</sup> derivative of the angular time plot at  $t_0$ , and  $\Delta\tau_t$  is the physical phase duration of acceleration and deceleration in wing sweep within 1 wing beat cycle. Therefore, the trapezoidal function kinematic model can be fully defined by the following piecewise continuous polynomial equations.

Table 3-3 Piecewise continuous polynomial function describing translational motion of flapping wing

Angular function	Angular velocity	$t$ range
$f_\phi = 1 - C_T t^2$	$\dot{f}_\phi = -2C_T t$	$0 \leq t \leq t_0$
$f_\phi = (1 + C_T t_0^2) - mt$	$\dot{f}_\phi = -m$	$t_0 \leq t \leq (0.5 - t_0)$
$f_\phi = C_T (t - 0.5)^2$	$\dot{f}_\phi = 2C_T (t - 0.5)$	$(0.5 - t_0) \leq t \leq (0.5 + t_0)$
$f_\phi = [1 - m(1 - t_0) - C_T t_0^2] + mt$	$\dot{f}_\phi = m$	$(0.5 + t_0) \leq t \leq (1.0 - t_0)$
$f_\phi = 1 - C_T (t - 1)^2$	$\dot{f}_\phi = -2C_T (t - 1)$	$(1.0 - t_0) \leq t \leq 1.0$

Where  $m = 2C_T t_0$ .

The corresponding wing rotation function can be described such that, rotation takes place rapidly during the stroke reversal (at the beginning or end of each stroke) until the desired wing attack angle is reached and held constant during the ensuing translational motion of the stroke. This kinematic model can also be described using a piecewise continuous sinusoidal function presented in the later sections.

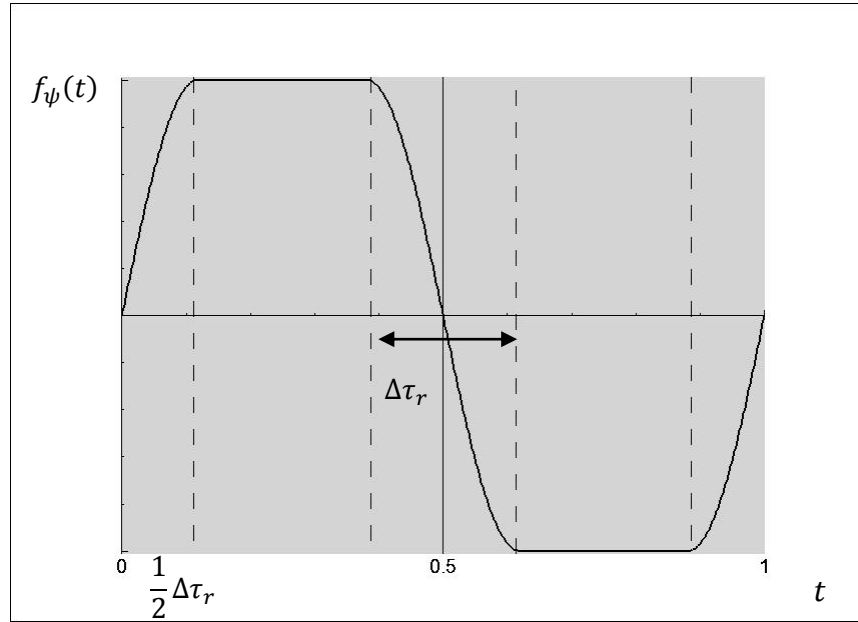


Figure 3.17 Kinematic model of the wing twisting showing rapid rotation of wing during stroke reversals and constant angle of attack during majority of wing translation

Table 3-4 Piecewise continuous sinusoidal polynomial function describing the rotational motion of the flapping wing

Angular function	Angular velocity	t range
$f_\psi = \sin\left(\frac{t}{\Delta\tau_r} \pi\right)$	$\dot{f}_\psi = \frac{\pi}{\Delta\tau_r} \cos\left(\frac{t}{\Delta\tau_r} \pi\right)$	$0 \leq t \leq \frac{1}{2} \Delta\tau_r$
$f_\psi = 1.0$	$\dot{f}_\psi = 0$	$\frac{1}{2} \Delta\tau_r \leq t \leq \left(0.5 - \frac{1}{2} \Delta\tau_r\right)$
$f_\psi = -\sin\left(\frac{(t-0.5)}{\Delta\tau_r} \pi\right)$	$\dot{f}_\psi = -\frac{\pi}{\Delta\tau_r} \cos\left(\frac{(t-0.5)}{\Delta\tau_r} \pi\right)$	$\left(0.5 - \frac{1}{2} \Delta\tau_r\right) \leq t \leq \left(0.5 + \frac{1}{2} \Delta\tau_r\right)$
$f_\psi = -1.0$	$\dot{f}_\psi = 0$	$\left(0.5 + \frac{1}{2} \Delta\tau_r\right) \leq t \leq \left(1.0 - \frac{1}{2} \Delta\tau_r\right)$
$f_\psi = \sin\left(\frac{(t-1)}{\Delta\tau_r} \pi\right)$	$\dot{f}_\psi = \frac{\pi}{\Delta\tau_r} \cos\left(\frac{(t-1)}{\Delta\tau_r} \pi\right)$	$\left(1.0 - \frac{1}{2} \Delta\tau_r\right) \leq t \leq 1.0$

In the wing twisting kinematic function, parameter  $\Delta\tau_r$  describes the phase

duration of the wing twisting before reaching constant angle of attack within 1 wing beat cycle.  $\Delta\tau_r$  may not necessarily be related to  $t_0$  in the sweep function as it is reasonable to assume that the wing twisting is independently controlled.

It is intuitive to argue that the trapezoidal function kinematics could lead to substantially more aerodynamic force productions during the beginning and end stages of wing strokes as compared to sinusoidal function kinematic models due to unsteady aerodynamics associated with the rapid wing accelerations and rotations. The analysis of this unsteady effect is shown in Chapter 4.

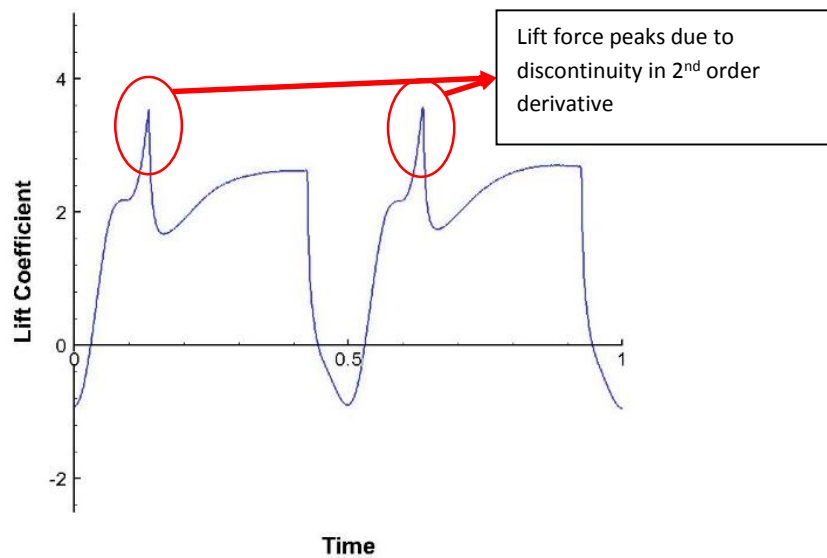


Figure 3.18 The transient lift coefficient within a wing beat cycle showing the aerodynamic force peaks produced due to discontinuity in the derived polynomial equation based trapezoidal function kinematic model

Although the aforementioned simplified trapezoidal function kinematic model was accurate and easy to define, its piecewise continuous polynomial functions are at maximum 2<sup>nd</sup> order in nature. It was discovered that, such polynomial equations ensure smooth continuity of angular  $f_\phi$  and angular velocity  $\dot{f}_\phi$  functions, but does not ensure smooth continuity of angular acceleration  $\ddot{f}_\phi$  function. Distinct aerodynamic force peaks are produced during numerical simulations that corresponds to points of discontinuity in the kinematic model which lead to impulsive actions of the wing. Such effects are more prominent when  $t_0$  values are small, and are considered unnatural. Figure 3.18 shows an example of force peaks associated with wing flapping motion at 2<sup>nd</sup> order discontinuity points in the trapezoidal function kinematic model definitions. An improvement can be achieved through definition of trapezoidal function using higher order polynomial equations or by following the next kinematic model approach described in the following section.

### 3.3.6 Natural Cubic Spline Fit Function Kinematic Model

A more flexible kinematic model is proposed in this study that adopts the idea of using a natural cubic spline curve to best fit a known kinematic model such as SHM and trapezoidal, or a naturally observed flapping behaviour of actual insects with a simple angle time plot. This method offers accuracy and repeatability while providing the capability of resolving any graphical kinematic models without a known mathematical description.

A natural cubic spline is a set of finite number of piecewise continuous cubic polynomial functions obtained from corresponding number of control points along a route without a known trajectory. It provides a smooth fit of the data point set, and is smooth up to 2<sup>nd</sup> order derivative. Each segment of the cubic spline is defined by a cubic polynomial function as below:

$$s_i(x) = a_i + b_i x + c_i x^2 + d_i x^3 \text{ where } x_{i-1} \leq x \leq x_i, i = 1, \dots, n \quad [3.22]$$

Where we have  $(n + 1)$  constraints from the condition

$$s(x_i) = y_i \text{ for } i = 0, 1, \dots, n$$

and  $(n - 1)$  constraints from the following conditions

$$s_i(x_i) = s_{i+1}(x_i)$$

$$s'_i(x_i) = s'_{i+1}(x_i)$$

$$s''_i(x_i) = s''_{i+1}(x_i) \text{ for } i = 1, \dots, n - 1$$

This set of cubic polynomial equations can be solved in a linear system and the coefficients  $a_i, b_i, c_i, d_i$  can be determined. A unique set of solution can be obtained if two additional conditions are added:

$$s''_1(x_0) = 0 \text{ and } s''_n(x_n) = 0$$

This condition can be easily satisfied physically in a natural or pre-defined kinematic model such that within each stroke, the insect wing always reaches a point where net translational and rotational forces acting on the wing reaches zero (independently) before reversing the direction leading to the next wing stroke. The natural cubic spline also has the advantage of generally displaying no oscillatory

behaviour as compared to higher order spline fit methods. Further reduction of oscillatory behaviour in sharp turning curves of natural kinematics plots could be achieved by careful selection of piecewise data segments.

The natural cubic spline fit kinematic model is mathematically derived according to supplied control points describing the full kinematics of a single wing beat cycle. The control point density is determined according to shape and complexity of the actual kinematic model and the accuracy requirement of the simulation. In addition, one should observe that the minimum gap between any two control points should be substantially larger than the computational time step to prevent data discontinuity. The kinematic function is translated directly into the wing motion using the determined set of piecewise continuous cubic polynomial functions that gives the values of  $f_\phi$ ,  $f_\theta$ ,  $f_\psi$  and their respective first derivatives at each time step.

By adopting the natural cubic spline fit kinematic model, the study is able to achieve a generalised kinematic function description for simulation of flapping wings covering all types of different kinematic models such as SHM kinematic model, trapezoidal function kinematic model and naturally obtained kinematic model without necessarily knowing the mathematical functions with high degree of accuracy and extreme flexibility.

Natural cubic spline fit ensures 2<sup>nd</sup> order continuity in the kinematic function and prevents the impulsive behaviour of the flapping wing that could lead to substantial numerical instability issues.

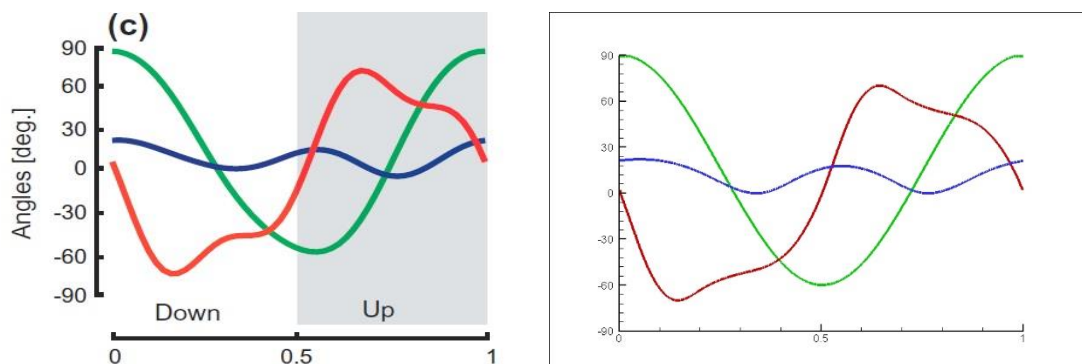


Figure 3.19 An example of natural fruit fly flapping kinematic model (Left) mapped through point segmentation and fitted by natural cubic spline for simulations (Right), courtesy Aono and Liu (Aono & Liu, 2012)

### 3.3.7 Other Implementations for Resolving Insect Flapping Kinematics

A “slow start” function is implemented in the numerical method of resolving the flapping kinematics of insect wing motions. It gradually increases the sweep, elevation, and rotation angle amplitudes from zero to full prescribed motion amplitudes at the start of the simulation to prevent an impulsive start of flapping wings in an originally steady computational flow field condition that could lead to instability and convergence issues in the numerical solution. The function can be described by equation [3.23].

$$\begin{aligned} 1) \quad \phi(t) &= \phi_0 \sin\left(\frac{\pi t}{2 t^*}\right) \\ 2) \quad \theta(t) &= \theta_0 \sin\left(\frac{\pi t}{2 t^*}\right) \\ 3) \quad \psi(t) &= \psi_0 \sin\left(\frac{\pi t}{2 t^*}\right), \quad \text{for } 0 \leq t \leq t^* \end{aligned} \quad [3.23]$$

Where,  $t^*$  is the time limit at which “slow start” function ends and is usually less than 1. Such implementation is acceptable in this study because there is no attempt in studying take-off performance of insects and instead will focus primarily on unsteady aerodynamic effects of insect flights during hovering and limited manoeuvring. The reduced initial disturbance to the flow leads to better convergence of numerical solution and have no effects on aerodynamic forces generated for wing beat cycles of 5 and beyond.

Further implementations in the kinematic model description of insect flapping flights are focused on parameterisation of the flapping motion beyond the simple time dependent functions of sweep, elevation and rotation angles. This can be achieved by introducing parameters that further characterise or modify simple kinematic models according to temporal and displacement functions attached to the existing time dependent functions of the respective rotational angles. Such functions could include relative phase time of the twisting angle function with respect to the sweep angle function, magnitude adjustments in amplitude of the rotational angles and so on. This would lead eventually to a systematic control model of insect flapping flights based on the fundamental idea of kinematic model adjustments of insect flapping wing motions. More details of this process and its approach will be discussed in later Chapter.

### 3.4 Non-dimensionalisation

The non-dimensionalisation of the the current numerical simulation follows the simple idea of specifying one single wing beat cycle as unit time and the wing length of the insect as unit length. Hence, the following dynamic quantities are non-dimensionalised accordingly.

$$\text{Non – Dimensionalised Mass: } m^n = \frac{m}{\rho_{air}R^3} \quad [3.24]$$

$$\text{Reference Velocity: } U_{ref} = 2\phi_0f\hat{r}_2R \quad [3.25]$$

$$\text{Non – Dimensionalised Reference Velocity: } U_{ref}^n = \frac{U_{ref}}{Rf} \quad [3.26]$$

$$\text{Non – Dimensionalised Time: } t^n = \frac{t}{f} \quad [3.27]$$

$$\text{Non – Dimensionalised Force: } F^n = \frac{F}{\rho_{air}f^2R^4} \quad [3.28]$$

$$\text{Non – Dimensionalised Gravitational Acceleration: } g^n = \frac{g}{f^2R} \quad [3.29]$$

Where,  $r_2$  is the 2<sup>nd</sup> moment of area of the insect wing and the velocity at the point  $r_2$  distance away from the wing root is taken as the reference velocity. However, it is to be noted that for some studies, wing tip velocity is used to compute the reference velocity (Aono et al., 2008).  $t^n = 1.0$  is the non-dimensionalised wing beat cycle time and  $R^n = 1.0$ , is the non-dimensionalised wing length in the simulation.

### 3.5 Definition of Reynolds Number, Lift Coefficient and Drag Coefficient

Reynolds number describes the ratio of inertia force to viscous force in aerodynamic analysis. In the study of unsteady aerodynamic effects of insect flapping wing, the definition of Reynolds number varies slightly among different researchers.

In this study, the Reynolds number is defined in equation [3.30]

$$Re = \frac{\bar{c}\overline{U_{tip}}}{\nu} \quad [3.30]$$

Where  $\bar{c}$  is the average chord length of the wing,  $\nu$  is kinematic viscosity and  $\overline{U_{tip}}$  the mean wing tip translation velocity is defined as  $\overline{U_{tip}} = \bar{\omega}R$ . Angular velocity is defined as  $\bar{\omega} = 2f\phi_0$ , where  $f$  is the flapping frequency,  $\phi_0$  is the amplitude of wing's translational motion.

The non-dimensionalised Reynolds number is defined similarly and matched to the actual insect's Reynolds number for the computational simulation.

The insect, fruit fly, chosen in this study have a Reynolds number around 120 to 150 in its typical hovering and forward flight. However, current numerical scheme is capable of simulating flapping flights of much higher Reynolds numbers not presented in the context of this thesis.

The lift coefficient and drag coefficients are defined as follows:

$$C_l = \frac{L}{\frac{1}{2}\rho U_{ref}^2 S} \quad [3.31]$$

$$C_d = \frac{D}{\frac{1}{2}\rho U_{ref}^2 S} \quad [3.32]$$

Where  $U_{ref} = \bar{\omega}\hat{r}_2R$ , in which  $\hat{r}_2$  is the dimensionless second moment of inertia, and is obtained from discretization of insect wing planform and perform subsequent summation of the integral 2<sup>nd</sup> moment of the wing surface. The wing planform is given as  $S = \bar{c}R$ , where  $\bar{c}$  is the mean chord of the wing.

### 3.6 Summary

In this chapter, a systematic approach to study insect flapping flight is explained. This included the morphologically accurate geometric modelling technique, the meshless nodal point generation scheme of the insect body and wing models and the definition of the prescribed kinematic models of the flapping wings.



The present geometric modelling technique has shown to allow the construction of complex geometrical shaped insect body and wings with high degrees of morphological accuracy and relative ease. The insect wing models are assumed rigid and very thin with sharp edges. The discretization technique shows that the meshless nodal generation technique is effective and efficient which is instrumental in the implementation of the present numerical simulations.

The detailed definition of the flapping kinematics established a basic framework for future studies of flapping wing problems. The simple mathematical descriptions of the most basic kinematic models of SHM and TF are derived. A natural spline interpolation based kinematic modelling technique is introduced. It is shown to provide accuracy, flexibility and robustness in the description of various flapping motions. These included simple flapping kinematic models such as SHM and TF and naturally observed insect flapping kinematics without actual knowledge of the mathematical functions.

The outlined current approach in defining insect flapping flight problems within the numerical framework provides the fundamental basis of modelling in current and future numerical studies of the unsteady aerodynamics associated with flapping wings.

## **CHAPTER 4: Analysis of Kinematic Effects on Unsteady Aerodynamics of Prescribed Flapping Flight**

### **4.1 Introduction**

The accuracy of the aforementioned numerical model with the methodology of geometric modelling and kinematic modelling are first verified by setting up a simple flapping wing simulation in reference to an existing experimental setup. The computational results are then demonstrated to be in good agreement with experimental results and establish the basis for further numerical analysis of unsteady aerodynamic effects of flapping wings.

A comprehensive study of a series of flapping flights of the same geometric wings at the same Reynolds number with different prescribed kinematic models are then carried out. The purpose of this study is to systematically differentiate the effect of aerodynamic lift and drag productions due to changes of kinematic models from Simple Harmonic Motion (SHM) to Trapezoidal Function (TF) based flapping motions and assess the power requirements for sustaining flight in each kinematic models. This approach could hopefully shed light on the reasons for observations by experimentalists that smaller insects such as fruit fly tends to deploy a TF kinematic model in flapping instead of the more conventional SHM based kinematics (Dickinson et al., 1999; Zanker & Gotz, 1990).

### **4.2 Verification of a Flapping Wing Pair Simulation**

An experimental setup is available in the Fluid Mechanics Labs of National University of Singapore (Lua et al., 2010) for testing of insect flapping flight at various Reynolds numbers from  $10^2$  to  $10^5$ . The experimental setup is capable of testing several different types of insect wings performing different flapping kinematic models with varying degree of rigidity of the wings, and much of the results have already been published in previous literature (Lua et al., 2010). Therefore, a comparative numerical study is setup in accordance to the specific experimental setup to establish the accuracy

of the numerical method and the accompanying geometric and kinematic models. And by further comparison of the obtained numerical results of the flow structure with already known unsteady aerodynamic effects, the confidence of the numerical simulation results could be further enhanced.

#### 4.2.1 Mechanical Setup

A CAD drawing of the 3D flapping wing mechanism used can be seen in Figure 4.1. The figure shows a pair of hawk moth wing models attached to the actuating gear box and driven by three stepper motors to achieve full rotational capabilities of an actual insect flapping motion. The right wing is mounted with force transducers to monitor and record forces generated during flapping motion. The figure also shows the axes of translation, elevation and twisting of the wings, which corresponds to the three axes of rotations defined in wing motion frame explained in the previous chapter (Chapter 3).

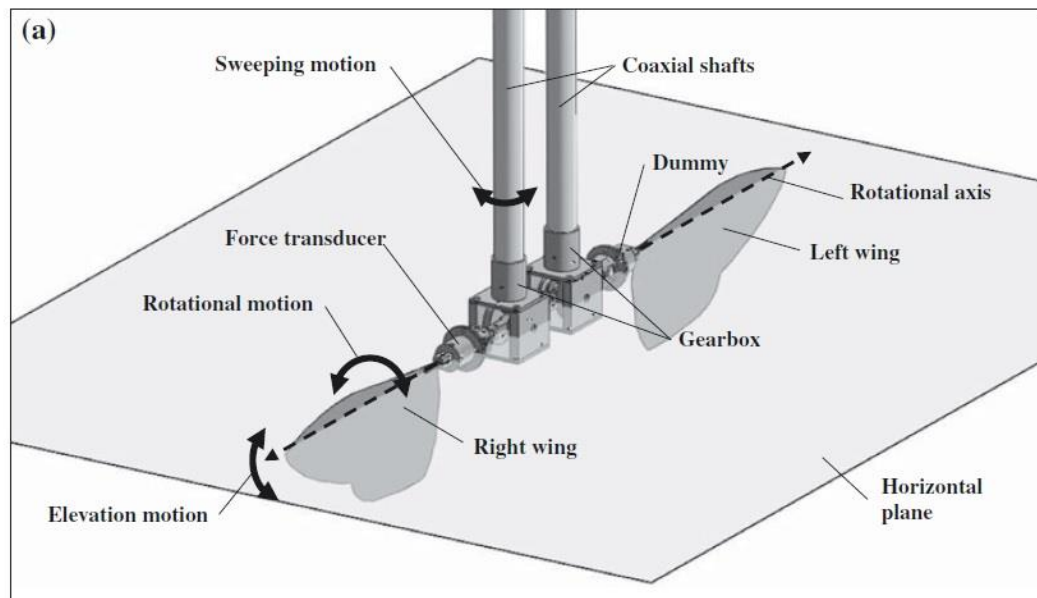


Figure 4.1 3D CAD drawing of physical experiment setup, courtesy of Lua (Lua et al., 2010)

The physical experiments are conducted in water or oil depending on the Reynolds number, and the wing model are measured 0.25m long. It is also worth pointing out that, due to the limitation of the drive shaft and gearbox mechanism, the wing is rotating about a centre of rotation somewhere within the gearbox, which is further away from the physical wing root described in geometric modelling in previous chapter (Chapter

3). This distance to centre of rotation is strictly followed in the numerical validation simulation. However, in subsequent studies, the centre of rotation is always defined at the physical wing root of the modelled insect wing.

The experiment is carried out on a set of fruit fly wing profile modelled after Dickinson (Dickinson et al., 1999) and shown in Figure 4.2(A). It is noted that, there is slight difference in planform of the above experimental fruit fly wing and the wing of an actual *drosophila melanogaster* as presented in the previous chapter. The experimental planform of Figure 4.2 and Figure 4.3 is used only in the present validation study, whereas the actual fruit fly wings derived from geometric studies in Chapter 3 are used in all other studies described in this thesis.

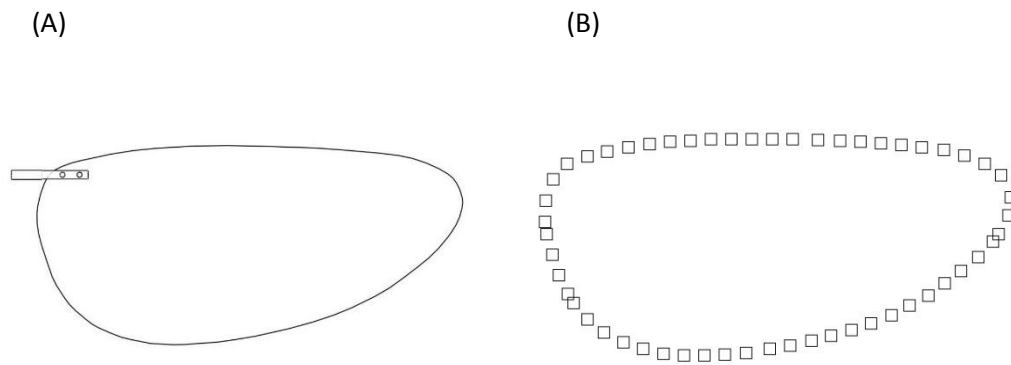


Figure 4.2 Fruit fly wing model used in the experimental investigation (A), and data points obtained from line tracing and smoothening for spline fit reconstruction of the wing morphology for numerical simulation (B)

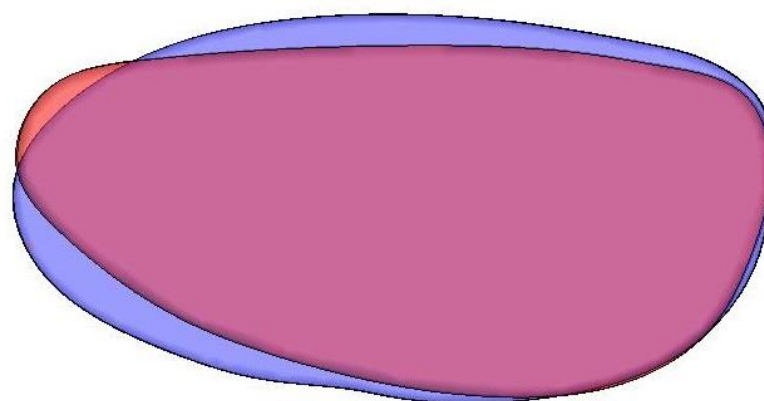


Figure 4.3 Dickinson fruit fly wing morphology (red) vs. actual *drosophila melanogaster* wing morphology (blue)

Table 4-1 Comparison of experimental wing morphology and actual wing morphology used in the following numerical studies

	Experimental wing	Actual wing
Wing length $R$	1	1
Mean cord $\bar{c}$	0.314	0.367
2 <sup>nd</sup> Moment of Inertia $\hat{r}_2$	0.534	0.660

#### 4.2.2 Numerical Setup

The numerical setup follows the set of flapping wing parameters that corresponds to the non-dimensional values of the experimental setup, shown in Table 4-2.

Table 4-2 Non-dimensionalised parameters of experimental setup for numerical simulation

	Experimental Parameters	Numerical Parameters
Wing length $R$	0.25m	1
Wing area $S$	0.019464m <sup>2</sup>	0.311
2 <sup>nd</sup> Moment of Inertia from centre of rotation	0.2386635m	0.658
Kinematic model	SHM	SHM

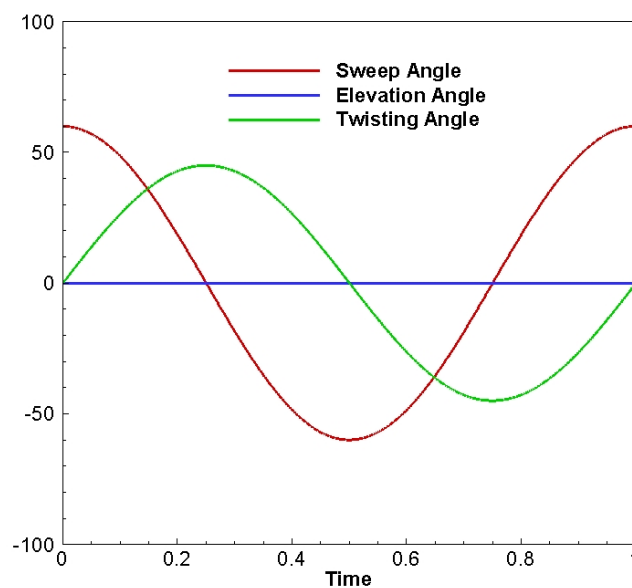


Figure 4.4 SHM kinematics used in the validation process

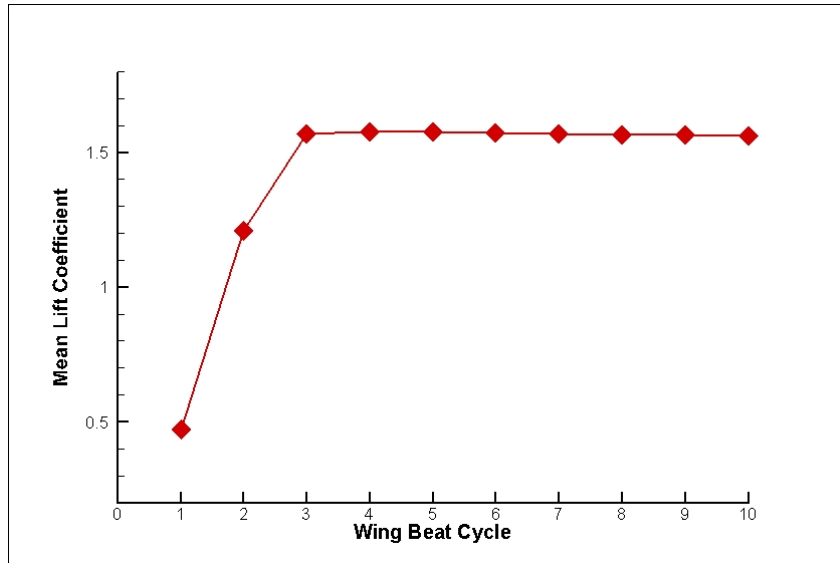


Figure 4.5 Mean lift coefficient computed per wing beat cycle showing that the effect of slow start diminishes after about 5 cycles

The kinematic model of flapping uses simple harmonic motion (SHM), and angular time plot in Figure 4.4 corresponds to this flapping motion. The maximum sweep amplitude is 120 degrees, the minimum angle of attack is 45 degrees. Wing elevation is set to zero similar to the setting of the experiment.

A pair of wings are made to flap with the shown kinematic model. No insect body is inserted in this case, similar to the experimental setup. Aerodynamic force measurements are computed only on the right wing of the pair to be consistent with the experimental setup.

The Reynolds number of the flapping motion in experiment is at  $Re = 150$ , and is matched in the numerical setup, well within the known operating Reynolds number regime of fruit fly wings. The simulation time step is set at  $\Delta t = 0.002$ , and results are extracted from the simulations only after 5 cycles of wing beat has been completed and compared with the experimental setup. This is to diminish the transient effect of impulsive start of the wing flapping motion in a still fluid domain at the beginning of the numerical simulations, which the gradual build-up of mean lift coefficient with increasing initial wing beat cycles can be seen in Figure 4.5

### 4.2.3 Validation with Experimental Data

At the 6<sup>th</sup> flapping cycle, the lift and drag force computed in the numerical study is extracted and converted to lift and drag coefficients according to the non-

dimensionalisation process explained in earlier chapters. The computed lift and drag coefficient during the wing beat cycle are presented in Figure 4.6, where they are compared against the results of similar quantities from experiments and show very good agreement.

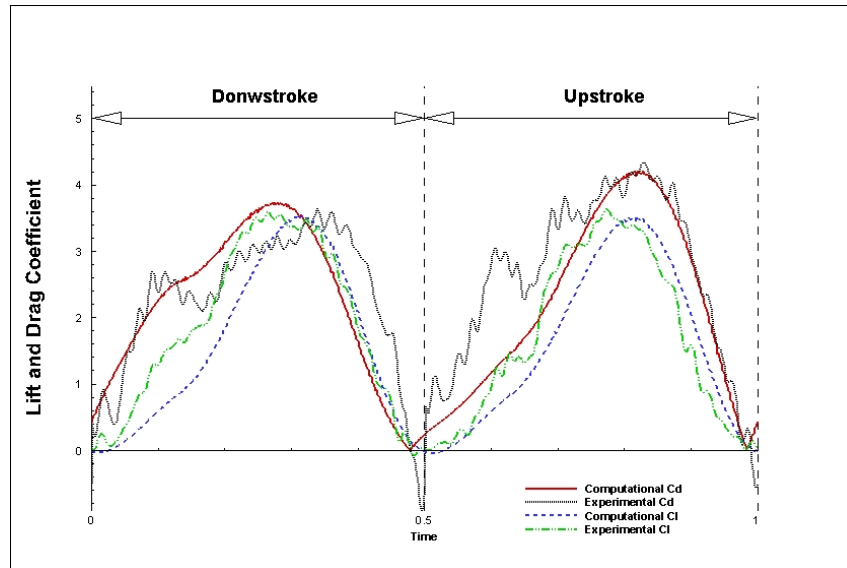


Figure 4.6 Computational Cd Cl compared with the experimental result

It can be observed that the experimental result tend to exhibit oscillatory behaviour in the force measurements, which is mainly due to the mechanical wing vibration during the experiment. This is a distinct advantage of numerical simulations where rigid body constraint can be enforced and the force measurements can be obtained smoothly with no noise effects.

The agreement in the lift and drag coefficients comparison shows that the numerical method is capable of capturing the unsteady aerodynamic effects in flapping wing flight problems and resolve the aerodynamic effects on the wing with good accuracy. This provides valuable validation for the method and boosts confidence in following studies.

#### 4.2.4 Flow Structure Analysis

More detailed flow field data are extracted from the verification simulations and visualizations are made to further verify that the numerical method is capable of capturing the full details of the flow structures around the wing during flapping flight. However, no in depth analysis of flow data are attempted in this study as the flow structure evolution are already well documented in literature and only rough

comparisons through flow structure visualizations are made to demonstrate the correctness of the computational results.

Figure 4.7 shows the pressure contour and velocity vector in the mid sweep plane cutting along the wing orientations at a particular time step. It clearly shows the pressure gradients in the local vicinity of the flow and the downwash of fluid generated by the flapping wings pointed out by the downward arrows of the velocity vectors in the plane. This agrees well with published numerical simulation results as well as experimental observations (Aono et al., 2008; Z. J. Wang, Birch, & Dickinson, 2004). A slightly modified version of the figure, Figure 4.8, shows the velocity magnitude contour map and the vortex contour lines in the same orientation. This figure clearly shows the amount of fluid being moved into downwash due to the flapping of the insect wings and should be proportional to the amount of aerodynamic forces generated. The vortical structures show vortex pairs being shed from the wing tip and wing root due to the translational motion of the wing and the downwash is closely associated with the shedding of the vortex pairs. The vortical structures remain active and prominent at least 5 chord length below the wings before they dissipate.

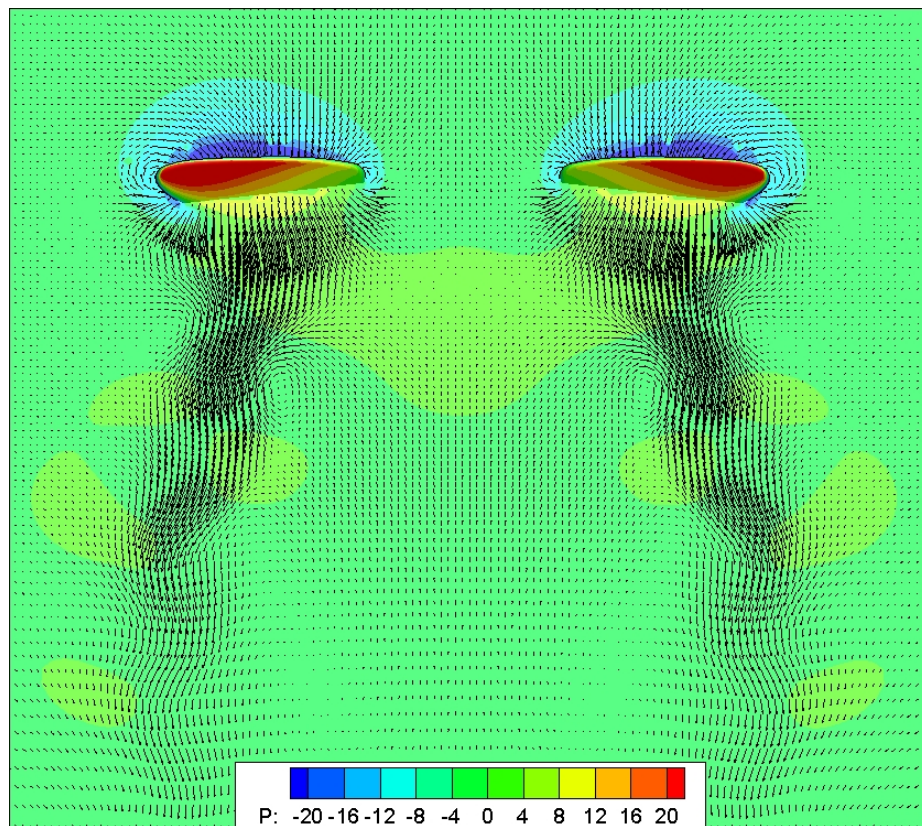


Figure 4.7 Pressure contour and velocity vector plot in the plane along the wing orientation during flapping motion at a time the wings reaches maximum translation velocity



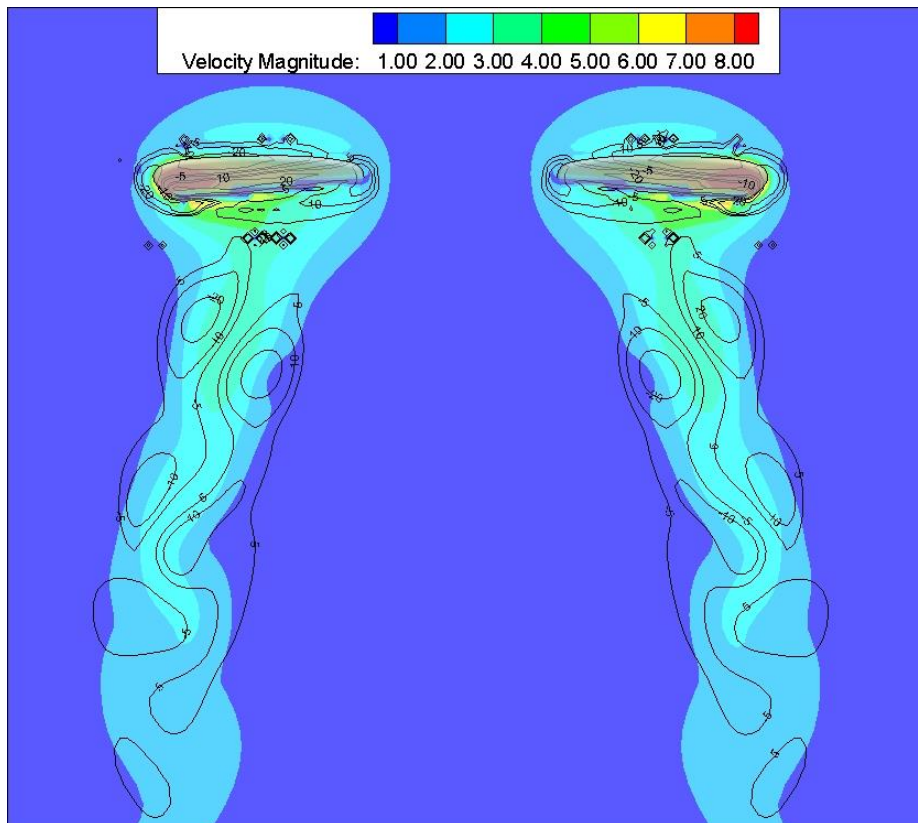


Figure 4.8 Velocity magnitude contour and vorticity contour lines showing the vortex pair structure driving the downwash before dissipation

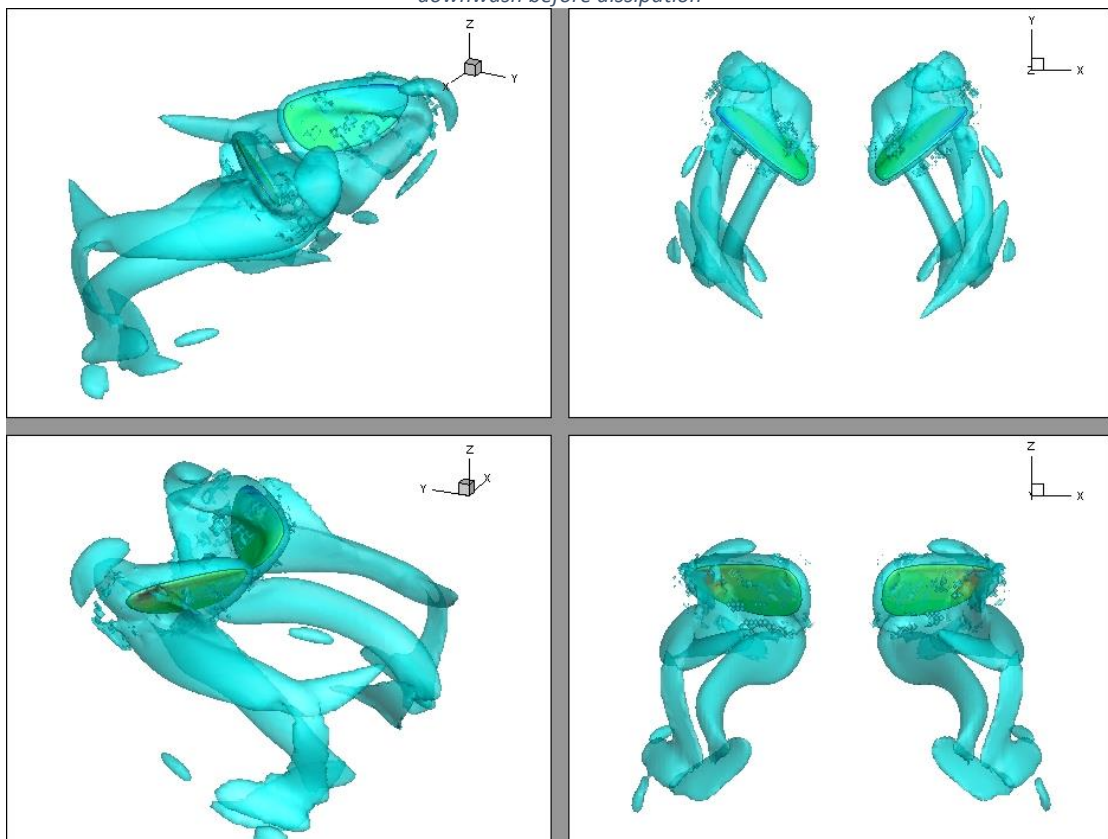


Figure 4.9 Vorticity iso-surface plots showing the vortex structure evolution during a wing flapping motion, the LEV, TEV and WTV during the beginning of wing down stroke are clearly seen from this plot

It is also noted that in a flapping wing pair setup, minimal wing-wing interaction

is observed. The flow structures are symmetrical as expected and the fluid being moved by each wing are clearly separated. Figure 4.9 shows the iso-vorticity plot of the flow field around the flapping wing at a time step when the wing is just about to start down stroke. Complex vortical structures can be observed here including leading edge vortex (LEV), trailing edge vortex (TEV), wing tip vortex (WTV) and the shed LEV, TEV from the previous upstroke. The ability of capturing detailed flow field information demonstrates the ability of the numerical method to correctly compute and solve the flow equations and provide detailed insights into complex flow structure evolutions associated with unsteady aerodynamic effects of flapping flights and is critical for the success of the following studies.

### **4.3 Kinematic Models of Insect Flapping Wings**

The flapping kinematics of insect wings plays the leading role in the generation of aerodynamic forces of flight. A rigid wing has three degrees of freedom in rotation (angular freedom), as we have already shown in Chapter 3. Each rotational angle is theoretically capable of infinite variations, and the relative phase difference of the 3 rotations add to further complexities. As a result, generally 3 kinematic models or approaches are adopted by research: the simple harmonic motion (SHM) based sinusoidal function kinematic model (Ansari, Zbikowski, & Knowles, 2006; Miyan & Ewing, 1985; Walker, Thomas, & Taylor, 2009), trapezoidal function kinematic models characterised by rapid acceleration and deceleration of translation and rotation of wings at beginning and end of wing strokes (S. N. Fry, Rohrseitz, Straw, & Dickinson, 2009; Sun, 2005), or natural kinematic models based on experimental measurements and data interpolation of a random observed kinematic model that has no simple mathematical descriptions (Aono et al., 2008; Lua et al., 2010). Simple combinations of the aforementioned simple kinematic models may not produce the natural observed flapping kinematic of insects, but could provide the opportunity of learning the unsteady aerodynamic effects associated with such simplified flapping motions and establish linear relationships. Therefore, if the unsteady aerodynamic effects associated with the simplified kinematic models could be fully understood, a mathematical description of complex kinematic model that was optimised through evolutionary model kinematic could then be found (Hedrick & Daniel, 2006).

Much effort in kinematic model analysis of flapping flights have so far been focused primarily on parametric data collection (Dickinson et al., 1999) and modifications of simple parametric variables to determine aerodynamic effect changes in wing flapping motions (Sane & Dickinson, 2001). Most researches simply follow a predetermined kinematic models such as SHM, trapezoidal function or naturally observed models in flapping flight. This however limits our understanding of how variations in wing flapping kinematics could affect the production of aerodynamic forces.

In the remaining sections of this chapter, the present author systematically evaluates the aerodynamic force productions of SHM and trapezoidal function kinematic models and their variations to gain insight into their contributions in unsteady aerodynamic behaviours, and find the correlated aerodynamic force production variations when key kinematic parameters are modified. This study is conducted with a full insect model consisting of 2 flapping wings and a body, which are tested at the same Reynolds number using different kinematic models. A proposed optimised flapping kinematic model is then shown to provide sufficient lift for hovering flight while improving the overall flight efficiency.

#### **4.3.1 Numerical Simulation Setup**

In this study, a full fruit fly geometric model is used, which consist of 3 body parts, namely the insect body and the left and right wings. The insect wing roots (centre of rotation) are placed at two sides of the upper thorax of the insect body and allowed to flap in the horizontal plane, simulating a hovering flight pattern. During hovering, the total aerodynamic lift can be estimated to be equal to the weight of the insect and the direction of lift force produced by the flapping wings are pointing vertically up, that eliminates the need of resolving force directions to obtain true lift produced. The symmetrical nature of the sweep motion of the insect wings also allows the vanished term of net thrust (horizontal) force acting on the insect as the drag forces are cancelled due to the alternating translational directions of the wings during up and down stroke. Therefore, the analysis can be solely focused on the evaluation of total lift force produced per wing beat cycle.

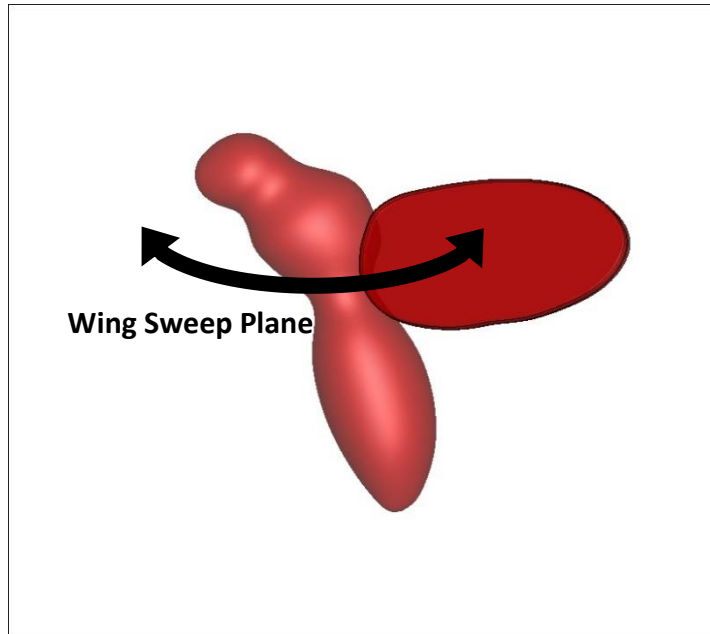


Figure 4.10 The full fruit fly model consisting of 2 wings and a body flapping in an horizontal plane simulating a hovering flight. This is the configuration used in current kinematic studies

The kinematic models are varied according to a systematic definition of parameters during the simulations. The details of such parameters are defined in the later sections. However, a few parameters associated with the flapping kinematic are maintained constant, so that the flapping flight are defined by the same Reynolds number for quantitative comparisons. The sweep amplitude is fixed at  $\phi_0 = 140^\circ$ , the minimum attack angle  $\alpha_{min} = 40^\circ$ , and the elevation angle  $\theta$  remains zero (horizontal stroke plane) throughout the flapping cycle. The Reynolds number is therefore a constant of  $Re = 140$ . This particular value of Reynolds number is determined in a separate study where the average lift production at this Reynolds number could provide just sufficient lift force for the insect to hover using normal SHM kinematic model.

The flapping motion of the wings are started with “slow start” feature described before to minimise effect of impulsive reaction from the fluid and are allowed to flap for more than 5 cycles before aerodynamic force data are collected and compared. This is to allow the surrounding flow circulation to stabilise and to simulate a quasi-steady state of actual insect hovering flight in which momentary hovering of small insects takes place during hundreds of wing beat cycles. This also maximises the unsteady aerodynamic effects on the insect due to wing-wake interactions as observed by other studies (Birch & Dickinson, 2003).

### 4.3.2 Comparison of Aerodynamic Lift Between SHM and TF Kinematic Models

The study first looks at the lift generation aspects of simplified kinematic models of SHM and trapezoidal function (TF). The main difference between a TF kinematic model and a SHM kinematic model is in the acceleration and deceleration of phases of the wing translations and rotations. In a SHM kinematic function, the acceleration deceleration in wing translation and rotations happens throughout the stroke smoothly, while in TF kinematic function, the acceleration and deceleration happens rapidly over a short phase time within each stroke, and the wing reaches constant velocity in translation and constant angle of attack in rotation. The comparison of kinematic models are plotted in Figure 4.11.

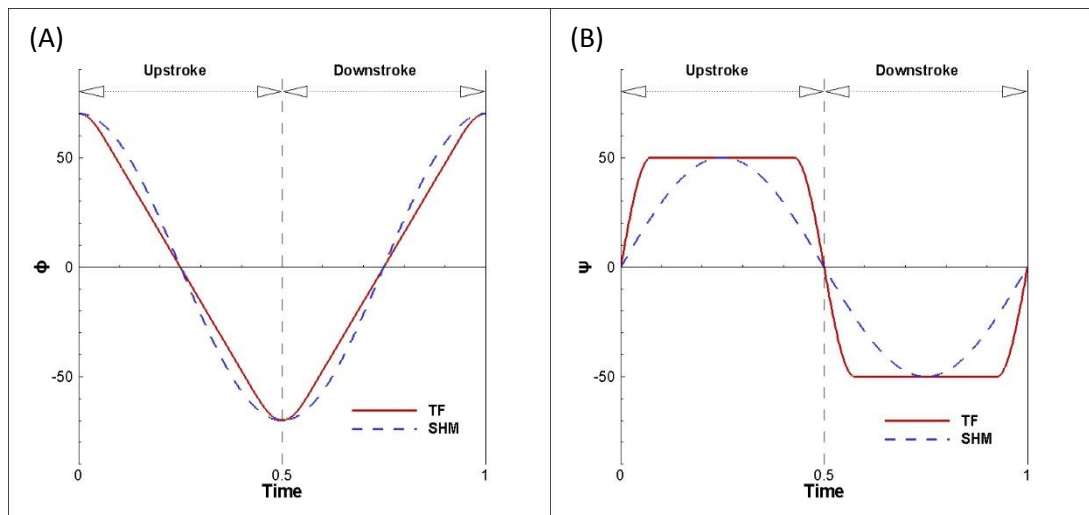


Figure 4.11 Comparison of SHM and TF kinematic models, (A) sweep angle and (B) twist angle

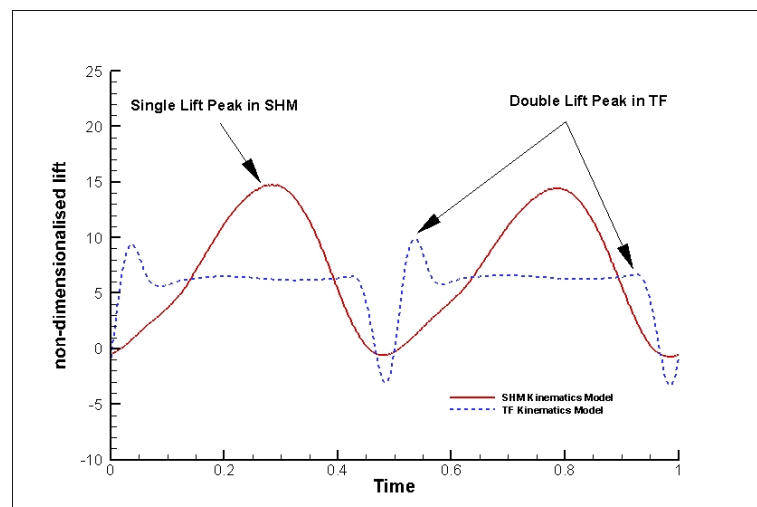


Figure 4.12 Non-dimensional lift production by a SHM and a TF kinematic model prescribed flapping flight as given in Figure 4.11

Table 4-3 Mean lift coefficient and mean drag coefficient of a SHM and a TF kinematic model prescribed flapping flight

	Mean Lift Coefficient	Mean Drag Coefficient
<b>SHM Kinematic Model</b>	1.17	1.54
<b>TF Kinematic Model</b>	0.96	1.66

The non-dimensional lift generated over one wing beat cycle when a full fruit fly model performed flapping flight according to a SHM kinematic model and a TF kinematic model are compared in Figure 4.12. The TF kinematic model has a phase duration for sweep acceleration and deceleration  $\Delta\tau_t = 0.15T$  and a phase duration for wing twisting  $\Delta\tau_r = 0.15T$ . It can be seen in the figure that the lift has single peaks in each stroke in a SHM prescribed flapping motion, whereas there are 2 lift peaks in each stroke in a TF prescribed flapping motion. This is expected as the main lift peak produced at each end of a stroke in TF kinematic modelled flapping flight is due to the additional circulation generated by rapid wing twisting together with the large acceleration in translational velocity of the wing that lead to a strong wing wake interaction. The wake capturing effect has been studied previously by Dickinson in a 2D analysis using simple stroke mechanisms (Dickinson, 1994). However, when the mean lift per wing beat cycle is calculated, a TF prescribed flapping motion generates about 18% less lift.

It can be argued that the SHM kinematic model is in fact a special case of a TF kinematic model in which the phase duration of sweep acceleration and deceleration spans half of a stroke,  $\Delta\tau_t = 0.5$  and the phase duration of the wing twisting equal to that of sweep acceleration,  $\Delta\tau_r = 0.5$ . Therefore, a generalised comparison can be achieved between a SHM prescribed flapping motion and a TF prescribed flapping motion. A systematic approach is adopted to vary the respective phase durations of sweep acceleration  $\Delta\tau_t$  and twisting  $\Delta\tau_r$  gradually and the effect on aerodynamic lift is observed. The results are presented in Figure 4.13 to Figure 4.20. It is worth to point out that, in order to understand the generalised relationship of lift to the specific parameters of  $\Delta\tau_t$  and  $\Delta\tau_r$ , each parameter is varied individually and then the combined effects tested to verify the consistency with individual results.

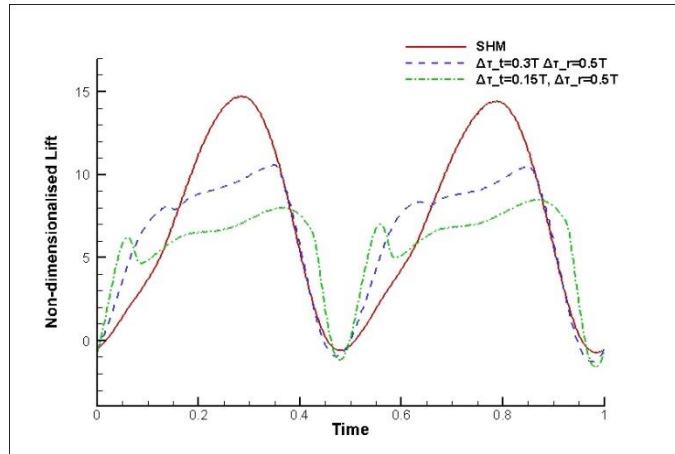


Figure 4.13 Comparison of non-dimensional lift generated by SHM kinematic model flapping flight vs. modification of the same SHM to TF in sweep only

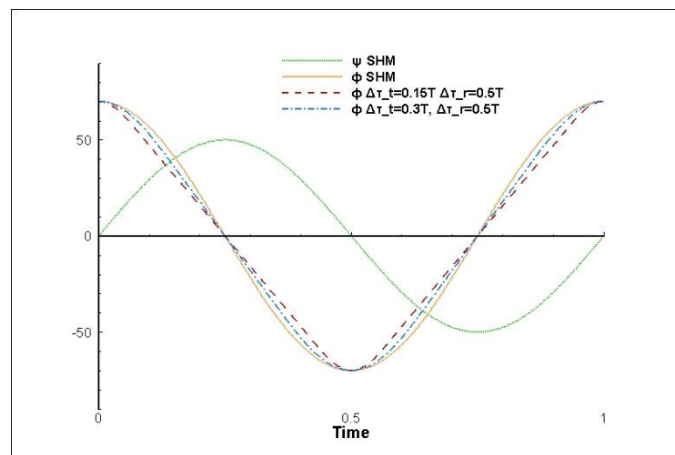


Figure 4.14 Angular time plot showing the difference of sweep motion when SHM kinematic function is changed to TF kinematic function

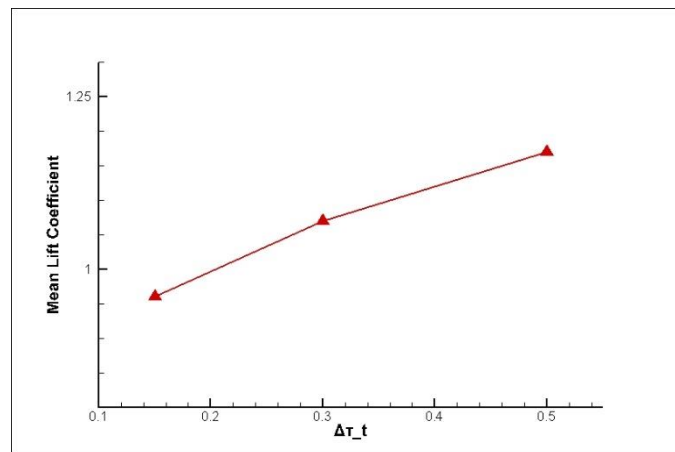


Figure 4.15 Mean lift coefficient per wing beat cycle showing a decreasing trend as phase duration of sweep acceleration and deceleration  $\Delta\tau_t$  is shortened as the SHM kinematic model is partially changed to TF

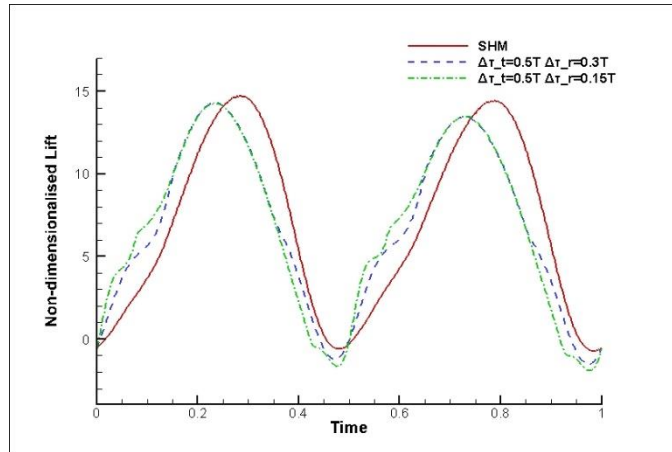


Figure 4.16 Comparison of non-dimensional lift generated by SHM kinematic model flapping flight vs. modification of the same SHM to TF in twist only

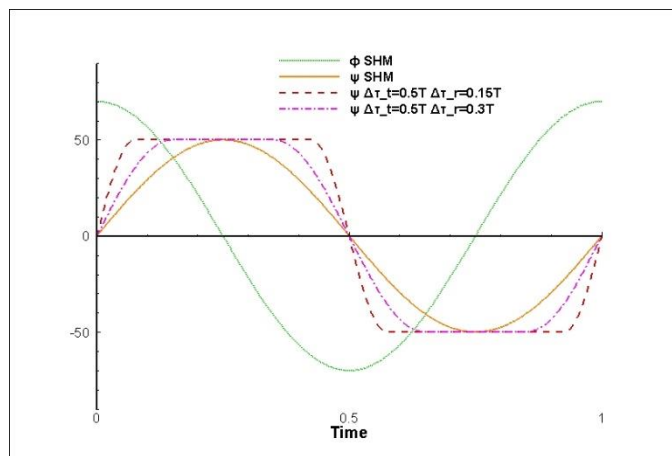


Figure 4.17 Angular time plot showing the difference of twist motion when SHM kinematic function is changed to TF kinematic function

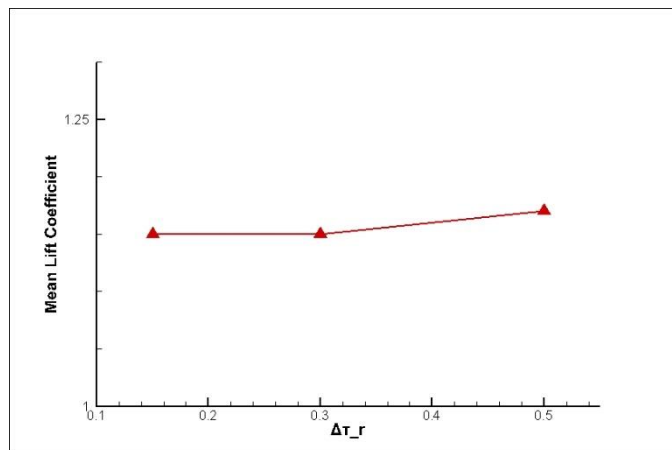


Figure 4.18 Mean lift coefficient per wing beat cycle shows that the lift force generated does not change due to the reduced rotation period  $\Delta\tau_r$  of the wing at ends of strokes



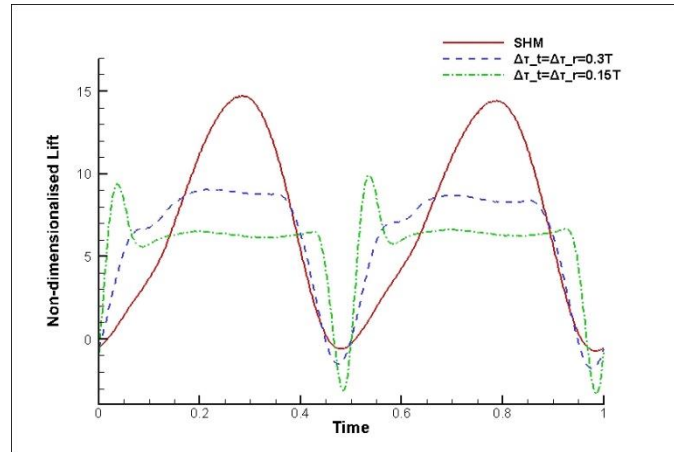


Figure 4.19 Comparison of non-dimensional lift generated by SHM kinematic model flapping flight vs. modification of the same SHM to TF in both sweep and twist, the phase durations of acceleration in sweep and rotation in twist are made the same

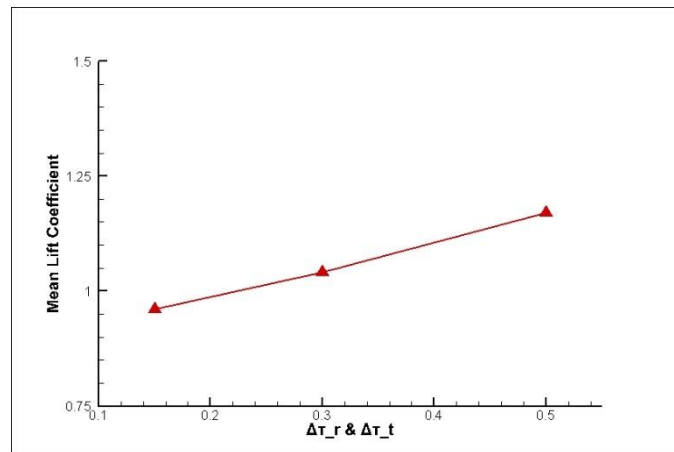


Figure 4.20 Mean lift coefficient per wing beat cycle shows that the lift force generated decreases as expected when the SHM kinematic model is changed to TF kinematic model at the same Reynolds number

The results show a general decrease of lift force generated as duration of acceleration and deceleration in the wing sweep motion reduces, which characterises the effect of changing the flapping wing kinematic from SHM to TF. This is expected as when phase duration of wing acceleration and deceleration in sweep reduces, the maximum translational velocity of the wing reduces which leads to substantially lower lift peak generated at mid-stroke of wing despite that the rapid acceleration of the wing at the beginning of the stroke enhances the lift generation at that moment and produces a lift peak. The reduction in phase duration of wing twisting, on the other hand does not produce much effect on the mean lift force produced. However, it shifts the lift peak forward due to the wing achieving minimum angle of attack earlier during the stroke.

In conclusion, a general trend of decreasing lift is observed when the flapping wing kinematic model changes from SHM to TF. The reduction is prominent and proves that SHM kinematic model in deed produces more lift than a TF kinematic model at the

same Reynolds number with the same wing geometric profile. This in fact agrees with the observations of natural insects in flapping flight that their wings' translational motion usually resembles a sinusoidal wave function, which maximises the lift production.

#### **4.3.3 Augmentation of Lift by Wing Twist Phase Leading in SHM Kinematic Model**

In a simplified kinematic model of flapping wing motions, the sweep angle rotations are usually synchronous with the twisting angle rotations of the wing in such a manner that the wing always rotates to the vertical orientation (90 degrees angle of attack) at the end of each stroke before stroke reversal changes direction of the translational velocity of the wing to begin next stroke action. This type of synchronous flapping motion can be considered as 0 phase difference between the twisting and sweeping of the wing in flapping motion. Therefore, a simple modification of the simplified kinematic model by introducing phase difference into the relationship between a prescribed twisting and sweeping angle functions, the flapping motion could produce varying amounts of aerodynamic force due to changing unsteady aerodynamic effects produced by interaction of the wing with the surrounding flow structures. Figure 4.21 to Figure 4.23 provide indicative illustrations of SHM kinematic models with changing phase difference between twisting and sweeping.

Three simulations are carried out by introducing different extent of leading phase difference into the SHM kinematic model prescribing the flapping wing motion. The average lift force produced by a normal SHM kinematic model prescribed flapping wing motion with 0 phase difference is used as reference. No lagging phase kinematic models are tested in this study as previous studies have shown that, an early flip of the wing angle of attack before end of wing stroke leads to a substantial wake capture lift peak at the start of next stroke, while a delay in the flip of wing angle of attack results in diminished wake capture lift peaks and instead produces negative lift peaks due to wing added mass inertia and a delayed rotational circulation build-up (Dickinson et al., 1999).

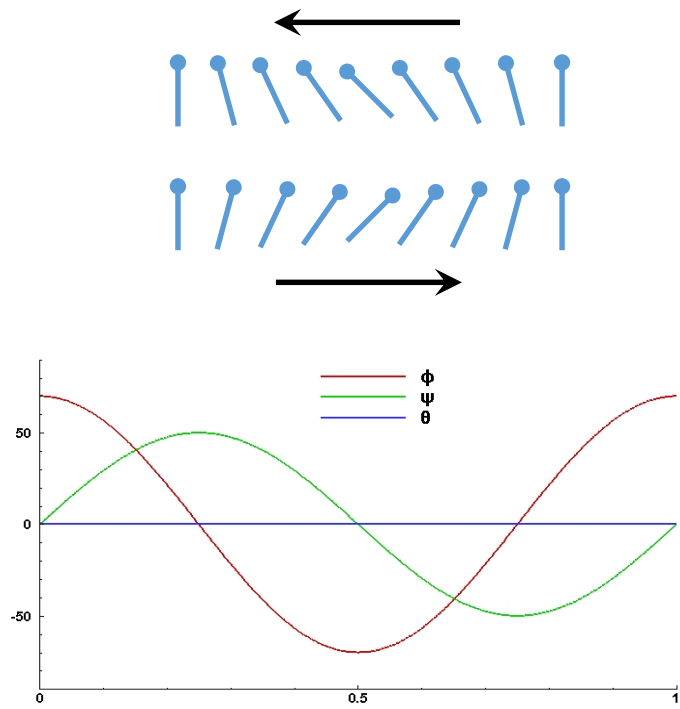


Figure 4.21 Typical SHM kinematic model prescribed flapping motion with no phase difference between twisting and sweeping angle

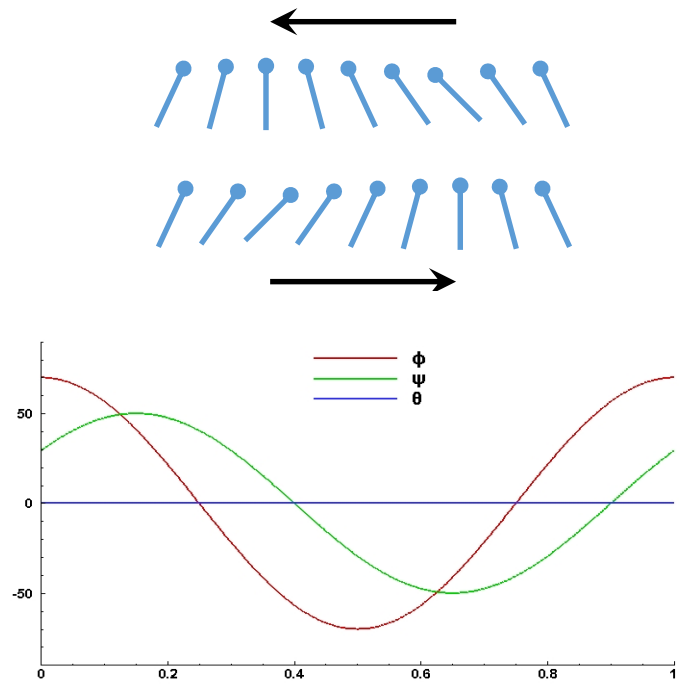


Figure 4.22 SHM kinematic model prescribed flapping motion with twisting angle leading sweeping angle by phase difference  $\tau = -0.1T$ , the wing twisting takes place before the wing reaches end of the stroke and the wing twists to minimum attack angle before reaching maximum translation velocity at mid-sweep point of the following stroke

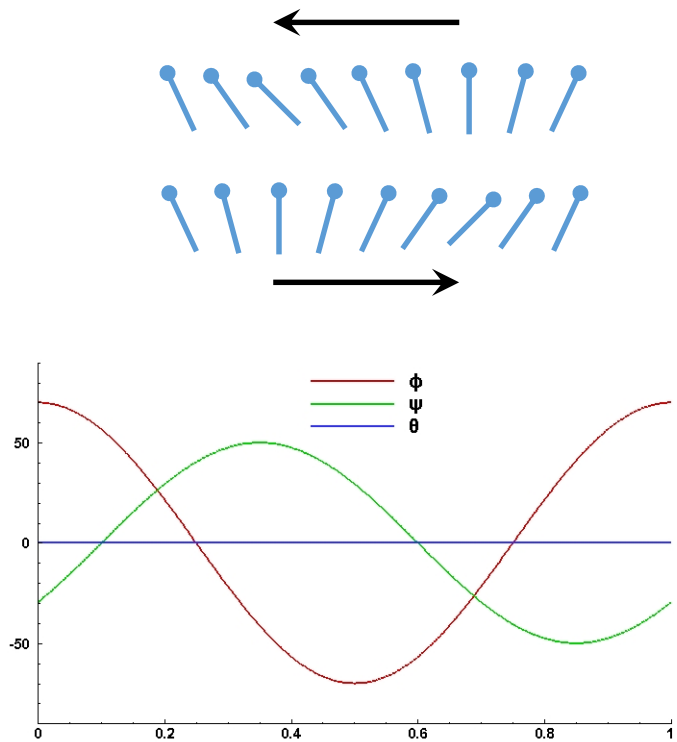


Figure 4.23 SHM kinematic model prescribed flapping motion with twisting angle lagging sweep angle by phase difference  $\tau = 0.1T$ , the wing twisting takes place after the wing reaches the end of the stroke and into the beginning of the next stroke, this delay causes the wing minimum angle of attack to be reached after the mid-stroke point of the following stroke

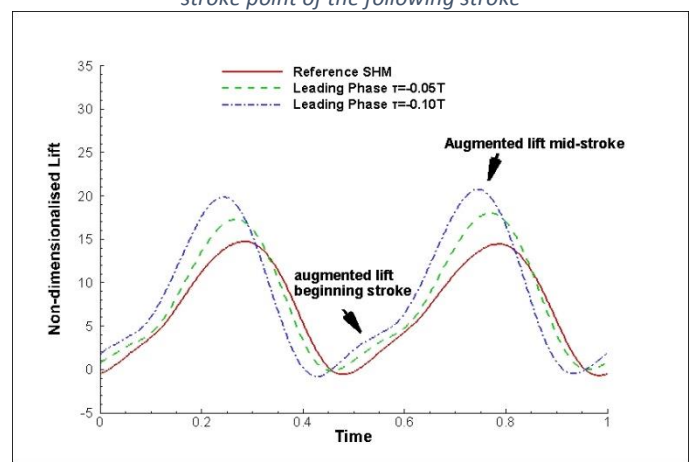


Figure 4.24 Non-dimensional combined lift produced by the fruit fly wing pair

Table 4-4 Table of mean lift coefficient  $\bar{C}_l$  comparison for variations of SHM kinematic model

	$\bar{C}_l$	Change
Reference SHM Kinematic model	1.17	0
SHM with twist leading sweep by $\tau = -0.05T$	1.35	15%
SHM with twist leading sweep by $\tau = -0.10T$	1.46	25%

The results of non-dimensional aerodynamic lift force production over a wing beat

cycle prescribed in SHM kinematic model are presented in Figure 4.24. The lift force are the combined effect of both wings. A mean lift coefficient calculation is carried out over the same wing beat cycle. The computed mean lift coefficient of 1.17 for the referenced SHM kinematic model agrees well with the corresponding  $\bar{C}_l = 1.15$  reported previously by Sun et al. (Sun & Wu, 2003).

As expected, the leading phase angle of twisting to sweeping action of the wing flapping motion leads to additional lift generations compared to the reference SHM kinematic model. In a SHM kinematics flapping motion, the early twisting of the wing results in an overall shift forward of the lift force plot in which the lift maximum and minimum occurs earlier than the reference case. The augmented lift force can be divided into 2 components. The first component of increasing lift can be seen at the blue arrow, and is due to the increased wing wake interaction, as the early twisting of the wing cuts into the shed trailing edge vortex from the previous stroke. The second component, at red arrow in the figure, shows a much higher lift peak produced at 0.25/0.75T wing beat cycle time, when the translational velocity of the wing is at maximum. It can be explained that when the twisting phase leads the sweeping phase in a SHM kinematic model, the minimum angle of attack is reached at a point before the maximum translational velocity of the wing is achieved. When the wing reaches mid-stroke position, the twisting leading phase angle would orient the wing at a larger angle of attack against the incoming flow resulting in a stronger LEV which is stabilised by span wise flow and stretching of the vortex core. The prolonged attachment of LEV over the wing at higher angles of attack leads to the enhanced lift force production at the middle of the stroke. As the wing twisting continues, eventually the LEV separates and the lift drops quickly. Figure 4.25 shows clearly the larger attached LEV and a stronger pressure differential above and below the wing at the time step slightly after the mid-stroke position in the case  $\tau = -0.1T$  in SHM.

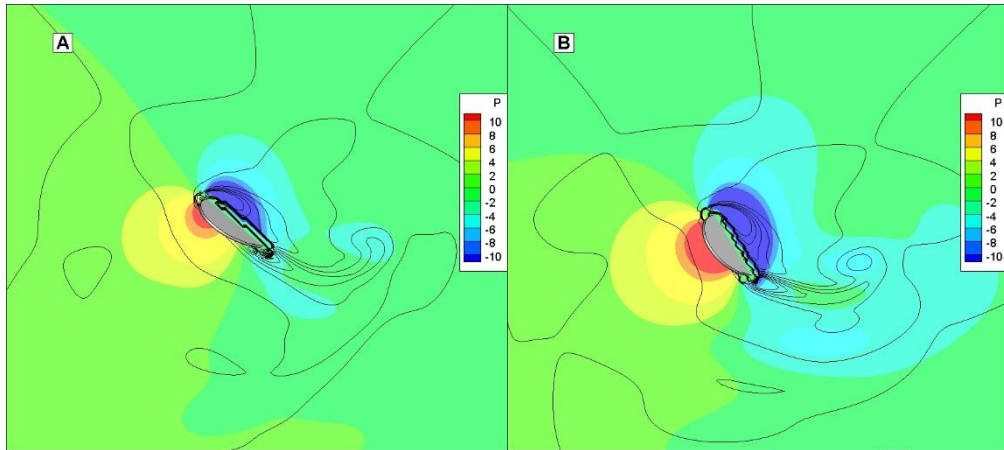


Figure 4.25 (A) The vorticity line plot and pressure field around the wing at slightly after mid-stroke position in a SHM kinematic model flapping flight, (B) the vorticity line plot and pressure field around the wing at the same time step in a SHM kinematic model with leading twist phase angle showing a stronger attached LEV and larger pressure field difference above and below the wing

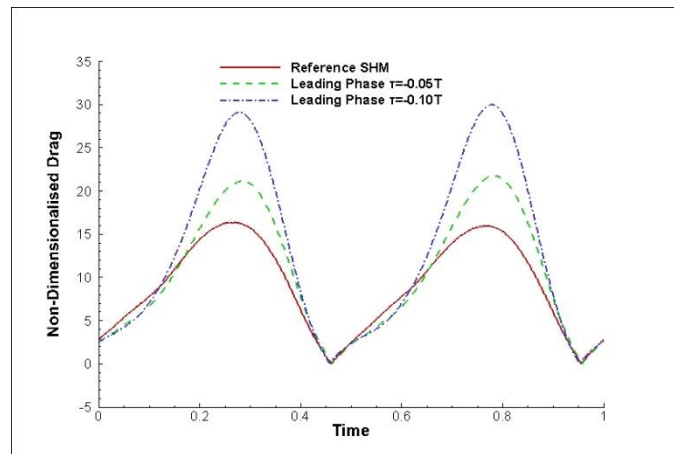


Figure 4.26 Non-dimensional combined drag force acting on the fruit fly wing pair, drag force changes direction from up stroke to down stroke, the plotted drag force is the magnitude force along the insect heading direction

Table 4-5 Decreasing Lift to Drag ratio and Lift to Power ratio as leading phase angle increases

	$\frac{\bar{L}}{\bar{D}}$	$\frac{\bar{L}}{\bar{P}}$
Reference SHM Kinematic model	0.76	0.140
SHM with twist leading sweep by $\tau = -0.05T$	0.74	0.134
SHM with twist leading sweep by $\tau = -0.10T$	0.65	0.114

Further analysis of drag force production shows that drag increases with leading phase angle difference of wing twisting to wing sweeping. The non-dimensional drag force are plotted in Figure 4.26 and mean lift to drag ratios are computed and shown in Table 4-5. The computed lift to drag ratio matches the reported experimental value of

0.8 for fruit fly wings in hovering (Sane & Dickinson, 2001). It could be seen that, leading phase angle in twisting of the wing results in more substantial drag increase than lift augmentation, which has also been demonstrated in separate studies (Sun & Wu, 2003). Furthermore, the calculated lift over aerodynamic power ratio also decreased exponentially, which shows the decreasing efficiency of lift generation at leading phase difference.

#### **4.3.4 Augmentation of Lift by Wing Twist Phase Leading in TF Kinematic model**

A similar systematic investigation of the lift force variations in TF kinematic model flapping wing motions are carried out. Figure 4.27 to Figure 4.29 show the angular time plots of various phase leading TF based kinematic models explored in the study. The illustration of wing chord trace shows slight difference from SHM analysed earlier. The lift force plot over 1 wing beat cycle is shown in Figure 4.30. The difference in mean lift coefficients are also calculated and tabulated in Table 4-6.

From Figure 4.30, it can be seen that by introducing leading phase angle into twist kinematic function, the aerodynamic lift can be increased in the same way as in the case of SHM kinematic model prescribed flapping motions analysed previously. Higher lift peaks can be observed at the beginning and near to the end of each stroke. Near to the end of a stroke, the wing twist starts while the sweep motion of the wing is still at constant translational velocity, the pitching-up rotation of the wing induces rotational circulation analogous to Magnus effect that contributes to higher velocity on the upper surface of the wing and lower velocity on the lower surface of the wing as have been explained by Dickinson et al (Dickinson et al., 1999). The lift peak produced immediately after stroke reversal is however, not due to wing twisting. The higher lift peak produced is due to the favourable wing angle of attack at the beginning of the stroke and a stronger interaction of the wing with the shed trailing edge vortex from the previous stroke that induces extra circulation. Therefore, as leading phase angle between twist and sweep increases, one can observe a higher lift peak at the beginning of the stroke and an earlier lift fall-off before the end of the stroke due to the earlier start of wing twisting. However, this benefit of additional lift is easily offset by a sudden drop in lift just before stroke reversal happens that could lead to diminished overall effect on total lift produced per wing beat cycle. This can be explained by the orientation

of the wing just before stroke reversal due to early wing twisting, which leads to negative angle of attack that produces negative translational lift for a short duration. As a result, it is expected to see a maximum in lift gain as the phase leading of wing twisting over sweeping increases. This maximum lies in between the tested phase leading values of  $\tau = -0.05T$  and  $\tau = -0.10T$ . Drag peaks are also observed in Figure 4.31 corresponding to the points of the lift peaks. Simple calculations carried out shows that the lift-to-drag ratio of a TF kinematic model prescribed flapping motion with leading phase of twist over sweep is improved with small leading phase and decreases when the leading phase becomes larger. This is very different observation from SHM based kinematics case, in which the lift-to-drag ratio continues to drop as leading phase angle is increased. This relationship provides crucial evidence of the possibility of finding a specific kinematic model that could provide the sufficient lift with minimal power requirements.

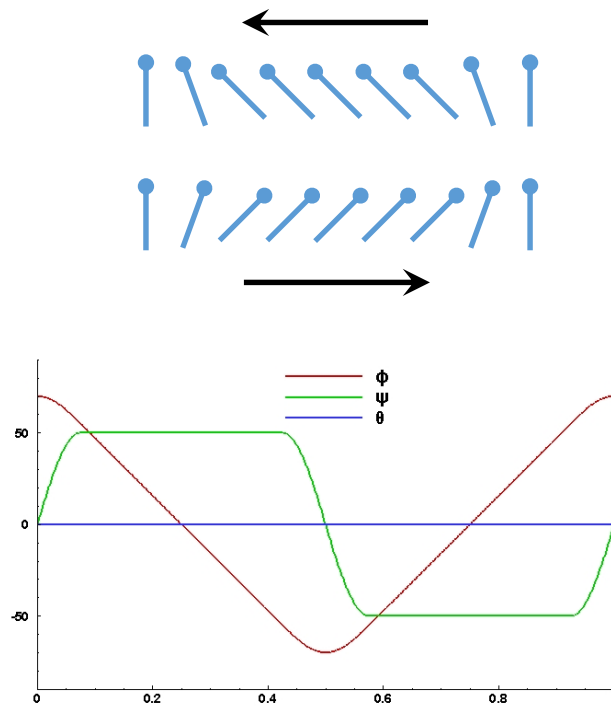


Figure 4.27 TF kinematics mode prescribed flapping kinematic model with no phase difference between twisting and sweeping angle



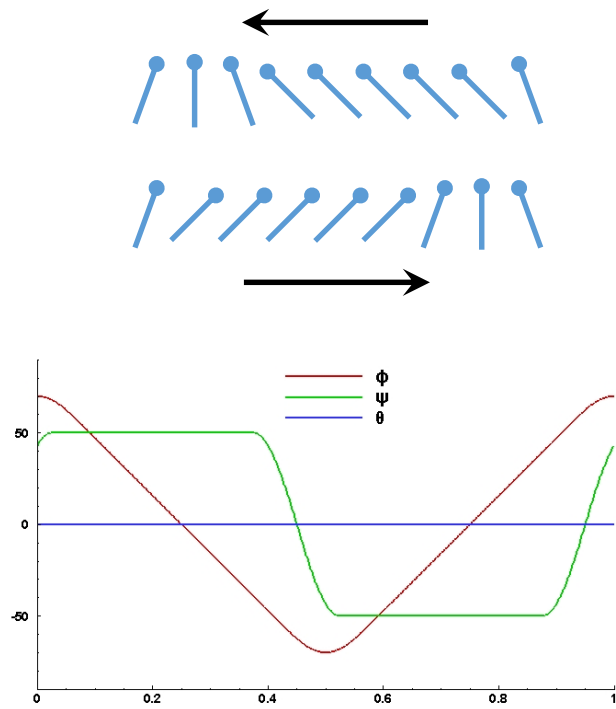


Figure 4.28 TF kinematic model prescribed flapping motion with twisting angle leading sweeping angle by phase difference  $\tau = -0.05T$ , the wing twisting starts before the wing sweep starts to decelerate near the end of the stroke

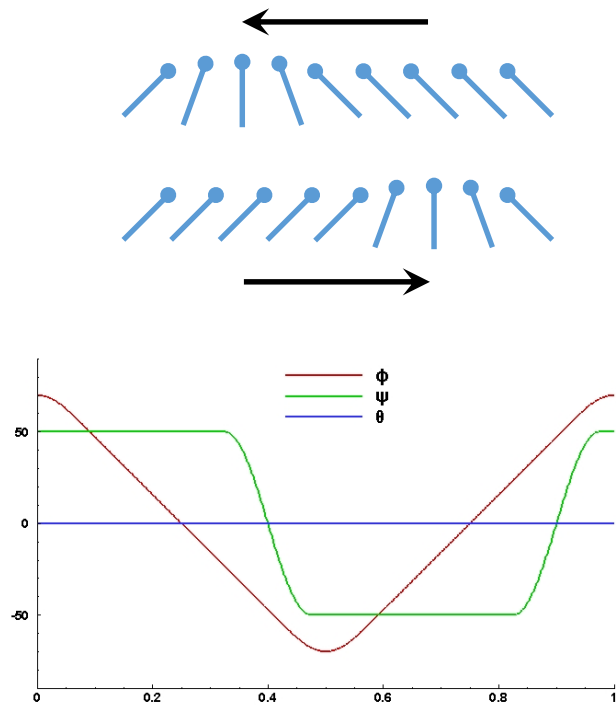


Figure 4.29 TF kinematic model prescribed flapping motion with twisting angle leading sweeping angle by phase difference  $\tau = -0.1T$ , the wing twisting starts before the wing sweep decelerates and completes before the wing reaches the end of the stroke.

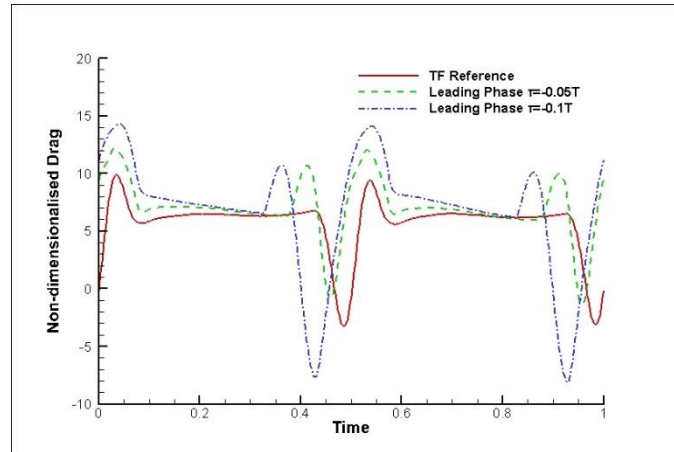


Figure 4.30 The combined aerodynamic lift produced by the wing pair in TF kinematic model prescribed flapping motion with slightly different phase leading of twist over sweep

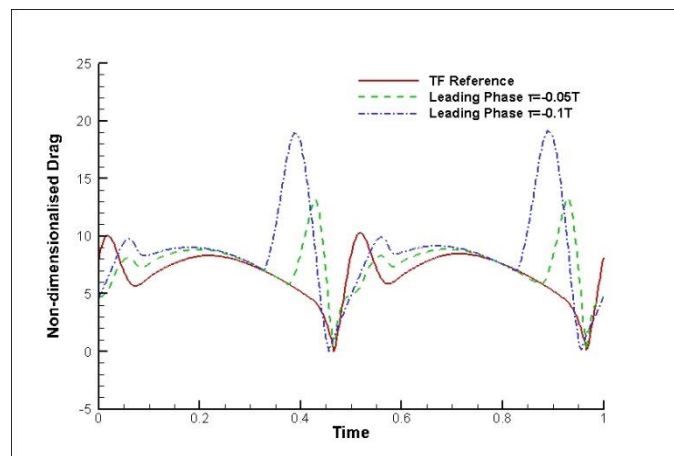


Figure 4.31 The drag force acting on the wing pairs in TF kinematic model prescribed flapping motion with slightly different phase leading of twist over sweep

Table 4-6 Calculated mean lift coefficient and lift to drag ratio and lift to power ratio of TF kinematic model prescribed flapping motions with different phase leading of twist over sweep

	$\bar{C}_L$	Change	$\frac{\bar{L}}{\bar{D}}$	$\frac{\bar{L}}{\bar{P}}$
Reference TF Kinematic model	0.9604	0	0.84	0.185
TF with twist leading sweep by $\tau = -0.05T$	1.1816	23%	0.92	0.191
TF with twist leading sweep by $\tau = -0.10T$	1.1478	19%	0.76	0.169

#### 4.3.5 A Proposed Trapezoidal Function Kinematic model

Based on the results shown in the previous section, the referenced TF kinematic model prescribed flapping motion at the same Reynolds number and with the same geometric wing could not produce as much lift as compared to the SHM counterpart.

The derived relationship from previous section also shows that, by introducing limited leading phase of wing twist over sweep, the aerodynamic lift generated can be increased. This could on the other hand provide the necessary additional lift required to support the insect in a hovering flight.

The study then proceeds to find a TF based kinematic model that could produce an equivalent lift as the reference SHM kinematic model prescribed flapping motion. The resulting angular time plot is shown in Figure 4.32.

The characteristic kinematic parameters obtained (Table 4-7) show that the proposed kinematic model agrees quite well with experimental findings of optimal kinematics setups for TF like kinematic models using fruit fly wing by Sane and Dickinson (Sane & Dickinson, 2001), who showed that lift decreases dramatically as leading phase of twist over sweep changes beyond the optimal value of around -0.05.

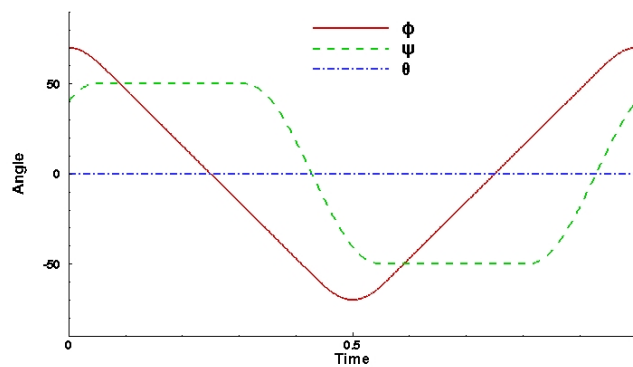


Figure 4.32 Angular time plot of the proposed TF based kinematic model

Table 4-7 The characteristic kinematic parameters describing the proposed kinematic model

<b>Sweep amplitude <math>\phi_0</math> (same as SHM)</b>	<b><math>140^\circ</math></b>
<b>Minimum angle of attack (same as SHM)</b>	<b><math>40^\circ</math></b>
<b>Duration of translation acceleration <math>\Delta\tau_t</math></b>	<b><math>0.142T</math></b>
<b>Duration of wing twisting <math>\Delta\tau_r</math></b>	<b><math>0.224T</math></b>
<b>Leading phase difference <math>\tau</math></b>	<b><math>-0.0721T</math></b>

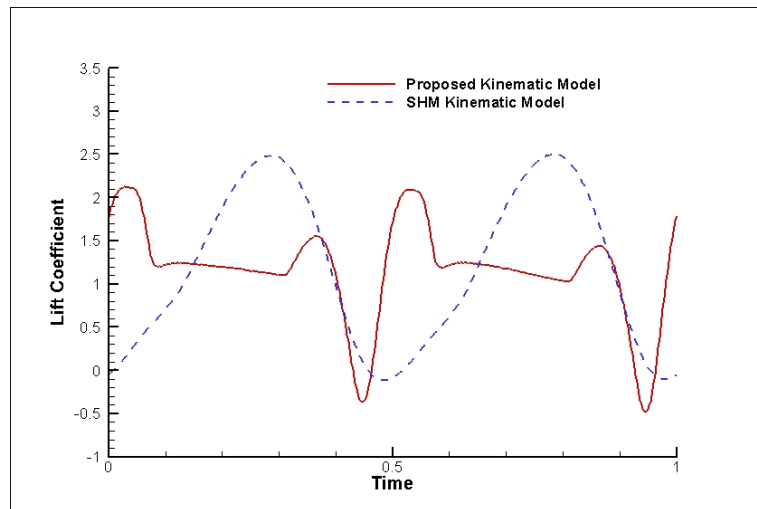


Figure 4.33 Comparing lift coefficient over a wing beat cycle between the proposed kinematic model and SHM kinematic model prescribed flapping motion

The mean lift coefficient per wing beat cycle is calculated to be 1.164, very close to the 1.17 for SHM kinematic model prescribed flapping motion that is thought to be required for fruit fly hovering.

A further comparison of pitch moment generated by the wings about the midpoint on the insect thorax in between the centres of rotations of the wing pair produced by the proposed TF based kinematic model prescribed flapping motion against that of SHM based flapping flight are shown in Figure 4.34. The higher peaks of pitch moment at the ends of strokes indicate a more effective and rapid pitch control in the insect performing TF kinematic model based flapping flight in each wing beat cycle. This may be desirable for insects to gain more effective control of body heading and orientation during hovering and free flights.

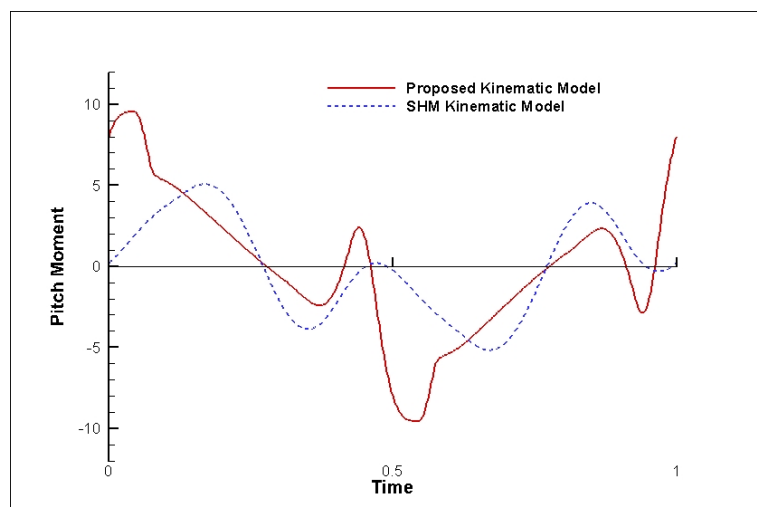


Figure 4.34 Pitch moment over a wing beat cycle showing the proposed kinematic model producing higher torque peaks at ends of strokes

### 4.3.6 Power Calculations of Flapping Flight Using Prescribed Kinematic models

Non-dimensional aerodynamic power is calculated by finding the dot product of force acting on the flapping wing surface and the velocity at that point and summed up over the entire wing surface. Then the non-dimensional power is converted to the actual aerodynamic power of flapping flight by fruit fly using the morphological data described in Chapter 3. The body-mass-specific aerodynamic power is calculated by dividing the obtained aerodynamic power by the average mass of the fruit fly. The results calculated for the various prescribed flapping flight motion cases discussed previously are in Table 4-8.

*Table 4-8 Specific aerodynamic power computed on the insect wings based on CFD solutions of different kinematic model prescribed flapping motions*

	<b>Body-mass-specific Power</b> <b>W/kg</b>
<b>Reference SHM</b>	33.25
<b>SHM with phase leading <math>\tau = -0.05T</math></b>	40.05
<b>SHM with phase leading <math>\tau = -0.10T</math></b>	50.90
<b>Reference TF</b>	20.66
<b>TF with phase leading <math>\tau = -0.05T</math></b>	24.65
<b>TF with phase leading <math>\tau = -0.10T</math></b>	28.40
<b>Proposed Kinematic model</b>	27.45

The result shows that despite an increase in power requirement for generating the additional lift by applying phase leading wing twist over sweep in the proposed kinematic model than the other TF kinematic model, the overall body-mass-specific power is significantly lower than that calculated for the same insect performing a SHM kinematic model based flapping flight. The body-mass-specific power of 27.45 W/kg matches very well with the computed body-mass-specific power for fruit fly hovering in a separate study by Sun et al (Sun & Tang, 2002a). This implies that by performing a modified TF kinematic model based flapping motion as proposed, the insect flapping

flight efficiency is much improved. This could be an explanation in the natural observation of small insect flapping following a TF based kinematic model (Zanker & Gotz, 1990), and likely a nature's solution to the energy constraints of small insects in maintaining flight.

#### **4.4 Summary**

In this chapter, the author first verified the current numerical scheme with the innovative implementation of geometric and kinematic modelling in solving insect flapping flight problems by comparing with existing experimental and numerical results. A specific equivalent case comparison is done against an experimental setup and the results show very good agreement. Flow visualizations of the obtained flow field information also agrees well with known unsteady aerodynamic effects associated with insect flapping flights.

In a systematic study, the author simulated hovering of a complete insect model using variations of SHM and TF kinematic model based flapping motions and measured the instantaneous and mean aerodynamic force, torque and power values. A general relationship is observed and agrees with the known effects of kinematics variations to aerodynamic performance. The author then further established that the same geometric wing at the same Reynolds number produces more aerodynamic lift in a SHM based flapping flight than a TF kinematic model based flapping flight using the same kinematic parameters. Then an optimised TF based kinematic model is proposed that is shown to provide equivalent lift but required lower aerodynamic power than the referenced SHM kinematic model flapping motion. This improved efficiency in flapping flight through adjustment of kinematic model provides a possible reference for future flapping wing micro air vehicles designs.

# CHAPTER 5: Numerical Study of 3D Clap-and-Fling of Flapping Wings

## 5.1 Introduction

A “clap-and-fling” flapping motion is characterised by a 2 part action which involves the wings coming into close proximity with the possibility of contact. The portion of kinematics during which the wings approach each other is called as “clap” motion. The clap motion is immediately followed by the “fling” motion resulting in the wings separating from each other. This well-known unsteady aerodynamic effect, “Clap-and-Fling”, is known to substantially increase lift force estimations in many insect flapping flights. Weis-Fogh, in his classic paper described the aerodynamic mechanisms clap-and-fling observed on the tiny wasp *Encarsia Formosa* (Weis-Fogh, 1973).

During clap, the insect first brings the leading edges of the two wings together and continued pronation of the wings diminishes the inverted “v-shape” gap in between the wing surfaces until the wings are parallel in physical contact or close proximity. During the fling, due to continued pronation at the start of downstroke, the wings start to separate along the leading edge while the trailing edge are still in contact and creates a growing “v-shaped” space in between the wing surfaces until the wings are completely pulled apart.

The “clap-and-fling” flapping motion has been found to be adopted by various species of insects such as in tiny *Encarsia Formosa* (Weis-Fogh, 1973), in tethered flying *Drosophila* (Götz, 1987; Zanker & Gotz, 1990), although it is observed that fruit fly *Drosophila Melanogaster* rarely employs clap-and-fling in free flight (Ennos, 1989; S. N. Fry et al., 2003), in white butterfly *Pieris Barssicae* (Ellington, 1984) and other larger insects while carrying loads or performing power demanding flight turns (Marden, 1987). Variation of actual clap-and-fling mechanism have also been observed on different insects including partial or near clap-and-fling, double clap then fling and clap-pause-fling (Ellington, 1984). The effectiveness of such variations are however not known and hypothetical explanations have been proposed (Ellington, 1984; Lehmann et al., 2005).

Many research work has been conducted to explore the underlying fluid dynamic of the flapping behaviour. Analytical studies by Weis-Fogh suggested that the function of fling is to strengthen the development of circulation at the beginning of the downstroke. The absence of trailing edge vortex (due to close proximity of the wing trailing edges) results in an enhanced overall circulation. This in-turn results in enhanced lift by diminishing the starting vortices due to Wagner effect (Weis-Fogh, 1973). Lighthill pointed out that this phenomenon could only operate within an inviscid fluid (Lighthill, 1973). Götz showed that clap could increase lift by producing a momentum jet of fluid downwards as the wings twists about the leading edge in a two dimensional consideration (Götz, 1987). Further experimental studies have however demonstrated that clap attenuates total force production at the stroke reversal and the generated lift is significantly lower than fling. Clap-and-fling behaviour could distort wake structure interaction with the wings and lead to influence of lift force productions throughout the stroke cycle (Lehmann et al., 2005). Recently, several numerical studies have investigated the fluid dynamic effect of clap-and-fling to overcome the experimental limitations in flow visualisation and mechanical setups. However, most of the numerical methods have focused on two dimensional simulations and low Reynolds numbers associated with tiny insect flights. (Kolomenskiy, Moffatt, Farge, & Schneider, 2011a; L. A. Miller & Peskin, 2005; Zhang, Chang, Duan, & Zhang, 2009). Three dimensional numerical simulations performed by Sun et al, have focused primarily on tiny insects of *Encarsia Formosa* where  $Re=15$  (Sun & Yu, 2006). Most other three dimensional numerical studies only provided limited relevant flow field information using a simple rectangular or elliptical wing models instead of a geometrically realistic insect wing (Kolomenskiy, Moffatt, Farge, & Schneider, 2011b; Sohn & Chang, 2007).

The primary motivation of the work is to perform a systematic and detailed numerical study to examine three dimensional clap-and-fling effects at a reasonable Reynolds number corresponding to small insects while using the a morphologically accurate fruit fly wing geometry. This study attempts to provide accurate flow field visualisation of three dimensional aerodynamic effects of insect wing clap-and-fling behaviour. Improvement of lift force generations and the relative increase of power requirements are calculated and compared to address the efficiency concern of a three dimensional clap-and-fling for small insects. Furthermore, a relationship between lift



enhancement and the physical separation of wing tips and wing roots (centre of rotation) of the insect performing clap-and-fling are examined and it provides a new interesting insight into the evolutionary consequence of the development of clap-and-fling flapping motion in only selected insect species.

## 5.2 The Kinematics of Clap-and-Fling

In this study, a pair of morphologically accurate fruit fly wings are used and the centre of rotation of the wings are specified according to actual fruit fly wing dimensions and parameters. No insect body is defined in this simulation as based on prior simulations and estimations, the effect of a static insect body interactions with flow field is much less significant compared to the unsteady aerodynamic effect of wing-wing interactions. A difference of less than 2% measured aerodynamic force generated is seen when compared to earlier results of prescribed flapping motions with insect body. However, arguably, the presence of body may pose as a flow constraint to air during wing clap-and-fling near to the wing root. We believe this effect is likely to be small as the clap-and-fling rate is small near the body. On an additional note, from the numerical considerations, the efficiency of the computation can be substantially improved as compared to the addition of roughly 60% more meshless nodes from the contribution of the insect body model. Hence, the saving in computational cost is significant compared to the marginal improvement of accuracy, justifying the absence of insect body in the current study.

It was pointed out by Weis-Fogh in his study of *Encarcia Formosa*, the two wings act essentially as rigid plates during clap-and-fling (Weis-Fogh, 1973). Although, in the ensuing observations and studies, it is suggested that many of the insects performing clap-and-fling behaviour had flexible wings, which during fling curved along their chords and peel apart (Ellington, 1984). This modified fling behaviour is suggested to decrease peak drag during fling by as much as 50% and at the same time slightly further enhance lift generated during the process (L. Miller & Peskin, 2009). The rigid body assumption used in the current study should not prevent the observation of augmentation of lift by clap-and-fling mechanism, This has also been proven by experimental works by Lehmann et al., in which enhancement of lift has been measured on a pair of mechanically driven Plexiglas wing models executing clap-and-fling

flapping motion (Lehmann et al., 2005).

The rigid nature of the fruit fly wings used in this study has a very important impact on the kinematic model applied. The basic kinematics parameters for simulating clap-and-fling in this case are defined according to the known fruit fly flapping kinematics such that the sweep amplitude  $\phi_0 = 140^\circ$ , the minimum angle of attack  $\alpha_{min} = 40^\circ$  and  $Re = 150$ . The kinematic model is essentially based on the derived trapezoidal function kinematic model from the previous study (Chapter 4) which has shown to generate sufficient lift for fruit fly hovering. According to this kinematic model, the wing sweep motion are symmetrical about the mean positional angle of the mid-sweep plane and hence the wings do not come into close proximity on either end of the strokes. However, in order to achieve clap-and-fling, the mean positional angles of the mid-sweep planes of both wings are rotated backwards and create a dorsal bias which reduces the wing separations at the end of upstroke (beginning of downstroke) to produce clap-and-fling behaviour. This is illustrated in Figure 5.1. The phase angle difference is zero between wing twisting and sweeping (such that  $\tau_\psi = 0$ ), so that the upper surfaces of the wings will be perfectly parallel when they are in the closest proximity to each other at end of the upstroke, as required by clap-and-fling mechanism. A trapezoidal function kinematic model characterises the wing sweep with quick deceleration and acceleration phase at the end of upstroke and beginning of downstroke, while the remainder of the stroke, the wing sweeps with constant angular velocity. Similarly, the wing twists rapidly during the deceleration and acceleration phase at the end of upstroke and beginning of downstroke to flip the wing around into a favourable angle of attack. These were combined together to give the basic kinematics of clap-and-fling.

It is suggested in previous analysis that for clap-and-fling to be most effective, the wing twisting motion at end of stroke should be rapid and the total time duration should be shorter compared to the translational acceleration phase of the wing (Ellington, 1984; Lighthill, 1973). This particular kinematic feature has been adopted in experimental work (Lehmann et al., 2005) and numerical works (Kolomenskiy et al., 2011b; L. A. Miller & Peskin, 2005) which demonstrated that the rapid rotation induced leading edge vortex (LEV) interactions could be the key reason in the significant boost of lift peak during fling. However, there is a problem in implementing the above in the present clap-and-fling kinematic model, which set the two wings to be parallel at the onset of

clap and the rapid rotation associated with the ensuing fling leads to wing-wing intrusions with each other and cause numerical problems. This problem was not encountered in the experimental work by Lehmann et al., because the mechanical setup of their experiments set the wing roots apart by a significant separation distance and no actual physical clap was explored in their study (Lehmann et al., 2005). In contrast, the present numerical study allows the separation of wing roots (centre of rotation) of the wings to be as close as  $0.1R$ , limited only by the numerical efficiency and stability analysis of the current numerical scheme, where  $R$  is the wing span. This separation of the wing surfaces is equivalent to  $0.3\bar{c}$ , where  $\bar{c}$  is the mean chord length and has been shown to be close enough to capture the aerodynamic effects of clap-and-fling (Ellington, 1984; Lehmann et al., 2005). The wing roots separation of  $0.1R$  is closer to observations on real insects and would allow us gain a better understanding of the dominant aerodynamic effects relevant to clap-and-fling in nature.

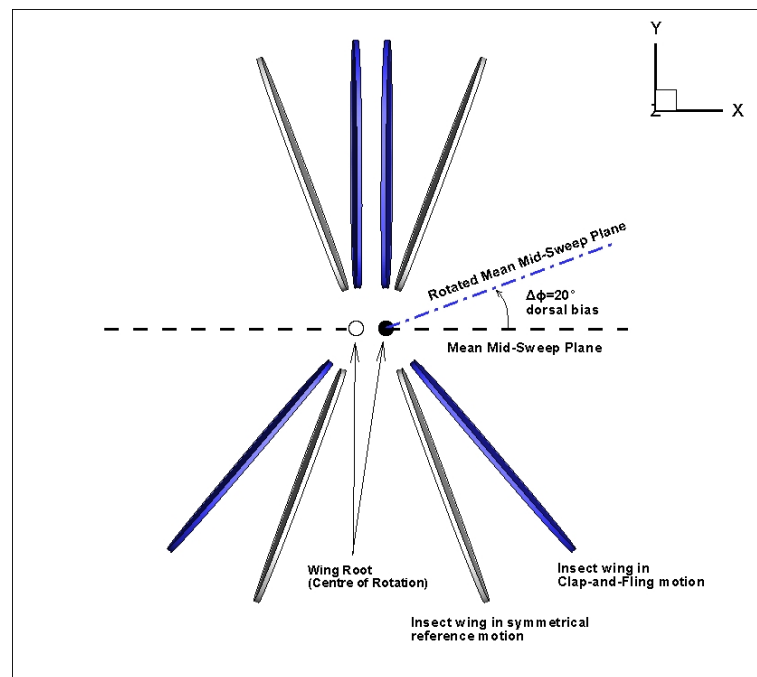


Figure 5.1 Illustration of the rotation of mean mid-sweep plane of the flapping wings in order to create the clap-and-fling flapping motion

However, unlike the commonly studied 2D clap-and-fling kinematics, establishing the clap-and-fling kinematics in 3D is further complicated by the three dimensional nature of the wing flapping motion with centre of rotation at the wing root, this requires significant effort to derive a suitable CF kinematics as well be detailed. To prevent inter-penetration of the two wings in such close-quarter interaction, the modelled insect would have to substantially increase the acceleration of the translational motion of the

wings to make for sufficient clearance for the onset rapid wing twisting motion; which in turn leads directly to a dramatic increase of drag force, as much as 10 times (L. Miller & Peskin, 2009). Thus the insect's muscle power required to perform the clap-and-fling with such high sweep accelerations would at least be as proportionally higher, which may not be biologically feasible.

The symmetrical and regular wing geometries employed in the three dimensional simulations of Kolomenskiy et al. and Sun and Yu (Kolomenskiy et al., 2011b; Sun & Yu, 2003) and the simplified kinematics description of wing rotations in two dimensional numerical studies by Miller et al. (L. A. Miller & Peskin, 2005) have neglected two very important aspects of natural insect wings, the wing planform geometry and the axis of wing twisting. The wing of small insects such as fruit fly has a generally elliptical planform which is narrower near to the wing tip and usually wider in the middle or closer to the wing root, as shown in Figure 5.2. In most two dimensional clap-and-fling wing kinematics descriptions, the wing rotations are defined by the relative motion of wing leading edge and trailing edge. However, this is not an accurate description of the natural insect wings, in which usually the axis of twisting is somewhere along the leading edge spar of the insect wing (Dudley, 2002) such that the displacement of the leading edge of insect wings are more dependent on the wing translational motion (sweep) than rotational motion (twist), while the trailing edge is more prominently affected by the later. A schematic drawing of the morphologically accurate fruit fly wing with the illustration of axis of twisting is shown in Figure 5.2.

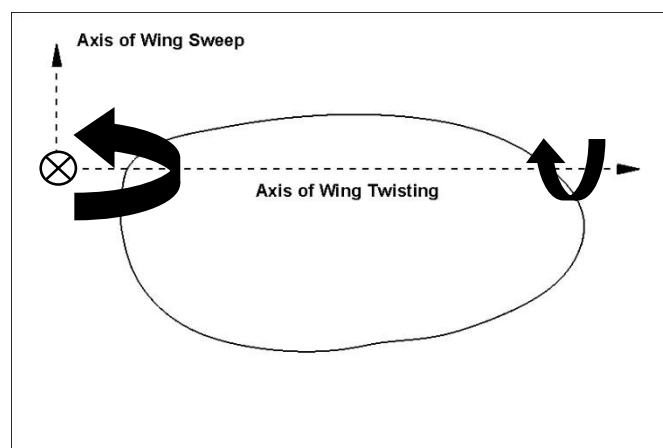


Figure 5.2 Illustration of wing planform and axis of wing sweep and axis of wing twist, the marked out point is the wing root

Therefore, it is apparent that, the displacement of the wing section closer to wing root would be much less affected by wing sweep due to the smaller radial distance from

the centre of rotation, while the much larger chord length at this section of the wing would lead to large displacement due to wing twisting. Hence, the kinematic model implemented must prevent the intrusion of the rigid wings closer to the wing root section by suitably timing the acceleration duration of sweep in relation to the lengthening of twisting duration of the wings. This generally requires that the duration of sweep acceleration to be reduced and the duration of the wing twist to be increased.

Hence, in the present kinematic design of wing motion, the wing twisting duration is suitably extended to reduce the translation acceleration in sweep motion and to prevent wing-wing collision. The final wing twist duration is thus chosen as  $\Delta\tau_r = 0.5T$ , resembling a sinusoidal function while the wing sweep acceleration and deceleration duration is set as  $\Delta\tau_t = 0.142T$  ( $\Delta\tau_t$  is the duration of translation acceleration phase explained in Chapter 3), matching the previously derived optimal TF kinematic model for fruit fly. The angular time plot of the current kinematic model for clap-and-fling study is presented in Figure 5.3.

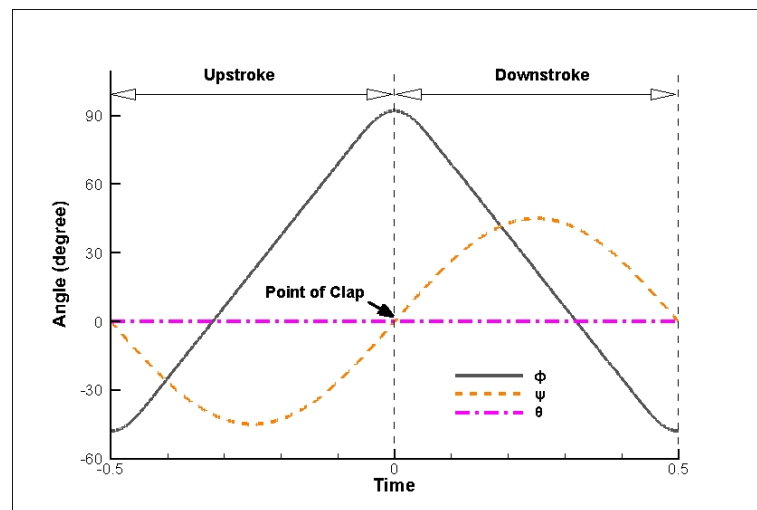


Figure 5.3 Angular time plot of kinematic model used for current clap-and-fling study where clap occurs at  $t = 0$

Due to the wing roots separation distance of  $0.1R$ , the two wings are parallel at the point of clap (without physically touching each other) when the mean mid-sweep plane is rotated by  $\Delta\phi = -20^\circ$  (refer to Figure 5.1). However, in order to achieve physical clap of the wings, the mean mid-sweep plane needs to be further rotated by  $2^\circ$  on dorsal bias so that  $\Delta\phi = -22^\circ$  and is further explained in Figure 5.4. (A) shows the wing pair at the point of clap and (B) shows the wings during fling. It is worth pointing out that the wing surfaces are not in physical contact with each other except near to the wing tip section, which is expected for small insects performing clap-and-fling on a pair of rigid

wings. This could in fact contribute to the resulting three dimensional aerodynamic effect that will be shown later. As the wings perform fling after the physical clap, the section of the trailing edges near to the wing tip section separate at the early stage of the fling motion, while the section of the trailing edges near to the wing root section remain in contact. As the fling continues, the length of the trailing edges that remain in physical contact reduces and eventually the two wings separate completely leading to the end of the fling phase. This is similar to the phenomenon of “peel” described by Ellington previously (Ellington, 1984).

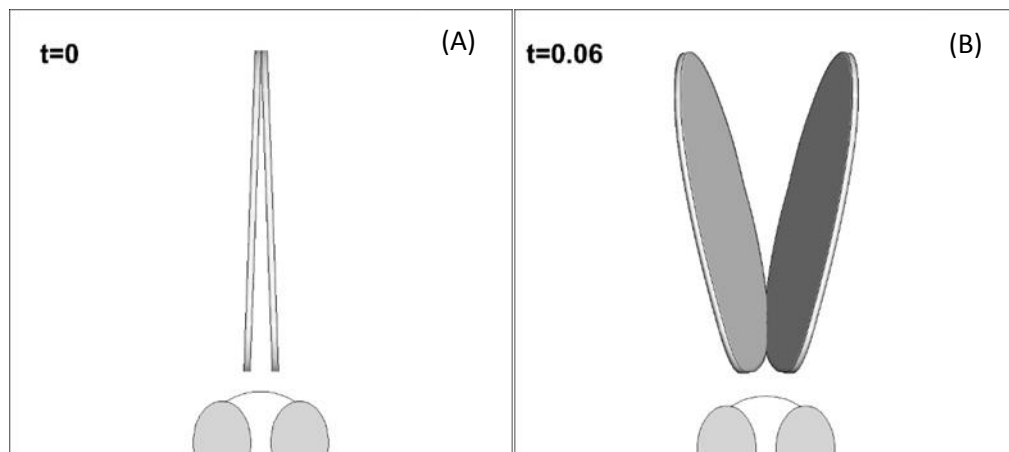


Figure 5.4 The top-down view on the stroke plane showing the onset of physical clap at  $t=0$ , where  $\Delta\phi = -22^\circ$  and the gradual separation of the wing trailing edges from wing tip to wing root section after  $t=0.06$  into the fling phase. The wing roots has a separation distance of  $0.1R$

### 5.3 Analysis of Flow in 3D Clap-and-Fling

A series of comparative numerical simulations are conducted on the aforementioned numerical setup on a pair of fruit fly wings. The mean mid-sweep plane is varied from  $\Delta\phi = 0^\circ$  to a dorsal bias of  $\Delta\phi = -22^\circ$ , during which the wing tips will be in physical contact during clap for a wing roots separation distance of  $0.1R$ . We are interested to investigate the effect of clap-and-fling on the generation of aerodynamic forces as compared to a symmetrical referenced flapping motion. Further analysis of the three dimensional flow evolution associated with clap-and-fling motion will be presented.

#### 5.3.1 Augmentation of Overall Lift and Drag due to Clap-and-Fling

In this numerical simulation, the symmetrical sweep case ( $\Delta\phi = 0^\circ$ ) is considered

as the reference for comparison with clap-and-fling results. For the symmetrical reference case, the two wings are separated by  $40^\circ$  at the dorsal end of the stroke and the wing tip separation are more than  $2\bar{c}$  apart. According to experimental findings by Lehmann et al (Lehmann et al., 2005), this separation would produce negligible wing-wing interaction such that the aerodynamic force generated on each wing is approximately the same as a single flapping wing case. Figure 5.5 shows the minimum wing tip separation of the symmetric sweep reference case.

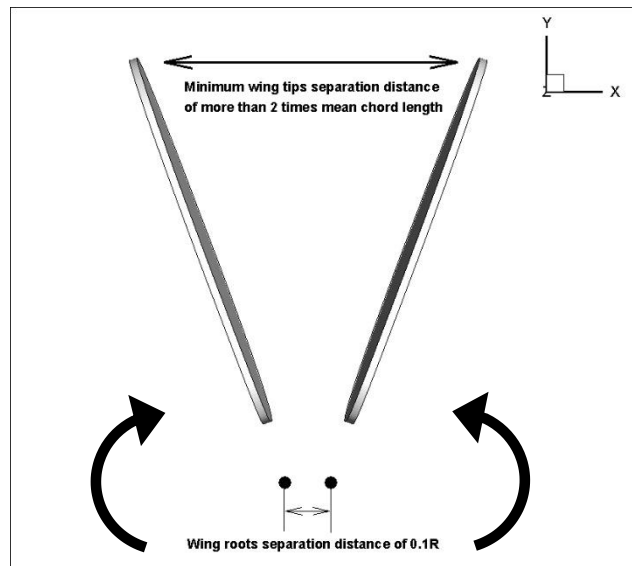


Figure 5.5 The top down view showing the minimum wing tips separation distance of the symmetric sweep reference kinematics of flapping wings

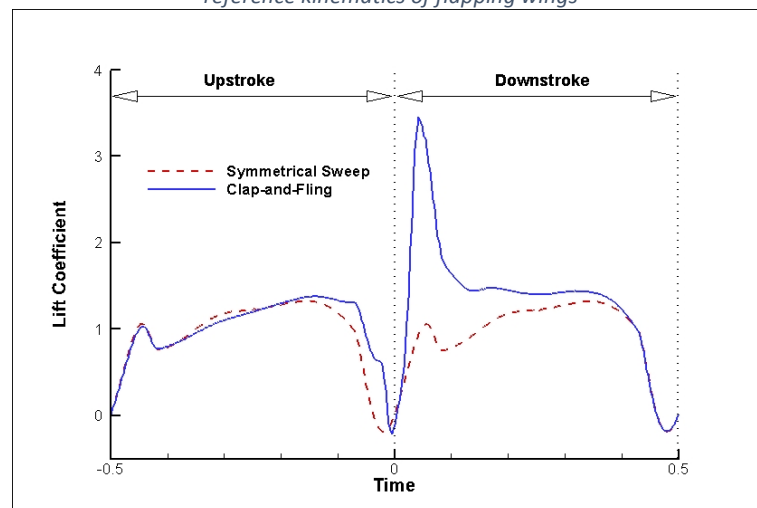


Figure 5.6 Comparison of lift coefficient throughout one wing beat cycle between the symmetrical sweep reference case and the clap-and-fling case

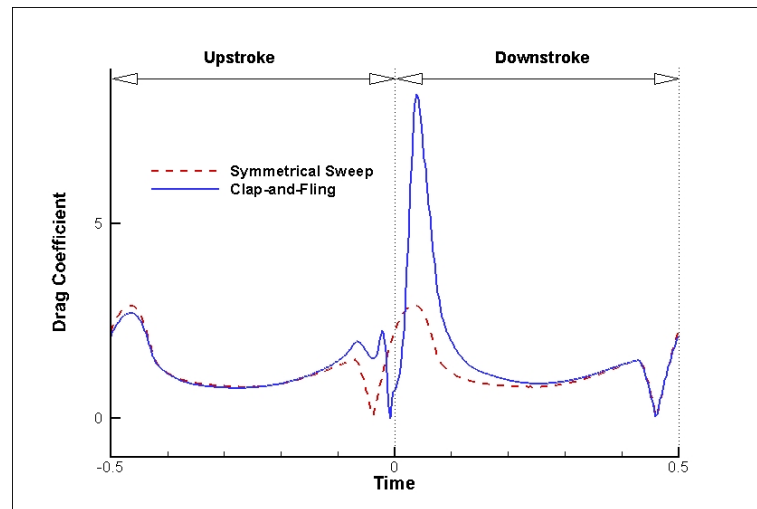


Figure 5.7 Comparison of drag coefficient throughout one wing beat cycle between the symmetrical sweep reference and the clap-and-fling case

The aerodynamic forces generated are captured on the left wing only and the lift coefficients and drag coefficients are compared between the reference case and the actual clap-and-fling case in Figure 5.6 and Figure 5.7. The curves are plotted against fraction time of a wing beat cycle in which  $t = 0$  is defined as the time for the beginning of downstroke and also the time at which physical clap occurs. The time axis is shifted by -0.5 in order to show the transition from the clap (towards the end of upstroke) to the fling phase (marking the beginning of the downstroke).

In the force coefficient plots, it clearly shows two lift peaks generated and the corresponding drag peaks produced just before the clap and after the onset of fling. This agrees well with the theoretical understandings of clap-and-fling mechanisms presented in earlier works by Weis-Fogh and Lighthill (Lighthill, 1973; Weis-Fogh, 1973). In particular the lift peak produced in the initial fling phase is estimated to be 3.5 times more than the symmetric reference case and the augmentation of lift is extended beyond the fling phase into the downstroke, which matches the observation of experimental works by Lehmann et al. (Lehmann et al., 2005). It can also be seen that, in the current study, no distinct lift peaks due to rapid wing twisting is observed during the fling phase of wing flapping motion. This is different from the observation of two dimensional numerical studies by Miller et al. (L. A. Miller & Peskin, 2005). This is expected as the current kinematic model used in this study has a much longer and wing twisting phase than translational acceleration phase, which prevents the observation of a distinct lift peak due to rapid wing rotation (twisting).

The mean lift and drag coefficients over one wing beat cycle are calculated and



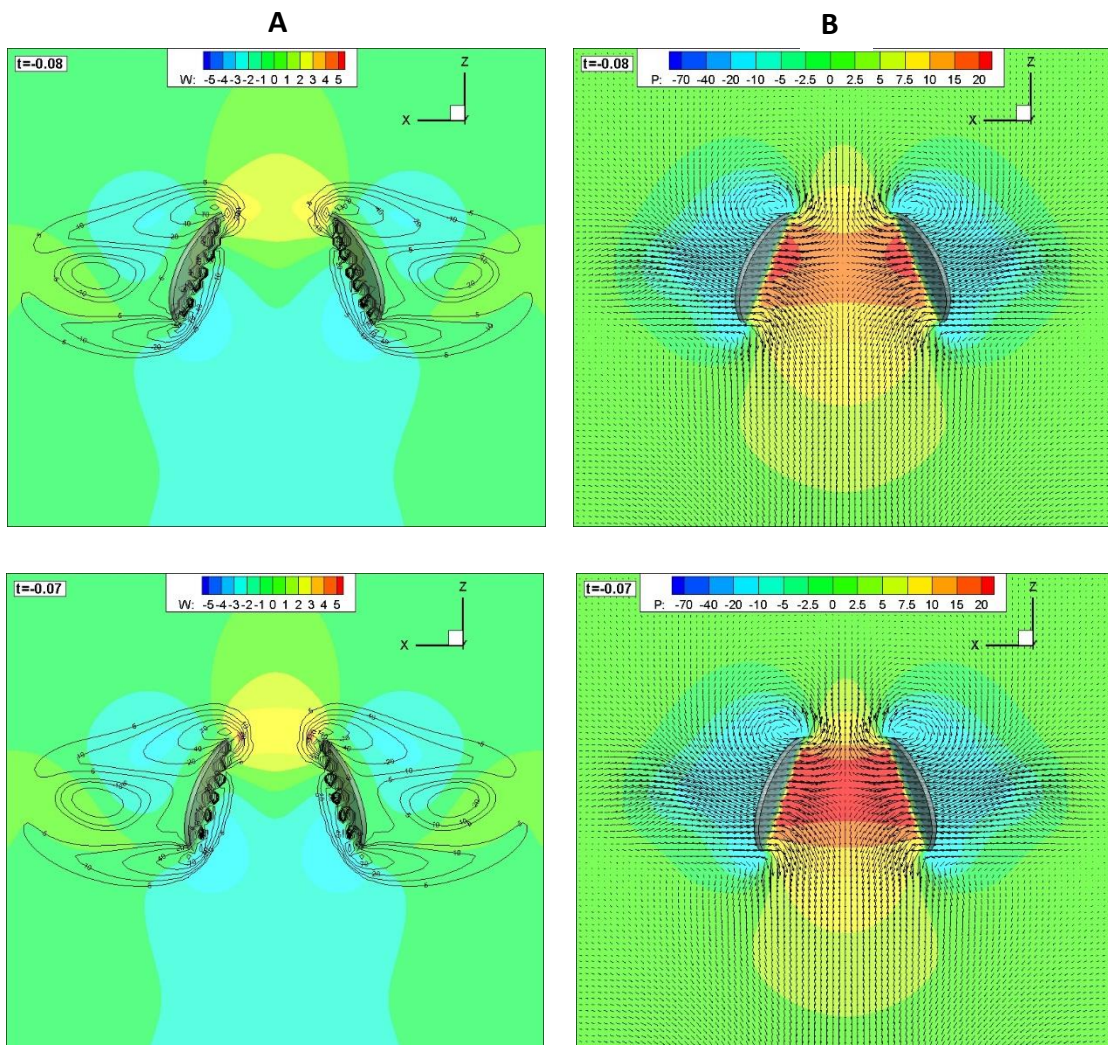
the fractional augmentation lift of 25% and fractional increase of drag of 22% are obtained. This is slightly higher than the measured mean lift coefficient increase of 7% and drag coefficient increase of about 7% from the experimental work by Lehman et al. (Lehmann et al., 2005). There are however three possible explanations. Firstly, the wing roots separation is estimated to be approximately 2 times wider in the experimental case, which in the current study (section 5.5) has shown that the overall lift augmentation of the clap-and-fling mechanism is affected by the wing roots separations. Secondly, the experimental work uses a different kinematic model from the current numerical simulations in which the aerodynamic force generation by insect fling is dependent on the duration of wing twisting such that the longer duration of wing twisting with the same minimum angle of attack the higher the percentage augmentation of measured lift, verified by the experimental results (Lehmann et al., 2005). Lastly, the maximum sweep amplitude in the current numerical simulation is based on the known hovering maximum sweep angle of *Drosophila Melanogaster* which is  $140^\circ$ , whereas in the experimental work,  $160^\circ$  was used. This could potentially affect the wing wake interaction of the insect wings during the majority of the downstroke translation phase which shows a continued lift augmentation in the numerical result.

### **5.3.2 3D Aerodynamic Aspects of Clap**

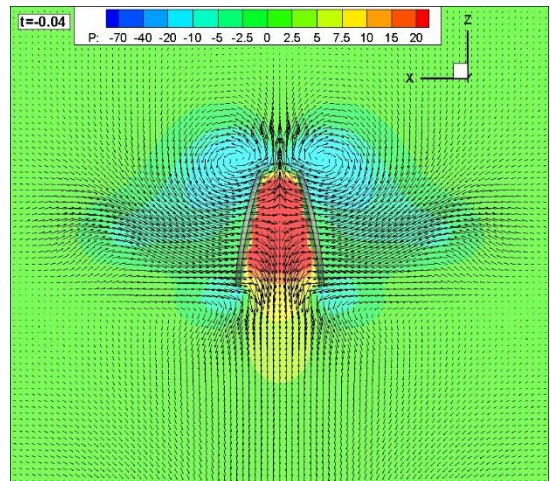
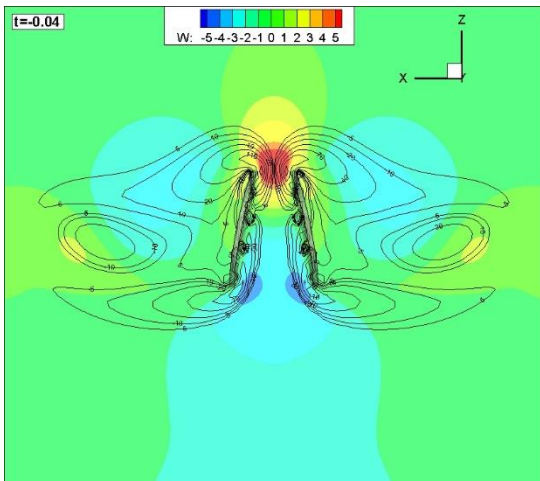
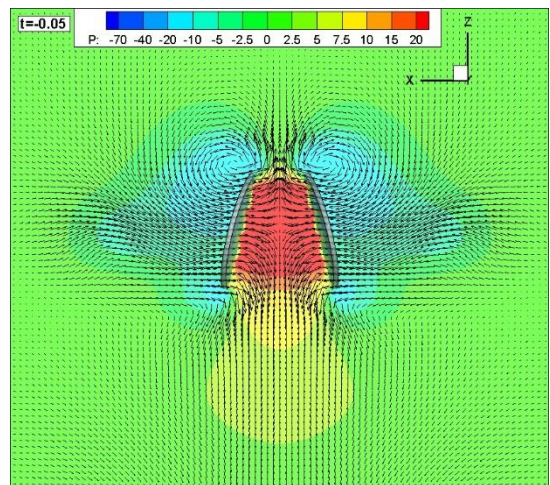
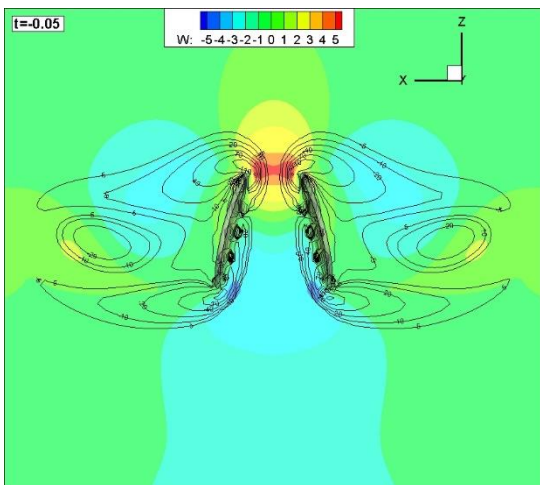
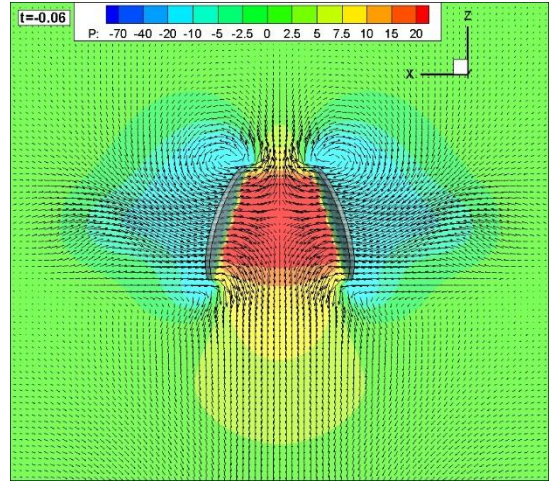
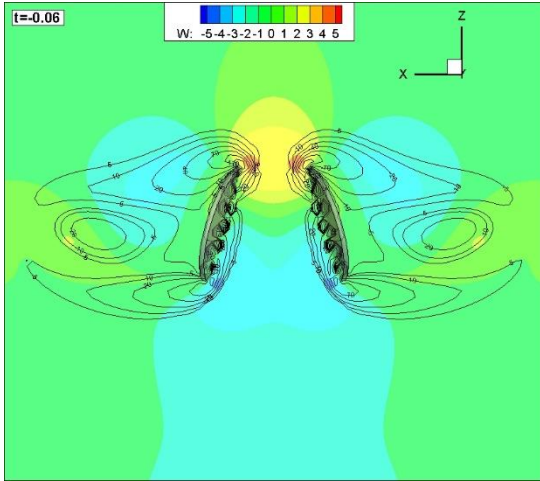
The effect of clap has been argued as not just a process to initiate the fling mechanism but at the same time producing additional lift force due to the two dimensional effects of the wing “squeezing” air out of the inverted “v-shape” opening causing a momentum jet downwards (Götz, 1987). This has also been shown in two dimensional studies to provide lift force augmentation just before the wings clap and the wing surfaces touch each other (Kolomenskiy et al., 2011a). However, in experimental studies, the effect of clap has been shown to attenuate aerodynamic force production and little or no lift peaks are observed in association with the clap mechanism (Lehmann et al., 2005).

In the current study, the evolution of the flow associated with the clap phenomenon in three dimensions will be presented and analysed to possibly explain the significantly reduced lift force enhancement effect of clap in contrast to 2D observations. In Figure 5.6, slight lift enhancement can be observed in the form of delayed lift fall-off just before the onset of physical clap of the wings.

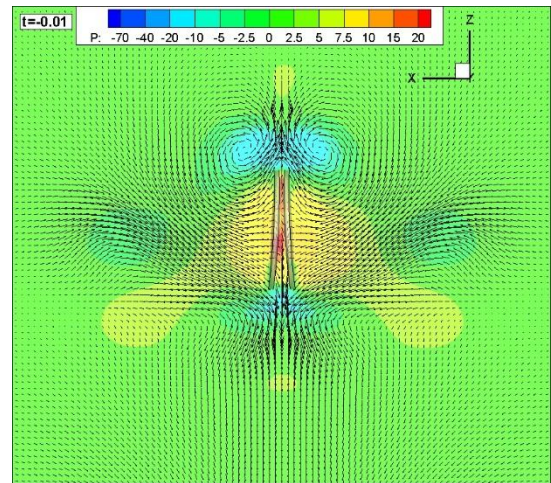
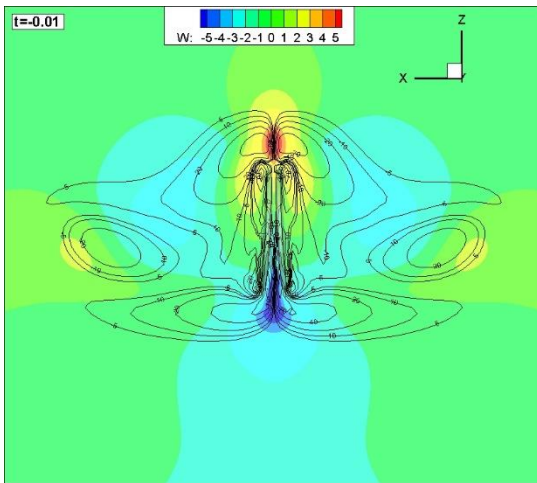
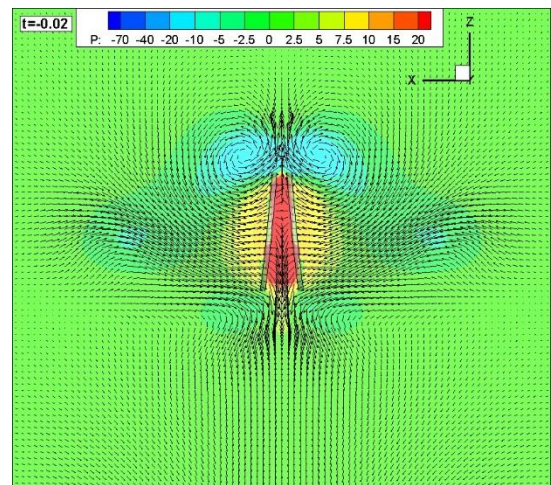
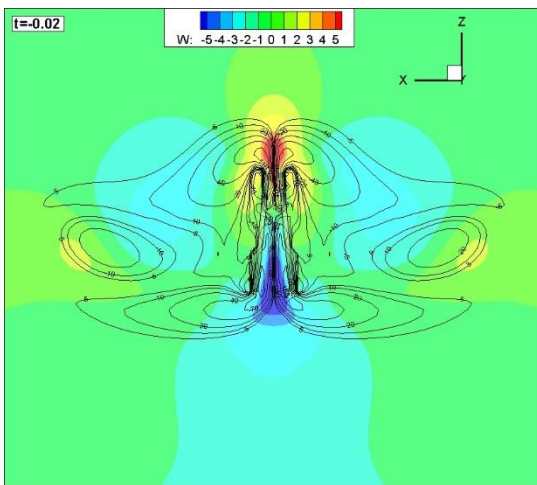
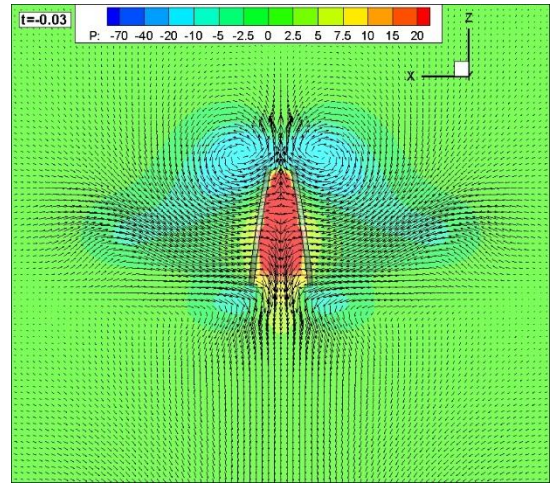
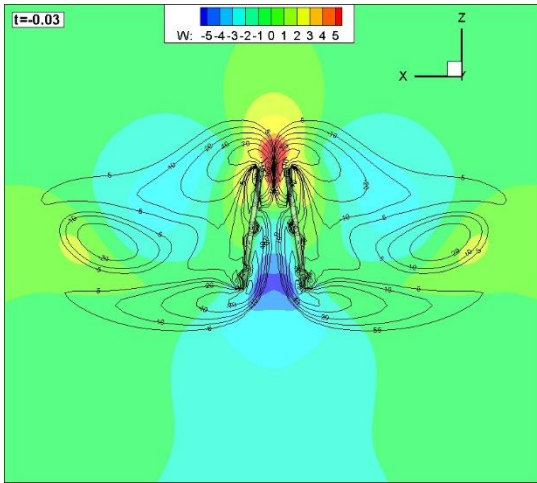
The changing flow field in the plane normal to y-axis (centre symmetry axis in between the wing pair) at about three quarter wing section measured from the wing root of the flapping wings are extracted and presented in Figure 5.8. The flow field sequence covers from  $t = -0.08$  before the onset of clap to  $t = 0.13$  after the completion of the fling phase. The side by side plot in Figure 5.8 show the colour contour of vertical velocity  $W$  in the plane (A) and pressure field at the same point (B) and the contour lines represent the Y vorticity illustrating the evolution of LEV, TEV and the shed vortices during the onset of clap (A), the arrows in (B) represent the in plane velocity vectors. The time  $t$  indicate the non-dimensional time within a wing beat cycle and the  $t = 0$  is set as the time of wing physical clap in the present case



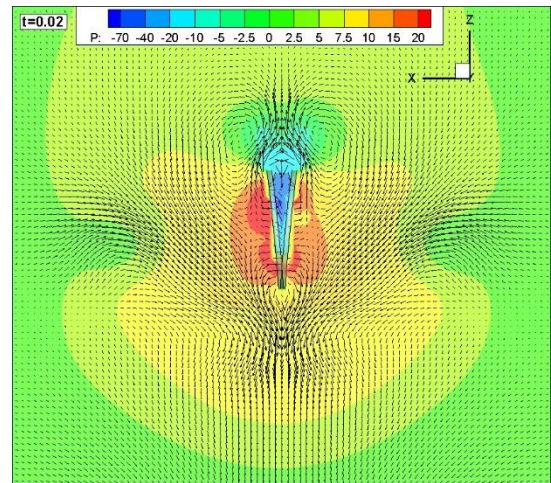
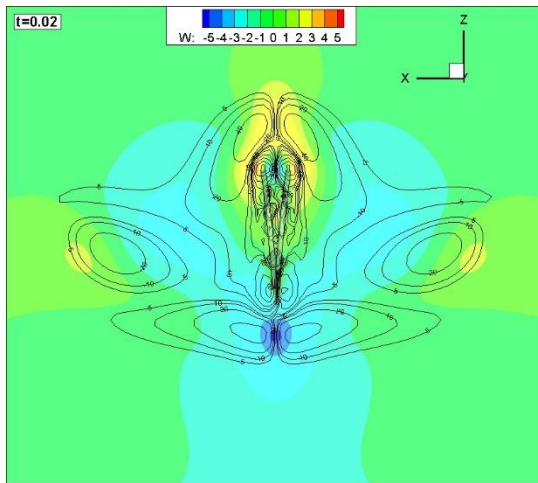
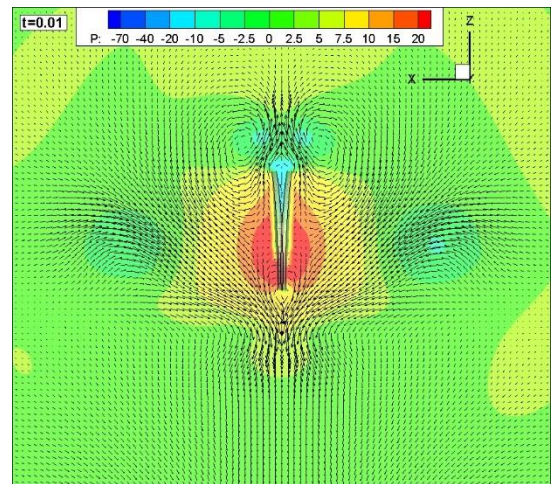
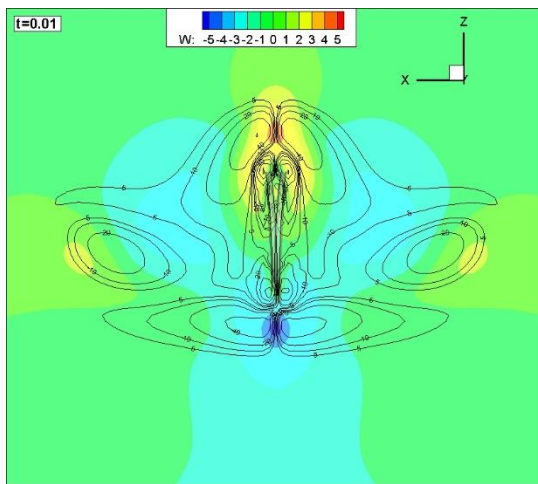
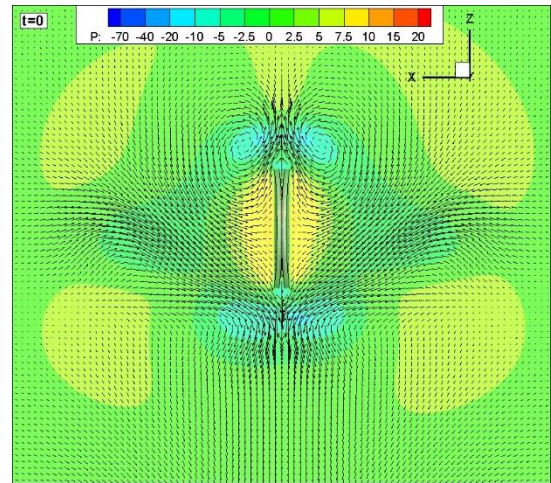
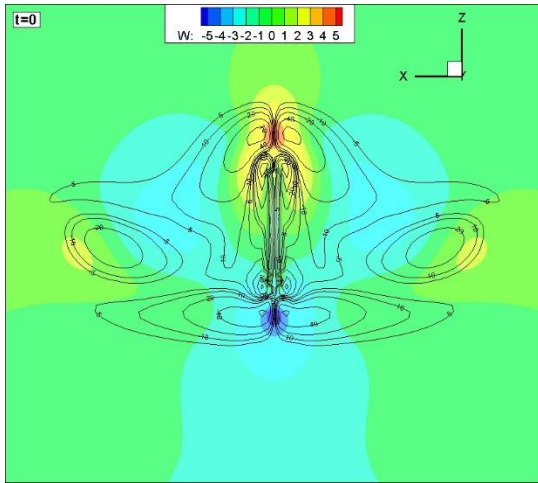




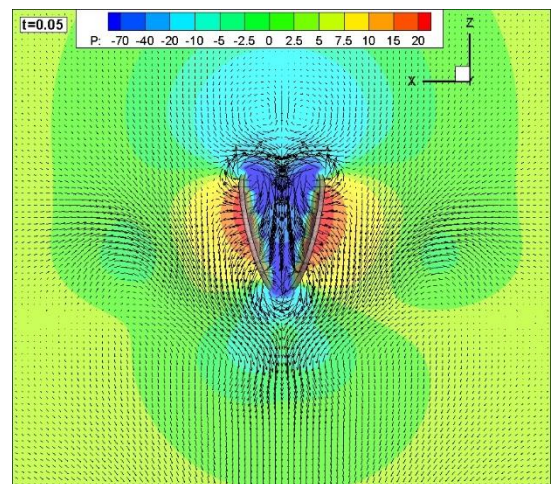
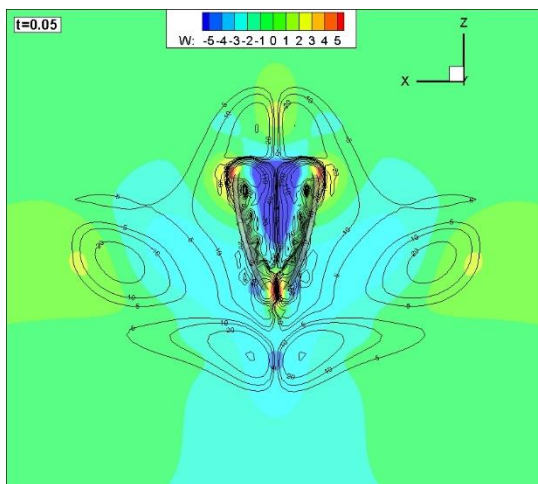
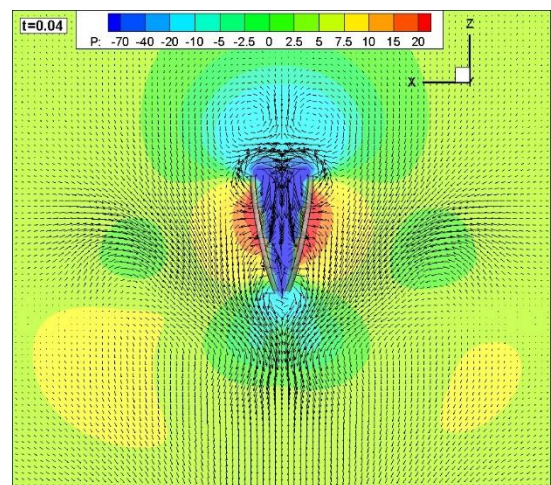
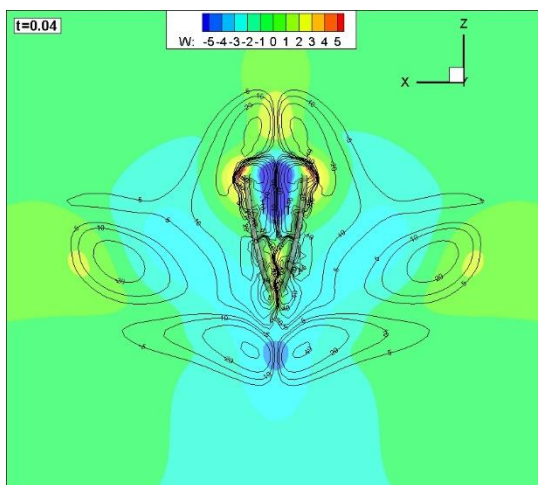
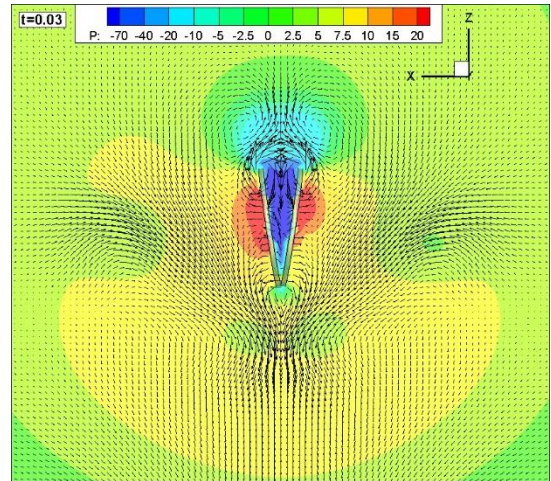
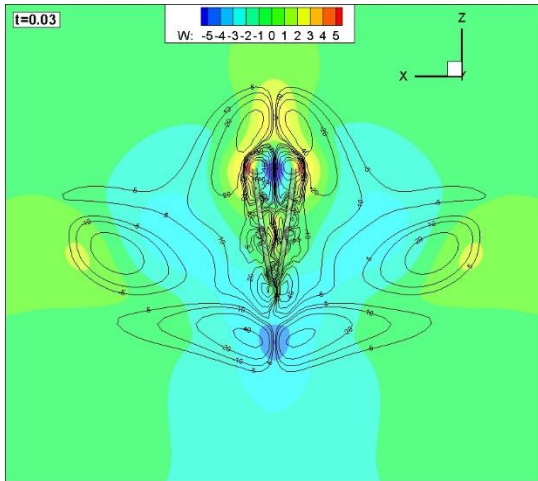




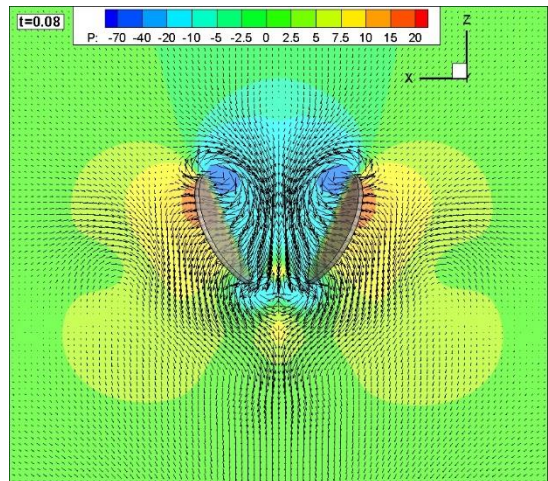
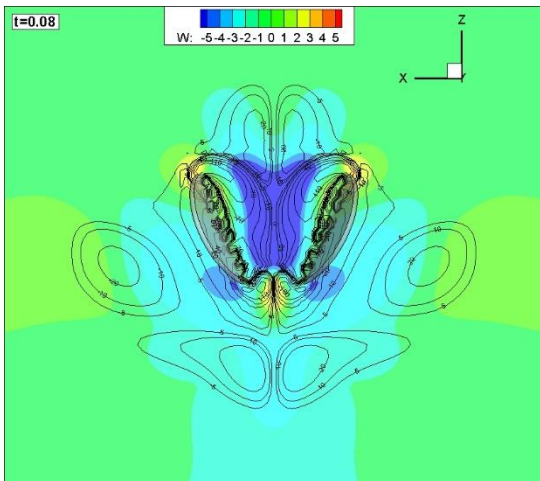
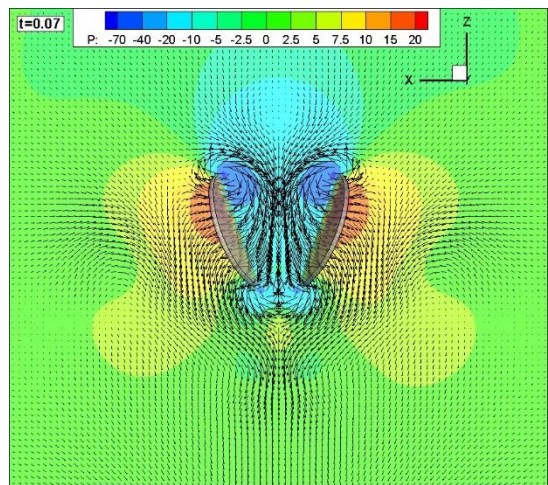
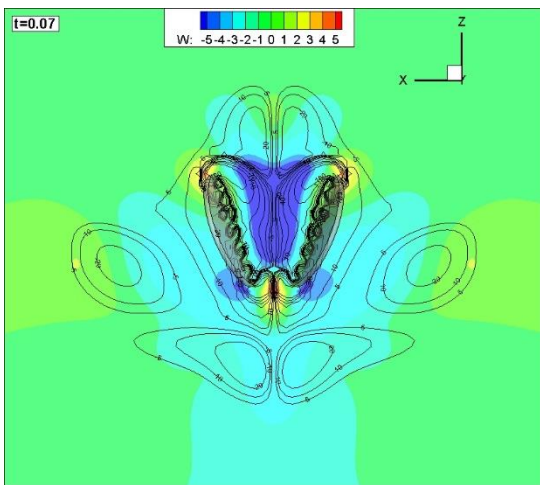
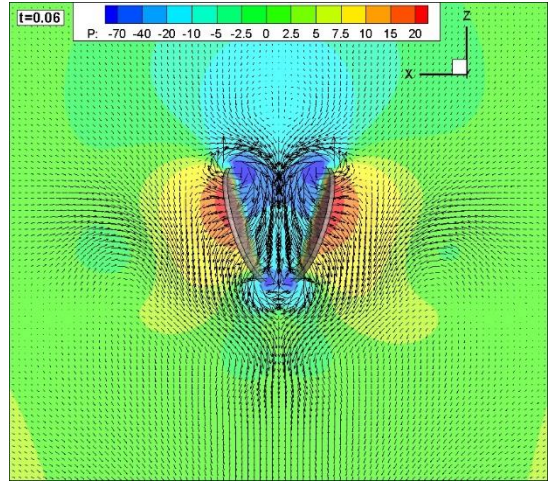
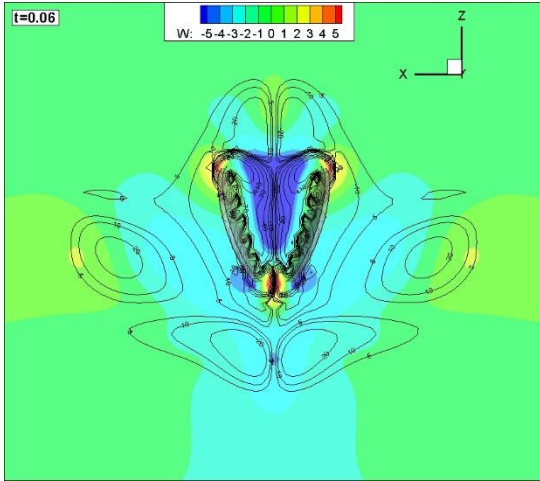




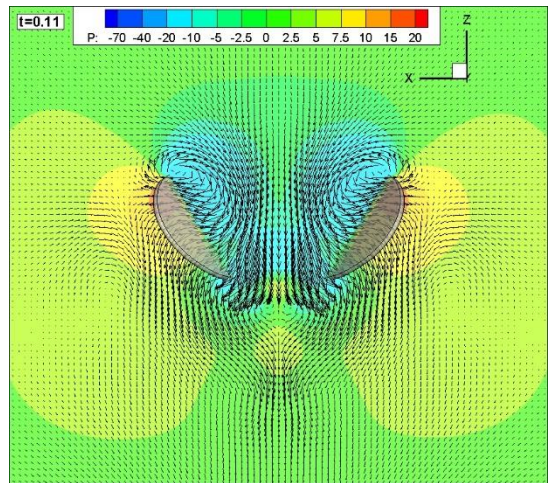
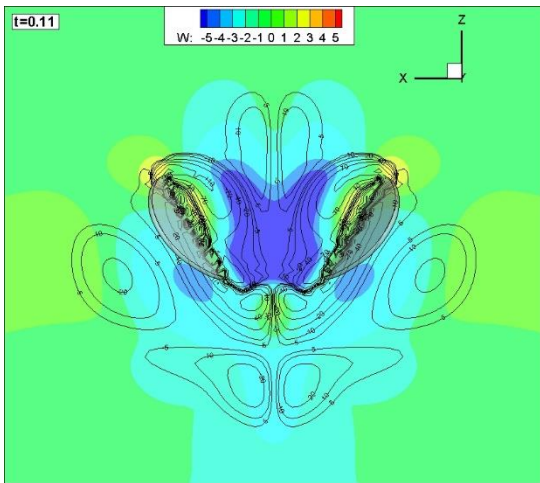
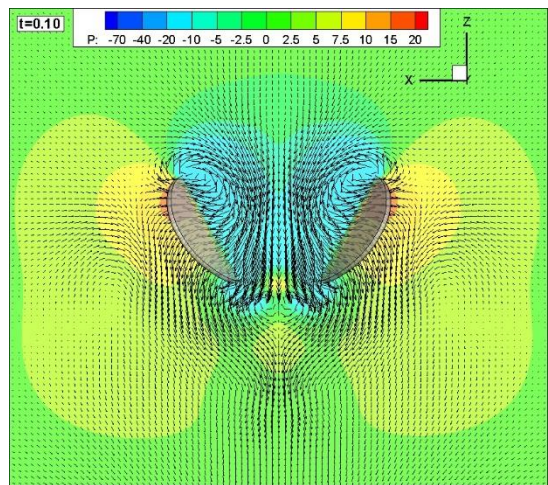
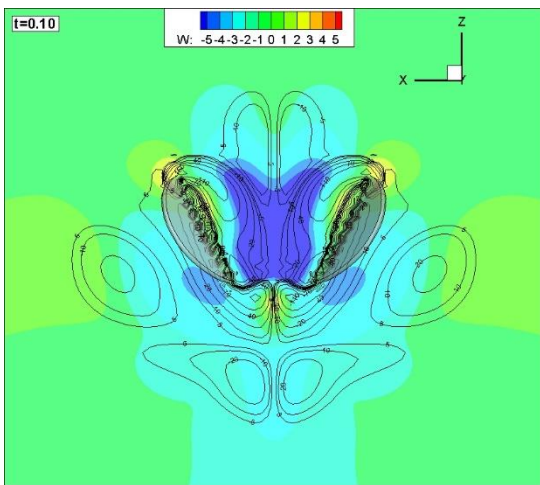
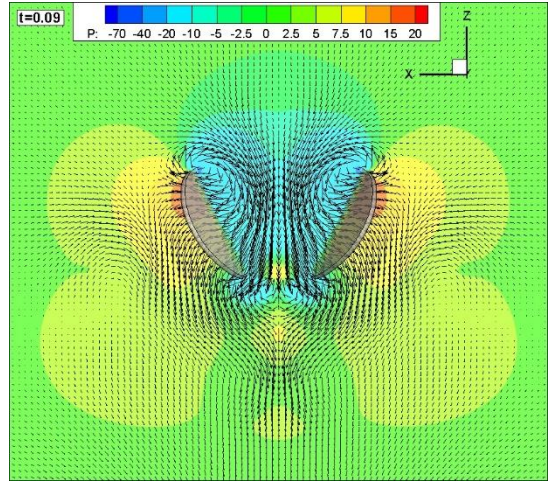
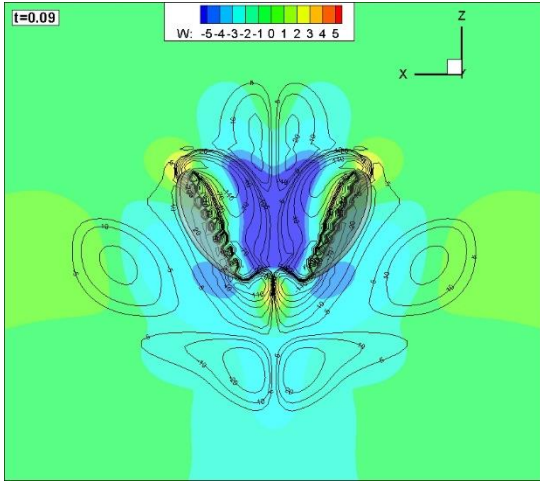














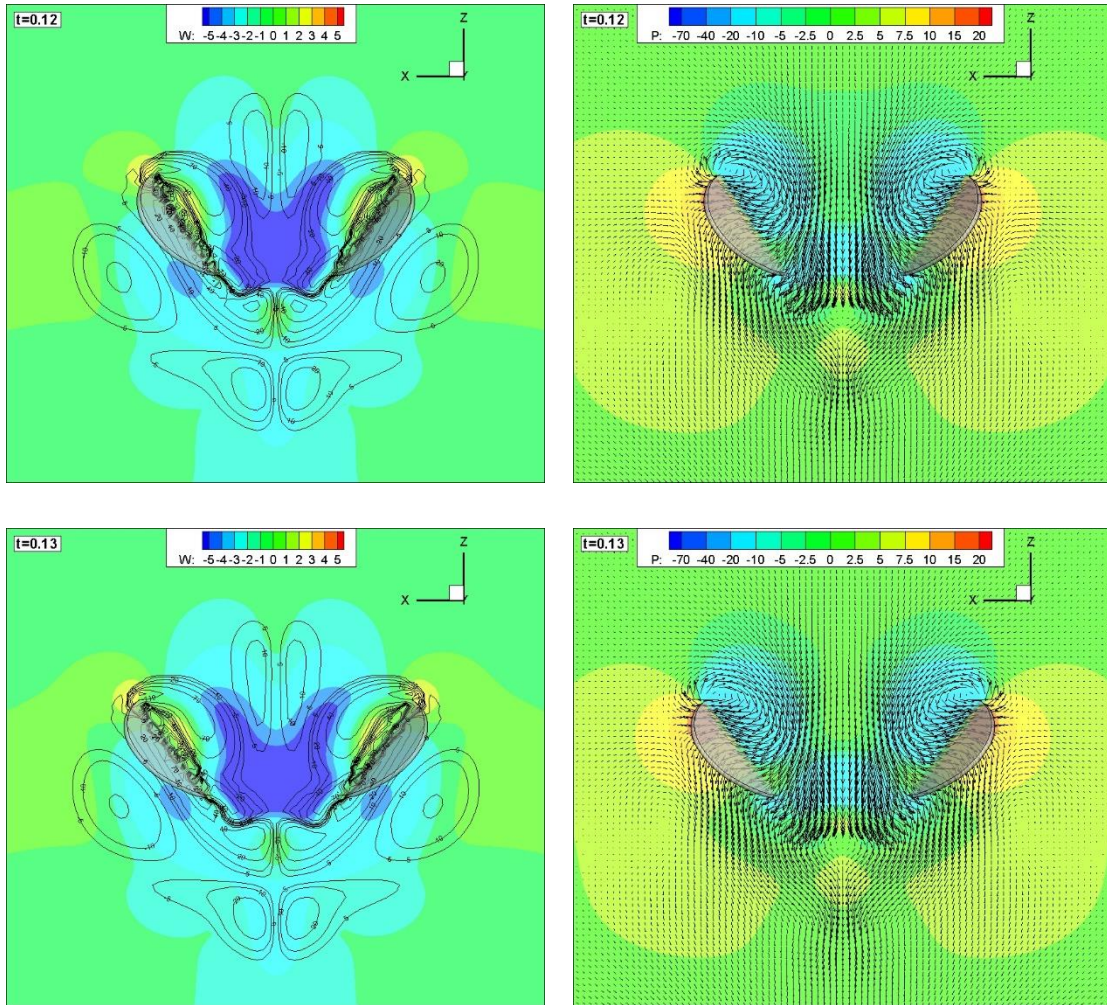


Figure 5.8 X-Z plane view (normal to y-axis) at about the  $\frac{3}{4}$  span of the fruit fly wing from wing roots showing the LEV and TEV and the downward velocity of fluid around the wing (A) and the pressure contour, the velocity vector (B) induced during clap-and-fling flapping motion

It can be observed from Figure 5.8 that the Leading Edge Vortex (LEV) generated by the wings' translation (sweep) persisted as the wings approach each other towards the end of the upstroke ( $t = -0.08$  to  $t = -0.06$ ). The LEVs of the two wings, together with the pressure build-up in the gap in between the wings, induce an upward flow which gain the appearance of an upward jet at  $t = -0.06$ . Simultaneously, the squeezing effect of the approaching wings and the their twisting motion begins to produce a downward jet, although this jet appears relatively weak at this point of time. The two jets (up and down) appear to be accelerated with the further approaching of the two wings, ( $t = -0.05$  to  $t = -0.01$ ) culminating in the extreme magnitude at time  $t = 0$ , when the wings physically clap at the wing tip. The upward jet appears to be more energetic than the downward jet. The LEVs remain attached along the wing leading edges until  $t = -0.04$ . Thereafter, they show regions of detachment and becomes part of the upward jet system. Although, there is reduced pressure in the LEVs,

they exert little influence on lift because of the nearly vertical orientation of the wing surfaces at this time. Hence, the lift drops to near zero at the point of clap. From the above, the LEVs appear to play an important role in motivating and influencing the development of the upwards jet, that undoubtedly would have an adverse effect on lift. Furthermore, the downward jet only becomes significant when the wings are in very close proximity and the squeezed volume of air is significantly small.

On the other hand, before the wings physically clap, the wings sweep motion decelerates and the wings gradually touches along the leading edges towards the end of the upstroke. Simultaneously, twisting of the wings take place and squeezes the gap in between the wing surfaces. However, due to the three dimensional nature of the wing sweep motion, the wing leading edges nearer to the wing tip section remains open until the physical clap at  $t = 0$  and allow air to exit the gap through the opening in three directions simultaneously (upwards, downwards and outwards). Hence it results in a cancellation effect of the overall momentum of air exiting the gap between the wings and the net lift generated due to the clap motion by causing a downwards momentum jet is diminished. This shows significant difference from the two dimensional analysis mentioned earlier (Götz, 1987). On the other hand, if a modified mechanism is adopted by the insect, such as clap-pause-fling mechanism explored theoretically by Ellington (Ellington, 1984) and experimentally by Sohn et al. (Sohn & Chang, 2007), the effectiveness of momentum jet may be maximised.

From Figure 5.6, a slight lift gain can be observed just before the physical clap of the wings. This is due to the high pressure build up in between the wings as the wings get into extremely close proximity, shown at  $t = -0.03$  and the slight deviation of twisting angles of the wings from the vertical orientation that results in a small net vertical pressure force acting upwards on the wing. Such effect could delay the lift drop off just before the end of the upstroke as compared to the symmetric reference case.

Furthermore, the clap could actually enhance lift generation in the ensuing fling phase of the wings, which has been observed in two dimensional studies at lower Reynolds numbers by Kolomenskiy (Kolomenskiy et al., 2011a). The three dimensional numerical result provides a possible explanation to this observation. The upward jet induced by the squeezing effect of the wings and the LEVs is further maintained by the shed LEVs and are kept energised in the close vicinity of the wings

can be seen at  $t = 0.01$ . As the wing starts to fling open, the low pressure created by the “v-shaped” gap in between the wings applies a suction effect on the flow near to the leading edges of the wings. At this instance, the region above the leading edges contains an upward jet that was induced during the previous clap motion. Due to this remaining upward momentum of the jet, stagnation is created initially just between the wing leading edges that prevented the suction flow and hence further reducing the pressure within the gap on the upper surface of the wings at the beginning of downstroke. This cause a surge of the lift force generated and hence a significantly higher lift peak observed immediately after fling in Figure 5.6. Further analysis of the effect of clap on fling is specifically studied in more detail by varying the relative duration of clap to fling in section 5.5.

### **5.3.3 3D Aerodynamic Aspects of Fling**

The aerodynamic effect of fling has been explored and explained both in two dimensional numerical and experimental analysis by various researchers (Kolomenskiy et al., 2011a; Lehmann et al., 2005; L. A. Miller & Peskin, 2005; Sun & Yu, 2003; Z. J. Wang et al., 2004). The main approach in most of the current theories lies in the interaction of leading edge vortices and the combined effect of enhanced circulation on the basis of a two dimensional analysis.

In this study, however, the author attempts to instead offer a new three dimensional approach in the analysis of the fling effect on aerodynamic lift generation by looking at the flow structure evolution from a different vantage point. As have been demonstrated in the earlier section, a realistic insect wing usually rotates about an axis near to the leading edge spar of the insect wings. This means that, in a viscous fluid, the initial twisting of the wings at the onset of the fling motion is constrained by the available room of rotation and thus contributes in a very limited way to the vorticity build up along the leading edge of the wings. Instead, the leading edge vortices are generated mainly due to the wing sweep (translational motion of the wing) from each other, which is a function of the distance of the wing section away from wing root where the centre of rotation for sweep is. Therefore, the vortex strength is highest along the wing tip region instead of the wing leading edge as shown in Figure 5.9. It shows the computed vorticity magnitude iso-surface contour in the flow field next to the wing edges in the

fling motion at  $t = 0.04$  after clap. This particular fraction time of a wing beat cycle is chosen, because it is observed from the lift coefficient plot in Figure 5.6 that the computed lift peak corresponds to it.

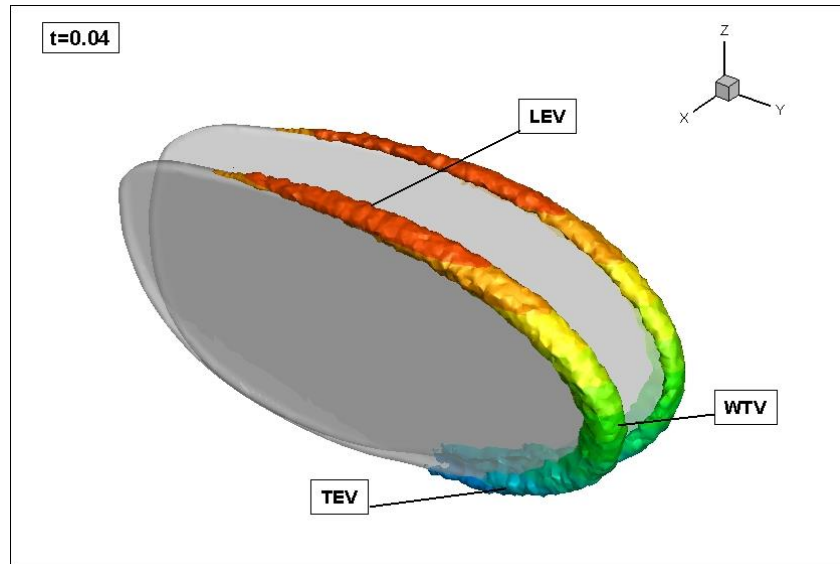
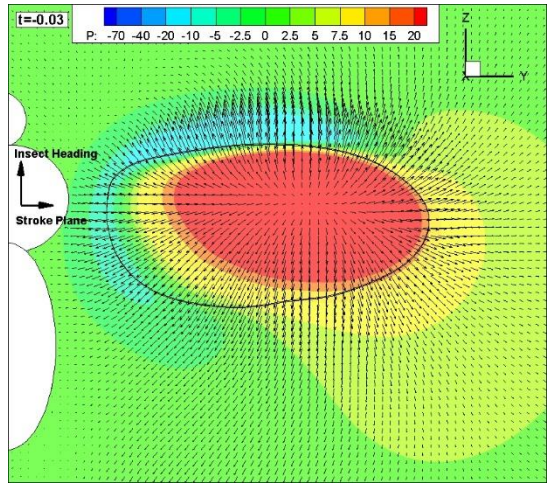
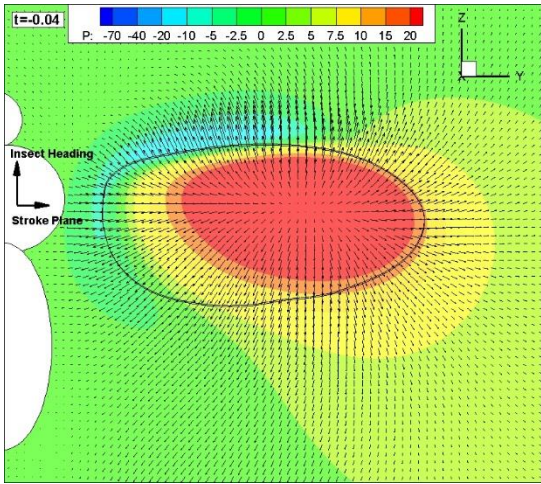
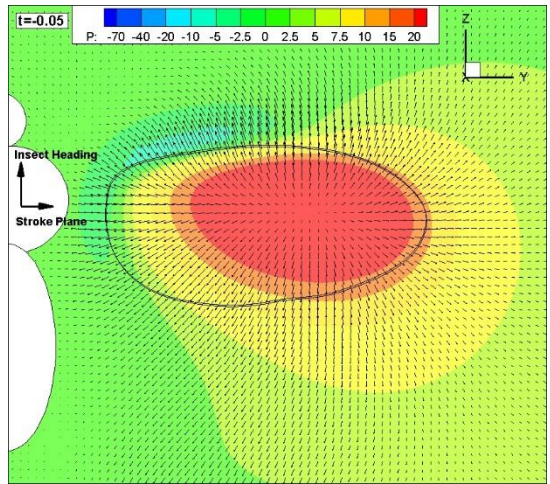
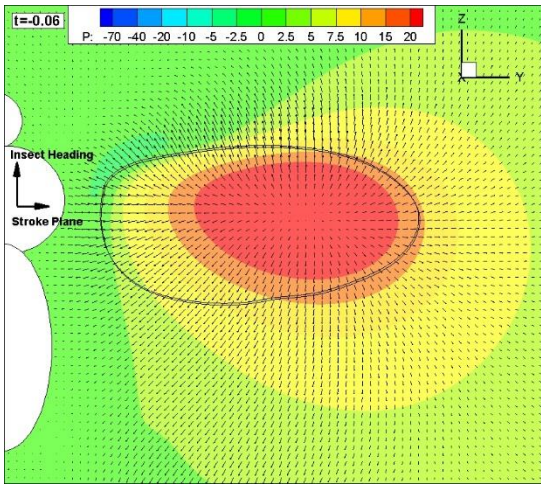
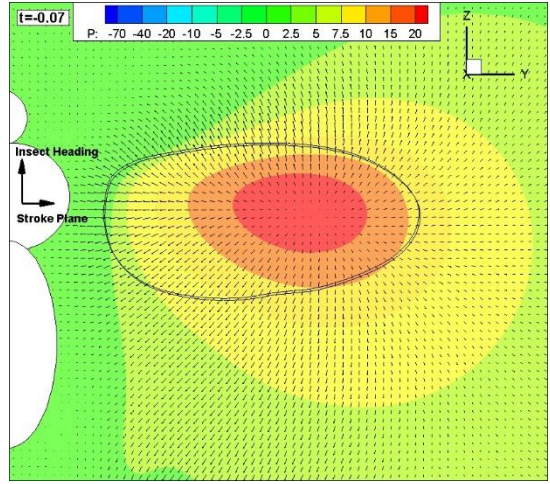
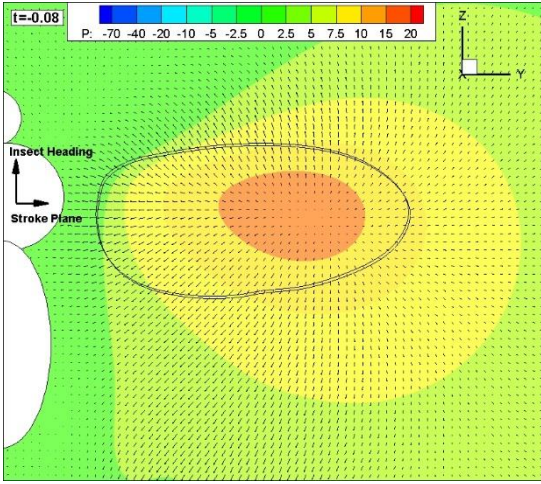


Figure 5.9 Vorticity magnitude iso-surface in the flow field close to the wing edge showing a generally higher vortex strength wing tip vortex (WTV) and relatively weaker leading edge vortex (LEV) and trailing edge vortex (TEV)

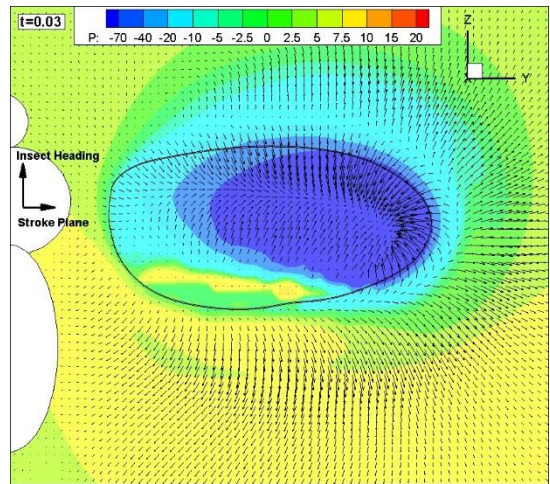
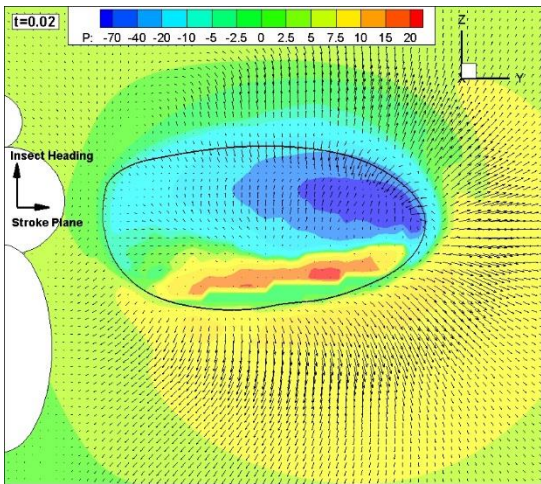
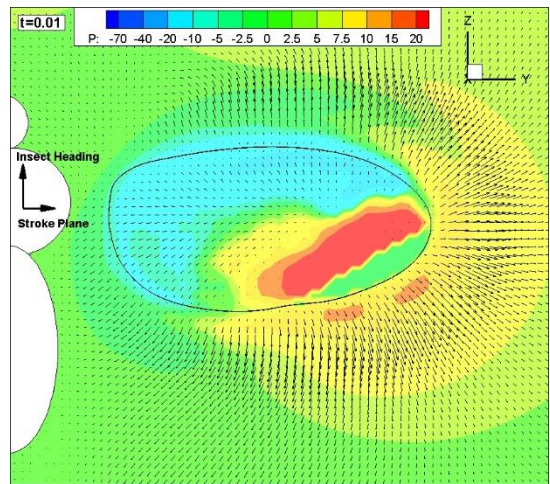
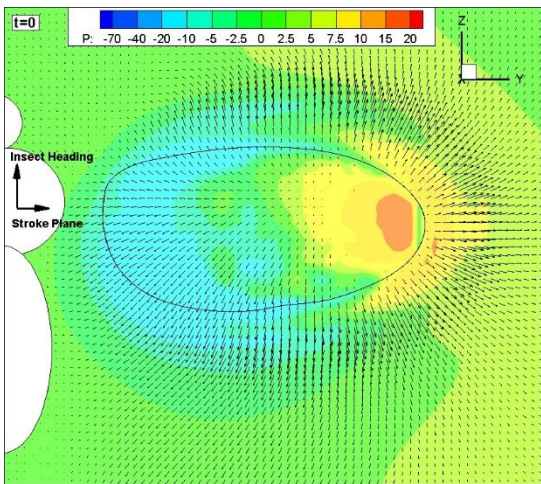
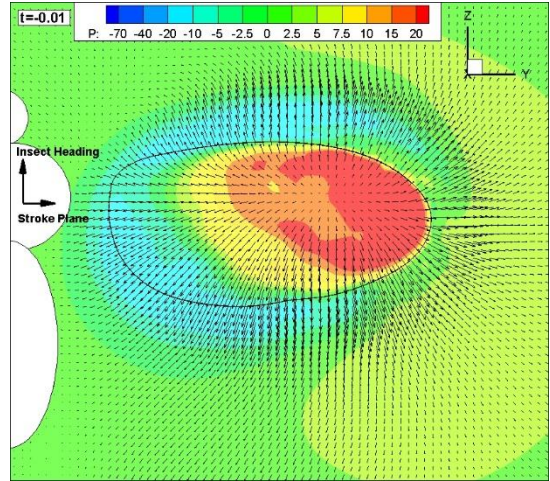
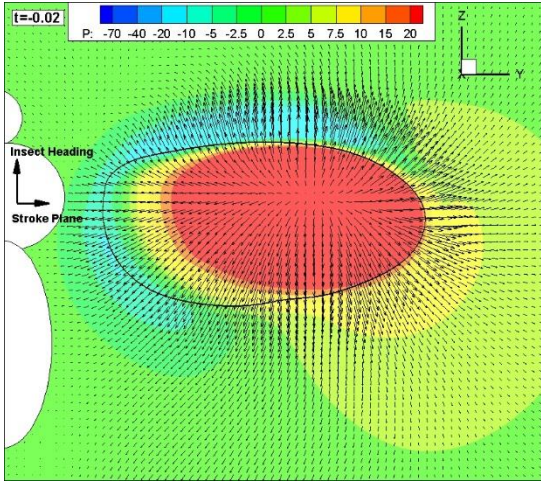
It can also be seen in Figure 5.9 that due to the three dimensionality of the wings and the rotational nature of the sweep, a strong trailing edge vortex is formed near to the wing tip section as the trailing edges there were rapidly separating due to the wing sweep motion. It may be possible that if the wings were flexible, this build-up of trailing edge vortices may be delayed and further enhancement of lift generation of the wings in fling motion may be achieved. Studies of three dimensional clap-and-fling with flexible wings may be conducted in the future to verify this hypothesis. Hence, the effect of the leading edge vortex interaction at the beginning of the fling motion may not be the prominent contribution to the observed lift peak, other unsteady aerodynamic effects should be explored.

With the benefit of three dimensional numerical simulation of the wings in clap-and-fling, full flow field information is accessible. Flows in the Y-Z plane between the wings are shown in Figure 5.10. They give further insight into the flow between the two wings during the clap-and-fling motion. Figure 5.10 provides sequential view of the pressure field contour and the velocity vector in the Y-Z plane throughout the clap-and-fling motion.

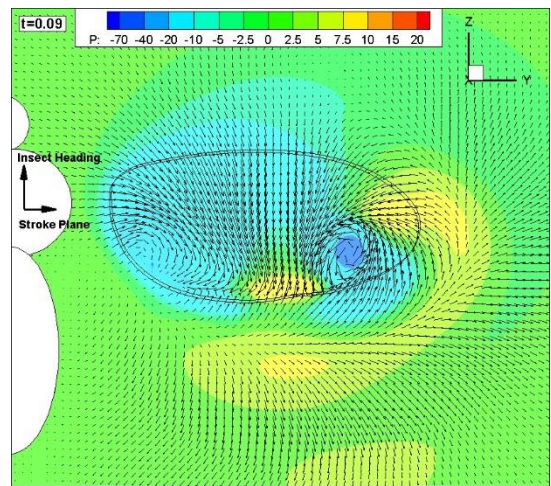
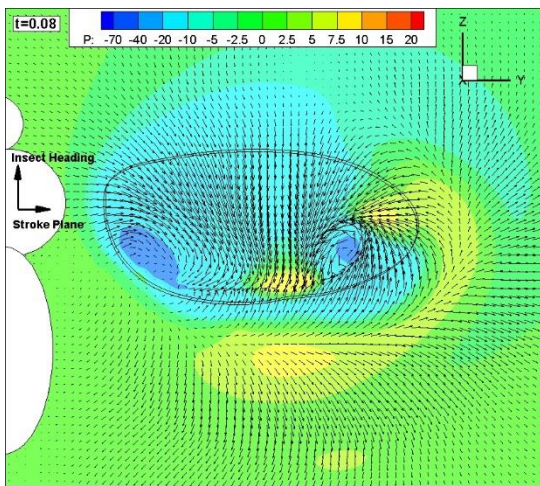
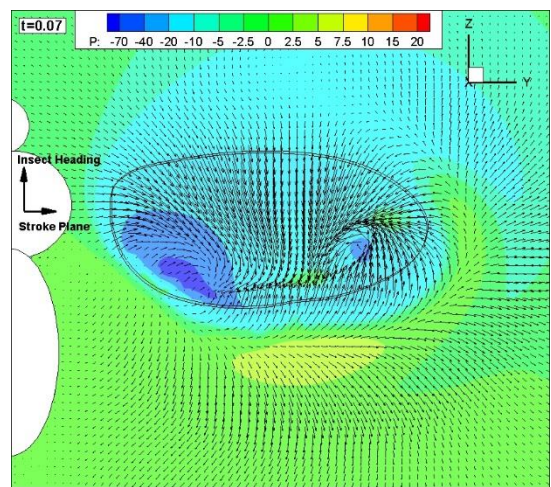
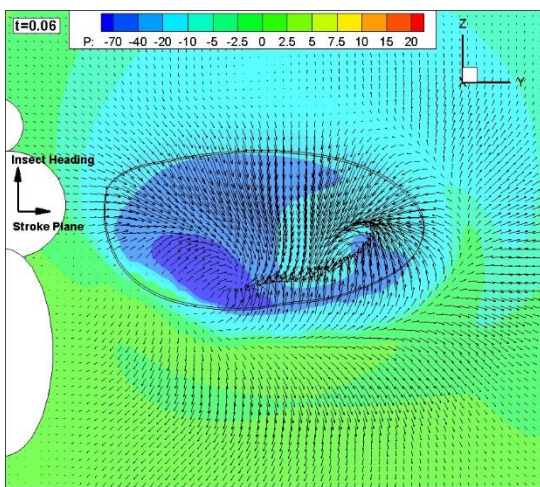
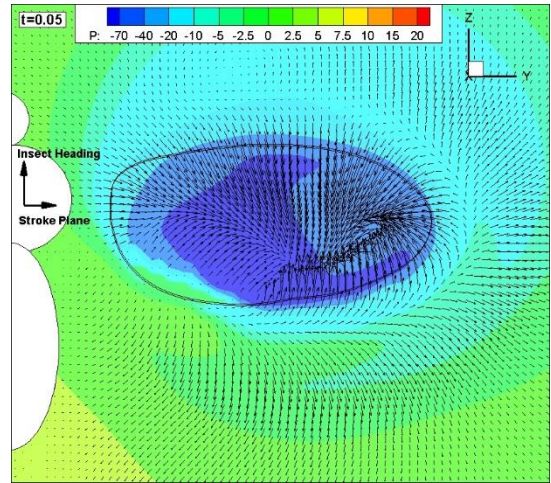
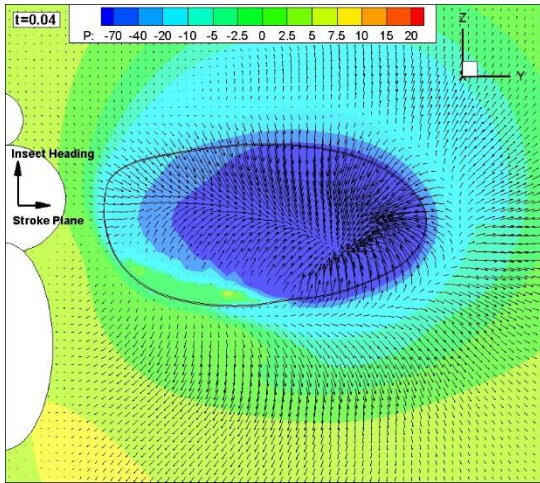




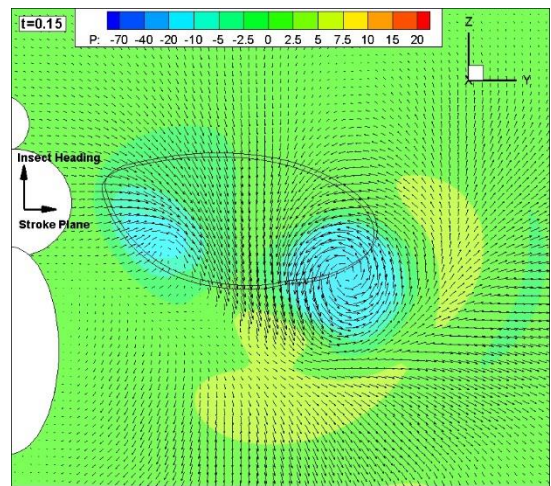
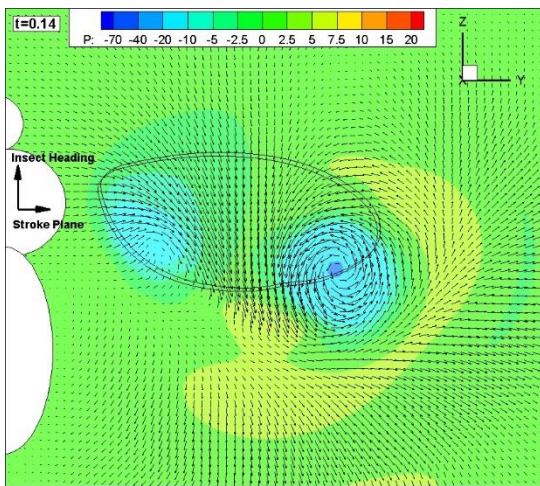
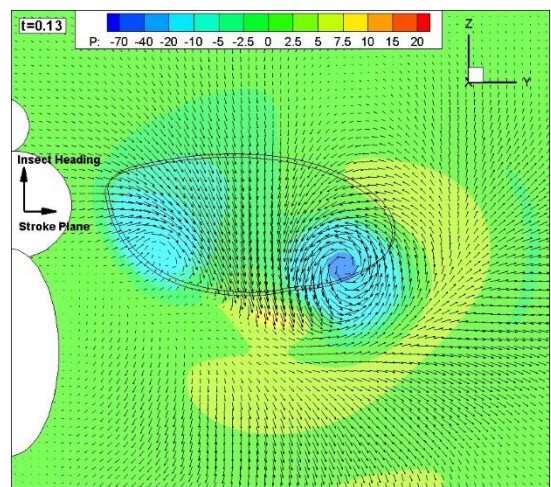
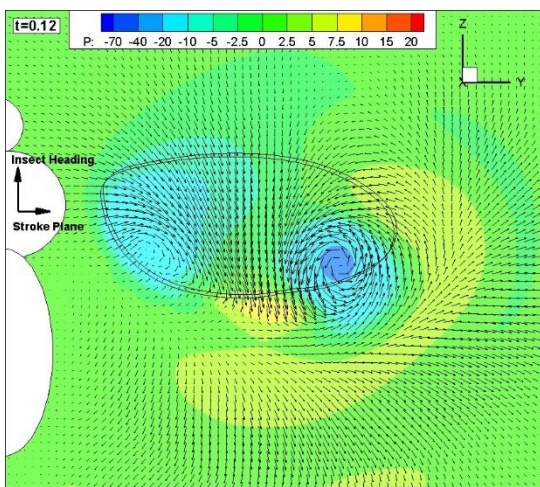
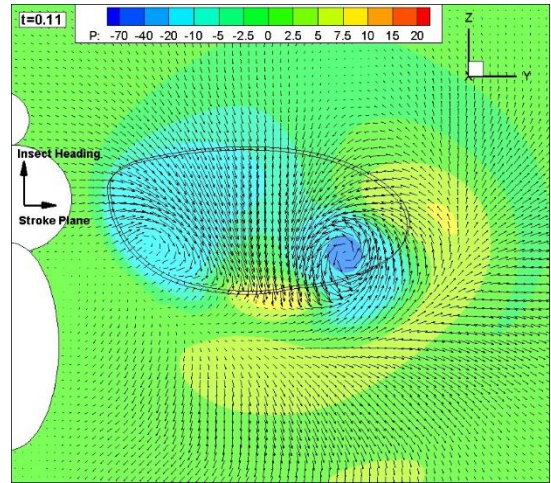
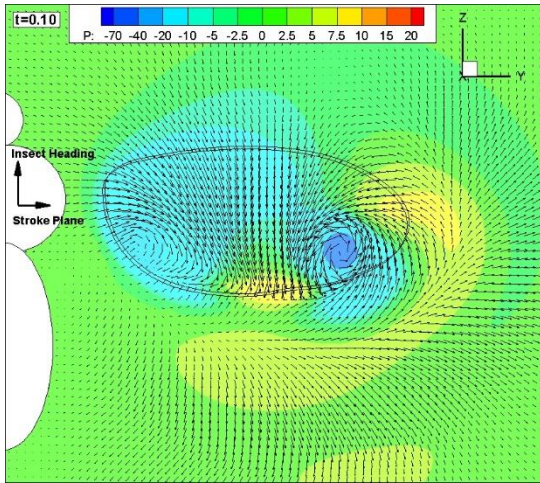














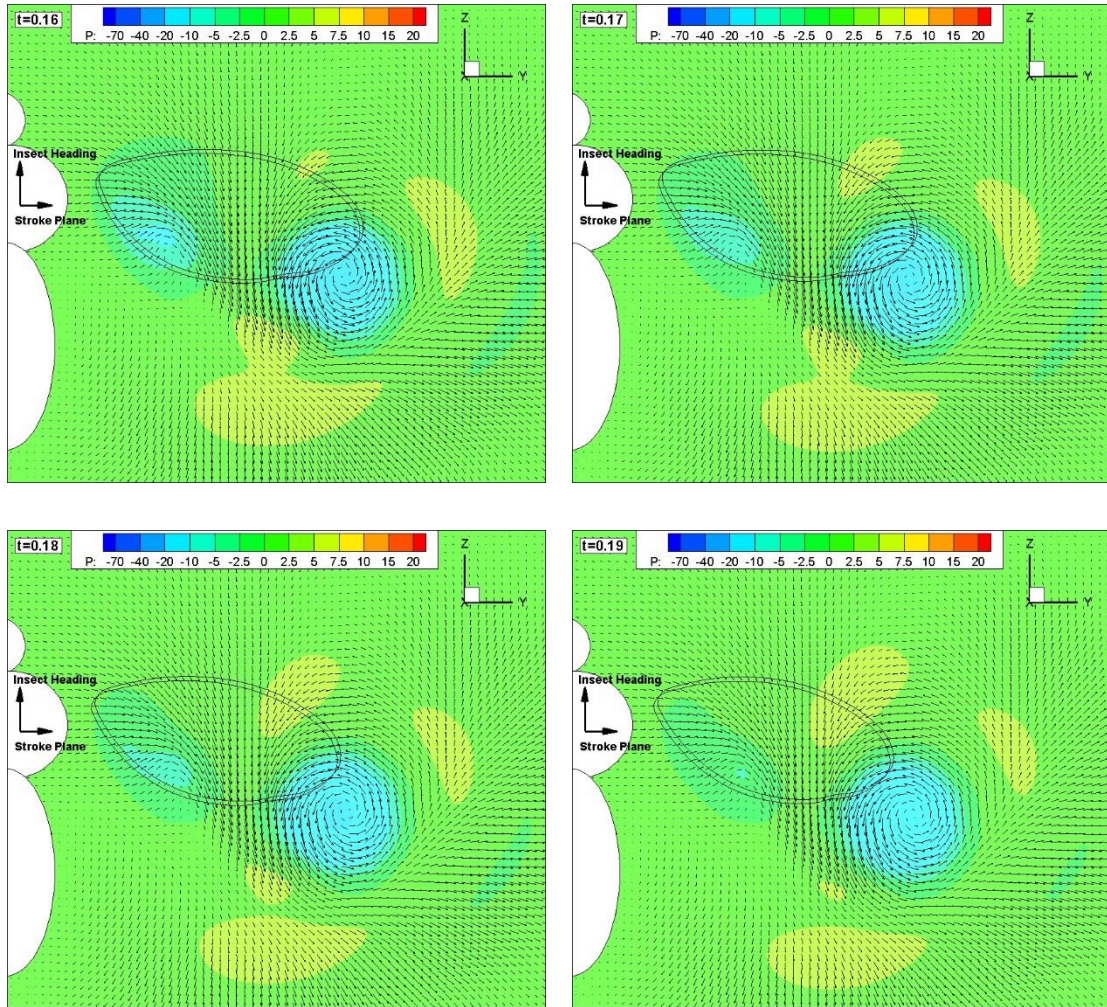


Figure 5.10 Y-Z plane view of pressure contour and velocity vector in between the wing pair during clap-and-fling motion

A few observations can be made from Figure 5.10. The coming together of the wings during the clap process from  $t = -0.08$  to  $t = 0$  shows a simple diverging flow field, which is consistent with the compression of the fluid during clap. Flow leaves the centre of Y-Z plane practically in all directions, with a stagnation point near to the  $\frac{2}{3}$  section of the wing, forming upwards flow and downwards flow as observed. This is consistent with the jet we learnt earlier from Figure 5.8. High pressure is observed near the wing tip region at  $t = -0.01$  to  $t = 0$  as the physical contact of the wings happens at  $t = 0$ . The high pressure near to the wing tip region gives way to a strong negative pressure as the wing surfaces start to separate in the beginning stages of the fling ( $t = 0.01$  to  $t = 0.03$ ). The negative pressure region grows to dominate the wing tip region and is biased towards the leading edge due to that the trailing edges are still closed at this moment.

The flow field in the Y-Z plane tells an interesting story. In the initial stage of fling,





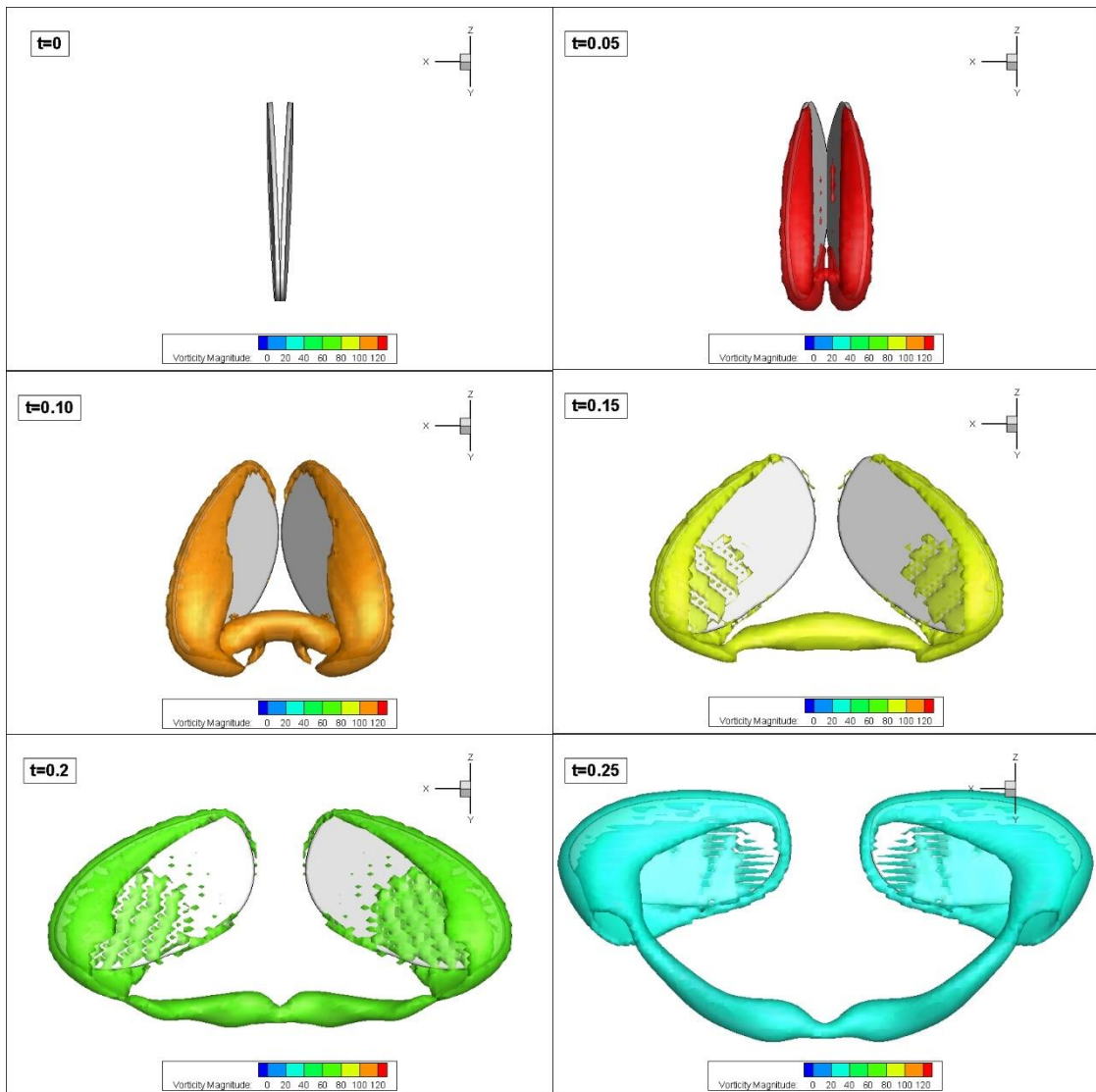


Figure 5.12 Three dimensional iso-vorticity surface plot showing the vortex link between the wings formed during fling phase persists further into downstroke

The vortex connection across the wing helps to drive the downwash jet and its existence due to the fling mechanism persists beyond the fling phase into downstroke, resulting in sustained enhancement of lift generation as observed in the lift coefficient plot in Figure 5.6. This persistent vortex link can also be observed in the three dimensional iso-vorticity contour plot shown in Figure 5.12. The colour in the iso-vorticity surface represent the strength of the vortex.

Additionally, the three dimensional flow visualisation at the point of clap  $t = 0$  shows that the wing physical clap along the wing tip section pushes the air jets in upward, downward and outward directions. While the lift force is not significant due to the cancellation of momentum effects on both upward and downward directions, the momentum force generated by the asymmetric strong outward flow and the very weak

inward flow of fluid can however be significant. This difference causes a radial force acting on the wing pointing towards the wing root direction. When the radial force generated by a single wing is computed, it shows that strong negative radial force (pointing towards wing root) is only observed when wings physically clap in a clap-and-fling mechanism, whereas the radial force is always positive (pointing towards wing tip) in all the other cases studied. This radial force then changes direction rapidly when clap mechanism transits to fling mechanism on the wing, this time significant amount of fluid rushes into the gap due to the suction effect from the wing tip section and results in a net inward momentum of the fluid, a significantly larger positive (outward) radial force peak is produced. Figure 5.13 shows the comparison of radial force coefficients of symmetric sweep reference case, the near clap-and-fling case and the physical clap-and-fling case. This interesting finding could possibly be exploited by insects as a source of thrust during take-off or rapid manoeuvre while traditionally clap-and-fling are known to enhance lift.

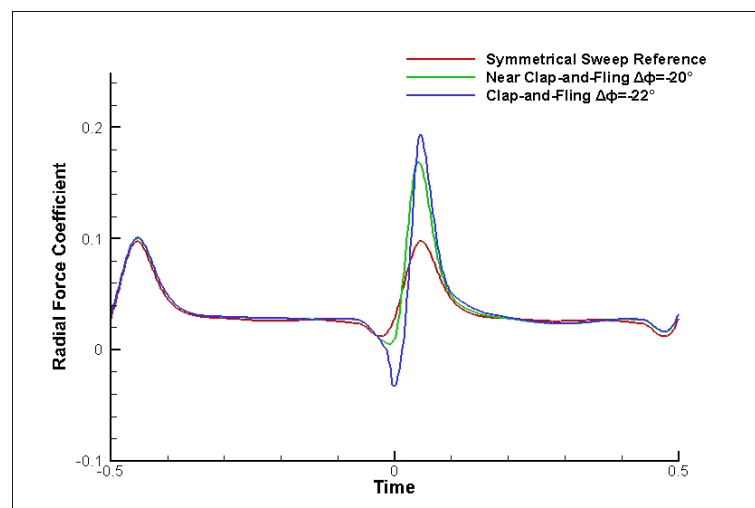


Figure 5.13 The radial force component computed on a single wing executing the reference symmetric flapping kinematics, the near clap-and-fling kinematics and the physical clap-and-fling kinematics

## 5.4 The Effect of Reynolds Number on Lift Enhancement by Clap-and-Fling

The current study has focused on the analysis of clap-and-fling mechanism at a common Reynolds number ( $Re=150$ ) for small sized insect such as fruit fly. However, most of previous numerical works (L. A. Miller & Peskin, 2005; Sun & Yu, 2006) have focused primarily on tiny insect clap-and-fling effects that takes place at lower

Reynolds numbers from 15 to 100. It is of great interest to investigate if Reynolds number play a significant role in the effectiveness of the clap-and-fling mechanism on lift enhancement. The present study adopts a different kinematic model from the aforementioned numerical studies and hence the simulations are repeated at lower Reynolds numbers to establish the relationship.

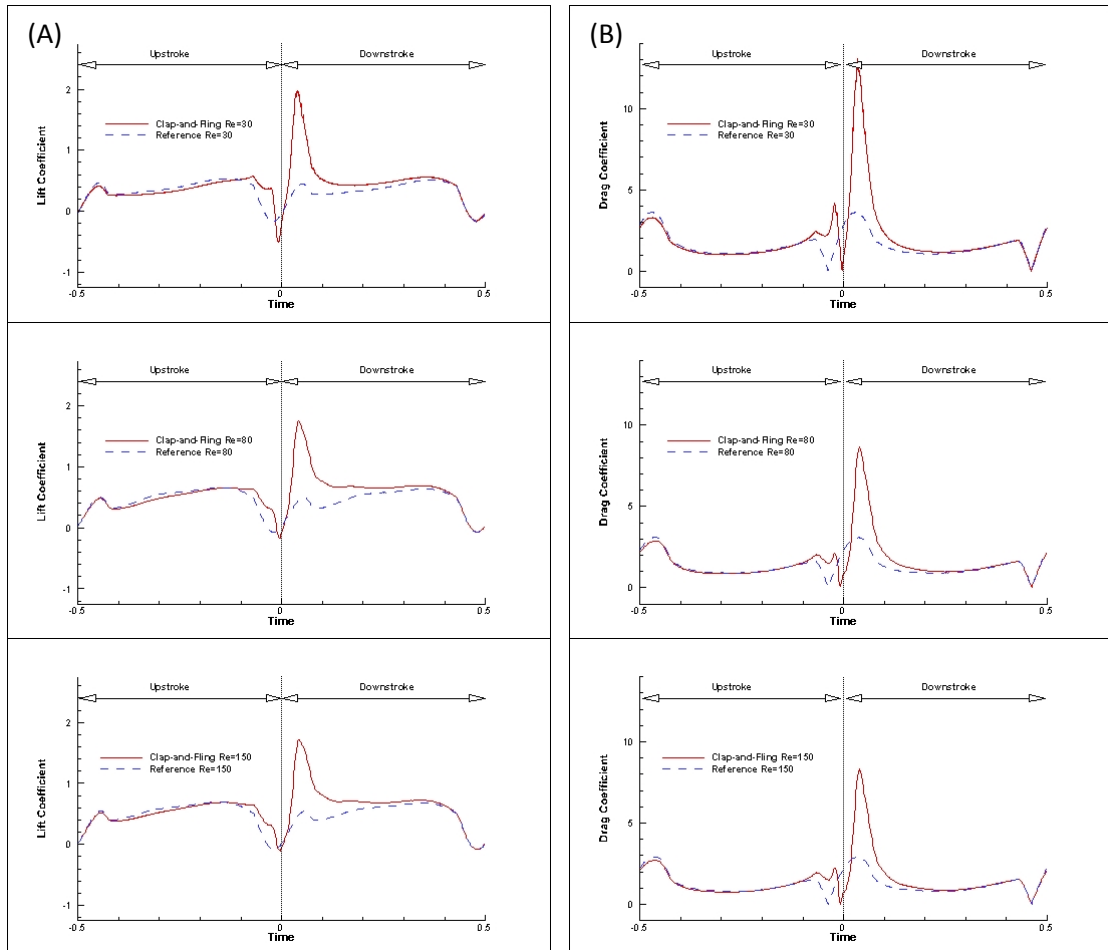


Figure 5.14 The Reynolds number effect on lift enhancement of clap-and-fling mechanism, lift coefficient (A) and drag coefficient (B) are computed based on the left wing

The lift coefficient and drag coefficient measured on the left wing in simulations of clap-and-fling flapping motions of a wing pair at Reynolds number of  $Re=30$ ,  $Re=80$  and  $Re=150$  (the default case discussed in previous sections) are presented in Figure 5.14. It can immediately be seen in the figures that the lift peak generated during the fling phase is higher at lower Reynolds number  $Re=30$  while the corresponding drag peak is more significantly higher. Closer inspection of the force curves also suggest that the slight lift enhancement just before the onset of the physical clap of the wings is also more obvious in lower Reynolds number case. This is expected as the stronger viscous effect at lower Reynolds number reduces the induced upward jet due to leading edge

vortex interactions and causing the downward jet created by the squeeze effect of the wings to be more significant.

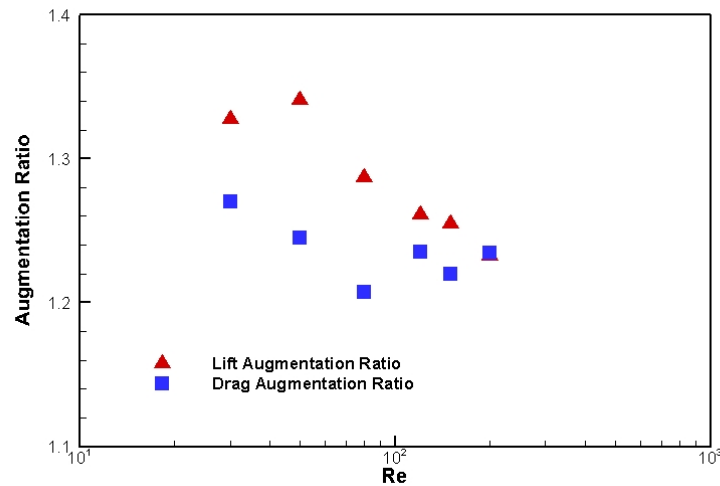


Figure 5.15 Lift augmentation ratio (mean lift force in clap-and-fling)/(mean lift in reference kinematics at same Reynolds number) and drag augmentation ratio (mean lift force in clap-and-fling)/(mean lift in reference kinematics at same Reynolds number) plotted against Reynolds number

Figure 5.15 further shows the trend of decreasing lift enhancement effect with respect to increasing Reynolds number. The trend agrees well with two dimensional computational clap-and-fling results by Miller and Peskin (L. A. Miller & Peskin, 2005). As pointed out by Miller and Peskin, this seems to suggest that the smaller insects have higher tendency of exploiting clap-and-fling mechanism to take advantage of the significant lift enhancement effect at lower Reynolds numbers while larger insects are less likely to do so.

However, as can be seen in Figure 5.14(B), drag is drastically increased during clap-and-fling and is even more significant at lower Reynolds number. This could have detrimental effect on the efficiency of this mechanism when performed by smaller insects. When the lift to drag ratio is computed, the results (in Figure 5.16(A)) show significantly lower ratio for smaller Reynolds number clap-and-fling flapping flights. The percentage gain of lift enhancement per additional aerodynamic power expended by the wing also falls off to a significantly lower value when the Reynolds number is very low ( $Re < 50$ ), whereas it maintains at almost a constant value in the range between  $Re = 80$  and  $Re = 200$ , shown in Figure 5.16(B). The result hence suggests that better aerodynamic efficiency of clap-and-fling motion is achieved at relatively larger Reynolds number compared to tiny insects as proposed by earlier studies, however,



more controlled studies are required to verify the result.

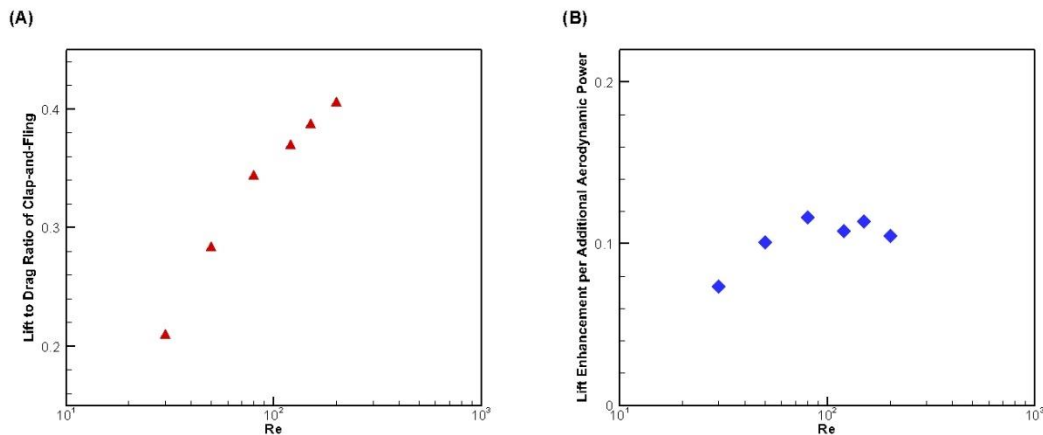


Figure 5.16 Lift to drag ratio of clap-and-fling mechanism at different Reynolds number (A), lift enhancement per additional aerodynamic power expenditure (B)

## 5.5 The Effect of Clap on Fling

As presented in the analysis of flow structures in section 5.3.2, clap could potentially enhance the ensuing fling to generate more significant lift augmentation for insects executing clap-and-fling mechanism during flight. A simple investigation of the effect of clap on fling is carried out in this study.

In order to observe the aerodynamic influence of clap on fling, the time duration of clap stage is varied while maintaining the time duration of fling stage during the execution of each flapping cycle of the model fruit fly at  $Re = 150$ . The reference case in this study is obtained from earlier presented results in which the time duration of clap ( $0.5T$ ) is identical to the time duration of fling ( $0.5T$ ) in each flapping cycle. As the time duration of clap is reduced, it corresponds to a shorter and more rapid clap preceding the following fling action of the wings. As the time duration of clap is increased, it corresponds to a longer and slower clap preceding the following fling action of the wing. Figure 5.17 shows the cases evaluated in the present study with up to 2 times faster clap compared to fling and up to 2 times slower clap compared to fling.

Figure 5.18 and Figure 5.19 show clearly the effect of varied speed of clap on the overall aerodynamic force productions. It is interesting to note that the shorter and more rapid clap results in significantly larger lift production at the onset of wing clap and a much more obvious lift peak is observed in the case of 2 times faster clap compared to

fling. However, the drag force at the onset of clap is not observed to be significantly higher with more rapid clap motion. This hence signifies that a more rapid clap is desirable in achieving larger lift augmentation in each flapping cycle.

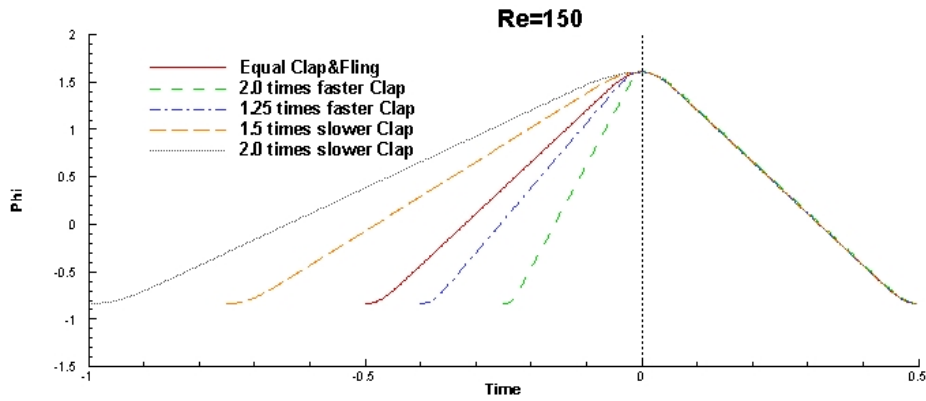


Figure 5.17 Sweep angle of the wing in a flapping cycle showing the different cases of relative clap to fling

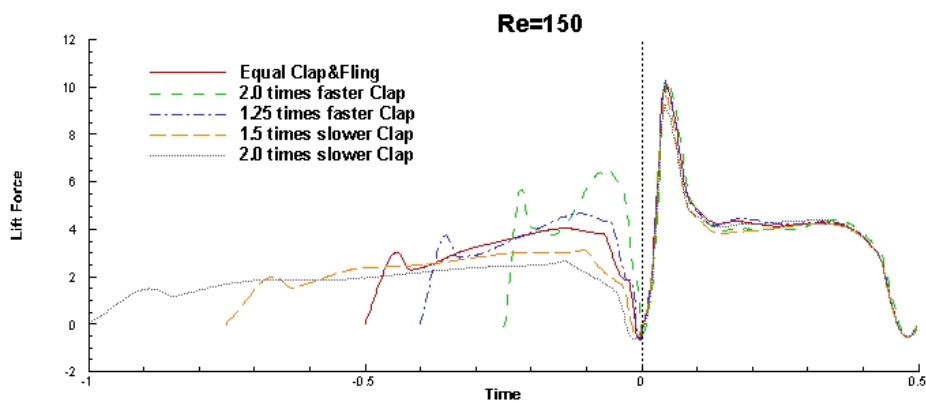


Figure 5.18 Comparison of aerodynamic lift produced in one flapping cycle in the case of varied clap speed with ensuing fling duration maintained constant

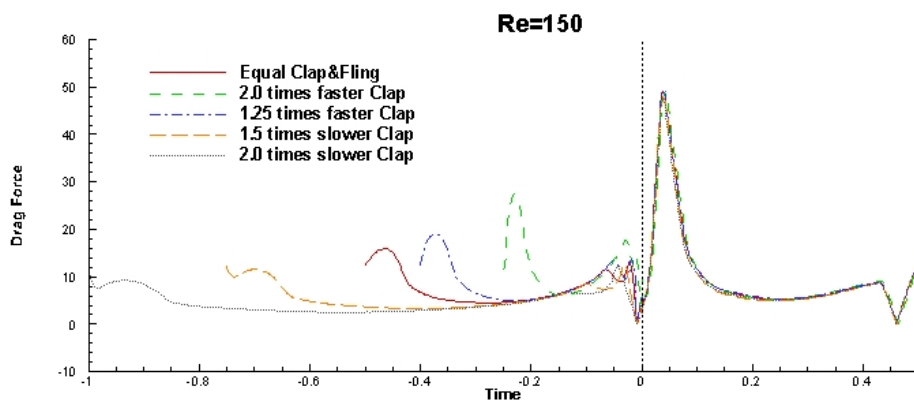


Figure 5.19 Comparison of aerodynamic drag produced in one flapping cycle in the case of varied clap speed with ensuing fling duration maintained constant



Upon closer inspection of the lift peak at the onset of wing fling motion shown in Figure 5.20, it can be seen that as the clap duration is increased (slower clap), the produced lift peak becomes lower. This suggests that without the presence of preceding clap motion, the lift enhancement of the ensuing fling motion of the wings is reduced. This agrees with the analysis in section 5.3.2. On the other hand, a more rapid clap may not further enhance the lift production in the fling motion as observed in the almost identical lift peaks between the reference case and the cases with faster clap motions. Hence, the only benefit of a faster clap in each flapping cycle comes from the enhanced squeezing effect of air in between the clapping wings to generate significantly higher lift force at the onset of clap.

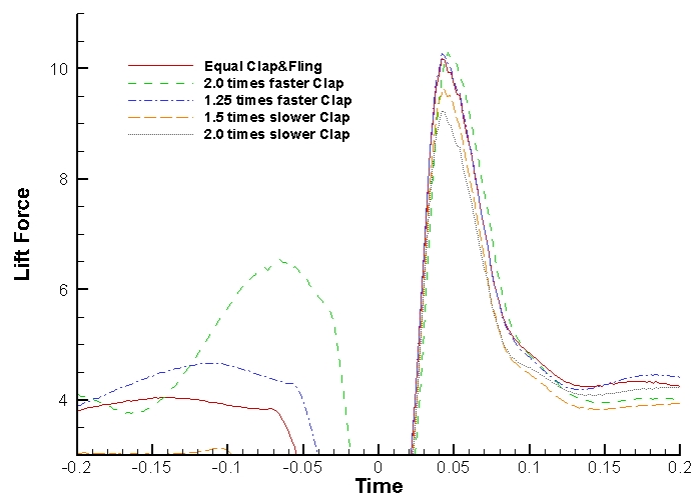


Figure 5.20 Effect of varying speed of clap on lift peak generation at the onset of fling motion of wings

## 5.6 The Effect of Wing Tips Separation Distance on Lift Enhancement

It was well established that the clap-and-fling effect could be partially achieved in insects with no actual physical claps performed, such phenomena is called near clap-and-fling mechanism (Willmott et al., 1997). Further evidence from experimental studies have also confirmed that the clap-and-fling augmentation of the lift can be realised at wing tip separation distance of less than 1 chord length, based on the angle plots by Lehmann et al. (Lehmann et al., 2005). The effect of lift augmentation as a function of wing tip separation is revisited in this study as the current study employs a

wing pair setup with closer wing root separation compared to the limitations of the mechanical setup in experimental work and the kinematic model in the present study differs quite significantly from that used in the experimental study.

The wing tip separation is controlled by the changes of mean positional angle of the mid-sweep plane of wing flapping motion from  $\Delta\phi = 0^\circ$  in symmetric reference case to  $\Delta\phi < 0^\circ$  in dorsal bias cases. Since the maximum amplitude of the sweep  $\phi_0 = 140^\circ$ , at the mean positional angle of mid-sweep plane with dorsal bias of  $\Delta\phi = -20^\circ$ , the two wings become parallel at the end of upstroke and the wing surfaces are separated only by the existing wing root separation of  $0.1R$  or  $0.3\bar{c}$ . A further dorsal bias to  $\Delta\phi = -22^\circ$  would allow the wing tips to just touch each other (creating a stronger clap-and-fling effect). Hence a systematic study is setup by gradually varying from the symmetric reference case of  $\Delta\phi = 0$  to  $\Delta\phi = -22^\circ$  in five separate steps and their mean lift coefficients are measured and compared. The lift coefficient over the span of the 11th wing beat cycle after the start of the numerical simulation is plotted in Figure 5.21. This particular flapping cycle is chosen as to minimise the unsteady effect due to the starting impulse of the wings in a still fluid domain at the beginning of the numerical simulation.

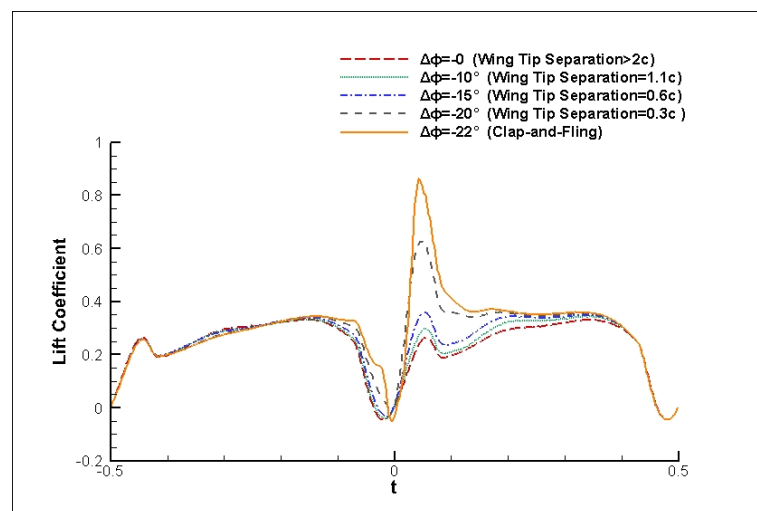


Figure 5.21 Comparison of lift coefficient over one wing beat cycle of cases from clap-and-fling to wing tip separation of larger than  $2\bar{c}$

Figure 5.21 shows clearly that the lift enhancement is increased when the wing tips separation distance is reduced. The effect becomes most significant when the wings are in physical contact during clap when  $\Delta\phi = -22^\circ$ . Furthermore, the lift enhancement effect extends beyond the completion of the fling phase and further into the downstroke flapping motion and the effect is more obvious when the wing tips separation distance

is less than  $0.1R$  or  $0.3\bar{c}$ . Additionally, the slight increase of lift force just before the onset of clap can be observed in the physical clap-and-fling case and but is almost absent in all the other cases which further suggests that this effect is too insignificant to be considered beneficial for the insect.

Figure 5.22 shows the lift augmentation as a function of wing-tip separation and the mean positional angle of the mid-sweep plane  $\Delta\phi$ . Lift augmentation is dependent on the ratio of the wing tips separation distance to the mean chord length of the wings and the plot is obtained by computing the ratio of increase in mean lift coefficient to that of the symmetric reference case. Hence a value of 1.0 represents no lift enhancement. The obtained trend agrees well with experimentally measured results in Lehmann et al. (Lehmann et al., 2005) Fig2.

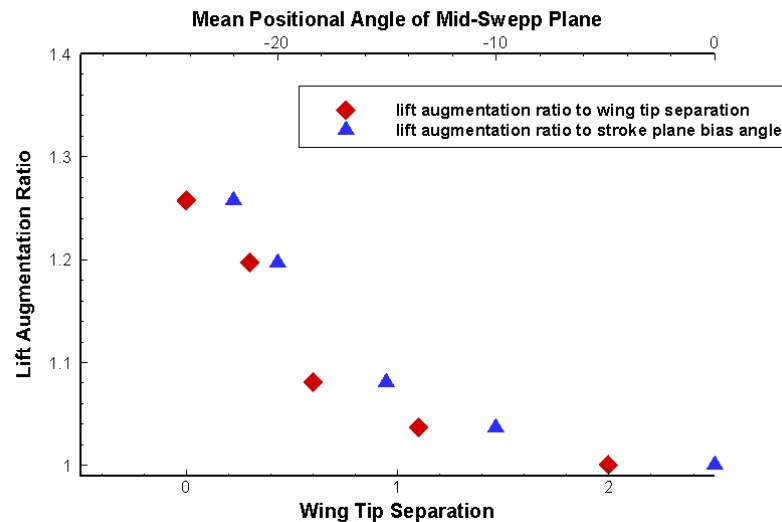


Figure 5.22 Lift augmentation ratio to wing tip separation and bias in mean positional angle of mid-sweep plane

## 5.7 Further Analysis of Wing Proximity Effect on Clap-and-Fling Lift Enhancement

As have shown in Figure 5.21, when the mean positional angle of the mid-sweep plane of the flapping motion is further rotated to dorsal bias from a near clap-and-fling case at  $\Delta\phi = -20^\circ$ , a significantly larger lift peak is produced at the beginning of the wing fling phase. This suggests that the proximity effect of the wings have predominant influence on the magnitude of lift enhancement due to clap-and-fling mechanism. By using the flow field plots presented in earlier sections, some analysis are offered to

explain the difference.

Due to the three dimensionality of flapping kinematics and the aforementioned morphological shape of the insect wings, the gap formed between the wing surfaces during fling phase does not form a perfect “v-shaped” space as assumed in two dimensional analysis. Hence, the trailing edges of the wings near to the wing tip section separate simultaneously with the leading edges of the wings due to the wing translation and rotation motions. The low pressure created causes a suction effect that allowed fluid to rush in to fill the gap between the wings as can be seen from the velocity vectors at  $t = 0.02$ . This fluid flow caused the shed leading edge vortices due to the previous upstroke to be sucked back into the gap and further enhancing the low pressure region between the wings. This contributes to the enhanced pressure difference across the upper and lower surfaces of the wings and producing extra lift. Figure 5.23 shows a comparison plot of the a top down view on the stroke plane of the wings executing the fling mechanism at  $t = 0.03$  for the physical clap-and-fling case where  $\Delta\phi = -22^\circ$  and a near clap-and-fling case where  $\Delta\phi = -20^\circ$ . The pressure contour plots shown clearly indicates an overall lower pressure field in the gap between the fling wings physical clap-and-fling case than that of the near clap-and-fling case. This difference is most obvious towards the wing tip section. On the other hand, the pressure contour upstream of the wings are almost identical for both cases and hence the difference must be produced due to the low pressure difference within the gaps between the wings. In addition, the aforementioned effect of flow stagnation region immediately next to the wing leading and wing tip edges due to the upward and outwards jet created by wing clap could prevent flow from rushing into the gap and further lower the low pressure region between the wings.

As the wings fling apart further, at  $t = 0.04$  the outboard section of the wings are completely detached from leading edge to trailing edge, while the section near to the wing root, the trailing edges are still attached. As have discussed in earlier sections, the converging flow pattern due to rushing in of fluid from the leading edges, the wing tip edges and trailing edges near to the wing tip section cause a roll-up of the wake vortex structure that connects the LEVs, WTVs and TEVs formed on both wings. The strength of this vortex is significantly larger in the physical clap-and-fling case compared to the near clap-and-fling case shown in Figure 5.24, further demonstrating the stronger effect due to closer proximity of the wings. Hence, larger induced downwash is created by

this stronger vortex link and a further lift enhancement can be achieved.

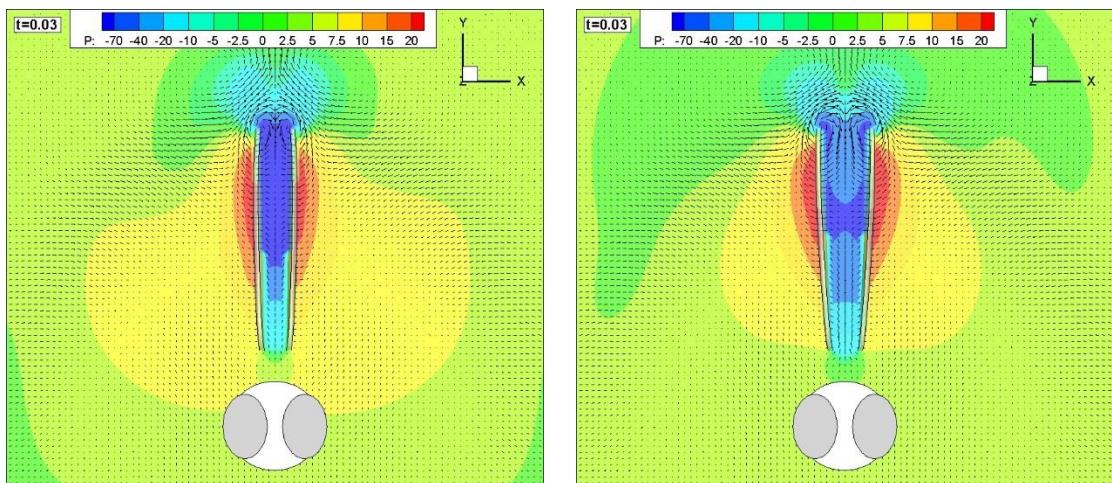


Figure 5.23 The pressure contour and velocity vector of physical clap-and-fling case (LEFT) compared to near clap-and-fling case (Right) at the same fraction time of a wing beat cycle

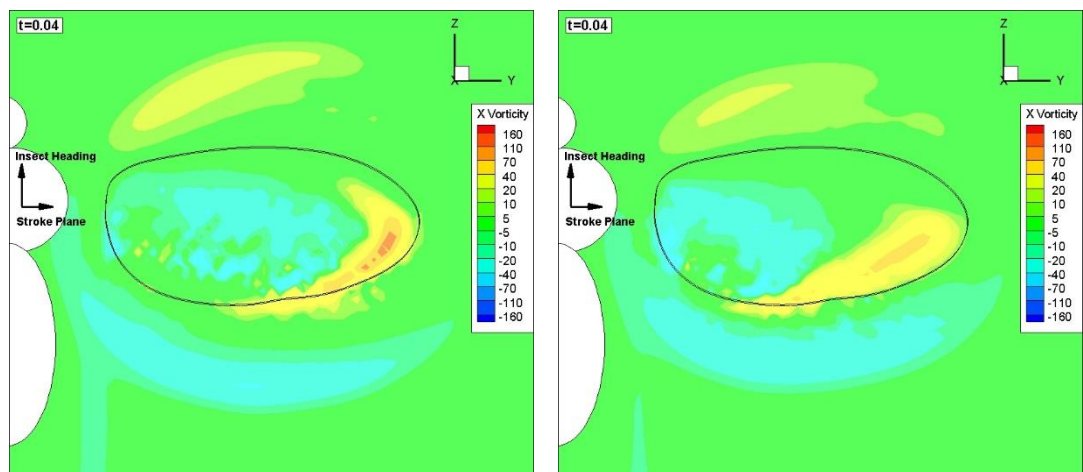


Figure 5.24 The comparison of vortex strength of the vortex link between the wings in physical clap-and-fling case (LEFT) and near clap-and-fling case (RIGHT)

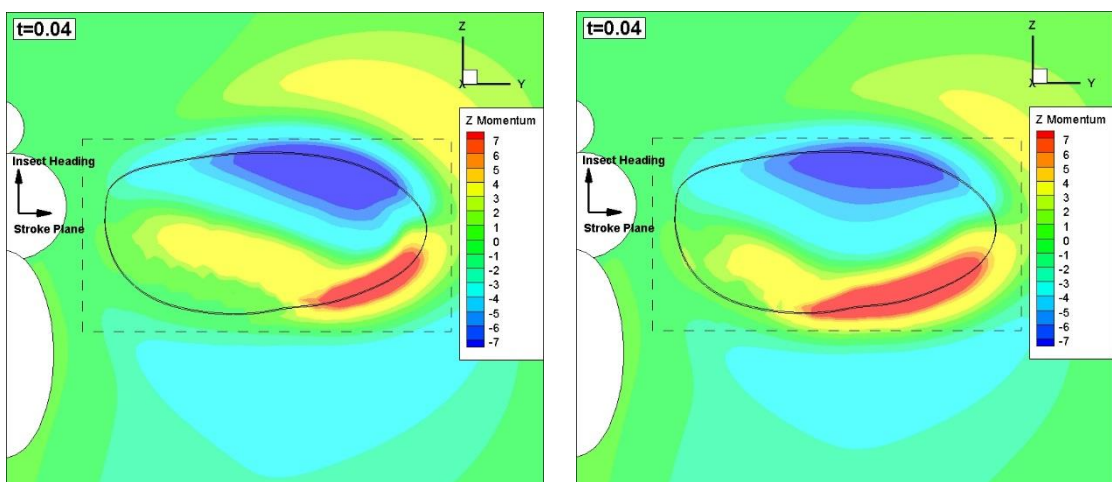


Figure 5.25 Comparison of vertically downward fluid momentum between the physical clap-and-fling case (Left) and the near clap-and-fling case (Right) at  $t = 0.04$

On the other hand, the flow field upstream of the wings are relatively unaffected

by the fling mechanism. Therefore, the strengthened downwash is mainly due to the vortices interaction in the wake region between the wings as they fling open. To further validate, a comparison of the calculated downward momentum of fluid around the wings between the aforementioned physical clap-and-fling case and the near clap-and-fling case at the fraction time of a wing beat cycle  $t = 0.04$ , where the lift peak is observed, are shown in Figure 5.25.

It can be clearly seen in Figure 5.25 that the region of fluid with downward momentum (blue) at  $t = 0.04$  is significantly larger in the physical clap-and-fling case. However, the upward momentum region (red) due to fluid rush in along the trailing edges is much larger in the near clap-and-fling case. The influence of the wake vortex link between the wings can be seen clearly in the physical clap-and-fling case where a significant portion of the fluid near to the wing tip is being directed downwards, revealing the main difference in area of the blue region as compared to the near clap-and-fling case. In addition, due to that the trailing edges of the wing near to the wing root section are still in physical contact at this time in physical clap-and-fling case, the red section indicating fluid with positive vertical momentum is only confined to the near wing tip section and much smaller than the near clap-and-fling case. A rectangular box is drawn in the figures and used as a volume in which the integral sum of total momentum of fluid continuum are roughly estimated. The spatial volumes in between the wings are very small at this time phase and hence the total momentum calculated is based on 2D estimations. The total non-dimensional fluid vertical momentum in the control volume is estimated to be 0.0461 for the near clap-and-fling case and 0.0606 for the physical clap-and-fling case, a difference ratio of 0.314. This rough estimation matches well with the measured lift peak difference of 33.6% shown in Figure 5.26. This suggests that the additional must be caused by the induced downwash by the stronger vortex link in the physical clap-and-fling case.

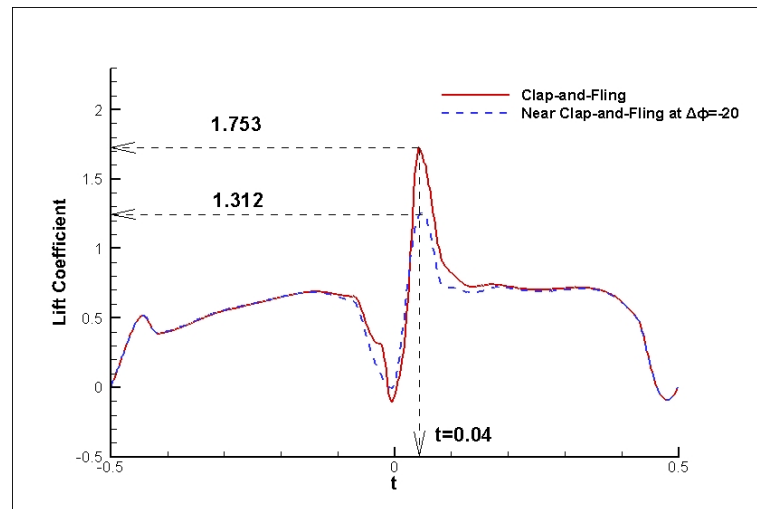


Figure 5.26 The lift coefficient comparison between the physical clap-and-fling case and the near clap-and-fling case with the measured peak values identified

## 5.8 The Effect of Wing Roots Separation Distance on Lift Enhancement

This proposed study is used to address the observed difference between the measured lift coefficient from the current three dimensional numerical study compared to that obtained from experimental methods without focusing on the difference in other aspects such as kinematic models. So the approach in this study is relatively simple, the separation of the pair of fruit fly wings at the wing roots in current numerical study is varied from the default value of  $0.1R$  or  $0.3\bar{c}$  to  $0.2R$  and  $0.3R$  and the changes in the mean lift coefficient per wing beat cycle is then compared to establish the relationship of lift force augmentation and the wing roots separation.

As the wing roots separation distance is increased, the wing tips separation distance will be increased at the same mean positional angle of mid-sweep plane  $\Delta\phi$ . Thus, in order to obtain a comparable clap-and-fling mechanism, the mean mid-sweep plane is further rotated in larger wing roots separation cases to always achieve physical clap of the wing tips at the end of upstroke. The kinematic model of the clap-and-fling simulation is unchanged. Therefore, a summary of changes in wing roots separation and the corresponding mean positional angle of the mid-sweep plane with dorsal bias is shown in Table 5-1.



Table 5-1 Parameters of wing roots separations and the corresponding dorsal bias of the mean positional angle of mid-sweep plane to achieve physical clap (\* default wing roots separation in current studies)

Wing Roots Separation	Dorsal Bias of Mean Positional Angle of Mid-Sweep Plane for Wing Tips Physical Clap
0.1 $R^*$	$-22^\circ$
0.2 $R$	$-24.5^\circ$
0.3 $R$	$-27^\circ$

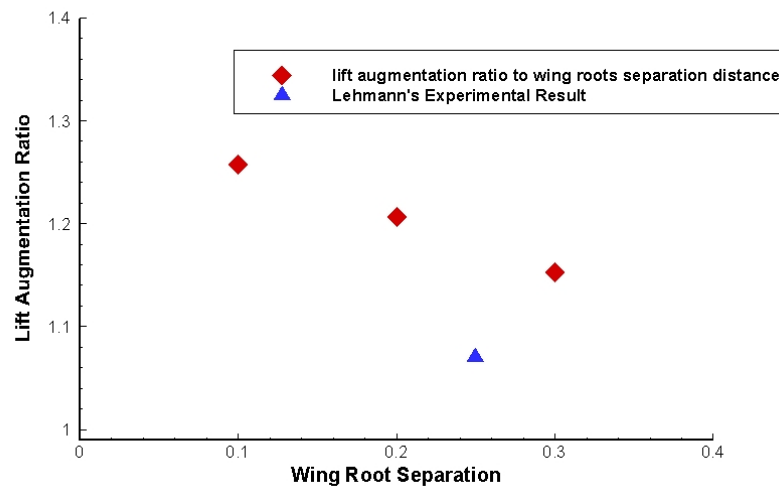


Figure 5.27 Lift augmentation ratio to wing roots separation distance plot

The relationship of lift augmentation ratio to the of wing roots separation distance are shown in Figure 5.27, with reference to the extracted lift augmentation ratio from Lehmann's experiment. It clearly shows a decreasing effectiveness of clap-and-fling mechanism as the wing roots separation increases. At the wing roots separation distance of  $0.2R$ , the measured lift augmentation ratio shows a much closer match with the results obtained in experiment by Lehmann et al. (Lehmann et al., 2005). This could well be due to the relatively weaker interaction of the leading edge vortex, the wing tip vortex and the trailing edge vortex in the wake due to a larger wing separation on a larger area of the wing surfaces when the wing roots separation is increased. This reduced wake interaction, as discussed in earlier sections, could be the main cause of lift reductions observed here.

This observation could in fact imply that, the clap-and-fling mechanism that are observed only in some insects are not just because of the Reynolds number at which their flapping flight is performing at, but also due to the anatomical structure that could determine the effectiveness of the mechanism and therefore the insect's choice to exploit it in natural evolution. One possible example could be observed between



Damselfly and Dragonfly, which fly at similar Reynolds number. Research has shown that dragonfly tends to flap their wings with small sweep amplitude and the opposite wings never come close together, whereas damselfly actively adopts clap-and-fling mechanism (mainly the fling mechanism) during take-off (Wakeling & Ellington, 1997). Damselfly tends to have long thin abdomen with a small and narrow thorax structure, the wing are long and slender, therefore a large wing span to wing roots separation ratio could be observed that makes the clap-and-fling mechanism to be very effective for its take-off manoeuvring. Dragonfly on the other hand has a much larger and wider thorax structure and a shorter and broader wings, the resulting wing roots separation ratio to that of the wing span is larger than Damselfly and may therefore produce much reduced clap-and-fling lift augmentation even if it attempts to do so. However, a rigid wings are assumed in the current study and flexibility effect may have a more prominent contribution to the actual effect of clap-and-fling mechanism on larger insects, which can be explored in further studies.

## **5.9 An Investigation of Lift Augmentation to Increased Power Requirement Relationship**

Another very important concern for insect clap-and-fling mechanism is the power required to do so and the specific lift to aerodynamic power ratio that will determine if it is actually favourable for the insects to perform clap-and-fling. Earlier two dimensional numerical investigations show that during fling, a substantial increase of drag (about 1 order of magnitude higher) is experienced by the wings (L. Miller & Peskin, 2009) and that could translate to substantially higher power requirement from the insect to obtain the lift augmentation from clap-and-fling. However, no actual power computations are presented in the literature to substantiate the aforementioned hypothesis and the author attempts to draw a relation in the lift augmentation to that of power requirement in the present study. It is worth to point out that the aerodynamic power computed is closely related to the kinematic model of the flapping motion, as have described in Chapter 4 and may not be generalised to all clap-and-fling mechanisms.

The mean non-dimensional lift force produced by a single wing is computed for

all the cases studied in the previous sections of the current study and divided by the respective mean aerodynamic power on a single wing over the wing beat cycle. The result below shows the scatter plot of these obtained ratio and its relationship to the wing tip separation from symmetrical sweep reference case to the physical clap-and-fling case.

The results show clearly that there is almost no difference in lift to power ratio throughout all the simulation configurations investigated in this study. In fact a slight increase of lift to power ratio is observed when near clap-and-fling cases are evaluated and this implies that the gain of lift is more than the requirement of extra power draw when insects execute near fling mechanisms. This further demonstrates that for insects whose anatomic configurations favour the execution of clap-and-fling or are capable of making use of clap-and-fling mechanisms to augment lift at demanding situations are more likely to perform this mechanism during take-off or manoeuvring during free flight as the extra power requirement is proportional to the improvement of lift.

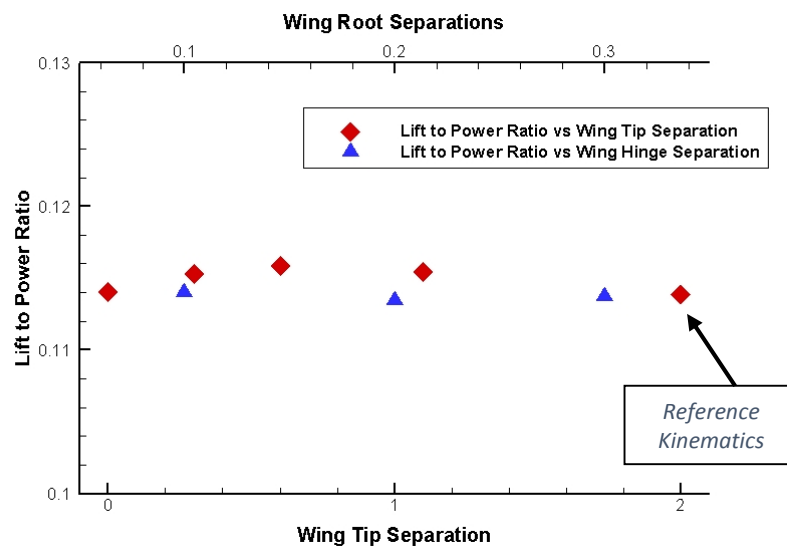


Figure 5.28 Lift to power ratio as relative to the different wing-wing kinematics configurations explored in the study of clap-and-fling

## 5.10 Summary

In this study, the three dimensional aerodynamic effects of clap-and-fling mechanism are investigated at  $Re=150$  and using a morphologically accurate fruit fly wing. The numerical method is carefully modified to allow the stable and accurate computations of rigid wings to be in extreme close proximity and even with physical

clap occurring at the wing tips. The kinematic model for the flapping motion is also redesigned to accommodate the use of rigid wings with choice of extended wing twist duration and shorter translational acceleration phase to prevent wing-wing penetrations (instead of rapid twisting motions adopted in earlier two dimensional numerical studies and experimental studies as explained). The lift peak captured and aerodynamic force computed have shown good agreement with existing published results.

Further detailed analysis of the flow field obtained from the numerical simulations showed many three dimensional unsteady aerodynamic effects associated with a rigid insect wing pair performing clap-and-fling mechanisms. Data analysis have revealed interesting phenomena that has been substantiated with three dimensional flow field observations clearly demonstrating the lift augmentation effects of “clap” and “fling” mechanisms separately. The strong vortex link forms in the opening gap between the wings when the wings fling apart is first observed in three dimensional flow visualisations and is argued to provide strong downwash which further enhances the lift beyond the completion of the fling phase. Additionally, clap-and-fling is shown to be capable of producing additional thrust force as shown by a higher positive (outward) radial force peak during fling, which acts as an additional source of thrust for take-off or rapid manoeuvre. This further demonstrates the significant difference of three dimensional flow evolution of clap-and-fling mechanism as compared to results from 2D analysis.

The lift enhancement effect of clap-and-fling is further investigated under different Reynolds numbers to verify the observations obtained by other researchers in earlier two dimensional studies. The result suggests an increasing lift enhancement with reducing Reynolds number, however, at the cost of substantially increased drag and reduced efficiency of the clap-and-fling motion to generate extra lift at a specific additional aerodynamic power required.

Additional studies on the relationship of the lift augmentation of clap-and-fling mechanism with variation of the wing tip or wing roots separations are presented. Results demonstrated that the lift augmentation decreases with increasing wing tips or wing roots separation, which further showed that the absence of clap-and-fling flapping motion in many insects may be an evolutionary result of anatomical wing roots separations on their thorax. The lift to power ratio of clap-and-fling has also been

explored by the study and show a generally linear trend between the enhanced lift and the extra power requirement for insect performing clap-and-fling mechanism, which suggest that it is favourable for insect to actively deploy clap-and-fling mechanisms when in need of extra lift during take-off and manoeuvring.

Lastly, it should be pointed out that, the current study have assumed the flapping wings are rigid. Based on observations, most insects performing clap-and-fling have their wings readily flex along both the spanwise and chordwise directions. Due to wing flexibility, insect may be able to temporarily align and conjoin their wings along the leading edges, despite non-zero wing roots separations. This suggests that insects are able to exploit the fling mechanism to a greater extent than predicted by our rigid models. The effect of wing flexibility on lift enhancement in three dimensional clap-and-fling flapping motions hence requires further investigation.

# CHAPTER 6: Parameterisation of Flapping Kinematics for Control

## 6.1 Introduction

It is generally accepted that exploitation of extensive unsteady aerodynamic effects through kinematic adjustments of the flapping wings allows insects to hover, fly forwards and backwards, manoeuvre with great agility and to switch rapidly in between flying modes. Hence, the study of flapping wing kinematics is critical in learning the unsteady aerodynamic effects associated with insect flights and would allow us to design and build flapping wing based MAVs that would have significant potential in both civil and military applications. However, the detailed and precise kinematic description of natural flapping wing motions and the basis of insect flight controls through adjustments of flapping kinematics are little known due to inherent complexities pertaining to insects' small size, rapid reciprocatory characteristics of flapping wing and the concomitant experimental difficulties.

There have been a few approaches in the attempt to understanding aerodynamic effects associated with the flapping wing kinematics for the eventual purpose of designing MAV applications with insect like manoeuvrability and controllability. The first, proposed by Ellington, is to adopt "design guidelines" based on scaling from nature and accurate mimicking of natural insect flapping characteristics (Ellington, 1999). This approach, however, does not give one the physical insight into the underlying aerodynamic processes and thus limit design optimization options. Another approach is by modelling aerodynamic effects associated with flapping kinematics by using quasi-steady model in which the aerodynamic forces are assumed to be the steady state value of the wing at the same velocity and angle of attack (Osborne, 1951). This approach is further developed by Weis-Fogh using blade-element theories and Ellington by proposing actuator disk and vortex wake estimations (Ansari et al., 2006; Ellington, 1984; Weis-Fogh, 1973). However, it is found to be severely underestimating the ability of insect wings in generating aerodynamic forces during flapping motion and neglecting important unsteady aerodynamic transient effects associated with the wing kinematics. A third approach is to model the aerodynamic force productions using

quasi-steady models with semi-empirical corrections based on extensive experimental results (Dickinson et al., 1999; Sane & Dickinson, 2002). However, this approach was found to be unable to predict wake capture effects of wings and wing-wing interaction phenomena which are kinematics dependent and highly non-linear. It was only very recently, that Computational Fluid Dynamics, has been harnessed in the study of unsteady aerodynamic effects generated by flapping insect wings. Numerous work has since been presented in the literature detailing the numerical results of the unsteady aerodynamics effects associated with flapping wing flights and attempts to quantify such aerodynamic force generations in relation to wing kinematics (Aono et al., 2008; Ramamurti & Sandberg, 2006; Z. J. Wang, 2008).

Nonetheless, knowledge of the relationship between wing kinematics and force and moment productions remain unavailable. An attempt to bridge this gap was made by Sane and Dickinson, who examined 191 separate sets of kinematic patterns that differed with respect to stroke amplitude, angle of attack, flip timing, flip duration and the shape and magnitude of stroke deviation. The information obtained in their study was highly valuable (Sane & Dickinson, 2001). However, there are two inherent limitations to the aforementioned study: the choice of some kinematic parameters, which describe complex functions of the physics of the flapping motions, are not apparent; due to limitations in mechanical setup, only a limited number of force and moment components are measured and evaluated, which would be inadequate for characterising wing performance in actual flight situations.

The current study attempts to provide a simple alternative of parameterisation of wing flapping kinematics by extracting 8 specific parameters external to the kinematic function description and by altering individual parameters to establish force and moment (6DOF) relations to the insect flapping kinematics within small range of perturbations about a stationary reference state. A simple dynamic modelling analysis is carried out on the obtained relationship data and linearization is performed. A simplified proportionality matrix is proposed as a preliminary step towards the design of a future control system for insect like flapping wing MAVs.

## 6.2 Parameterisation of Flapping Kinematics

The insect wing flapping mechanism is unique in that all actuations are carried out at the wing root, which limits the insect wings to three degrees of freedom with respect to insect. These are essentially the rotations of the wings about the wing root (centre of rotation) in three axes as described in Chapter 3. This makes systematic description of flapping wing kinematics possible, and in most approaches, the kinematic models of the wing rotations about azimuthal, twisting and elevation are described by separate functions of time. However, as have observed from nature, the actual flapping mechanisms of the insect wings are in fact a highly coupled effect of the aforementioned three degrees of freedom. The complexity of wing kinematics is further compounded by the flexible nature of the wings. The objective of this study is not to mimic actual insect flapping kinematics, but instead to establish the effect of wing kinematics on mean aerodynamic force and moment production and propose a simple control model for the design of flapping wing based MAVs. To do so, the current study first propose an alternative parameterisation approach to flapping kinematics which we feel is most robust and easily modified during flight.

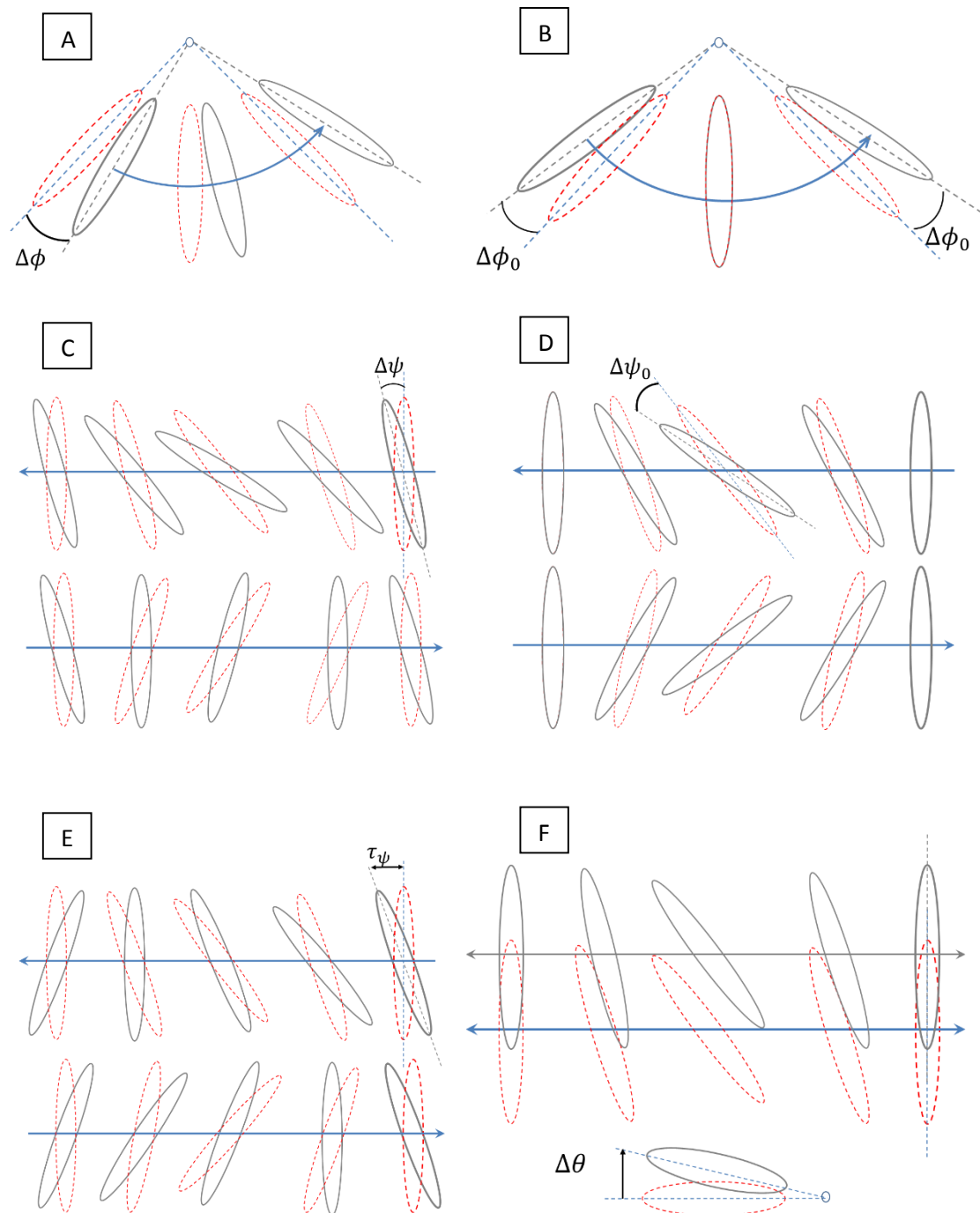
### 6.2.1 Definition of Kinematic Parameters

As have mentioned earlier, the wing motion can be represented in terms of rotations about 3 axes. For each axis, a set of parameters for the respective kinematic function can be defined. Three parameters, 2 displacement parameters and 1 temporal parameter, are identified for each kinematic function and are added into the original kinematics descriptions presented in Chapter 3. The following table lists the parameters identified for each rotational axis.

*Table 6-1 Parameterisation of kinematic functions*

	<b>Mean Positional Angle of Mid- plane</b>	<b>Amplitude</b>	<b>Phase Relation</b>
<b>SWEEP</b>	$\Delta\phi$	$\phi_0$	$\tau_\phi$ (phase reference)
<b>TWIST</b>	$\Delta\psi$	$\psi_0$	$\tau_\psi$
<b>ELEVATION</b>	$\Delta\theta$	$\theta_0$	$\tau_\theta$

There are a total of 9 parameters can be defined in the aforementioned parameterisation. However, only 8 parameters are effective in modifying flapping kinematics, as  $\tau_\phi$  is taken as the reference phase which coincides with the global phase fraction time of one wing beat cycle. The parameters  $\tau_\psi$  and  $\tau_\theta$  are defined as the phase difference of the respective kinematic function to that of the sweep motion. A more detailed explanation of the parameters with the help of figures are shown in Figure 6.1.





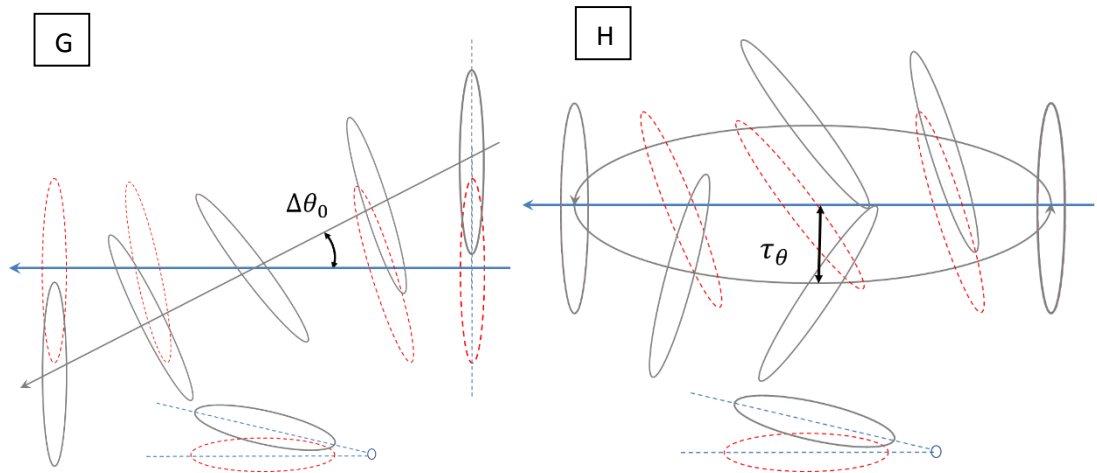


Figure 6.1 Visualisation of effect of changing flapping kinematic parameters, where dotted lines represent wing in reference symmetric flapping motion, dark lines represent wing in flapping motion kinematics with individually adjusted parameters and blue arrow represent the reference stroke plane. (A)  $\Delta\phi$ , variation of mean positional angle of the mid-sweep plane, (B)  $\Delta\phi_0$ , the change in sweep amplitude, (C)  $\Delta\psi$  variation of mean positional angle of the mid-twist plane, (D)  $\Delta\psi_0$  the change in twist amplitude, (E)  $\tau_{psi}$  the phase change of twist kinematic function relative to sweep kinematic function, (F)  $\Delta\theta$ , variation of the mean positional angle of the mid-elevation plane, (G)  $\Delta\theta_0$  the change in elevation amplitude, (H)  $\tau_\theta$ , the phase change of elevation kinematic function relative to sweep kinematic function, results in change of wing tip path of a cycle, ie. "figure of 8".

$\Delta\phi$  (A) represents variation of the mean positional angle of the mid-sweep plane, and affects the symmetry of the sweep action of the wings. By adjusting this parameter, the insect can shift the mean positional angle of mid-sweep plane towards dorsal bias or ventral bias, hence results in aerodynamic force production bias towards the front or back of the insect body in order to create rotational moment for pitch control.

$\Delta\phi_0$  (B) represents the sweep amplitude changes from a referenced sweep motion, and mainly affects the total aerodynamic force productions. When varied, allows the insect to gain or lose altitude by gaining or losing lift. It has been observed that insects such as honey bee increases stroke amplitude in order to carry the extra weight of nectar (Altshuler, Dickson, Vance, Roberts, & Dickinson, 2005). In addition, it was suggested that insects such as fruit fly use different sweep amplitude between left and right wings to produce yaw moment during rapid maneuvering (Lehmann & Dickinson, 2001).

$\Delta\psi$  (C) represents variation of mean mid-twist plane of the wing twisting motion. This effectively causes the angle of attack difference in upstroke and downstroke of flapping wing motions, and leads to the increase of net drag force produced in a horizontal stroke plane. This is in contrast to the almost zero net drag force produced in symmetric reference flapping wing kinematics, and in which drag force produced in upstroke is equal in magnitude and opposite in sign from downstroke. When coupled with inclined stroke plane, this could result in net thrust production with limited effect

on lift force produced, similar to the observation that most insects in forward flight adopt an inclined stroke plane.

$\Delta\psi_0$  (D) represents the changes in wing twist amplitude with respect to the reference flapping motion. An increase in  $\Delta\psi_0$  is equivalent to a reduction of the minimum angle of attack of the wing. This parameter could also affect the mean lift force generation during each wing beat cycle, while maintaining symmetry of the flapping motion and results in no increase of net drag force. The amount of rotation of the wing along the twisting axis is also affected by this parameter, as have discussed previously in Chapter 3, that it will result in lower or higher lift peaks at the ends of each stroke and hence affect the moment of lift and drag forces produced by the wings.

$\tau_\psi$  (E) represents the relative phase time difference of twisting kinematic function to the sweeping kinematic function. Therefore, this parameter changes the effective leading or lagging of the wing rotation to that of translation. As have shown in Chapter 3, this will affect the overall lift production of the flapping motion.

$\Delta\theta$  (F) represents variation of the mean positional angle of the mid-elevation plane of the flapping wing. This effectively causes the wings to have a fixed elevation angle during flapping instead of 0 in the symmetric reference kinematics. When a positive value is applied to both wings, it leads to a dihedral formation of wings similar to the configuration of wings on many conventional aircrafts. However, unlike the conventional case on aircrafts, the actual unsteady aerodynamic effect of wing elevations are not well known, and the results will be discussed in the later sections to quantify the influence of this parameter.

$\Delta\theta_0$  (G) represents the elevation amplitude when the wings changes elevations periodically during flapping motion. The kinematic function for elevation of insect wings in flapping motion could be described by a simple sinusoidal function as described in Chapter 3. Insects are observed to usually deploy constant elevation angles during hovering while using a periodic changing elevation angles “figure of 8” or “oval” shape during forward flights (Ellington, 1984). This parameter is isolated as the kinematic function for elevation angle is fixed in this study as a simple sinusoidal function with periodicity of 1, same as the periodicity of the wing beat cycle. The effect of this parameter is also believed to be highly coupled with the next discussed parameter, which affects the shape of the actual wing path.

$\tau_{theta}$  (H) represents the relative phase time difference of the elevation kinematic function from the sweep kinematic function. When the kinematic function for elevation of the wing is specified to be a sinusoidal function with single periodicity, this parameter changes the location of the maximum elevation and minimum elevation within each stroke and results in the flapping wing tip path to vary anywhere from a flat inclined stroke plane to an “oval shape”. This can be observed from Figure 6.1 above. It is also worth to point out that, this parameter when coupled with  $\Delta\theta_0$  and  $\Delta\psi$  would result in an equivalent flapping motion trajectory as if the stroke plane is inclined without modification of the flapping kinematics. Therefore, the aerodynamic force variation due to this parameter could be quite non-linear, more of the effect will be discussed with the result in the later sections.

Therefore, as explained, each parameter is a description of a physical quantity that is capable of defining the flapping motion of the wings independently of each other or the kinematic function applied. Hence, the kinematic model for full description of wing flapping motion presented in Chapter 3 changes into the following form:

$$\begin{cases} \phi(t) = \Delta\phi + (\phi_0 + \Delta\phi_0)f_\phi(t) & \text{where } 0 \leq f_\phi(t) \leq 1 \\ \theta(t) = \Delta\theta + (\theta_0 + \Delta\theta_0)f_\theta(t + \tau_\theta) & \text{where } 0 \leq f_\theta(t) \leq 1 \\ \psi(t) = \Delta\psi + (\psi_0 + \Delta\psi_0)f_\psi(t + \tau_\psi) & \text{where } 0 \leq f_\psi(t) \leq 1 \end{cases} \quad [6.1]$$

Where  $\phi(t), \theta(t), \psi(t)$  are the angular functions specifying the wing rotations at any specific fraction time of a wing beat cycle,  $f_\phi(t), f_\theta(t), f_\psi(t)$  are periodic kinematic functions of the wing flapping motion, that has a value between 0 and 1, which are specified and assumed to be unchanged throughout flight of the insect. Hence, the entire flapping kinematics is controlled by specification of the 8 parameters. The following study analyses the influence of each of the parameters on the flapping kinematics and hence the net forces/moments experienced at the wing root.

## 6.2.2 The Reference Kinematics

The effect of the parameters are analysed by making small deviations of the parameter values from a referenced state value. The reference kinematic model is adopted from results of the kinematic studies presented in Chapter 4, in which an optimised trapezoidal function based kinematic model was derived. The choice of the flapping kinematic model is such that according to earlier simulations and aerodynamic

force computation results, the mean lift force produced by both wings of the insect is approximately equal to the weight. In addition, this flapping motion is symmetrical and hence, the wing pair produces zero net drag (thrust) force, lateral force and moments about the pitch, roll and yaw directions. Assuming a statically steady-state, this allows the insect to hover if the insect body is oriented such that its centre of mass is directly below the mid-point of the line joining the two wing roots where the wing rotations originate.

By evaluating the effect of the parameters on aerodynamic force productions of the flapping wings, one can obtain a linearised relationship of the parameters to that of the forces and moments produced. This can be exploited to derive a simple coefficient matrix that could form the preliminary theoretical basis for the development of a control model directly coupled to the flapping kinematics of the flyer. Such a control model can be used to prescribe small variations of kinematic parameters to produce counterbalancing forces and moments such that quasi-steady hovering motion maintained even when the model insect is subjected to small perturbations from the reference state.

### **6.2.3 Force and Moment Evaluations**

An insect in hovering or free flight has six degrees of kinematic freedom and is subjected to the effect of lift force, drag force, lateral force, pitch moment, roll moment and yaw moment respectively. Since each wing of an insect is attached to the thorax on a single point at the wing root, and is the primary source that produces the forces and moments required for the insect to stay in flight, it is valid to treat each individual wing of the insect as a power plant on which the respective forces and moments are produced and act on the wing root. The net forces and moments of the insect can then be computed from the forces and moments produced by each wing, thereby establishing the dynamic behaviour of the insect. Figure 6.2 illustrates, in the body frame, the definition of lift force, drag force, lateral force, pitch moment, roll moment and yaw moment.

In the ensuing simulation, although the computations are carried out for a pair of wings, the force and moment measurements are only done on the left wing of the insect. The forces and moments are computed in the body frame and with respect to the centre point of the line joining the two wing roots (which coincides with the centres of rotation of the wings). It is assumed here that the right wing produces a mirrored symmetry of

forces and moments as the left wing with the same kinematic parameter sets. In this simplified dynamic scenario, the net lateral force, yaw moment and roll moment on the flyer would be zero. In the present scenario, the mass of the wings of the insect is also assumed to be negligible relative to the mass of the body.

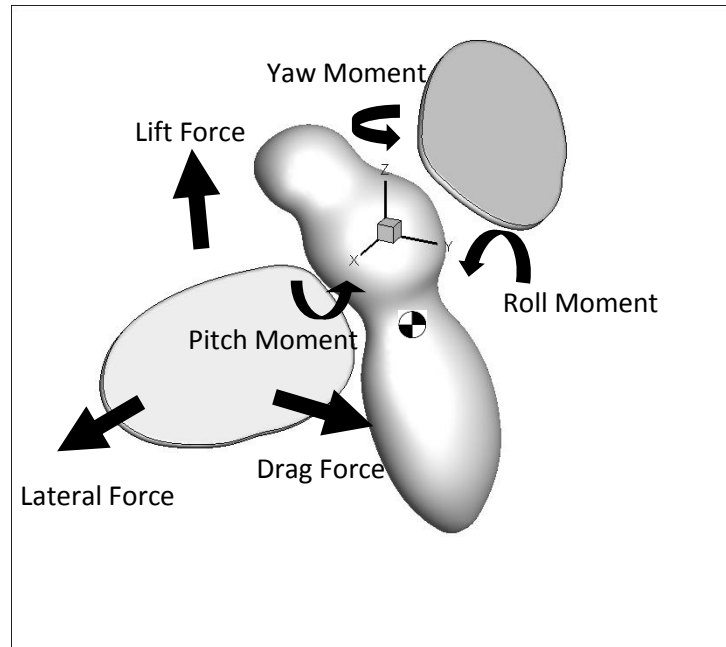


Figure 6.2 Illustration of the force and moment definition produced by the left wing in the body frame, the cube represents the body coordinate centre, which is the mid-point of the line joining the two wing roots, and indicates the coordinate axes respectively. The symbol  $\oplus$  represents the centre of mass of the insect which usually lies in the abdomen.

### 6.3 Effects of Kinematic Parameters on Aerodynamic Force and Moment Productions

3D simulations are conducted on a full insect body with wing pair initially performing flapping motion with the referenced kinematic model. The mean aerodynamic force and moment produced by the left wing per wing beat cycle, after 7 cycles, is measured and taken as reference. It is worth to point out that, due to the unsteady aerodynamic effects and the continued flow field interactions, the mean aerodynamic forces are not measured to reach steady state even after 7 cycles, however, the variation in the mean force produced is reduced to less than 2% per cycle. The parameters are varied individually to a small range variation from the referenced value and the plot of the aerodynamic force and moment variations are obtained with respect to the change. The right wing is always made to perform the same kinematics in mirrored symmetry as the left wing. Hence the aerodynamic force and moment

measurements are subjected flow interaction due to the wing pair. The results are analysed and discussed separately in the following subsections.

### **6.3.1 Effect of Variations in Mean Positional Angle of Mid-Sweep Plane on Mean Aerodynamic Force and Moment Productions**

The earlier findings in clap-and-fling studies suggest that as the bias of the mean positional angle of mid-sweep plane increases beyond  $10^\circ$ , the close proximity of the wings would result in significant wing-wing interaction and this would cause the increase of lift force to be non-linear. Therefore, linearity can only be assumed within this range of variations. Hence, the mean positional angle of mid-sweep plane is varied gradually from  $0$  to  $10^\circ$  and the corresponding mean aerodynamic force produced after 7 cycles are plotted in Figure 6.3. Only the positive variations of this parameter is evaluated. Due to symmetry of sweep (mean positional angle of mid-sweep plane is zero) in the reference kinematics, it is justified to assume that the negative change of the parameter would produce a mirror image of the effect of the current results, and hence can be extrapolated within the same magnitude limit.

It can be observed from the results that the net drag force increases as the bias of the mean positional angle of mid-sweep plane is increased. The lateral force produced by the left wing is also significantly increased in magnitude, but this effect can be cancelled by the opposite wing doing the same flapping kinematics and resulting in no net lateral force produced. As expected, the shifting of centre of lift produces net pitch moment on the insect body that could be used to counter balance the moment due to the aft-position of the centre of mass when the insect is hovering. Changes in roll moment and yaw moment are very small and are cancelled out by the symmetry of wing flapping motion by the right wing. In addition, it can be seen that at  $10^\circ$ , there is 2% increase in lift due to most likely wing-wing interaction, and hence the limit of variation of this parameter was decided to be reduced to within the range of  $-5^\circ$  to  $5^\circ$ . Hence, in general, one can conclude that the aerodynamic force changes are linear with respect to this parameter within this small range specified.

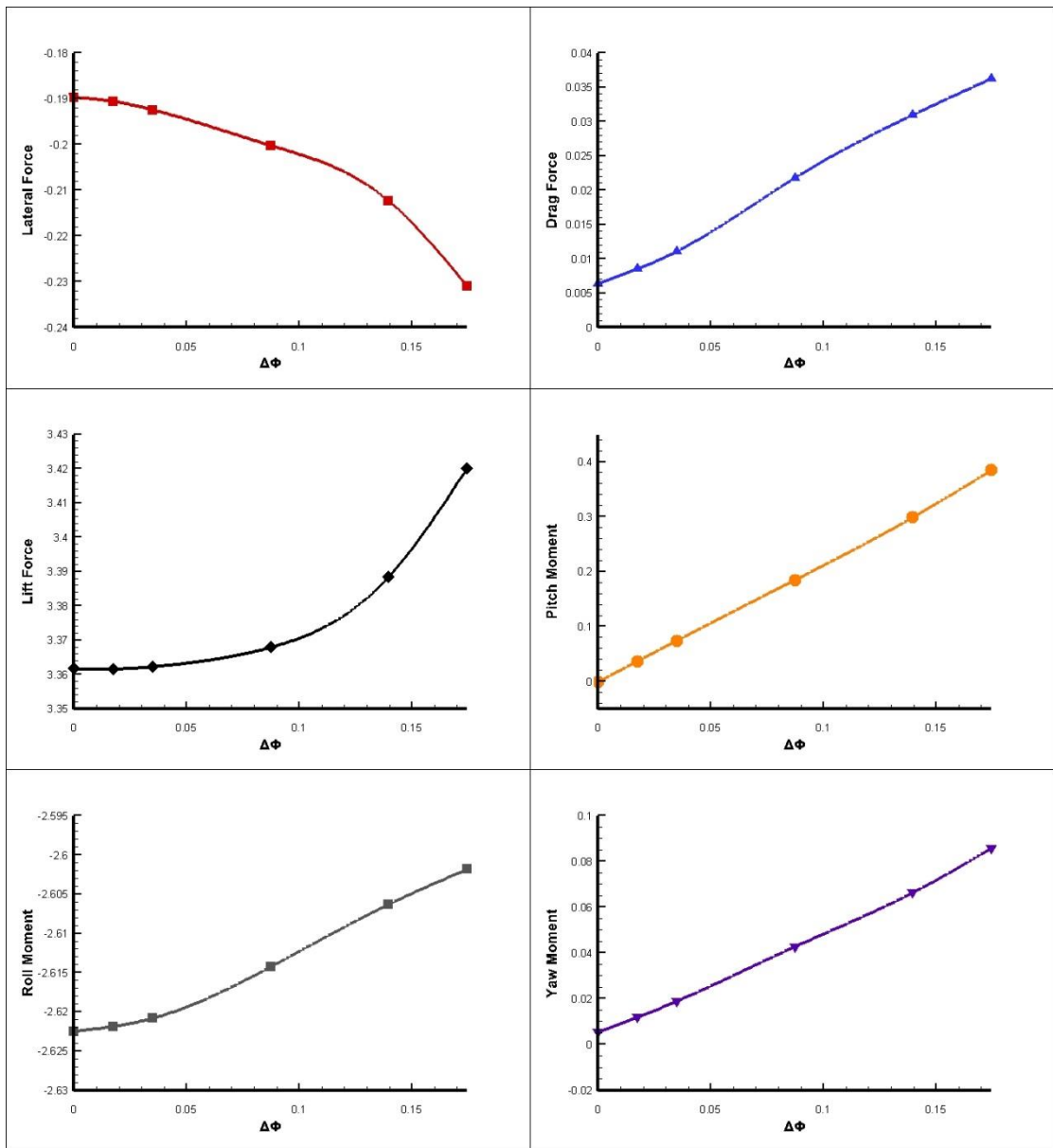


Figure 6.3 The effect of variations in mean positional angle of mid-sweep plane on aerodynamic force and moment productions of flapping wings

### 6.3.2 Effect of Changes in Sweep Amplitude on Mean Aerodynamic Force and Moment Productions

The maximum sweep angle of the referenced flapping kinematics is  $140^\circ$ , and the sweep amplitude is therefore  $70^\circ$ . The small variation for this parameter is specified to be from  $-5^\circ$  to  $10^\circ$ , and the resulting mean aerodynamic forces and moments produced are plotted in Figure 6.4. The wing-wing interaction effect at angles larger than  $160^\circ$  is expected and the range limit is decided to be not larger than  $10^\circ$ .

It can be seen that the lift force produced by the wing is most affected by the

changes of this parameter. This is expected due to the increasing translational velocity of the wing when the sweep amplitude is increased and hence larger lift force produced. This agrees well with observations of insects increasing stroke amplitudes when carrying loads. Due to symmetry of the sweep mid-plane, no net drag force is affected, so are the pitch and yaw moments. The roll moment is substantially increased in magnitude in conjunction with the increasing lift force as a result.

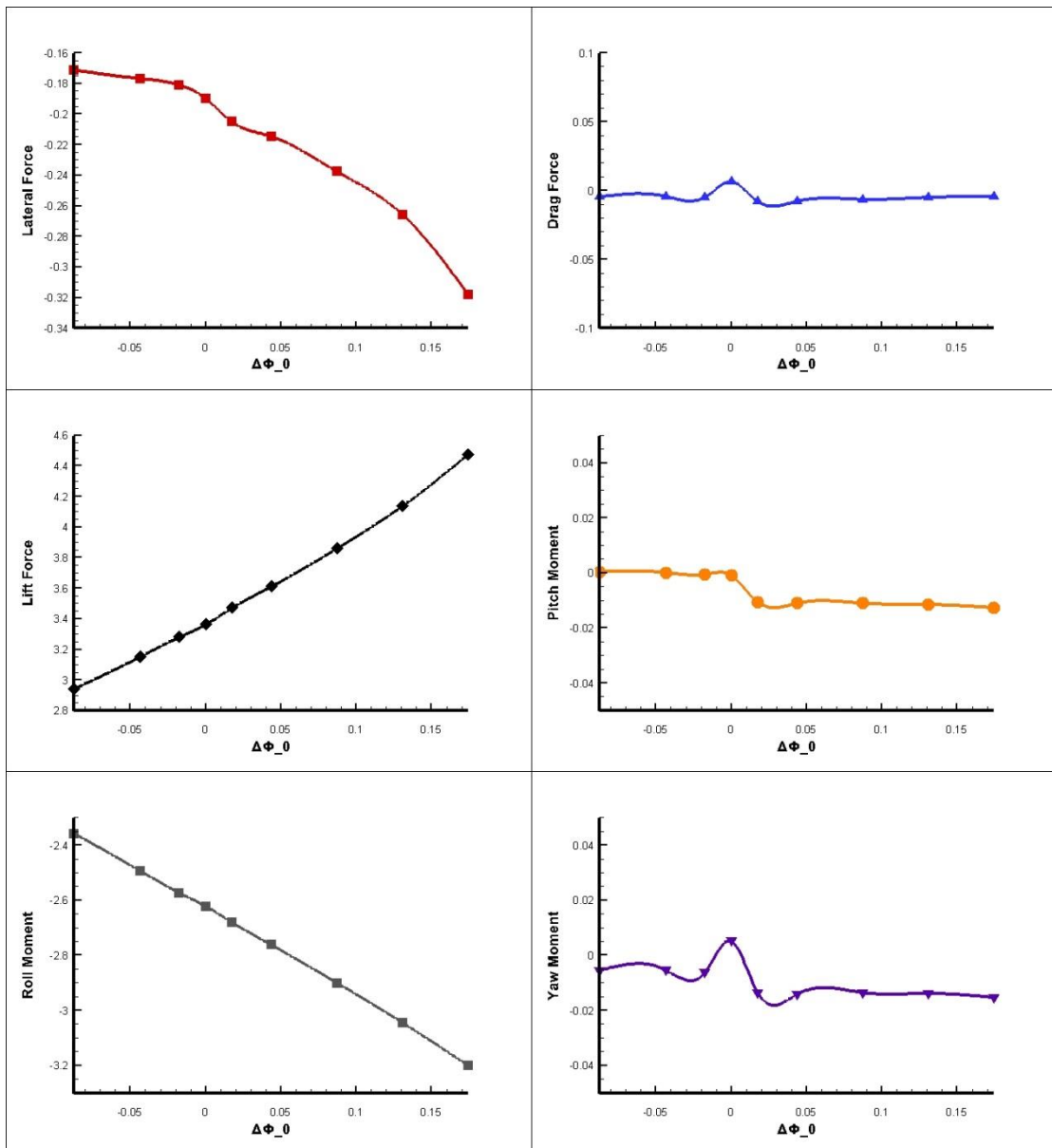


Figure 6.4 The effect of changes in sweep amplitude on aerodynamic force and moment productions of flapping wings



### 6.3.3 Effect of Variations in Mean Positional Angle of Mid-Twist Plane on Mean Aerodynamic Force and Moments Productions

The mean positional angle of mid-twist plane of flapping wing affect the angle of attack in upstroke and downstroke flapping motions together and results in larger minimum angle of attack in one stroke than the other. The variation of this parameter is changed from 0 to 20°, and the negative quantities can be extrapolated due to symmetry equivalence of the up and down stroke in a reference wing beat cycle. The result are plotted in Figure 6.5.

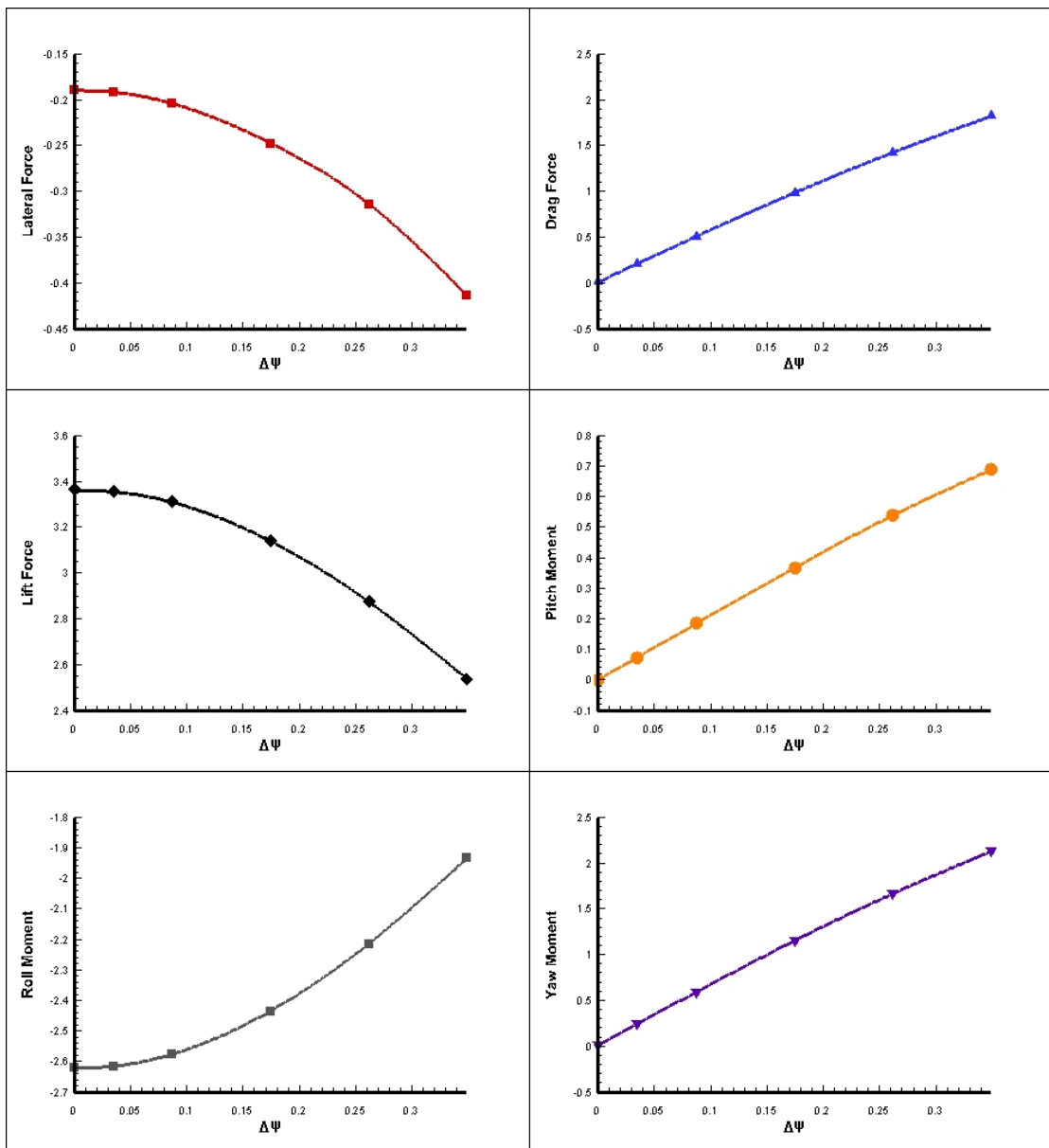


Figure 6.5 The effect of variations in mean positional angle of mid-twist plane on mean aerodynamic force and moment productions of flapping wings

It can be seen that the increasing value of the parameter causes substantial increase

of the drag (thrust) force in the positive direction. This could provide means for the insect to generate thrust while maintaining almost horizontal stroke plane during flapping. At the same time, the lift force drops and the corresponding roll moment magnitude drops as well. However, a net pitch moment is increased, as can be seen in the results, which indicates an off-centre mean lift production which is higher in upstroke (large angle of attack) than in downstroke. In addition, the yaw moment which is affected by the drag force also increases. A generally linear variation of all the force and moment quantities are observed with respect to the changes of this parameter and hence the variation limit of this parameter can be specified to be from  $-20^\circ$  to  $20^\circ$ .

#### **6.3.4 Effect of Changes in Twist Amplitude on Mean Aerodynamic Force and Moment Productions**

The twist amplitude affects the angle of attack of both upstroke and downstroke simultaneously while keeping symmetry of the twist rotation of the wing by maintaining zero bias of the mean positional angle of mid-twist plane. The variation of this parameter is limited to from  $-20^\circ$  to  $15^\circ$ , which corresponds to minimum angles of attack of the wings during each stroke from  $60^\circ$  to  $25^\circ$ . The results are plotted in Figure 6.6.

Simple analysis of Figure 6.6 shows that the variation of the aerodynamic forces and moments generated is linear proportional to the change in twist amplitude in the range from  $-5^\circ$  to  $15^\circ$ , during which the lift force continues to decrease with increasing twist amplitude (smaller minimum angle). It also reveals a maximum lift force generation at a minimum angle of attack of between  $45^\circ$  and  $50^\circ$  when the prescribed flapping kinematic model is used. This agrees well with experimental observations by Sane and Dickinson (Sane & Dickinson, 2001). Furthermore, due to symmetry of the wing sweep (zero bias of the mean positional angle of mid-sweep plane), almost zero net drag (thrust) force is generated due to the parameter changes.

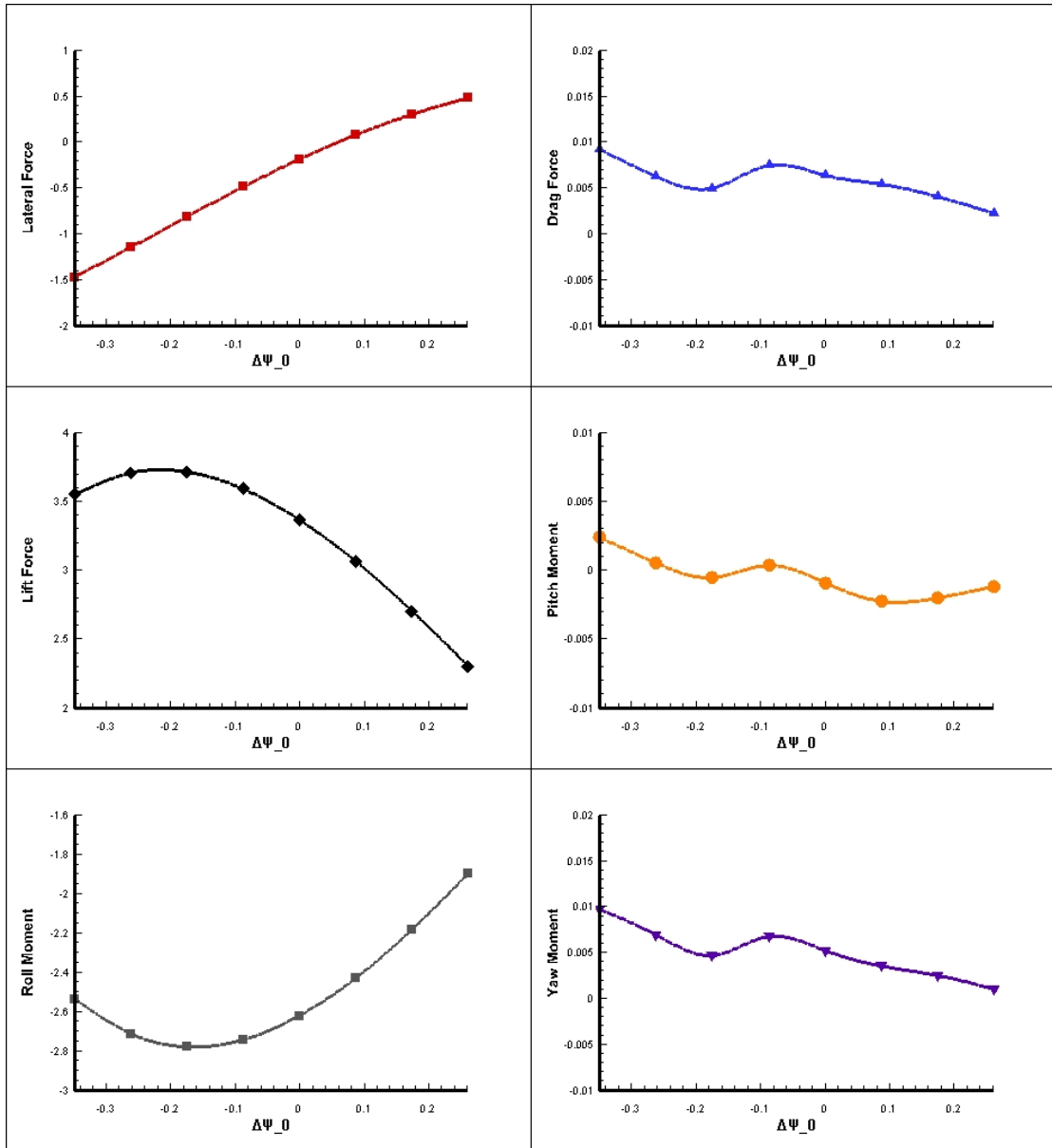


Figure 6.6 The effect of changes in twist amplitude on mean aerodynamic force and moment productions of flapping wings

### 6.3.5 Effect of Variations in Twist Phase Difference on Mean Aerodynamic Force and Moment Productions

In the referenced kinematic model with trapezoidal kinematic function, there is an existing prescribed leading phase difference of wing twisting to sweeping by  $-0.0721T$  (Where  $T$  is the unit time of one wing beat cycle). Therefore, the changes in the twist phase angle difference in the current study adds onto the existing phase difference and does not represent an actual phase leading difference value. The twist phase difference is investigated from a limit of  $-0.10T$  to  $0.15T$ , in which negative values represent increased phase leading and positive value represent increased phase lagging. And at a

value of  $0.0721T$ , there is no phase difference between twisting and sweeping motion of the wing in the flapping kinematic model. The results are plotted in Figure 6.7.

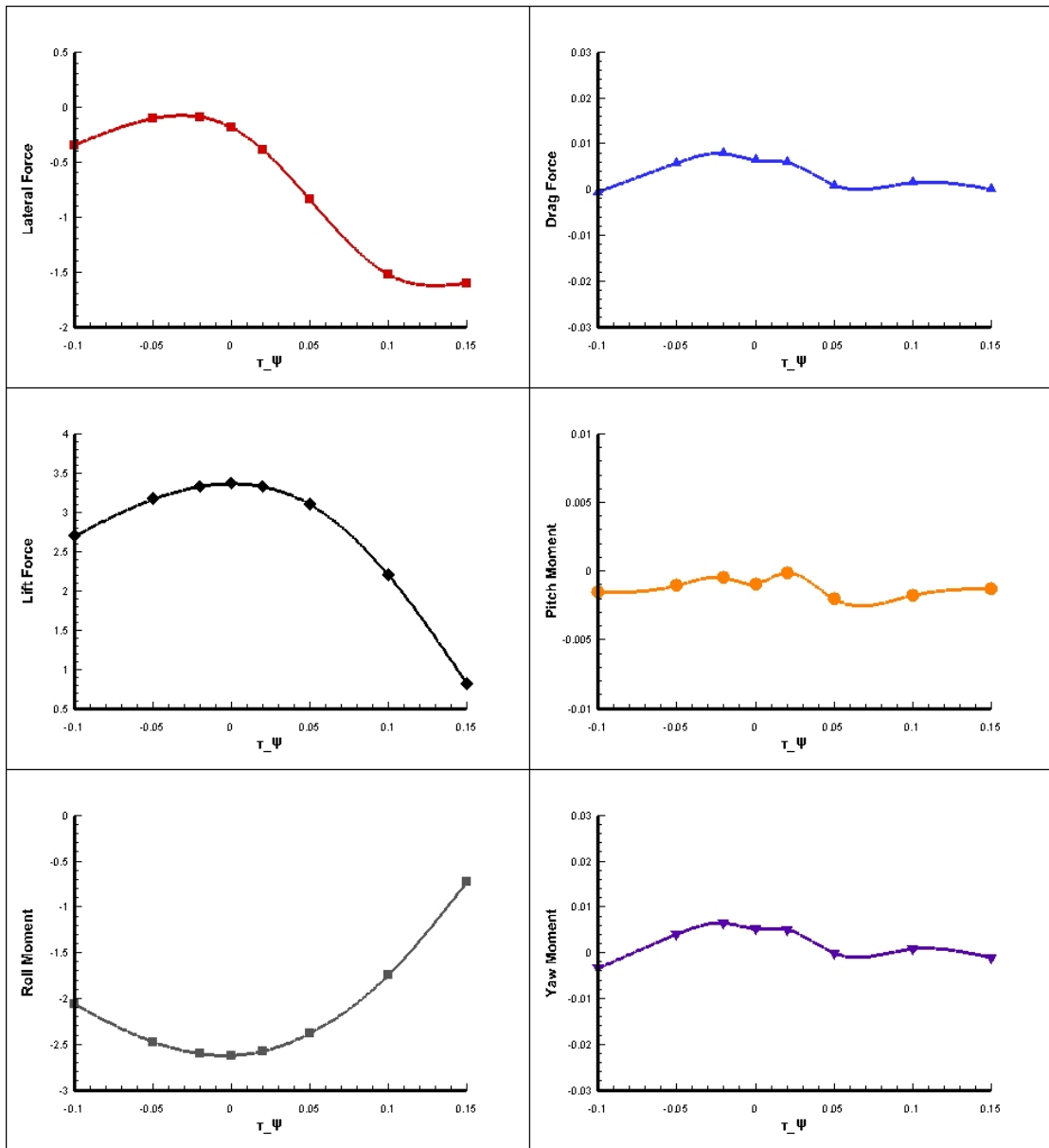


Figure 6.7 The effect of variations in twist phase angle difference on mean aerodynamic force and moment productions of flapping wings

It can be seen that the relationship of the aerodynamic force and moment productions and the twist phase angle variations is quite non-linear. This could be due to the complex transient effects associated with wing wake interaction, which has been discussed in Chapter 4. Hence, a much reduced limit of proportionality in this particular parameter needs to be introduced and the resulting limit is hence set to be within the range of  $-0.05$  and  $0.05$ , where variations in lift force is less than 3%. Furthermore, these results reinforce the conclusion of the earlier kinematics analysis studies that the maximum lift is achieved at around  $-0.07$  to  $-0.08$  phase difference (leading), agreeing

well with experimental observations (Dickinson et al., 1999). However, it should be pointed out that, due to non-linearity, the applicability of this parameter in the definition of the preliminary control model is limited.

### **6.3.6 Effect of Variations in Mean Positional Angle of Mid-Elevation Plane on Mean Aerodynamic Force and Moment Productions**

It is important to point out here that, in the reference kinematic model, no elevation angle is introduced, which is equivalent to 0 bias of the mean positional angle of mid-elevation plane, so the wing stroke takes place in a horizontal plane. Therefore, the variation in bias of the mean positional angle of mid-elevation plane would lead to the flapping wing to sweep in a plane with a constant elevation angle from the horizontal plane. When viewed from the front and frozen in time at mid-stroke, the wings exhibit a similar configuration to the dihedral or anhedral aircraft wings in this configuration. It is known that dihedral formation of swept wings on aircraft enhances the static stability of the aircraft, however, the effect of dihedral angle of flapping wings in the case of insect flight is not known.

The present study varies the mean positional angle of the mid-elevation plane from  $-10^\circ$  to  $20^\circ$  to investigate the effects on mean aerodynamic force and moment productions, and the results are shown in Figure 6.8.

It can be seen that, as the bias of the mean positional angle of the mid-elevation plane is increased in the positive direction (a more dihedral configuration), the lift force produced increases. This could be a potentially unstable configuration for which when the insect rolls, higher wing generates higher lift and lower wing generates lower lift, resulting in further rotation in the same direction. However, as the elevation angle is increased beyond  $10\sim 15^\circ$ , this relationship reverses (negative gradient in the lift curve), which could theoretically produce restoring moment on rolling perturbations and enhance roll stability. This effect is further explored in an FSI study where 2 insect models are simulated to perform same kinematic flapping motion in hovering with the only difference of a  $15^\circ$  bias of mean positional angle of mid-elevation plane introduced into the second insect model (large dihedral configuration). The results show reduced maximum roll angle deviations from reference state after 20 cycles ( $0.02^\circ$  vs  $0.1^\circ$ ) for the case with large dihedral configuration.

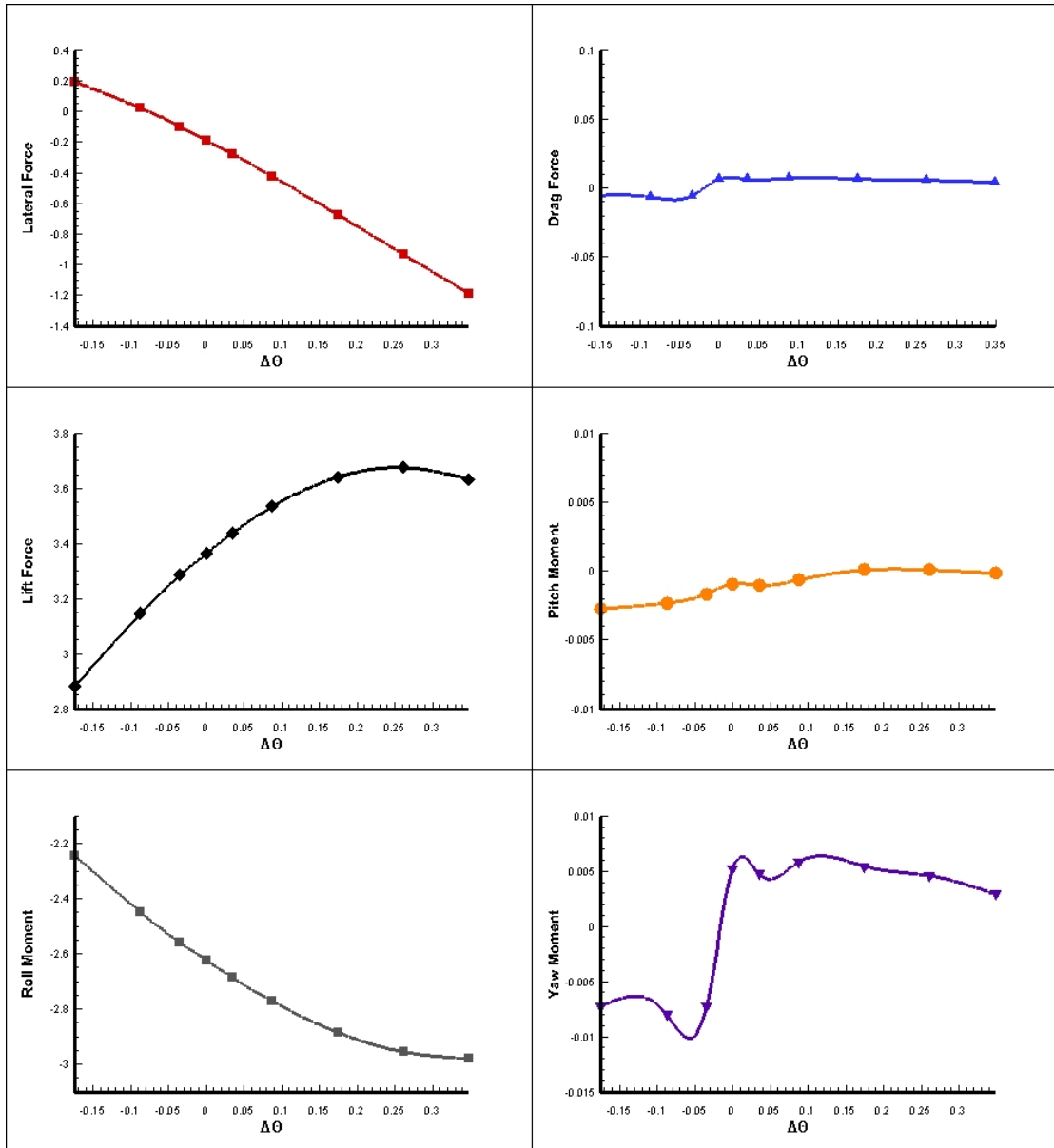


Figure 6.8 The effect of variations in mean positional angle of mid-elevation plane on mean aerodynamic force and moment productions of flapping wings

A generally linear relationship is observed for all forces and moments evaluated. The lift force and the lateral force increases (in negative direction) with increasing bias of the mean positional angle of mid-elevation plane. No change of net drag force is observed and the rolling moment, as a result of increasing lift force, increases in magnitude too. In the interest of developing an active control model, the range of limit is set from  $-10^\circ$  to  $10^\circ$ . The larger positive bias in the mean positional angle of the mid-elevation plane is excluded despite its effect on better static roll stability with dihedral wing configuration.

### **6.3.7 Effect of Changes in Elevation Amplitude on Mean Aerodynamic Force and Moment Productions**

In this case, the elevation angle is modelled using a sinusoidal kinematic function, the amplitude is 0 in the referenced case. The parameter is varied from 0 to 20 ° to obtain the effect on the mean aerodynamic force and moment productions. The negative range is not explored for the reason that the elevation angle kinematic function is set to have no phase angle difference from the sweep kinematic function. This means that the wing reaches maximum elevation before the start of downstroke and minimum elevation before the start of upstroke and the negative elevation amplitude simply reverses the order. Since the sweep is symmetrical (described by the reference kinematics), the effect of negative values of the parameter can be extrapolated from the obtained results of the current study.

In addition, the flapping wing motion when observed from the side of the insect will have a similar path as a rotated stroke plane of the flapping wings. However, it should be noted that they are not identical. When the stroke plane is rotated, the entire wing motion frame is rotated and so the relative angle of attack of the wings to the flow is unchanged (assuming hovering in still air). On the other hand, when changes of elevation amplitude is implemented, the wing twisting kinematic model is unaffected and hence the resulting wing flapping motion has a larger relative angle of attack in downstroke and smaller relative angle of attack in upstroke (in the same hovering case). It is however, possible to simulate a stroke plane rotation by carefully incorporating both the change in elevation amplitude and the mean positional angle of mid-twist plane.

As expected, the results reveal significant effect of this parameter on net drag force produced, the main source of thrust for insects in forward flight. The relationship is linear on the mean drag force produced with respect to increasing elevation amplitude. The pitch and yaw moments are also influenced by this parameter in a linear manner. The changes in lift is very small, less than 2% within the range and hence the roll moment is not affected significantly either. One should note, however that, the sinusoidal function used to describe elevation kinematics in the current study is restricted to a periodicity of 1, higher order periodicity is not specifically explored due to the higher order of complexity in the unsteady aerodynamic effects associated and it is not known if insects are actually capable of changing periodicity of elevation

kinematics during actual flight.

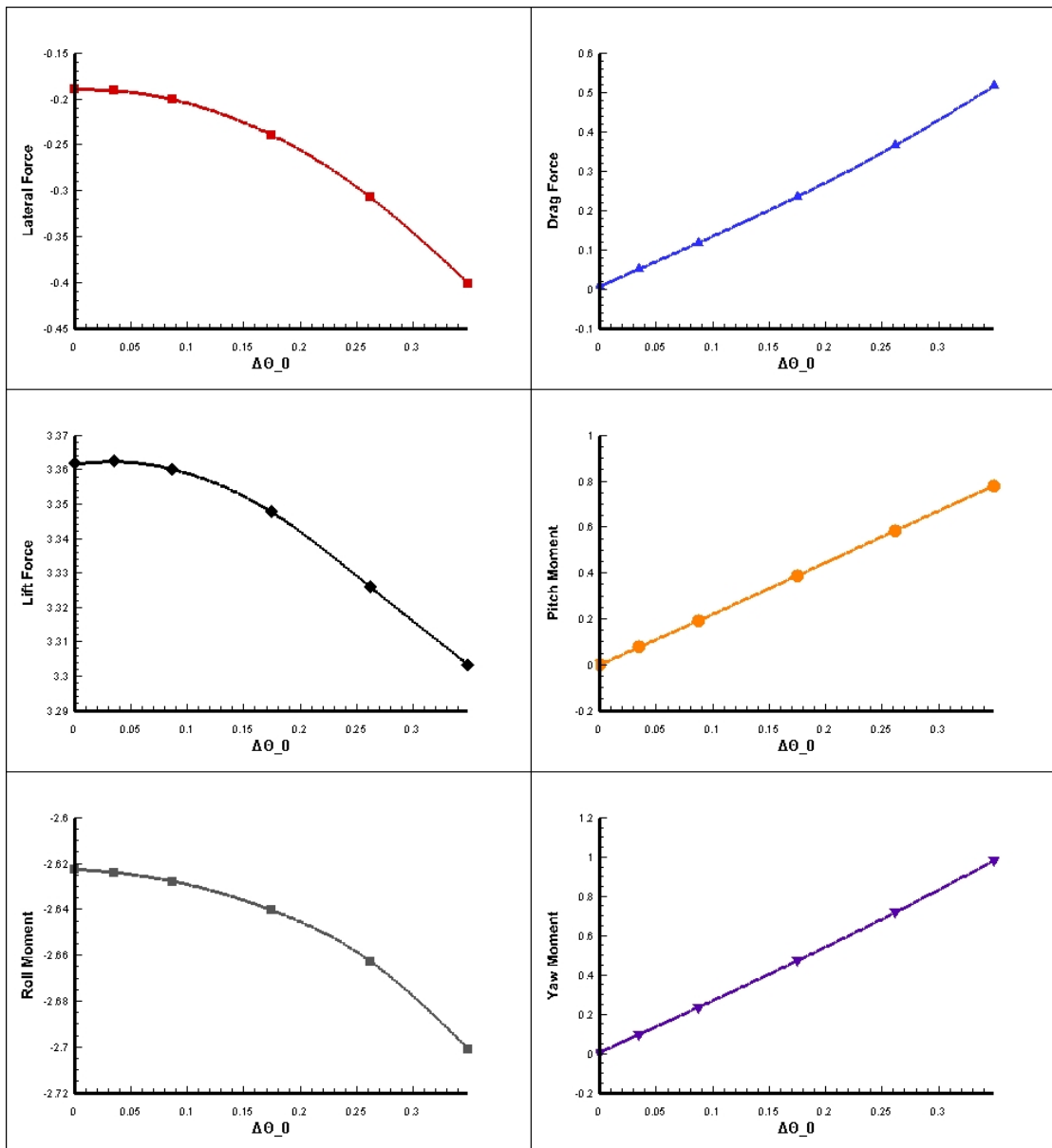


Figure 6.9 The effect of changes in elevation amplitude on mean aerodynamic force and moment productions of flapping wings

### 6.3.8 Effect of Changes in Elevation Phase Difference on Mean Aerodynamic Force and Moment Productions

The elevation kinematic is modelled by a sinusoidal function with single periodicity in each wing beat cycle. Therefore, the change in the parameter of elevation phase difference relative to wing sweep changes the shape of the wing tip path from single line trace, when  $\tau_\theta = 0$ , to an “oval” shape, when  $\tau_\theta = 0.25$ . Hence, in this investigation, the wing elevation phase difference is changed from 0 to 0.25, and the



prescribed elevation amplitude is  $10^\circ$  and fixed. The reference data at  $\tau_\theta = 0$  in this particular study is in fact the result obtained in a case with  $10^\circ$  elevation amplitude in the earlier analysis. The comparison of the results are shown in Figure 6.10.

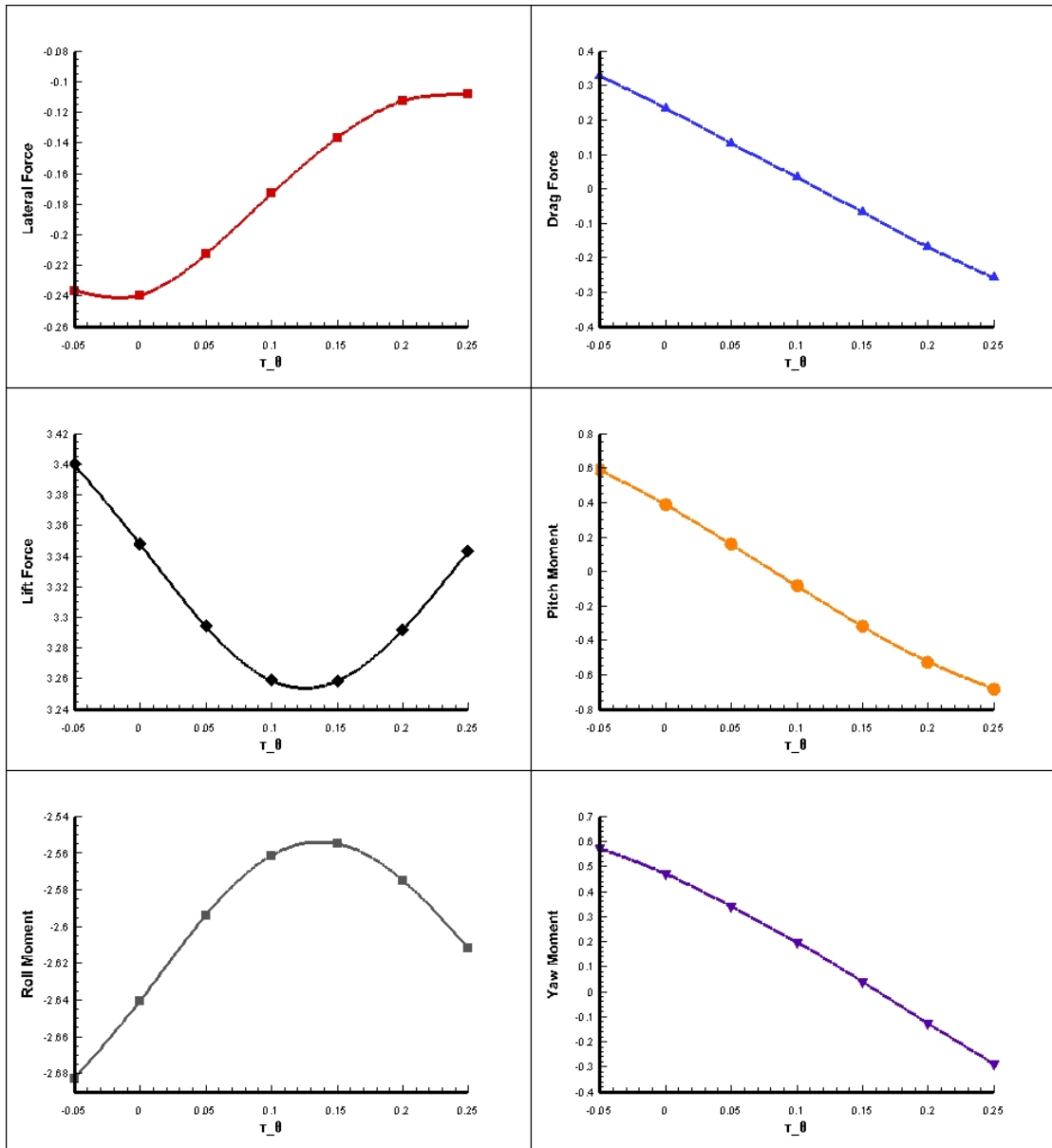


Figure 6.10 The effect of variations in elevation phase difference on mean aerodynamic force and moment productions of flapping wings

A generally linear relationship can be observed from the results shown in most of the aerodynamic force and moment produced. The most significant effect is observed in net drag (thrust) force which continues to decrease and changes direction (then continue to increase in magnitude) until the wing tip path forms an “oval” shaped pattern. It is interesting to note that the net drag force in this case is not zero as one would expect. Instead, the wing produces a net drag (thrust) force towards the front. When forces are analysed with respect to the wing elevation angles, it could be seen

that during the upstroke, as the wing is moving with a negative elevation angle, it travels into the shed vortices of the previous downstroke and the interaction is strong enough to produce a larger drag force peak at the beginning of upstroke shown in the plot, which explains the gain of drag force towards the front of the insect. On the other hand, the lift force is also slightly influenced by this parameter in which a minimum lift is observed in between  $\tau_\theta = 0.1$  and  $\tau_\theta = 0.15$ , this could also be due to the wing wake interaction and requires further extensive investigations.

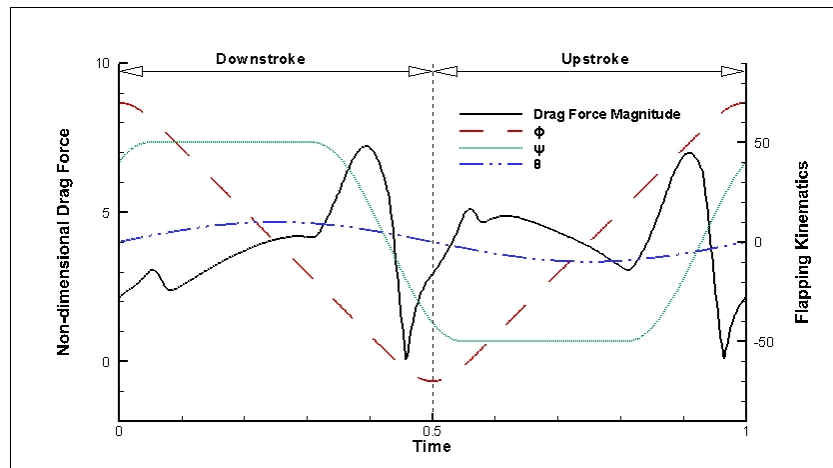


Figure 6.11 The observed difference of drag force in upstroke compared to downstroke due to wing wake interaction in an "oval" shaped wing flapping kinematics

## 6.4 The Proposed Model for Preliminary Control of Flapping Flight

The lack of inherent stability in insect flapping flight during hovering and low speed flight suggests that insects actively adjust flapping kinematic parameters during flying (Mou & Sun, 2012). As identified by Vogel (Vogel, 1967) and later quantified experimentally by fry et al. (S. N. Fry et al., 2003), insects are capable of controlling the time forces and moments generated by the flapping wings during each wing stroke by modification of several flapping kinematic parameters. Parameter variations during such control inputs are remarkably small even for aggressive manoeuvres such as fast 90 ° collision avoidance manoeuvre known as saccades (S. N. Fry et al., 2003). However, due to the complexity of flapping wing kinematics, current control models have not yet achieved effect control of flapping flights with insect like agility and stability.

The parameterisation of flapping kinematics in the present study has obtained a

linearised relationship of identified key kinematic parameters and the aerodynamic forces and moments produced within small constraint of perturbation limits. This allows the further reduction of parameters for proposing a preliminary simplified model to demonstrate the possibility of 6DOF control of the insect model in flapping flight.

#### 6.4.1 The Approach for Derivation of a Simplified Model

To simplify the model derivation, the inertia effect of the wings are neglected in the present study. It is assumed that the wings simply provide aerodynamic forces and moments on the insect body and are constrained to the flapping motion based on the kinematic model specified. Hence, the motion of the insect has only 6 degree of freedom on its body, which are subjected to the 3 translational forces  $F_x$ ,  $F_y$ ,  $F_z$  and the 3 rotational moments  $M_x$ ,  $M_y$ ,  $M_z$  from aerodynamic forces and moments generated by the flapping wings. In this study, the simplified model is only limited to the application of hovering of insects, and therefore, the initial values of  $U$ ,  $V$ ,  $W$ ,  $P$ ,  $Q$  and  $R$  describing the translational and rotational velocities are zero.

Therefore, a simple model is suggested as follows:

$$\Delta O = M \cdot \Delta P \quad [6.1]$$

Where  $\Delta O = \begin{pmatrix} \Delta F_x \\ \Delta F_y \\ \Delta F_z \\ \Delta M_x \\ \Delta M_y \\ \Delta M_z \end{pmatrix}$  describes the perturbation forces and moments acting on the insect.  $\Delta P = \begin{pmatrix} \Delta P_1 \\ \Delta P_2 \\ \vdots \\ \Delta P_n \end{pmatrix}$  represent the control input of kinematic parameter terms

derived earlier, where  $n \geq 6$ .  $M$  is the coefficient matrix which describes the relationship of the parametric inputs to the forces and moments output by the flapping wings. The information of matrix  $M$  can be obtained from the linearised gradient of the earlier analysed effects of the variation in parameters on the mean aerodynamic forces and moments produced in a pre-set small limited range from the referenced state.

#### 6.4.2 Determination of the Coefficient Matrix

Since an insect has at least 1 pair of wings, each wing flapping independently can be described by a combination of 8 parameters presented in the parameterisation. Hence, a total of 16 parameters are available for the determination of the coefficient matrix. Despite the relative linear relationship of each parameters to the mean aerodynamic force results presented earlier, the coupled effect of combined parameter changes are not known and may not be assumed linear. Hence, the choice of parameters for the determination of the coefficient matrix is limited and only a very basic approach (without in depth matrix optimizations) is adopted in this study to quickly yield results for further analysis of the dynamic response of the system in a coupled mode simulation.

In the study, the proposed control model can be summarised in equation form below:

$$\begin{pmatrix} \Delta F_x \\ \Delta F_y \\ \Delta F_z \\ \Delta M_x \\ \Delta M_y \\ \Delta M_z \end{pmatrix} = M \cdot \begin{pmatrix} \Delta \phi_0^{(L)} \\ \Delta \phi_0^{(R)} \\ \Delta \psi^{(L)} \\ \Delta \psi^{(R)} \\ \Delta \theta_0^{(L)} \\ \Delta \theta_0^{(R)} \end{pmatrix} \quad [6.2]$$

$$\text{Where } M = \begin{pmatrix} -0.2497, & 0.0127, & 2.6946, & -0.0572, & -1.5455, & -0.0149 \\ 0.2497, & 0.0127, & 2.6946, & -0.0572, & 1.5455, & 0.0149 \\ -0.3350, & 5.5295, & -1.2713, & 2.0723, & 1.0652, & 6.4774 \\ 0.3350, & 5.5295, & -1.2713, & 2.0723, & -1.0652, & -6.4774 \\ -0.3000, & 1.3296, & -0.0762, & 2.2165, & -0.1162, & 2.6817 \\ 0.3000, & 1.3296, & -0.0762, & 2.2165, & 0.1162, & -2.6817 \end{pmatrix}$$

By inverting the coefficient matrix, we can obtain the formulation

$$M^{-1} \cdot \begin{pmatrix} \Delta F_x \\ \Delta F_y \\ \Delta F_z \\ \Delta M_x \\ \Delta M_y \\ \Delta M_z \end{pmatrix} = \begin{pmatrix} \Delta \phi_0^{(L)} \\ \Delta \phi_0^{(R)} \\ \Delta \psi^{(L)} \\ \Delta \psi^{(R)} \\ \Delta \theta_0^{(L)} \\ \Delta \theta_0^{(R)} \end{pmatrix} \quad [6.3]$$

Hence we can determine the required values of the changes in the kinematic parameters for each required force variation during perturbation. This provides the preliminary framework for further derivation of a control model.

### **6.4.3 Verification of the Model**

Equation [6.2] and [6.3] describes the linearized relations between force/moment increments and variations in kinematic parameters about an appropriate equilibrium reference state. In the sections below, we experimented using the applications of these relations. The application scenarios involve the specification of a required force or moment increment which is then reproduced by gradually applying the kinematic variations indicated by equation [6.3]. The kinematic changes given by [6.3] are typically applied over 3 wing beat cycles. The flyer initially perform referenced kinematic model flapping motion and the kinematic input is activated at the 10<sup>th</sup> wing beat cycle and increased to the target value given by the equation [6.3] in the 13<sup>th</sup> wing beat cycle. A total of 25 wing beat cycles are simulated. The mean aerodynamic forces and moments measured are plotted over wing beat cycles and the dynamic response is analysed. The results are shown and discussed in the following sections.

### **6.4.4 The Dynamic Response to Parameter Adjustments Based on the Preliminary Model for Targeted Mean Non-Dimensional Lift Force Increase of 0.5**

Figure 6.12 shows the mean aerodynamic force and moment variations as the parameter adjustments are introduced for the targeted mean non-dimensional lift force increase of 0.5, while maintaining the other forces and moments constant.

The results show clearly a linear increase of non-dimensional lift force from 10<sup>th</sup> wing beat cycle to 13<sup>th</sup> wing beat cycle as predicted by the model (the initial spike of the mean non-dimensional lift force before wing beat cycle 2 is due to impulse caused by the starting of the flapping wings in a still fluid). The magnitude of lift increase is however larger than expected, indicating that a correction function or factor may be added into the current preliminary model. The other force variations are unaffected as shown by the relative constant mean forces and moments over the same wing beat cycle. After the 13<sup>th</sup> wing beat cycle, as the targeted variation of kinematic parameters have

been reached, the mean non-dimensional lift force curve becomes flat again indicating little transient effect due to the small range variations as previously expected. The effectiveness of the preliminary model on control of the lift force is hence demonstrated.

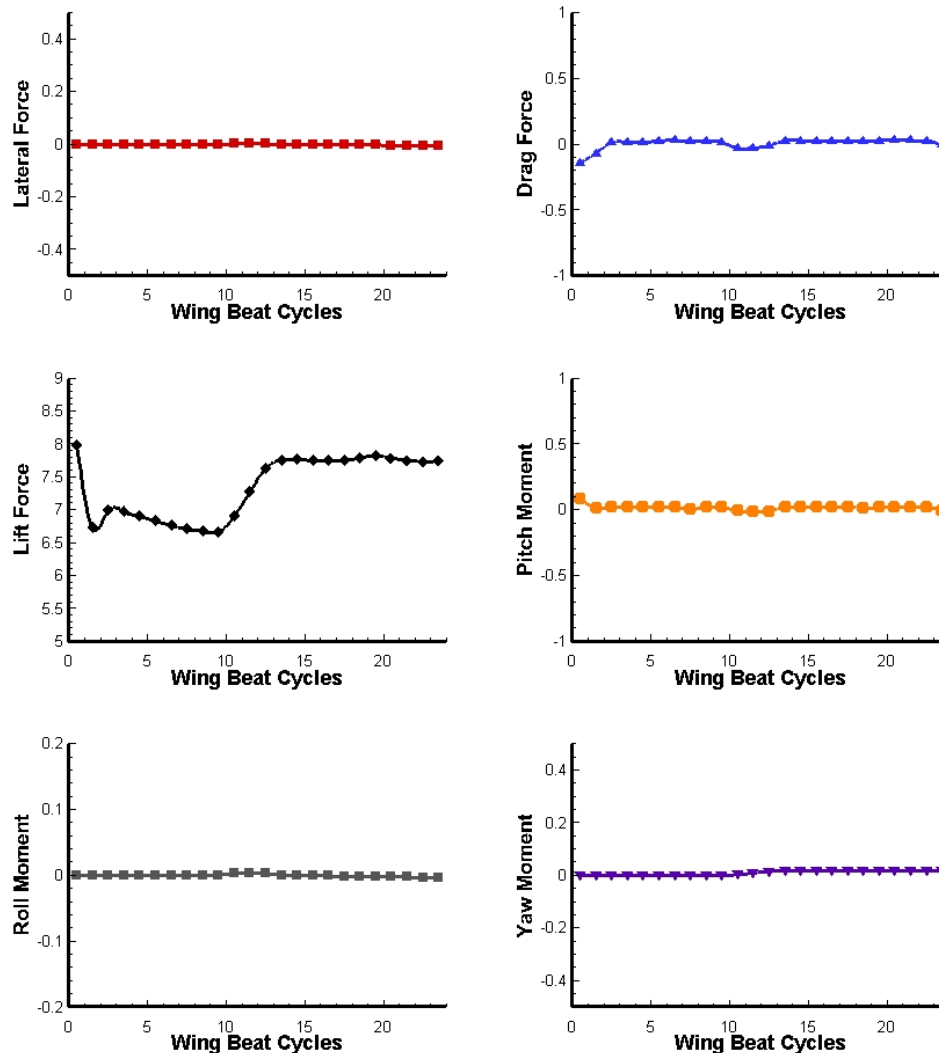


Figure 6.12 The dynamic response of parameter adjustments based on the preliminary model for targeted mean non-dimensional lift force increase of 0.5 while maintaining the other forces and moments constant

#### 6.4.5 The Dynamic Response to Parameter Adjustments Based on the Preliminary Model for Targeted Mean non-dimensional Drag (Thrust) Force Increase of 0.5

Figure 6.13 shows the mean aerodynamic force and moment variations as the parameter adjustments are introduced for the targeted mean non-dimensional drag (thrust) force increase of 0.5, while maintaining the other forces and moments constant.

It can be seen that the drag (thrust) force response shows linear increase in

magnitude from 10<sup>th</sup> wing beat cycle to 13<sup>th</sup> wing beat cycle and then becomes steady further on. However, the direction of the force variation is opposite of the model predictions and the magnitude is slightly higher than the expected value of 0.5. This, nonetheless, still shows the relative linear dynamic behaviour within the constrained limit of the parameter variations and provides as proof of concept for the current preliminary model. Additionally, the pitch moment is also affected as a result of the parameter variations, which suggests more complex non-linearity of the coupled effect of the elevation amplitude and bias in mean positional angle of mid-twist plane. The pitch-up moment caused may be counter-balanced by introduction of bias in mean positional angle of mid-sweep plane, which is not included in the present preliminary model and its effect may be further evaluated in future studies.

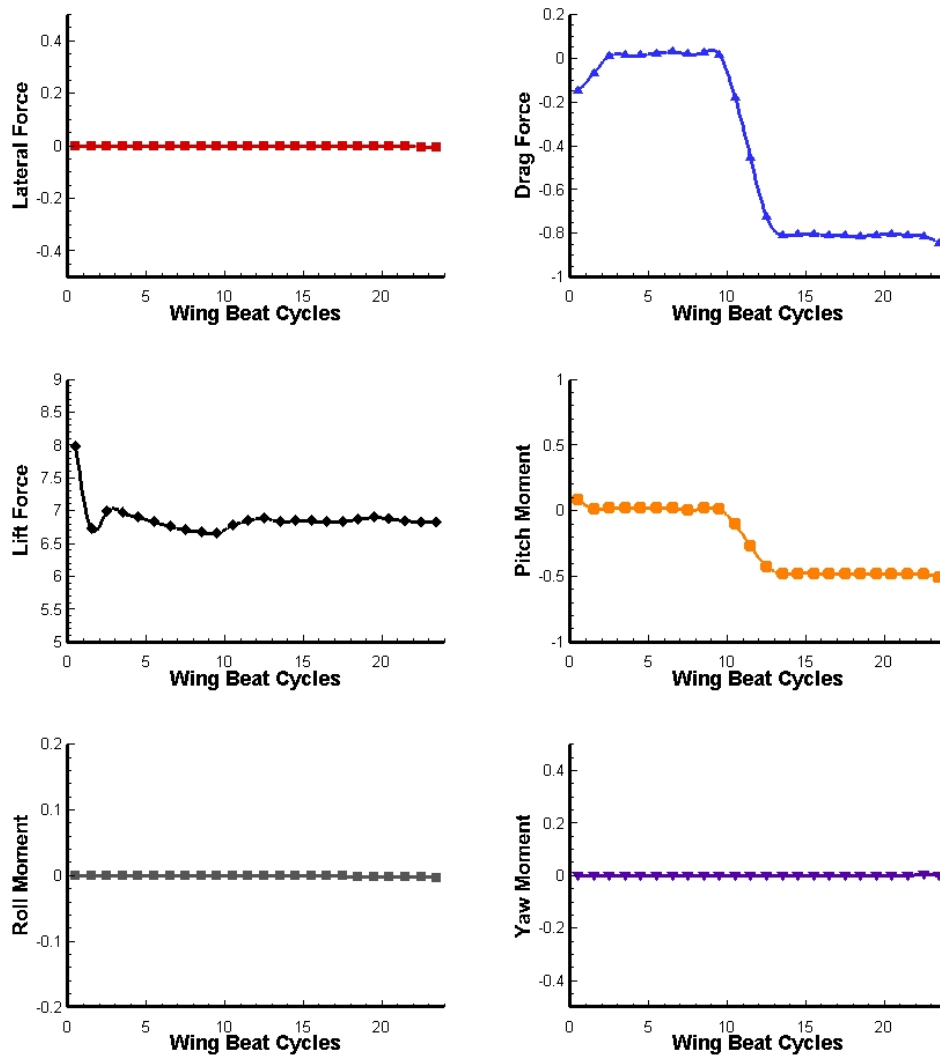


Figure 6.13 The dynamic response of parameter adjustments based on the preliminary model for targeted mean non-dimensional drag (thrust) force increase of 0.5 while maintaining the other forces and moments constant

### 6.4.6 The Dynamic Response to Parameter Adjustments Based on the Preliminary Model for Targeted Mean Non-Dimensional Lateral Force Increase of 0.02

Figure 6.14 shows the mean aerodynamic force and moment variations as the parameter adjustments are introduced for the targeted mean non-dimensional lateral force increase of 0.02, while maintaining the other forces and moments constant.

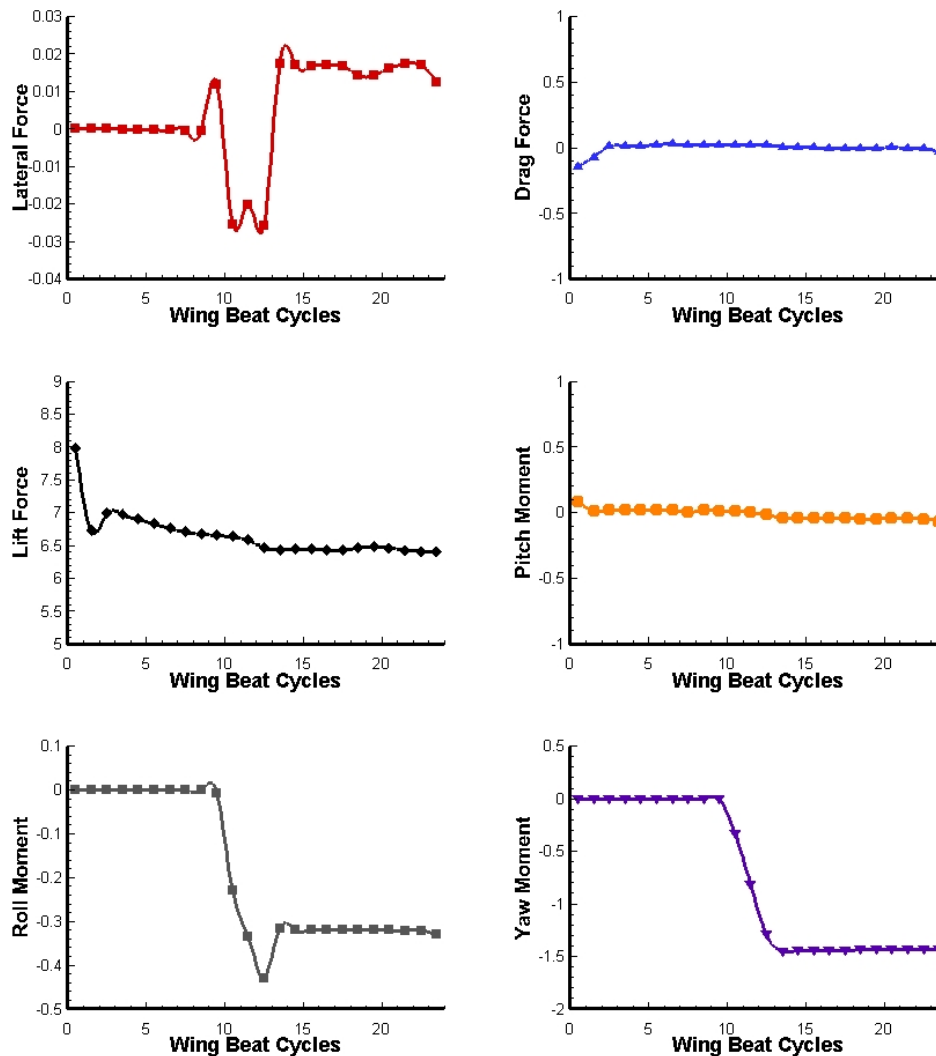


Figure 6.14 The dynamic response of parameter adjustments based on the preliminary model for targeted mean non-dimensional lateral force increase of 0.02 while maintaining the other forces and moments constant

The curve shows a clear increase of mean non-dimensional lateral force of magnitude 0.02 after 13<sup>th</sup> wing beat cycle as compare to the mean before 10<sup>th</sup> wing beat cycle. However, the variation in between was not linear and may have been due to extensive unsteady aerodynamic interactions. On the other hand, the net roll and yaw moments have also been altered during the process and results in a significant



asymmetry on the left and right wings. This could be due to the simplification of the assumption during the derivation of the current preliminary model, as the coefficient matrix is determined from simulation results of symmetric flapping kinematics. Hence, the current preliminary model may have inherent disadvantage in predicting the dynamic response of asymmetric aerodynamic forces and moments produced by flapping wings of the insect such as lateral force, roll moment and yaw moment.

#### 6.4.7 The Dynamic Response to Parameter Adjustments Based on the Preliminary Model for Targeted Mean Non-Dimensional Pitch Moment Increase of 0.2

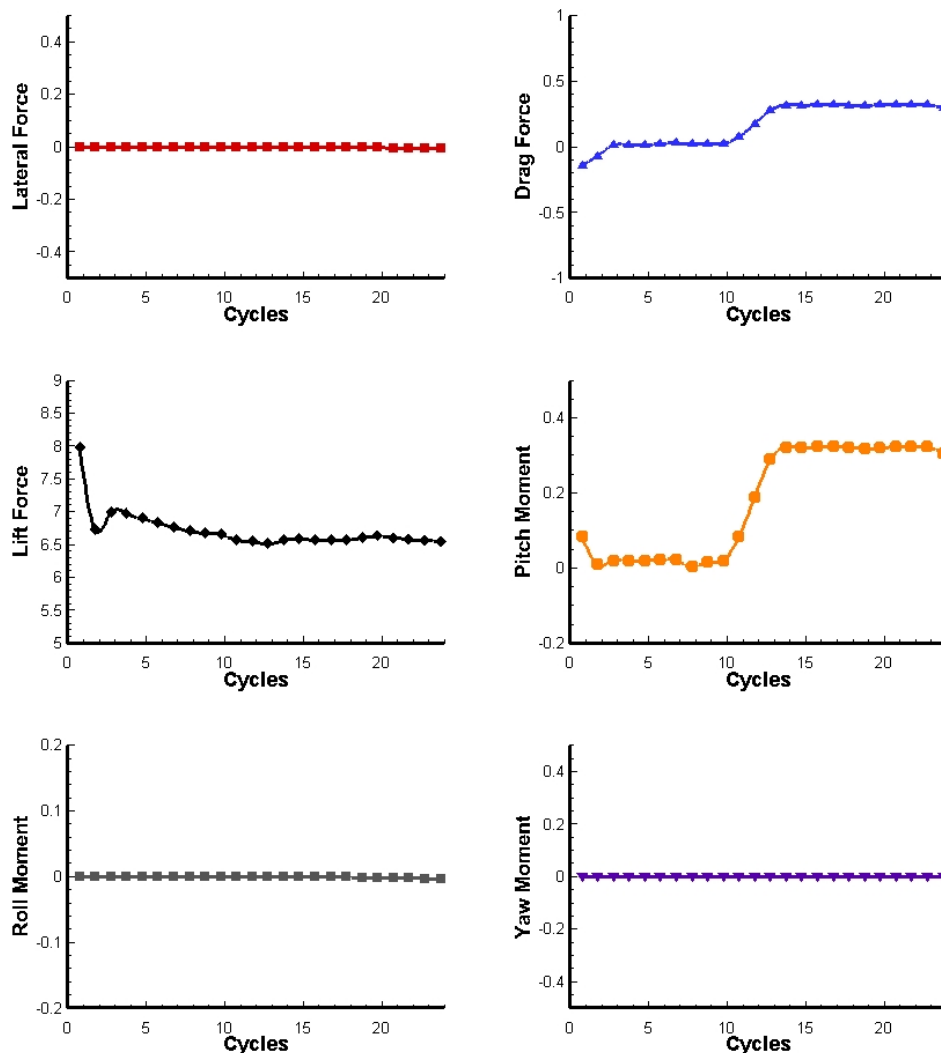


Figure 6.15 The dynamic response of parameter adjustments based on the preliminary model for targeted mean non-dimensional pitch moment increase of 0.2 while maintaining the other forces and moments constant

Figure 6.15 shows the mean aerodynamic force and moment variations as the parameter adjustments are introduced for the targeted mean non-dimensional pitch

moment increase of 0.2, while maintaining the other forces and moments constant.

The original mean non-dimensional pitch moment produced by the insect flapping wings in reference kinematics is zero. It can be seen that the pitch moment increased by approximately 0.3 from the 10<sup>th</sup> wing beat cycle to the 13<sup>th</sup> wing beat cycle, matching very closely with the preliminary model predictions. The other forces and moments show almost no variations in mean magnitude, except a small increase of mean non-dimensional drag (thrust) force during the same process.

#### **6.4.8 The Dynamic Response to Parameter Adjustments Based on the Preliminary Model for Targeted Mean Non-Dimensional Roll Moment Increase of 0.05**

Figure 6.16 shows the mean aerodynamic force and moment variations as the parameter adjustments are introduced for the targeted mean non-dimensional roll moment increase of 0.05, while maintaining the other forces and moments constant.

It can be seen that the net roll moment on the insect increased by approximately 0.23 from a value of 0 in the reference state, and the variation from the 10<sup>th</sup> wing beat cycle to the 13<sup>th</sup> wing beat cycle is linear. It can also be seen that the mean translational aerodynamic forces (lift, drag and lateral forces) show no variations through the same wing beat cycles. However, a coupled effect on the yaw moment can be clearly identified in the plot. This is similar to the observation of lateral force effects previously and hence other parameter adjustments may be introduced to counter balance the yaw moment side effect of the present preliminary model.

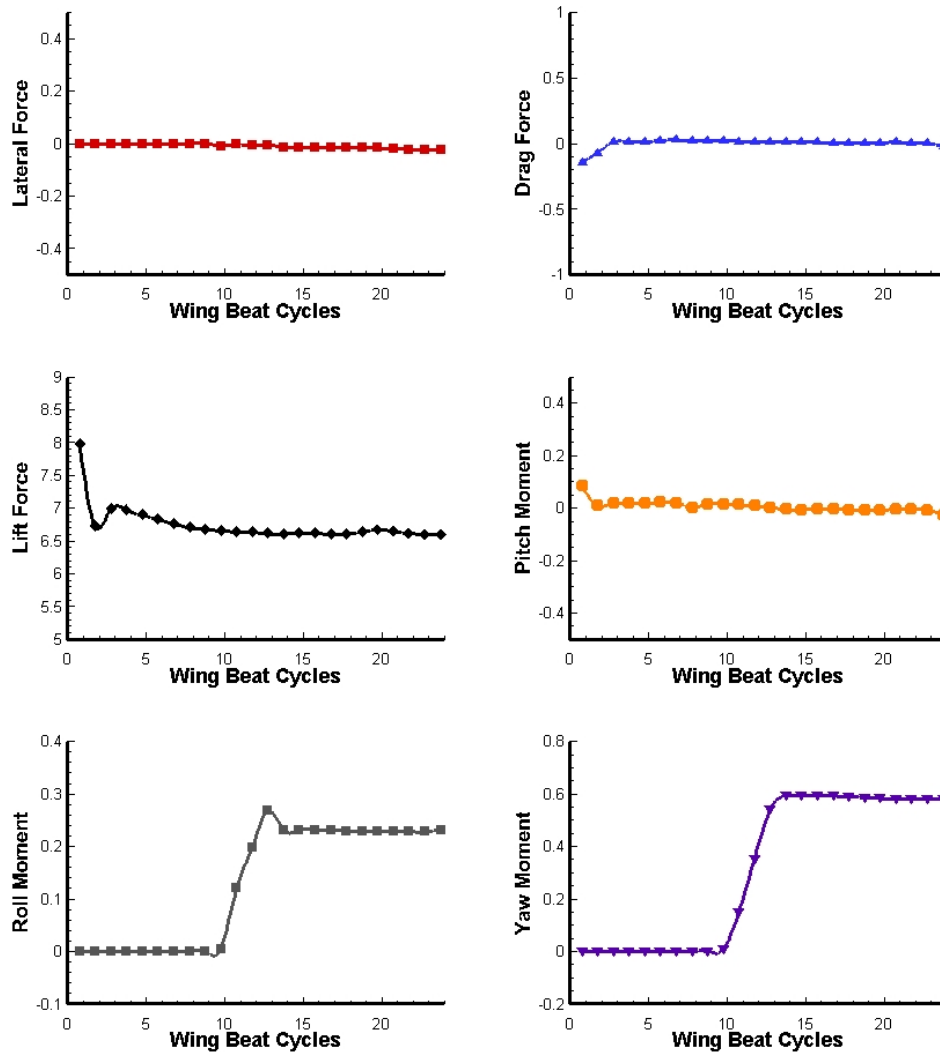


Figure 6.16 The dynamic response of parameter adjustments based on the preliminary model for targeted mean non-dimensional roll moment increase of 0.05 while maintaining the other forces and moments constant

#### 6.4.9 The Dynamic Response to Parameter Adjustments Based on the Preliminary Model for Targeted Mean Non-Dimensional Yaw Moment Increase of 0.2

Figure 6.17 shows the mean aerodynamic force and moment variations as the parameter adjustments are introduced for the targeted mean non-dimensional yaw moment increase of 0.2, while maintaining the other forces and moments constant.

The result further shows the coupling effect of yaw and roll moment in the current preliminary model, despite the linear variations of both when the parameter adjustments are gradually introduced. The magnitude of the net yaw moment produced is also significantly higher than the model prediction of 0.2 showing strong asymmetric unsteady aerodynamic effects caused by the flapping wings. Additionally, the model is

accurate in the prediction of the translational force components which show no significant variations as a result of the parameter adjustments.

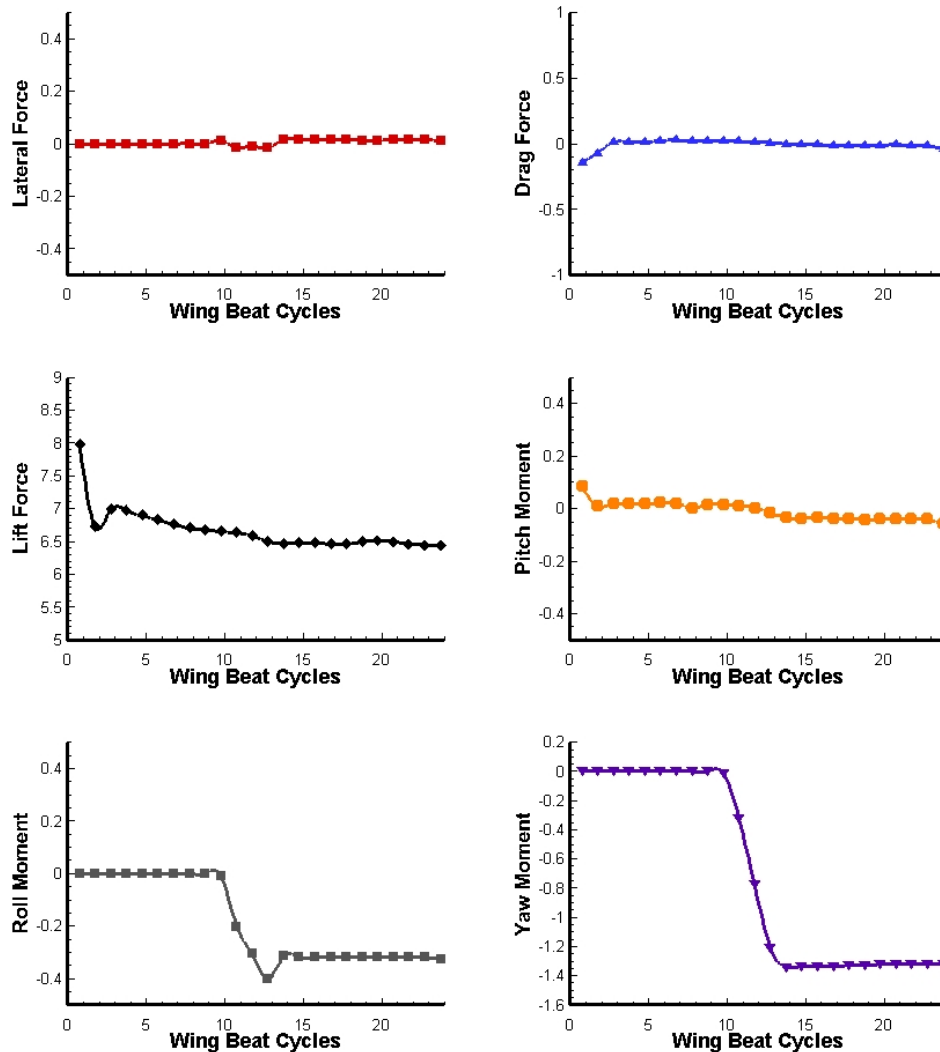


Figure 6.17 The dynamic response of parameter adjustments based on the preliminary model for targeted mean non-dimensional yaw moment increase of 0.2 while maintaining the other forces and moments constant

#### 6.4.10 FSI Testing of the Preliminary Model

A further proof of concept using a set of simulations of the full insect in flapping flight with prescribed kinematics are carried out with the full implementation of FSI as described in Chapter 2. The insect has 6 degrees of freedom and are allowed to start flying from the centre of the flow domain. The position of its centre of mass and the orientation of the body is recorded over time (wing beat cycle) to track the behaviour of the insect due to the aerodynamic forces and moments variations caused by changes

in the kinematic parameters in accordance to the proposed preliminary model. No active control of the insect is introduced in this study and only the effectiveness of the parameter variation provided by the preliminary model in a realistic flow domain with FSI is evaluated.

A total of 3 cases are tested. The first case is the reference case in which the insect performs the aforementioned reference kinematic model. The flapping frequency is slightly reduced and therefore slightly reducing the Reynolds number of the reference case leading to reduced lift generation, so the insect is expected to sink during the simulation. In the second case, an increase of mean non-dimensional lift force of 0.1 is introduced by adjusting the parameters based on the present preliminary model so as to reduce the sink rate of the insect during the same course of wing beat cycles as the reference case. In the third case, an increase of the mean non-dimensional drag force towards the positive y-axis direction with a magnitude of 0.2 is introduced. The results are obtained and compared with the reference case in Figure 6.18 and Figure 6.19.

The plot starts in the 5<sup>th</sup> cycle as prior to which FSI evaluation was not carried out and the insect was simply performing prescribed flapping motion while being fixed in position and orientation. Figure 6.18 shows clearly the effect of increase of mean lift force on the movement of the centre of mass of the insect along the z-axis (vertical). The model insect is better able to maintain altitude with the increased mean lift force due to the parameter adjustment. The movement of centre of mass in the y-axis (forward) is almost identical to the referenced case as expected. Figure 6.19 shows the effect of increasing the mean drag force on the insect's centre of mass. The observed forward movement of the insect in the reference kinematics is due to a small pitch down moment on the body generated by a very slight forward positioning of its centre of mass relative to the centre of lift produced by the wing pair. The positive drag reduces the forward movement of the insect due to the pitch down moment effectively as seen in the plot, whereas the effect on the downward (sinking) motion of the insect is almost unaffected.

The aforementioned results hence justify the applicability of the present preliminary model for prediction of the mean aerodynamic forces and moments of a flapping wing pair through small variation of kinematic parameters and provide the proof of concept for the possibility of deriving an effective flapping wing control model through the current approach.

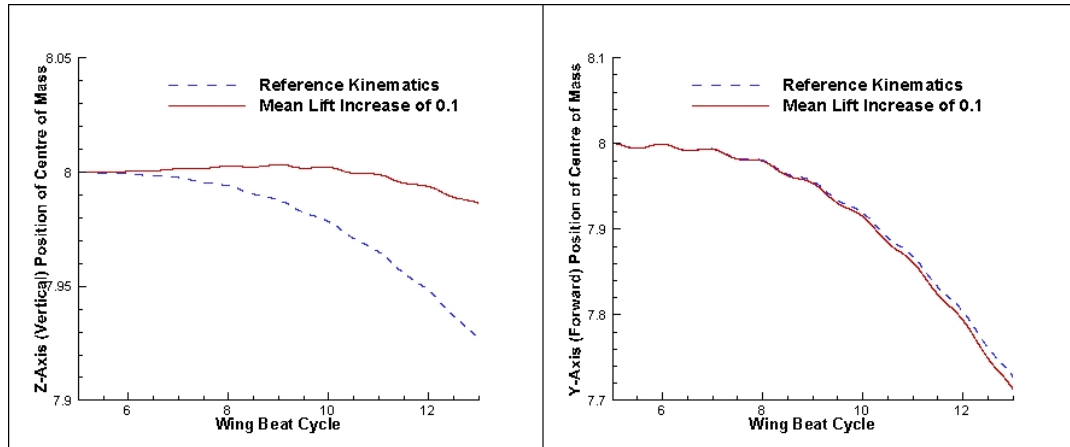


Figure 6.18 The effect of parameter variation to cause non-dimensional lift force increase of 0.1 in accordance to the preliminary model on Z-Axis (vertical) positional change and Y-Axis (forward) position change of the centre of mass over the wing beat cycles in a simulation with FSI computations

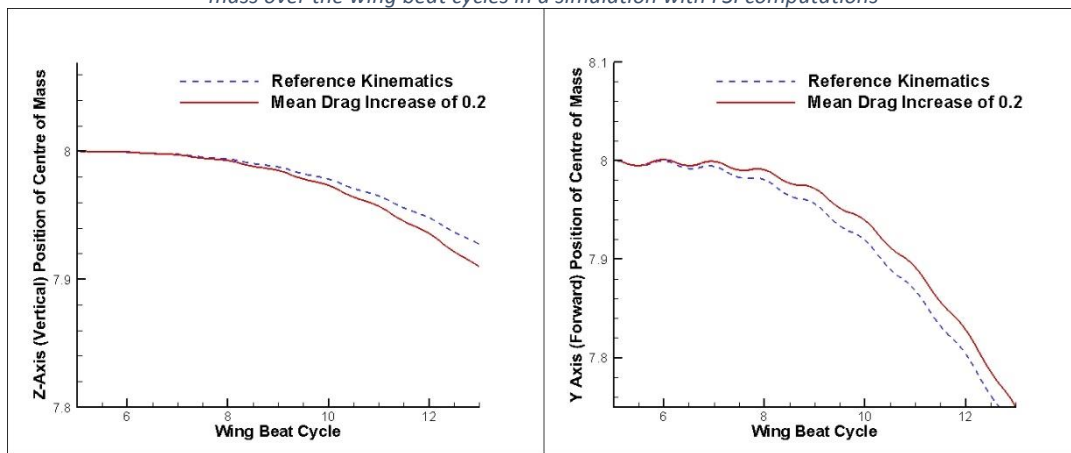


Figure 6.19 The effect of parameter variation to cause non-dimensional drag force increase of 0.2 in accordance to the preliminary model on Z-Axis (vertical) positional change and Y-Axis (forward) position change of the centre of mass over the wing beat cycles in a simulation with FSI computations

## 6.5 Summary

This study has provided a systematic approach to describing flapping flight kinematics using a set of 8 specific parameters external to the mathematical description of kinematic functions. The parameters can be effectively and individually modified for control purposes. The relationship of the mean aerodynamic forces and moments produced by a flapping wing with respect to each individual kinematic parameter is evaluated and the result shows generally linear variations within the confinement of very small perturbation limits. The linear correlations are used to derive a preliminary control model of the insect on 6DOF forces and moments by a limited selection of the proposed parameters and a simple coefficient matrix. The series of verification simulations further reinforced the confidence of such approach by showing good agreement in dynamic response and the model predictions. FSI simulation of full insect

flapping flight also demonstrated the effectiveness of the present approach and provide the proof of concept for the possibility of deriving an effective flapping wing control model based on the preliminary model presented.

Other interesting unsteady aerodynamic effects due to kinematic adjustments have also been observed and presented in this chapter. The dihedral configuration of flapping wings have been observed to improve roll stability of flapping flight. However, the static roll stability can only be achieved at a bias of mean positional angle of mid-elevation plane of large magnitude (beyond  $15^\circ$ ). The “oval” shape flapping kinematics are observed to produce net mean drag (thrust) force even in a horizontal mean stroke plane due to significant wing-wake interactions of the flapping wings. Non-linearity effects beyond the perturbation limit and coupling of kinematic parameter effects on the resultant dynamic response are also demonstrated.

Further studies are hence required to extend the current preliminary model to a full active control model for flapping flights in hovering, free flight and manoeuvring. Investigation of the stability modes of the control model and derivation of higher order and more robust correlations of the parameters with the mean aerodynamic forces and moments produced by flapping wings can be carried out. The unsteady transient aerodynamic effects of changes in flapping kinematics can also be further explored to supplement the current understanding of the mean aerodynamic effects of the flapping kinematic parameters.

# CHAPTER 7: Conclusions and Recommendations

## 7.1 Conclusions

In the present study, the Singular Value Decomposition-General Finite Difference based computational fluid dynamics solver for three dimensional incompressible, viscous fluid flow at low Reynolds number with immersed moving boundaries is further developed and adapted to study the unsteady aerodynamics of flapping wings. Numerical improvements and implementations such as artificial dissipation, fluid-structure-interaction and meshless nodal selection schemes are carried out. The numerical scheme's efficiency and convergence behaviour using different Poisson solvers are studied. Validations of simple unsteady 3D flow past sphere problem and FSI simulation of falling sphere demonstrate the capabilities and accuracies of the current numerical solver.

The study establishes a systematic and accurate geometric modelling method to construct and mesh a complex irregular shaped body and wings of natural insects with reasonable rigid body assumptions. The detailed kinematic modelling technique developed in this study provided the ground work of setting up and constructing flapping motion mechanisms for future numerical studies. The proposed natural spline interpolation based flapping kinematics definition framework is proven to be robust and effective at simulating observed natural flapping flight motions of real insects as well as describing simple flapping kinematics such as SHM.

Validation of the present numerical scheme with an experimental simulation of a flapping fruit fly wing with SHM kinematics shows very good agreement in aerodynamic force productions. This sets the fundamental confidence of the numerical scheme including the implementations of geometric and kinematic modelling methods in the present studies. The investigation of unsteady aerodynamics associated with different flapping kinematics reveals that SHM flapping kinematics of geometrically accurate insect wing is capable of generating more lift force as compared TF based flapping kinematics at the same Reynolds. An optimised TF based flapping kinematic model is proposed that is capable of producing equivalent mean aerodynamic lift as the corresponding SHM flapping kinematics model. The aerodynamic power analysis of



the two revealed that a TF based kinematic model is more efficient and hence a possibly better design for future flapping wing based MAVs.

The systematic three dimensional numerical study of clap-and-fling mechanism for a pair of rigid fruit fly wings at Reynolds number of 150 provided important evidence of three dimensional unsteady aerodynamic behaviours associated with the mechanism. Aerodynamic force measurements show that the 3D clap mechanism provides insignificant lift, unlike the observations of 2D simulations. Instead, it could enhance lift generation of the following fling mechanism. Further flow analysis revealed that lift enhancement of fling mechanism may be due to an enhanced wake interaction of vortices as the formation of a strong vortex link in the opening gap between the wings that are first observed in 3D flow visualisations. Significant difference of the 3D flow evolution of clap-and-fling mechanism as compared to 2D analysis is further demonstrated by the observation of a higher positive (outward) radial force peak during fling when compared to the symmetric reference kinematics. The effect of Reynolds number on the lift enhancement of clap-and-fling mechanism is investigated and show a reducing efficiency of lift to aerodynamic power ratio with reducing Reynolds number.

The study also established that the lift enhancement of clap-and-fling mechanism is not only dependent on the wing tip separation of the wings but also the wing root (hinge) separation. This could suggest that the ability of insects for using clap-and-fling mechanism in flapping flights is determined by the natural evolution of their anatomies. Furthermore, the specific lift augmentation to aerodynamic power ratio is evaluated and shown to be linear. Hence, it suggests that the unsteady aerodynamic effects of clap-and-fling could be readily exploited by insects with no significant penalties on the requirement of effort.

A systematic approach of parameterisation of flapping wing kinematics based on a set of 8 independently varied parameters for control purpose is provided and evaluated. A linear relationship of the mean aerodynamic forces and moments produced by a flapping wing with respect to each individual kinematic parameter is identified within small limit of perturbations from the reference state. The linear correlation is used to derive a preliminary control model of the insect on 6DOF forces and moments by a selection of a few parameters. The dynamic response of this preliminary model is

analysed and possible limitations of the present preliminary model are discussed. A proof of concept test of the present preliminary model in FSI simulation demonstrates the effectiveness of the approach. Hence, further development of a full active control model based on the present preliminary model can be continued.

## **7.2 Recommended Future Works**

The systematic approach of simulating insect flapping wing flights using SVD-GFD numerical scheme with accurate geometric and kinematic modelling techniques developed in the present study have made available many possibilities of further studies on unsteady aerodynamic effects of flapping wings. The research topics covered in the thesis are recommended to be extended in the following directions.

1. The effect of wing flexibility on clap-and-fling flapping kinematics and the resultant three dimensional unsteady aerodynamic effects can be investigated. The lift augmentation ratio and the aerodynamic power efficiency can be compared with present rigid wing results.
2. The flow field analysis of 3D clap-and-fling mechanisms can be further extended and the unsteady aerodynamic effects quantified.
3. The current preliminary flapping flight control model based on small kinematic perturbations can be further extended into a full active control model for flapping flight.
4. Derivation of higher order and more robust correlations of the kinematic parameters with the mean aerodynamic forces and moments produced by flapping wings can be carried out and the perturbation limit of the current preliminary model can be extended.

The investigation of unsteady aerodynamics of flapping wings in the present study have achieved significant results and should be expanded to provide the knowledge foundations for the eventual design of flapping wing based MAVs.

## Reference

- Abraham, F. (1970). Functional dependence of drag coefficient of a sphere on Reynolds number. *Physics of Fluids*, *13*, 2194–2195.
- Altshuler, D. L., Dickson, W. B., Vance, J. T., Roberts, S. P., & Dickinson, M. H. (2005). Short-amplitude high-frequency wing strokes determine the aerodynamics of honeybee flight. *Proceedings of the National Academy of Sciences of the United States of America*, *102*(50), 18213–8.
- Amritkar, A., Tafti, D., Liu, R., Kufrin, R., & Chapman, B. (2012). OpenMP parallelism for fluid and fluid-particulate systems. *Parallel Computing*, *38*(9), 501.
- Ansari, S. A., Zbikowski, R., & Knowles, K. (2006). Aerodynamic modelling of insect-like flapping flight for micro air vehicles. *Progress in Aerospace Sciences*, *42*(2), 129–172.
- Aono, H., Liang, F., & Liu, H. (2008). Near- and far-field aerodynamics in insect hovering flight: an integrated computational study. *Journal of Experimental Biology*, *211*(2), 239–257.
- Aono, H., & Liu, H. (2012). Flapping wing aerodynamics of a numerical biological flyer model in hovering flight. *Computers & Fluids*.
- Berg, C., & Ellington, C. P. (1997). The three-dimensional leading-edge vortex of a “hovering” model hawkmoth. *Philosophical Transactions: Biological Sciences*, *352*(1351), 329–340.
- Birch, J. M., & Dickinson, M. H. (2001). Spanwise flow and the attachment of the leading-edge vortex on insect wings. *Nature*, *412*(6848), 729–733.
- Birch, J. M., & Dickinson, M. H. (2003). The influence of wing-wake interactions on the production of aerodynamic forces in flapping flight. *Journal of Experimental Biology*, *206*(13), 2257–2272.
- Chew, C. S., Yeo, K. S., & Shu, C. (2006). A generalized finite-difference (GFD) ALE scheme for incompressible flows around moving solid bodies on hybrid meshfree- Cartesian grids. *Journal of Computational Physics*, *218*, 510–548.
- Chorin, A. J. (1969). On the convergence of discrete approximations to the Navier-Stokes equations. *Mathematics of Computation*, *23*(106), 341.
- Dickinson, M. H. (1994). The effects of wing rotation on unsteady aerodynamic performance at low Reynolds numbers. *Journal of Experimental Biology*, *192*, 179–206.

- Dickinson, M. H., & Gotz, K. G. (1993). Unsteady aerodynamic performance of model wings at low Reynolds numbers. *Journal of Experimental Biology*, *174*(1), 45–64.
- Dickinson, M. H., Lehmann, F.-O., & Sane, S. P. (1999). Wing rotation and the aerodynamic basis of insect flight. *Science*, *284*(5422), 1954–1960.
- Dickinson, M. H., & Tu, M. S. (1997). The function of dipteran flight muscle. *Comparative Biochemistry and Physiology - A Physiology*, *116*(3), 223–238.
- Ding, H., Yeo, K. S., & Xu, D. (2004). Development of least-square-based two-dimensional finite-difference schemes and their application to simulate natural convection in a cavity. *Computational Fluids*, *33*, 137–154.
- Duan, Y., & Tan, Y. (2005). Meshless Galerkin method based on regions partitioned into subdomains. *Applied Mathematics and Computation*, *162*, 317–327.
- Duarte, C. A., Liszka, T. J., & Tworzydło, M. (1996). Hp-Meshless cloud method. *Computational Methods in Applied Mechanics and Engineering*, *139*, 263–288.
- Dudley, R. (2002). *The biomechanics of insect flight: form, function, evolution*.
- Ellington, C. P. (1984). The aerodynamics of hovering insect flight. *Philosophical Transactions of the Royal Society of London. Series B, Biological Sciences*, *305*(1122), 1–181.
- Ellington, C. P. (1999). The novel aerodynamics of insect flight: applications to micro-air vehicles. *Journal of Experimental Biology*, *202*(23), 3439–3448.
- Ennos, A. R. (1989). The kinematics and aerodynamics of the free flight of some Diptera. *J. Exp. Biol.*, *142*, 49–85.
- Fletcher, R. (1976). Conjugate gradient methods for indefinite systems. In G. A. Watson (Ed.), *Lecture Notes in Mathematics 506* (Vol. 506, pp. 73–89).
- Fry, S. N., Rohrseitz, N., Straw, A. D., & Dickinson, M. H. (2009). Visual control of flight speed in *Drosophila Melanogaster*. *The Journal of Experimental Biology*, *212*(Pt 8), 1120–30.
- Fry, S. N., Sayaman, R., & Dickinson, M. H. (2003). The aerodynamics of free-flight, maneuvers in *Drosophila*. *Science*, *300*(5618), 495–498.
- Fry, S., Sayaman, R., & Dickinson, M. H. (2005). The aerodynamics of hovering flight in *Drosophila*. *Journal of Experimental Biology*, *208*(Pt 12), 2303–18.
- Gilmanov, A., & Sotiropoulos, F. (2005). A hybrid Cartesian/immersed boundary method for simulating flows with 3D, geometrically complex, moving bodies. *Journal of Computational Physics*, *207*(2), 457–492.

- Götz, K. G. (1987). Course-control, metabolism and wing interference during ultralong tethered flight in *Drosophila melanogaster*. *Journal of Experimental Biology*, *128*, 35–46.
- Hedrick, T. L., & Daniel, T. L. (2006). Flight control in the hawkmoth *Manduca sexta*: the inverse problem of hovering. *Journal of Experimental Biology*, *209*(Pt 16), 3114–30.
- Hilgenstock, A. (1988). A fast method for the elliptic generation of three-dimensional grids with full boundary control. *Numerical Grid Generation in Computational Fluid Mechanics '88*, 137–146.
- <http://flybase.org/>. (2013).
- Johnson, T. A., & Patel, V. C. (1999). Flow past a sphere up to a Reynolds number of 300. *Journal of Fluid Mechanics*, *378*(-1), 19–70.
- Kim, D., & Choi, H. (2006). Immersed boundary method for flow around an arbitrarily moving body. *Journal of Computational Physics*, *212*, 662–680.
- Kolomenskiy, D., Moffatt, H. K., Farge, M., & Schneider, K. (2011a). The Lighthill-Weis-Fogh clap-fling-sweep mechanism revisited. *Journal of Fluid Mechanics*, *676*, 572–606.
- Kolomenskiy, D., Moffatt, H. K., Farge, M., & Schneider, K. (2011b). Two- and three-dimensional numerical simulations of the clap-fling-sweep of hovering insects. *Journal of Fluids and Structures*, *27*(5-6), 784–791.
- Lehmann, F.-O., & Dickinson, M. H. (2001). The production of elevated flight force compromises manoeuvrability in the fruit fly *Drosophila melanogaster*. *The Journal of experimental biology*, *204*(Pt 4), 627–35.
- Lehmann, F.-O., Sane, S. P., & Dickinson, M. H. (2005). The aerodynamic effects of wing-wing interaction in flapping insect wings. *Journal of Experimental Biology*, *208*(16), 3075–3092.
- Li, Z., & Lai, M.-C. (2001). The immersed interface method for the Navier- Stokes equations with singular forces. *Journal of Computational Physics*, *171*, 822–842.
- Lighthill, M. (1973). On Weis-Fogh mechanism of lift generation. *Journal of Fluid Mechanics*, *60*, 1–17.
- Liszka, T. J., & Orkisz, J. (1980). The finite difference method at arbitrary irregular grids and its application in applied mechanics. *Computational Structures*, *11*, 83–95.
- Liu, H. (2009). Integrated modeling of insect flight: from morphology, kinematics to aerodynamics. *Journal of Computational Physics*, *228*(2), 439–459.

- Liu, H., & Kawachi, K. (1998). A numerical study of insect flight. *Journal of Computational Physics*, 146(1), 124–156.
- Lua, K. B., Lai, K. C., Lim, T. T., & Yeo, K. S. (2010). On the aerodynamic characteristics of hovering rigid and flexible hawkmoth-like wings. *Experiments in Fluids*, 49(6), 1263–1291.
- Marden, J. H. (1987). Maximum Lift Production During Takeoff in Flying Animals. *Journal of Experimental Biology*, 130(1), 235–258.
- Maxworthy, T. (1979). Experiments on the Weis-Fogh mechanism of lift generation by insects in hovering flight. Part 1. Dynamics of the. *Journal of Fluid Mechanics Digital Archive*, 93(01), 47–63.
- Miller, L. A., & Peskin, C. S. (2005). A computational fluid dynamics of 'clap and fling' in the smallest insects. *Journal of Experimental Biology*, 208(2), 195–212.
- Miller, L., & Peskin, C. S. (2009). Flexible clap and fling in tiny insect flight. *Journal of Experimental Biology*, 212(19), 3076–90.
- Miyan, J. A., & Ewing, A. W. (1985). How diptera move their wings: a re-examination of the wing base articulation and muscle systems concerned with flight. *Philosophical Transactions of the Royal Society of London, B* 311, 271–302.
- Morris, J. P., Fox, P. J., & Zhu, Y. (1997). Modeling Low Reynolds Number Incompressible Flows Using SPH. *Journal of Computational Physics*, 136, 214–226.
- Mou, X., & Sun, M. (2012). Dynamic flight stability of a model hoverfly in inclined-stroke-plane hovering. *Journal of Bionic Engineering*, 9(3), 294–303.
- Osborne, M. F. M. (1951). Aerodynamics of flapping flight with application to insects. *Journal of Experimental Biology*, 28(2), 221–245.
- Palma, P. D., Tullio, M. D., Pascazio, G., & Napolitano, M. (2006). An immersed-boundary method for compressible viscous flows. *Computational Fluids*, 35, 693–702.
- Ramamurti, R., & Sandberg, W. C. (2006). A computational investigation of the three-dimensional unsteady aerodynamics of *Drosophila* hovering and maneuvering. *Journal of Experimental Biology*, 210(5), 881–896.
- Rogers, S. E., & Kwak, D. (1990). An upwind differencing scheme for the time-accurate incompressible Navier-Stokes equations. *AIAA Journal*, 28, 253–262.
- Rogers, S. E., Kwak, D., & Kiris, C. (1991). Steady and unsteady solutions of the incompressible Navier-Stokes equations. *AIAA Journal*, 29, 603–610.

- Roos, F. W., & Willmarth, W. W. (1971). Some experimental results on sphere and disk drag. *AIAA Journal*, 9, 285–291.
- Saad, Y., & Schultz, M. H. (1986). GMRES: a generalized minimal residual algorithm for solving nonsymmetric linear systems. *SIAM Journal on Scientific and Statistical Computing*, 7(3), 856–869.
- Sane, S. P., & Dickinson, M. H. (2001). The control of flight force by a flapping wing: lift and drag production. *Journal of Experimental Biology*, 204(15), 2607–2626.
- Sane, S. P., & Dickinson, M. H. (2002). The aerodynamic effects of wing rotation and a revised quasi-steady model of flapping flight. *Journal of Experimental Biology*, 205(8), 1087–1096.
- Sato, M. (2002). OpenMP: parallel programming API for shared memory multiprocessors and on-chip multiprocessors. *International Symposium on System Synthesis*, 15, 109–111.
- Shyy, W., Aono, H., Chimakurthi, S. K., Trizila, P., Kang, C. K., Cesnik, C. E. S., & Liu, H. (2010). Recent progress in flapping wing aerodynamics and aeroelasticity. *Progress in Aerospace Sciences, Prog Aeros.*
- Sohn, M. H., & Chang, J. W. (2007). Flow visualization and aerodynamic load calculation of three types of clap-fling motions in a Weis-Fogh mechanism. *Aerospace Science and Technology*, 11(2-3), 119–129.
- Sun, M. (2005). High-lift generation and power requirements of insect flight. *Fluid Dynamics Research*, 37(1-2), 21–39.
- Sun, M., & Tang, J. (2002a). Lift and power requirements of hovering flight in *Drosophila virilis*. *Journal of Experimental Biology*, 205(16), 2413–2427.
- Sun, M., & Tang, J. (2002b). Unsteady aerodynamic force generation by a model fruit fly wing in flapping motion. *Journal of Experimental Biology*, 205(1), 55–70.
- Sun, M., & Wu, J. H. (2003). Aerodynamic force generation and power requirements in forward flight in a fruit fly with modeled wing motion. *Journal of Experimental Biology*, 206(17), 3065–3083.
- Sun, M., & Yu, X. (2003). Flows around two airfoils performing fling and subsequent translation and translation and subsequent clap. *Acta Mechanica Sinica/Lixue Xuebao*, 19(2), 103–117.
- Sun, M., & Yu, X. (2006). Aerodynamic force generation in hovering flight in a tiny insect. *AIAA Journal*, 44(7), 1532–1540.
- Thürmer, F., & Wüthrich, C. A. (1997). Normal computation for discrete surfaces in 3D space. *Computer Graphics forum*, 16, C15–C26.

- Vogel, S. (1967). Flight in *Drosophila*. II. Variations in stroke parameters and wing contour. *Journal of Experimental Biology*, 46, 431–443.
- Vorst, H. A. (1992). Bi-CGSTAB: A fast and smoothly converging variant of Bi-CG for the solution of nonsymmetric linear systems. *SIAM Journal on Scientific and Statistical Computing*, 13(2), 631–644.
- Wagner, H. (1925). Ueber die Entstehung des dynamischen Auftriebes von Tragflügeln. *Zeitschrift für Angewandte Mathematik und Mechanik*, 5, 17–35.
- Wakeling, J. M., & Ellington, C. P. (1997). Dragonfly flight. II. Velocities, accelerations and kinematics of flapping flight. *Journal of Experimental Biology*, 200(3), 543–556.
- Walker, S. M., Thomas, A. L. R., & Taylor, G. K. (2009). Deformable wing kinematics in free-flying hoverflies. *Journal of The Royal Society Interface*, -.
- Wang, H. (2003). Measuring wing kinematics, flight trajectory and body attitude during forward flight and turning maneuvers in dragonflies. *Journal of Experimental Biology*, 206(4), 745–757.
- Wang, X. Y., Yeo, K. S., Chew, C. S., & Khoo, B. C. (2008). A SVD-GFD scheme for computing 3D incompressible viscous fluid flows. *Computers & Fluids*, 37(6), 733–746.
- Wang, Z. J. (2008). Aerodynamic efficiency of flapping flight: analysis of a two-stroke model. *Journal of Experimental Biology*, 211(2), 234–238.
- Wang, Z. J., Birch, J. M., & Dickinson, M. H. (2004). Unsteady forces and flows in low Reynolds number hovering flight: two-dimensional computations vs robotic wing experiments. *Journal of Experimental Biology*, 207(3), 449–460.
- Weis-Fogh, T. (1973). Quick Estimates of Flight Fitness in Hovering Animals, Including Novel Mechanisms for Lift Production. *Journal of Experimental Biology*, 59, 169–230.
- Willmott, A. P., Ellington, C. P., & Thomas, A. L. R. (1997). Flow Visualization and Unsteady Aerodynamics in the Flight of the Hawkmoth, *Manduca sexta*. *Philosophical Transactions: Biological Sciences*, 352(1351), 303–316.
- Wu, D., Yeo, K. S., Lim, T. T., & Zhang, L. (2013). A numerical study of free hovering flight of a model insect at low-Re. *Unpublished*.
- Xu, J.-J., Li, Z., Lowengrub, J., & Zhao, H. (2006). A level-set method for interfacial flows with surfactant. *Journal of Computational Physics*, 212, 590–616.
- Yeo, K. S., Ang, S. J., & Shu, C. (2010). Simulation of fish swimming and manoeuvring by an SVD-GFD method on a hybrid meshfree-Cartesian grid. *Computers & Fluids*, 39(3), 403–430.



- Young, D. M. (1950). *Iterative methods for solving partial difference equations of elliptical type*.
- Yu, P., Yeo, K. S., Sundar, D. S., & Ang, S. J. (2011). A three-dimensional hybrid meshfree-Cartesian scheme for fluid-body interaction. *International Journal for Numerical Methods in Engineering*, 88(4), 385–408.
- Zanker, J. M., & Gotz, K. G. (1990). The Wing Beat of *Drosophila Melanogaster*. II. Dynamics. *Philosophical Transactions of the Royal Society of London. Series B, Biological Sciences*, 327(1238), 19–44.
- Zhang, L.-P., Chang, X.-H., Duan, X.-P., & Zhang, H.-X. (2009). Numerical simulations of the “clap-fling” motion for tiny insect wings. *Kongqi Donglixue Xuebao/Acta Aerodynamica Sinica*, 27(2), 246–254.